

Trick and treat: Cell-instructive and bactericidal nanopatterns for bone implants

Modaresifar, K.

DOI

[10.4233/uuid:aa5409dc-edb7-44f7-92ed-529e2cb575b3](https://doi.org/10.4233/uuid:aa5409dc-edb7-44f7-92ed-529e2cb575b3)

Publication date

2022

Document Version

Final published version

Citation (APA)

Modaresifar, K. (2022). *Trick and treat: Cell-instructive and bactericidal nanopatterns for bone implants*. [Dissertation (TU Delft), Delft University of Technology]. <https://doi.org/10.4233/uuid:aa5409dc-edb7-44f7-92ed-529e2cb575b3>

Important note

To cite this publication, please use the final published version (if applicable). Please check the document version above.

Copyright

Other than for strictly personal use, it is not permitted to download, forward or distribute the text or part of it, without the consent of the author(s) and/or copyright holder(s), unless the work is under an open content license such as Creative Commons.

Takedown policy

Please contact us and provide details if you believe this document breaches copyrights. We will remove access to the work immediately and investigate your claim.

Trick and treat

Cell-instructive and bactericidal nanopatterns
for bone implants

Trick and treat

Cell-instructive and bactericidal nanopatterns for bone implants

Proefschrift

ter verkrijging van de graad van doctor

aan de Technische Universiteit Delft,

op gezag van de Rector Magnificus, Prof.dr.ir. T.H.J.J. van der Hagen,

voorzitter van het College voor Promoties,

in het openbaar te verdedigen op woensdag 25 mei 2022 om 12:30 uur.

door

Khashayar MODARESIFAR

Master of Science in Biomedical Engineering,

Amirkabir University of Technology, Iran,

geboren te Teheran, Iran.

Dit proefschrift is goedgekeurd door de promotoren.

Samenstelling promotiecommissie bestaat uit:

Rector magnificus,	Voorzitter
Prof. dr. A.A. Zadpoor,	Technische Universiteit Delft, promotor
Dr. ir. L.E. Fratila-Apachitei,	Technische Universiteit Delft, copromotor

Onafhankelijke leden:

Dr. M. Riehle,	Universiteit van Glasgow
Prof. dr. J. de Boer,	Technische Universiteit Eindhoven
Prof. dr. G.J.V.M. van Osch,	Erasmus MC
Prof. dr. J. Dankelman,	Technische Universiteit Delft

Reserve lid:

Prof. dr. P.J. French,	Technische Universiteit Delft
------------------------	-------------------------------



The research leading to these results has received funding from the European Research Council under ERC agreement no. [677575].

Keywords: nanopatterns, bactericidal, osteogenic, mechanotransduction

Printed by: Gildeprint

Copyright © 2022 by K. Modaresifar

ISBN 978-94-6419-502-6

An electronic version of this dissertation is available at <http://repository.tudelft.nl/>

In memory of
Mohammad Ali Foroughi

To the Iranian people

Summary

Protecting orthopedic implants against aseptic and septic loosening is crucial for preserving their proper function until they outlive the patient, thereby avoiding additional costs and pain for the patients undergoing revision surgeries, and diminishing the risks of morbidity, and even mortality. Combating implant-associated infections has been a major research interest in the field of biomaterials science and engineering as they are among the major causes of implant failure. Up to now, extensive research has been carried out to develop surface coatings and advanced drug delivery systems that release antimicrobial agents at the implantation site. However, this approach to prevent/treat such infections has several potential adverse consequences such as developing antimicrobial resistance in pathogenic bacteria. On the other hand, integration of the implant to the host tissue is also essential for its proper function. Therefore, novel strategies that give rise to two functionalities, namely bactericidal and osteogenic properties, would be game-changers in this field.

Here, we took an alternative approach and shifted our focus to the physicochemical aspects of biomaterial's surface design to achieve the above-mentioned functionalities. In particular, we investigated the effects of precise nanoscale surface topographies, also known as nanopatterns, on the behavior of both prokaryotes and eukaryotes. Accordingly, different chapters of this thesis strive to answer fundamental questions regarding the effective geometrical designs of bactericidal and osteogenic nanopatterned surfaces and their underlying mechanisms following the overarching aim of providing new insights into the use of such advanced biointerfaces in orthopedic applications.

We started off by identifying the effective range of dimensions for nanopatterns that exhibit bactericidal properties based on the existing literature in Chapter 2. Our systematic review describes how geometrical parameters of nanopatterns, among other factors, influence the killing efficiency of bactericidal nanopatterns. We then used electron beam-induced deposition as a highly precise nanofabrication technique to create bioinspired nanopatterns with controlled geometry and arrangement that killed both Gram-negative and Gram-positive bacteria (Chapter 3). The killing efficiency was, however, significantly higher against Gram-negative bacteria. In Chapter 4, we further

studied the role of interspace and controlled disorder in the bactericidal properties of nanopatterns. While the controlled disorder was shown to be ineffective in enhancing the killing efficiency, decreasing the interspace significantly increased the percentage of damaged/dead bacteria by rupturing the bacterial cell wall.

To advance our knowledge of the interactions of mammalian cells with the nanopatterned surfaces, we fabricated a wide range of nanopatterns with systematically varied dimensions and investigated the early-stage adaptation of cells as well as their long-term osteogenic response to these nanopatterned surfaces (Chapter 5). We showed that cells residing on tall and dense nanopatterns generate a larger adhesion force, have a higher elastic modulus, and express higher levels of osteogenic markers compared to the cells residing on short nanopatterns or flat surfaces. In Chapter 6, we developed a new nanofabrication process that combines electron beam lithography and nanoimprint lithography to allow for the rapid high-throughput fabrication of highly precise nanopatterns over a large area and on different substrates. Our cell experiments confirmed that different geometrical designs of nanopatterns can significantly influence cell morphology, formation of focal adhesions, and cytoskeleton organization, resulting in differential levels of osteogenic markers expression.

Chapter 7 revolves around the use of black Ti as a dual-functional nanopatterned surface. We showed that inductively coupled plasma reactive ion etching can be used as a facile subtractive fabrication method to generate diverse configurations of high aspect ratio nanopillars on the titanium surface. Moreover, we achieved a nanopatterned surface with balanced bactericidal and osteogenic properties under certain processing parameters. This surface could kill Gram-positive bacteria through mechanical interactions and promote mineralization in preosteoblasts, a process most likely being regulated through focal adhesion-mediated signaling.

To elucidate the intracellular mechanotransduction pathways that direct cells toward osteogenic fate when residing on black Ti, we evaluated various hypotheses regarding the role of regulators of cell adhesion, contractility, and transcriptional factors (Chapter 8). Our results revealed that human mesenchymal stem cells are highly dependent on the activity of focal adhesion kinase and Rho-associated protein kinase to express osteogenic markers. The nuclear translocation of Yes-associated protein was also identified to be linked with the expression of osteogenic markers in response to the morphological changes in cells.

Overall, this work addresses several fundamental questions regarding the interactions of bacteria and mammalian cells with nanopatterned surfaces. Our insights, derived from an experimental approach, provide principles needed for the rational design of nanopatterned surfaces with outstanding and specific functionalities, suitable for and beyond orthopedic applications.

Samenvatting

Het beschermen van orthopedische implantaten tegen infectie en aseptisch losraken is cruciaal voor het behoud van hun goede functie gedurende de levensduur van de patiënt. Hierdoor worden extra kosten en pijn voor de patiënten die revisieoperaties ondergaan vermeden en het risico op morbiditeit alsook mortaliteit verminderd. De bestrijding van implantaat-geassocieerde infecties is een belangrijk onderzoeksonderwerp geweest op het gebied van biomaterialenwetenschap en -techniek, aangezien ze een van de belangrijkste oorzaken zijn van implantaatfalen. Tot op heden is er uitgebreid onderzoek gedaan om oppervlakcoatings en geavanceerde medicijnafgiftesystemen te ontwikkelen die antimicrobiële middelen afgeven vanaf het implantaatoppervlakte. Deze benadering om dergelijke infecties te voorkomen of te behandelen heeft echter verschillende, mogelijk nadelige gevolgen, zoals het ontwikkelen van antimicrobiële resistentie bij pathogene bacteriën. Aan de andere kant is de integratie van het implantaat in het botweefsel ook essentieel voor de goede werking ervan. Daarom zouden nieuwe strategieën die aanleiding geven tot beide functionaliteiten, namelijk bacteriedodende en osteogene eigenschappen, een doorbraak zijn op dit gebied.

In dit proefschrift hebben we een alternatieve benadering gekozen en onze focus verlegd naar de fysisch-mechanische aspecten van het oppervlakteontwerp van biomaterialen om de bovengenoemde functionaliteiten te bereiken. In het bijzonder hebben we de effecten onderzocht van precieze oppervlakteopografieën op nanoschaal, ook wel nanopatronen genoemd, op het gedrag van zowel prokaryoten als eukaryoten. Dienovereenkomstig streven verschillende hoofdstukken van dit proefschrift ernaar om fundamentele vragen te beantwoorden met betrekking tot de effectieve geometrische ontwerpen van bacteriedodende en osteogene oppervlakken met nanopatronen en hun onderliggende mechanismen, met als overkoepelend doel om nieuwe inzichten te verschaffen in het gebruik van dergelijke geavanceerde bio-interfaces in orthopedische toepassingen.

We zijn begonnen met het identificeren van het effectieve bereik van de dimensies van nanopatronen die bacteriedodende eigenschappen vertonen op basis van de bestaande literatuur in hoofdstuk 2. Onze systematische review beschrijft onder andere hoe geometrische parameters van nanopatronen de efficiëntie van bacteriedodende

nanopatronen beïnvloeden. Vervolgens gebruikten we elektronenstraal-geïnduceerde depositie, een zeer nauwkeurige nanofabricagetechniek, om bio-geïnspireerde nanopatronen te creëren met gecontroleerde geometrie en rangschikking die zowel Gram-negatieve als Gram-positieve bacteriën elimineerden (hoofdstuk 3). De efficiëntie van de nanopatronen waren echter significant hoger tegen Gram-negatieve bacteriën. In hoofdstuk 4 hebben we de rol van tussenruimte en gecontroleerde wanorde in de bacteriedodende eigenschappen van nanopatronen verder bestudeerd. Hoewel werd aangetoond dat de gecontroleerde wanorde niet effectief was in het verbeteren van de bacteriedodende eigenschappen, verhoogde het verminderen van de tussenruimte wel het percentage beschadigde/dode bacteriën aanzienlijk door de bacteriële celwand te beschadigen.

Om ons begrip van de interacties van zoogdiercellen met de oppervlakken met nanopatroon te vergroten, hebben we een breed scala aan nanopatronen met systematisch gevarieerde afmetingen gefabriceerd en de aanpassing van cellen in een vroeg stadium onderzocht, evenals hun osteogene respons op lange termijn op deze oppervlakken met nanopatronen (hoofdstuk 5). We toonden aan dat cellen die zich op hoge en dichte nanopatronen bevinden een grotere adhesiekracht genereren, een hogere elasticiteitsmodulus hebben en hogere niveaus van osteogene markers tot expressie brengen in vergelijking met de cellen die zich op korte nanopatronen of vlakke oppervlakken bevinden. In hoofdstuk 6 hebben we een nieuw nanofabricageproces ontwikkeld dat elektronenstraallithografie en nano-imprintlithografie combineert om de fabricage van grote aantallen zeer nauwkeurige nanopatronen over een groot oppervlak binnen een korte tijd en op verschillende substraten mogelijk te maken. Onze celexperimenten bevestigden dat verschillende geometrische ontwerpen van nanopatronen de cel morfologie, vorming van focale adhesies en cytoskeletorganisatie aanzienlijk kunnen beïnvloeden, wat resulteert in verschillende niveaus van expressie van osteogene markers.

Hoofdstuk 7 draait om het gebruik van zwarte Ti als een tweevoudig-functioneel nanopatroon oppervlak. We toonden aan dat inductief gekoppeld plasma etsen met reactieve ionen kan worden gebruikt als een gemakkelijke subtractieve fabricagemethode om verschillende configuraties van nanopilaren met een hoge aspectverhouding op het titaniumoppervlak te genereren. Bovendien bereikten we een oppervlak met nanopatroon met gebalanceerde bacteriedodende en osteogene eigenschappen onder bepaalde

verwerkingsparameters. Dit oppervlak kan Gram-positieve bacteriën doden door mechanische interacties en mineralisatie in preosteoblasten bevorderen, een proces dat hoogstwaarschijnlijk wordt gereguleerd door focale adhesie-gemedieerde signalering.

Om de intracellulaire mechanotransductieroutes bloot te leggen waardoor cellen die op Black Ti gekweekt worden naar het osteogene fenotype differentiëren, hebben we verschillende hypothesen geëvalueerd met betrekking tot de rol van regulatoren van celadhesie, contractiliteit en transcriptionele factoren (hoofdstuk 8). Onze resultaten lieten zien dat menselijke mesenchymale stamcellen sterk afhankelijk zijn van de activiteit van focal adhesion kinase en Rho-associated protein kinase om osteogene markers tot expressie te brengen. De nucleaire translocatie van Yes-associated protein werd ook gekoppeld aan de expressie van osteogene markers als reactie op de morfologische veranderingen in de cellen.

Over het algemeen behandelt dit werk verschillende fundamentele vragen met betrekking tot de interacties van bacteriën en zoogdiercellen met oppervlakken met nanopatronen. Onze inzichten, verkregen door middel van een experimentele benadering, bieden een basis voor het rationele ontwerp van oppervlakken met nanopatronen met uitstekende en specifieke functionaliteiten, geschikt voor orthopedische alsmede vele andere toepassingen.

Content

Summary	vii
Samenvatting	xi
1 Introduction	21
1.1 Background.....	22
1.2 Problem definition and thesis objectives.....	23
1.3 Thesis outline.....	24
Bibliography.....	26
2 Bactericidal nanopatterns	29
2.1 Introduction.....	30
2.2 Methods.....	32
2.3 Results.....	33
2.3.1 Literature search output.....	33
2.3.2 Effective dimensions of bactericidal nanopatterns.....	33
2.3.3 Cytocompatibility of nanopatterns.....	34
2.4 Discussion	35
2.4.1 Bactericidal mechanisms of nanopatterns.....	36
2.4.2 The role of surface affinity and surface adhesion	38
2.4.3 The effects of other nanopattern design parameters.....	39
2.4.4 The effects of bacterial-dependent characteristics.....	39
2.4.5 The role of extracellular polymeric substance (EPS).....	40
2.4.6 Interactions of mammalian cells with the nanopatterns	41
2.5 Conclusions.....	42
2.6 Supplementary information	43
Bibliography.....	53
3 Toward bioinspired bactericidal nanopatterns	61
3.1 Introduction.....	62
3.2 Materials and Methods.....	64

3.2.1 Nanopatterns design, fabrication, and characterization.....	64
3.2.2 Bacterial growth conditions.....	66
3.2.3 Evaluation of bactericidal properties.....	66
3.2.4 Statistical analysis.....	67
3.3 Results.....	67
3.3.1 Characterization of nanopatterns	67
3.3.2 Bactericidal activity of nanopatterns	68
3.4 Discussion	72
3.5 Conclusions.....	76
Bibliography.....	78
4 The effects of geometry on bactericidal properties.....	83
4.1 Introduction.....	84
4.2 Materials and Methods.....	85
4.2.1 Nanopatterns design, fabrication, and characterization.....	85
4.2.2 Preparation of bacterial cultures.....	87
4.2.3 Investigation of bactericidal properties.....	87
4.2.4 Investigation of nanopattern-bacteria interface	88
4.2.5 Statistical analysis.....	88
4.3 Results.....	89
4.3.1 Characteristics of the fabricated nanopatterns	89
4.3.2 Effect of interspacing on bactericidal properties	91
4.3.3 The effects of controlled disorder on bactericidal properties	92
4.3.4 Nanopattern-bacteria interface	93
4.4 Discussion	94
4.5 Conclusions.....	96
Bibliography.....	97
5 Cell adhesion, mechanics, and osteogenesis.....	101
5.1 Introduction.....	102
5.2 Materials and Methods.....	104
5.2.1 Fabrication of the patterns.....	104

5.2.2 Characterization of the patterns.....	105
5.2.3 Cell experiments.....	106
5.2.4 Computational models.....	109
5.3 Results and discussion.....	110
5.3.1 Characterization of the patterns.....	110
5.3.2 Differential effects of the patterns on cell adhesion, morphology, and elastic modulus.....	112
5.3.3 Effects of the patterns on the ECM.....	125
5.4 Conclusions.....	128
Bibliography.....	129
6 Nanoimprinting for upscaling the osteogenic nanopatterns.....	135
6.1 Introduction.....	136
6.2 Materials and Methods.....	138
6.2.1 Master mold fabrication by EBL.....	138
6.2.2 Interactions of MC3T3-E1 preosteoblast cells with the patterned surfaces.....	141
6.2.3 Contact angle measurements.....	142
6.2.4 Fabrication of the hybrid PDMS replica molds.....	142
6.2.5 Cross-sectional characterization using FIB milling.....	143
6.2.6 Pattern transfer from the hybrid PDMS replica mold to the substrate of interest by thermal nanoimprint.....	145
6.2.7 Statistical analysis.....	146
6.3 Results.....	146
6.3.1 Fabrication and characterization of the master mold.....	146
6.3.2 Adaptation of preosteoblasts to the patterned surfaces.....	147
6.3.3 Water contact angle.....	150
6.3.4 Fabrication and characterization of the replica mold.....	150
6.3.5 Characterization of the patterns transferred into the fused silica substrate through thermal nanoimprinting.....	151
6.4 Discussion.....	153
6.4.1 Interactions of MC3T3-E1 cells with patterns.....	153

6.4.2 Water contact angle	155
6.4.3 Hybrid PDMS molding	156
6.4.4 Thermal nanoimprint lithography	156
6.5 Conclusions.....	158
6.6 Supplementary information	160
Bibliography.....	161
7 On the use of black titanium	167
7.1 Introduction.....	168
7.2 Materials and Methods.....	171
7.2.1 Fabrication and characterization of bTi samples.....	171
7.2.2 Preosteoblast cell response to bTi surfaces.....	172
7.2.3 Bacterial studies.....	175
7.2.4 Statistical analysis.....	177
7.3 Results.....	177
7.3.1 Physicochemical characterization of bTi surfaces.....	177
7.3.2 Short-term response of preosteoblast cells	180
7.3.3 Expression of osteogenic markers in preosteoblast cells	185
7.3.4 Early bactericidal effects of bTi surfaces	185
7.4 Discussion	186
7.4.1 Looking at the Ti pillars from a physicochemical perspective.....	189
7.4.2 Adaptation of preosteoblast cells to bTi surfaces.....	190
7.4.3 FA-mediated mechanical interactions with the surface	191
7.4.4 Osteogenic properties of bTi from a mechanotransduction perspective	192
7.4.5 Early interactions of bacteria with bTi.....	194
7.5 Conclusions.....	195
7.6 Supplementary information	197
Bibliography.....	199
8 Mechanotransduction in high aspect ratio nanopatterns	205
8.1 Introduction.....	206
8.2 Materials and Methods.....	209

8.2.1 Fabrication and characterization of high aspect ratio bTi nanopillars.....	209
8.2.2 Investigating the response of hMSCs to high aspect ratio nanopillars.....	209
8.2.3 Inhibition studies	211
8.2.4 Fluorescence image analysis	212
8.2.5 Statistical analysis	213
8.3 Results.....	213
8.3.1 Characteristics of high aspect ratio bTi nanopillars.....	213
8.3.2 Effects of high aspect ratio nanopillars on the behavior of hMSCs	215
8.3.3 Effects of FAK inhibition on hMSCs.....	217
8.3.4 Effects of ROCK inhibition on hMSCs	219
8.3.5 Effects of YAP inhibition on hMSCs.....	219
8.4 Discussion	222
8.5 Conclusions.....	226
Bibliography.....	227
9 Concluding remarks.....	231
9.1 Main findings of this thesis.....	232
9.2 Additional remarks and recommendations	235
9.3 Future research outlook	239
Bibliography.....	241
Acknowledgements.....	243
List of publications	249
A. Peer-reviewed journal publications.....	249
B. Selected conference presentations.....	251
Curriculum Vitae.....	253

1

Introduction

“There is plenty of room at the bottom.”

- Richard Feynman

1.1 Background

Ever since the cognitive revolution in *Homo Sapiens*, our species has been dreaming of avoiding death and if not possible, redefining it, with the help of myths and ideologies. The modern-day human, however, is striving to enhance his/her lifetime and quality with the help of science and technology^{1,2}. The increased life expectancy worldwide during the last century is not merely a result of sustained global peace and welfare. The groundbreaking technologies and discoveries in life sciences have significantly contributed to this improvement. The vast efforts and investments in developing new drugs, vaccines, medical instruments, surgical techniques, artificial organs, and biomaterials have opened previously unimaginable horizons in which several highly contagious, lethal diseases have been eradicated, numerous surgeries are being done in a minimally invasive manner, and complications associated with aging may be undone through personalized medicine.

As a part of this general trend, millions of surgical procedures are being performed annually around the globe to implant a bone substitute or to replace joints in the bodies of patients who suffer from a critical-sized bone defect (for instance, caused by bone tumor resections or car accidents) or need a total joint replacement (for instance, due to osteoarthritis)³. Since such defects cannot be healed spontaneously, the rational design of the implanted biomaterial (*i.e.*, orthopedic implant) is crucial for its proper function, and to eventually assist tissue regeneration⁴. However, orthopedic implants may fail due to aseptic and/or septic loosening. Lack of stability, mismatching mechanical properties, and poor support of *de novo* tissue formation are some of the problems leading to aseptic loosening⁴. Besides, implant-associated infections (IAIs) are the main cause of the failure of orthopedic implants, resulting in morbidity and even mortality⁵. IAIs, which are caused by bacteria attachment and the formation of biofilms, are commonly treated by local delivery of antibiotics in the clinic⁶. To improve the methods for prevention/treatment of the IAIs, research laboratories have extensively attempted to develop surface modification techniques that allow for tunable and controlled release of antimicrobial agents³. Nevertheless, the growing crisis of antimicrobial resistance⁷⁻⁹, among other adverse consequences^{10, 11}, may eventually render such approaches inadequate. Non-adhesive surfaces are not very helpful either as they may hamper osteogenesis and osseointegration¹².

An alternative approach, inspired by several naturally occurring biosystems¹³, is to exploit the topography of a surface on which the bacteria attach to kill them via physicochemical interactions. Those biosystems (*e.g.*, certain insects' wings) contain complex and precise nanoscale topographies, also known as nanopatterns. Given that the behavior of mammalian cells (*e.g.*, adhesion, proliferation, migration, and differentiation) can be affected by surface nanotopography^{14,15} as well, an effective strategy can be devised to benefit from the unique properties of nanopatterns that enables them to simultaneously induce bactericidal and osteogenic properties. Achieving this goal would mark the emergence of a new generation of biomaterials: cell-instructive, self-defending implants with selective behavior toward pathogenic prokaryotic cells and the host eukaryotic cells.

1.2 Problem definition and thesis objectives

As already discussed, surface nanopatterns can induce a vast range of responses to bacteria and mammalian cells. Yet, the optimum geometrical characteristics of such nanopatterns and the effective range of the shapes and dimensions of the nanofeatures to be created on the surface of the biomaterials remain largely elusive. In addition, the mechanisms by which a certain type of nanopattern can trigger those responses in the cells and bacteria are not fully understood.

The early reports on the observation of the bactericidal effects of naturally occurring nanopatterns in 2012¹⁶ were followed by attempts to synthetically replicate them¹⁷. In 2017, when the studies presented in this thesis started, the effective dimensions for bactericidal nanopatterns were still not clearly known. Furthermore, controversy existed over the action mechanisms of these nanopatterns^{18,19}. On the other hand, despite the striking findings over the osteogenic properties of nanopatterned surfaces, dating back to the 2000s, these studies were mainly concerned with nanopatterns of a very different shape as compared to the later bactericidal ones (*i.e.*, nanopits *vs.* nanopillars)²⁰, making it difficult to hypothesize/conclude over their possible dual-functionalities. Today, the design and fabrication of dual-functional nanopatterns remains an inadequately met challenge, especially due to the yet insufficient understanding of the factors governing the interactions of the nanopatterns with the bacteria/cells.

Given such a state-of-the-art, this thesis aims to advance our understanding of dual-functional nanopatterned surfaces and to shed light on the origins of these functionalities. As explained before, several aspects of the design and fabrication of nanopatterns, which

are governed by the limitations and capabilities of the available nanofabrication techniques, have significantly influenced the consequent functionalities. Moreover, the complexity of living systems and the dynamic nature of their intracellular pathways make the control over cell-biomaterial interactions even more intricate. The overall aim of this thesis can, therefore, be defined in terms of five major research objectives as follows:

1. To identify the effective range of dimensions for bactericidal nanopatterns.
2. To explore the efficiency of a rationally designed nanopatterned surface with dimensions within the identified range against different types of bacteria, and study the role of the most influential geometrical characteristic of that nanopattern in determining the killing mechanism and efficiency.
3. To study the adaptation and osteogenic response of bone-making cells to nanopatterns with systematically altered dimensions.
4. To design, fabricate, and study a nanopatterned surface exhibiting both bactericidal and osteogenic properties, appropriate for translational applications.
5. To explore the subcellular events through which the dual-functional nanopattern can enhance osteogenesis.

Overall, this thesis tries to answer several important ‘*whats*’ and ‘*whys*’ regarding the rare and/or unprecedented properties and functionalities of nanopatterned surfaces from a (mechano)biological point of view.

1.3 Thesis outline

Eight chapters follow this introductory chapter, covering the research objectives outlined above.

In **Chapter 2**, we review the existing literature on the relationship between the geometrical parameters of nanopatterns (*e.g.*, height, diameter, interspacing, aspect ratio, *etc.*) and their bactericidal properties. While identifying an effective range of dimensions, we also briefly discuss another factors affecting the killing efficiency of bactericidal nanopatterns, such as surface affinity and strain-dependent characteristics, *etc.* In **Chapters 3 and 4**, a nanoscale additive manufacturing technique (*i.e.*, electron beam-induced deposition) is exploited to fabricate precisely controlled nanopatterns with dimensions within the identified effective range. We first study what impact these nanopatterned surfaces has on the survival of both Gram-positive and Gram-negative

bacteria, and then evaluate the hypothesis that interspacing is a key design parameter to enhance the bactericidal properties of the nanopatterns.

The highly precise nanofabrication techniques usually suffer from a low throughput that makes them far from ideal for patterning a large area required for mammalian cell studies. Moreover, mammalian cells are known to be affected by nanopatterns with a wider range of dimensions. Therefore, we continue our studies by exploiting alternative nanofabrication techniques to cover a broader range of dimensions (*i.e.*, submicron scale) and shift our focus to the interactions of bone-making cells (*e.g.*, preosteoblasts) with these scaled-up nanopatterned areas. In **Chapter 5**, we explore the early-stage adaptation of the cells to nanopatterns with systematically varied dimensions that are fabricated by two-photon polymerization technology. We also study the long-term osteogenic response to the surface. The connection between the early-stage confrontation of the cells with nanopatterns and the cell fate is another topic studied here. **Chapter 6** describes the development of a new nanofabrication process that combines electron beam lithography and nanoimprint lithography to resolve the irreconcilable contradiction between the precision and throughput of common fabrication techniques, making it possible to pattern an enlarged area with nanopatterns of interest within a short time and on different substrates. Exploiting this new fabrication process, we investigate whether nanopatterns studied in the preceding chapter exhibit the same functionality when made of a different material.

Based on the findings obtained in the preceding chapters, we present the design and fabrication of dual-functional nanopatterned titanium surfaces (known as black Ti) in **Chapter 7**. Here, inductively coupled plasma reactive ion etching is used as a facile subtractive fabrication method to generate multiple configurations of high aspect ratio nanopillars on the titanium surface. We explore the effects of distinct configurations on the fate of bacteria and preosteoblasts via comprehensive biological assessments and conclude what combination of processing parameters yields a surface with balanced osteogenic and bactericidal properties. Moreover, to identify the intracellular mechanotransduction pathways which trigger the osteogenic differentiation of the cells residing on black Ti, we evaluate various hypotheses regarding the role of regulators of cell adhesion, contractility, and transcriptional factors (**Chapter 8**).

Finally, we review the main findings of this thesis and present some concluding remarks, and provide an outlook toward future research directions (**Chapter 9**).

Bibliography

- [1] J.R. Fishman, R.H. Binstock, M.A. Lambrix, Anti-aging science: The emergence, maintenance, and enhancement of a discipline, *Journal of Aging Studies*, 22(4), 295-303, 2008.
- [2] J. Harris, Intimations of immortality, *Science*, 288(5463), 59-59, 2000.
- [3] C.R. Arciola, D. Campoccia, L. Montanaro, Implant infections: adhesion, biofilm formation and immune evasion, *Nature Reviews Microbiology*, 397-409, 2018.
- [4] A.A. Zadpoor, Meta-biomaterials, *Biomaterials Science*, 8(1), 18-38, 2020.
- [5] W. Zimmerli, A. Trampuz, P.E. Ochsner, Prosthetic-joint infections, *New England Journal of Medicine*, 351(16), 1645-1654, 2004.
- [6] S. Amin Yavari, S.M. Castenmiller, J.A. van Strijp, M. Croes, Combating Implant Infections: Shifting Focus from Bacteria to Host, *Advanced Materials*, 32(43), 2002962, 2020.
- [7] S.B. Levy, B. Marshall, Antibacterial resistance worldwide: causes, challenges and responses, *Nature Medicine*, 10(12), S122-S129, 2004.
- [8] K. Bush, P. Courvalin, G. Dantas, J. Davies, B. Eisenstein, P. Huovinen, G.A. Jacoby, R. Kishony, B.N. Kreiswirth, E. Kutter, Tackling antibiotic resistance, *Nature Reviews Microbiology*, 9(12), 894-896, 2011.
- [9] A. Panáček, L. Kvítek, M. Smékalová, R. Večeřová, M. Kolář, M. Röderová, F. Dyčka, M. Šebela, R. Prucek, O. Tomanec, Bacterial resistance to silver nanoparticles and how to overcome it, *Nature Nanotechnology*, 13(1), 65-71, 2018.
- [10] L.Q. Chen, L. Fang, J. Ling, C.Z. Ding, B. Kang, C.Z. Huang, Nanotoxicity of silver nanoparticles to red blood cells: size dependent adsorption, uptake, and hemolytic activity, *Chemical Research in Toxicology*, 28(3), 501-509, 2015.
- [11] R.P. Singh, P. Ramarao, Cellular uptake, intracellular trafficking and cytotoxicity of silver nanoparticles, *Toxicology Letters*, 213(2), 249-259, 2012.
- [12] D. Puleo, A. Nanci, Understanding and controlling the bone-implant interface, *Biomaterials*, 20(23-24), 2311-2321, 1999.
- [13] A. Elbourne, R.J. Crawford, E.P. Ivanova, Nano-structured antimicrobial surfaces: From nature to synthetic analogues, *Journal of Colloid and Interface Science*, 508, 603-616, 2017.
- [14] M.J. Dalby, N. Gadegaard, R.O. Oreffo, Harnessing nanotopography and integrin-matrix interactions to influence stem cell fate, *Nature Materials*, 13(6), 558-569, 2014.
- [15] M.M. Stevens, J.H. George, Exploring and engineering the cell surface interface, *Science*, 310(5751), 1135-1138, 2005.
- [16] E.P. Ivanova, J. Hasan, H.K. Webb, V.K. Truong, G.S. Watson, J.A. Watson, V.A. Baulin, S. Pogodin, J.Y. Wang, M.J. Tobin, Natural bactericidal surfaces: mechanical rupture of *Pseudomonas aeruginosa* cells by cicada wings, *Small*, 8(16), 2489-2494, 2012.
- [17] A. Tripathy, P. Sen, B. Su, W.H. Briscoe, Natural and bioinspired nanostructured bactericidal surfaces, *Advances in Colloid and Interface Science*, 248, 85-104, 2017.
- [18] C.D. Bandara, S. Singh, I.O. Afara, A. Wolff, T. Tesfamichael, K. Ostrikov, A. Oloyede, Bactericidal effects of natural nanotopography of dragonfly wing on *Escherichia coli*, *ACS Applied Materials & Interfaces*, 9(8), 6746-6760, 2017.

-
- [19] D.P. Linklater, S. Juodkazis, S. Rubanov, E.P. Ivanova, Comment on “Bactericidal Effects of Natural Nanotopography of Dragonfly Wing on *Escherichia coli*”, *ACS Applied Materials & Interfaces*, 9(35), 29387-29393, 2017.
- [20] M.J. Dalby, N. Gadegaard, R. Tare, A. Andar, M.O. Riehle, P. Herzyk, C.D. Wilkinson, R.O. Oreffo, The control of human mesenchymal cell differentiation using nanoscale symmetry and disorder, *Nature Materials*, 6(12), 997-1003, 2007.

Bactericidal nanopatterns

We systematically review the currently available evidence on how the design parameters of surface nanopatterns (*e.g.*, height, diameter, and interspacing) relate to their bactericidal behavior. The systematic search of the literature resulted in 46 studies that satisfied the inclusion criteria of examining the bactericidal behavior of nanopatterns with known design parameters in absence of antibacterial agents. Twelve of the included studies also assessed the cytocompatibility of the nanopatterns. Natural and synthetic nanopatterns with a wide range of design parameters were reported in the included studies to exhibit bactericidal behavior. However, most design parameters were in the following ranges: heights of 100-1000 nm, diameters of 10-300 nm, and interspacings of < 500 nm. The most commonly used type of nanopatterns were nanopillars, which could kill bacteria in the following range of design parameters: heights of 100-900 nm, diameters of 20-207 nm, and interspacings of 9-380 nm. The vast majority of the cytocompatibility studies (11 out of 12) showed no adverse effects of bactericidal nanopatterns with the only exception being nanopatterns with extremely high aspect ratios. This chapter concludes with a discussion on the evidence available in the literature regarding the killing mechanisms of nanopatterns and the effects of other parameters including surface affinity of bacteria, cell size, and extracellular polymeric substance (EPS) on the killing efficiency.

2.1 Introduction

Recurrent bacterial infection is one of the major causes of implant failure¹, hugely impacting the patients' quality of life and ultimately resulting in morbidity and even mortality². This type of infection starts off with the attachment of the bacteria to the implant surface, leading to biofilm formation and, thus, high resistance against antibacterial agents³. To date, numerous strategies have been proposed to prevent biofilm formation and implant-associated infections. The main working mechanisms of the proposed strategies are preventing bacteria from adhering to surfaces, killing bacteria that manage to attach to the surface, and a combination of both aforementioned approaches. Examples of the first approach are antibiofouling surfaces that are made by altering the chemical and/or physical properties of the surface, thereby making them highly unfavorable for cell and bacteria attachment. The result is a non-adhesive or cell-repellent surface (Figure 2.1)⁴. This strategy may be suitable for implants whose integration in the body is not dependent on tissue regeneration. However, many implantable medical devices, in general, and orthopedic implants, in particular, require a substantial amount of tissue regeneration to support osseointegration and implant fixation. It is, therefore, important that the implant surface supports cell attachment and proliferation while inhibiting bacterial growth⁵.

The second approach is based upon surfaces that allow for cell adhesion but kill the bacteria upon contact. They are sometimes called bactericidal surfaces and are the holy grail of implant surface design. The primary working mechanism of bactericidal surfaces is either chemical or physical. Common chemical methods use surface bio-functionalization or surface coatings to enhance the antibacterial properties of the surface. For instance, coatings releasing antibiotics⁶⁻⁸ and silver ions⁹⁻¹³ have been shown to be effective in killing bacteria and preventing biofilm formation. However, antibacterial agents such as antibiotics or silver nanoparticles may cause different types of toxicity including cytotoxicity^{9, 14}, nanotoxicity¹⁵, or nephrotoxicity¹⁶. In addition, the continuous low-dose release of antibacterial agents, which is required for long-term protection against implant-associated infections, may cause the bacterial strains to develop resistance against those agents¹⁷. Furthermore, it has been recently shown that after repeated exposure to silver nanoparticles, some bacterial strains develop resistance against them even without mutations¹⁸.

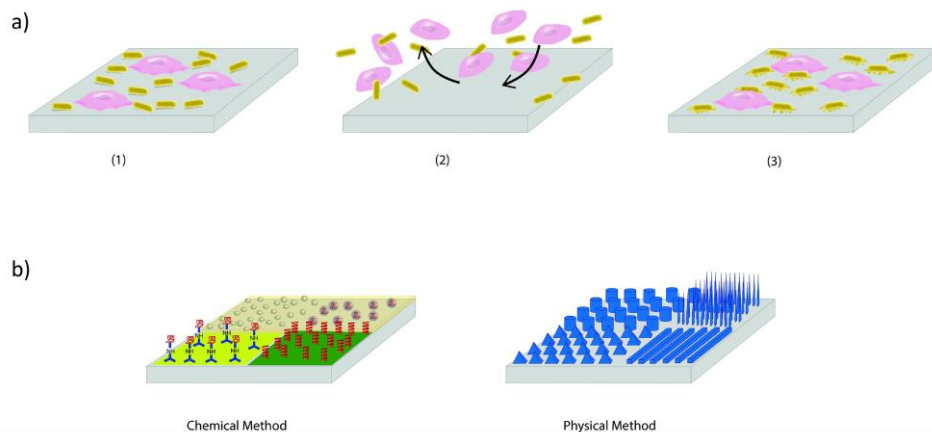


Figure 2.1. Different approaches to design antibacterial surfaces. a) 1. Common surfaces, which were traditionally used in biomaterials engineering, are a favorable place for attachment and growth of both bacteria and human cells; 2. Antibiofouling surfaces have been developed that do not allow microorganisms to adhere to the biomaterial surface and prevent possible bacterial infections; 3. Novel desirable advanced surfaces, which are designed and fabricated to kill the bacteria while supporting human cells growth in order to improve the function of implants and tissue engineering scaffolds. b) Two main approaches in the design of surfaces of advanced biomaterials are chemical and physical modifications. The former is usually associated with coating or chemical grafting of functional groups and/or antibiotics to the surface in order to kill the bacteria. The physical methods, on the other hand, concern with fabricating nanoscale structures with specific dimensions on the surface that could mechanically kill the bacteria through different mechanisms. Recent advances in nanofabrication methods and the problem of antibiotic resistance have made the physical approach more interesting.

The above-mentioned limitations of the chemical approach underscore the importance of physical mechanisms to combat implant-associated infections. The fact that physical cues such as substrate stiffness and roughness, or surface micro/nanotopography influence the behavior of both bacterial¹⁹⁻²² and mammalian cells²³⁻²⁷, is a relatively recent discovery. Several studies during the past decades have investigated the effects of surface topography on cell attachment, proliferation, and differentiation, as well as bacterial adhesion and motility, revealing the fact that both eukaryote and prokaryote cells could sense the surface topography at both micro- and nano-scales²⁸⁻³⁰. Due to the recent advances in micro- and nano-fabrication techniques, it is now feasible to produce surfaces with arbitrarily complex and precisely controlled surface nanotopography, also known as nanopatterns^{29, 31-33}. It has been shown that nanopatterns are powerful tools for directing the stem cell fate³⁴. Nanopatterns appear in

different shapes like nanopillars, nanogrooves, and nanopits with different sizes in height, width, depth, and spacing, which are dependent on the fabrication technique. Subsequently, the feature size modulates the interaction of nanopatterns with cells. Not only could surface nanotopography determine stem cell fate, many studies have shown that high aspect ratio nanopatterns are capable of killing bacteria^{35, 36} and preventing biofilm formation³⁷.

An important question regarding the bactericidal behavior of nanopatterns is the optimum design parameters to maximize the bactericidal behavior while minimizing the potential adverse effects such as cytotoxicity. An increasing number of studies have addressed this research question during the last decade. Given that nature has always been a great source of inspiration for developing advanced materials and systems with a wide range of applications such as self-cleaning surfaces³⁸, antibiofouling surfaces³⁹, and reversible adhesive surfaces⁴⁰, bioinspired surfaces have been studied in this context too. For instance, cicada wings are known to be lethal against a wide range of Gram-negative bacteria⁴¹. Further studies on similar surfaces have led to reproducing nanopatterns of similar size and shape on implantable biomaterials^{37, 42}. Despite a growing body of knowledge in this area, there is currently no systematic study of the available evidence to understand how the different design parameters of nanopatterns influence their bactericidal behavior. Here, we present a systematic review of the relevant data available in the literature to provide a guideline for designing bactericidal nanopatterns and to contribute toward the development of a quantitative theory of how nanopatterns kill bacteria.

2.2 Methods

We used Web of Science and Scopus as our primary search databases, while Google Scholar served as a supplementary database. Different combinations of the following groups of keywords were searched for: (nanotopography OR nanopattern OR nanotube OR nanopillar OR nanopit OR nanocolumn), (bactericidal OR antibacterial), (bacterial adhesion OR bacterial proliferation OR bacteria), and (mechanotransduction OR mechanosensing). The keyword search resulted in 642 initial hits. Two inclusion criteria were used when screening the abstracts of the articles.

Firstly, the articles should have investigated the antibacterial effects of nanopatterns with controlled or characterized shapes and dimensions. This criterion excluded the studies on surface nano-roughness and the studies in which antibiotic-releasing

nanoparticles have been used. Secondly, the studies should have provided evidence of antibacterial activity or at least discuss the possible killing mechanism induced by the nanopatterns. Based on the above-mentioned inclusion criteria, 105 documents were further examined to determine if they meet the following two conditions: 1) the article is an original research paper and not a review paper, book chapter, or a thesis; 2) the effects of nanopatterns are investigated in the absence of antibacterial agents. Moreover, reference tracking was carried out in the full-text of all articles in order to avoid missing any relevant studies. A total of 46 studies satisfied the inclusion criteria and are further discussed in the remainder of this chapter.

2.3 Results

The results of the literature search are detailed in Table S2.1 (see supplementary information) and summarized in this section.

2.3.1 Literature search output

Only 23 papers provided a comprehensive discussion or clearly presented a hypothesis regarding the possible killing mechanism of the nanopatterns and compared it to other studies. Moreover, Gram-negative and Gram-positive bacteria were respectively used in 34 and 32 studies, and 21 studies used both. Twelve studies also reported the effects of nanopatterns on mammalian cells.

The most common types of nanopatterns were nanopillars (21), nanowires (5), nanocolumns (3), nanopores (3), nanocones (3), spinule-like nanostructures (3), and nanospikes (2). From the 46 studies, 8 investigated nanopatterns found in nature and did not specify any fabrication method. The most common methods for fabrication of the nanopatterns included reactive ion etching (RIE) (9), hydrothermal treatment (5), anodizing (3), chemical etching (2), plasma etching (2), glancing angle sputter deposition (2), electrodeposition (2), and nanoimprint lithography (2). The most common types of materials used for creating the nanopatterns were silicon (13), titanium oxide (TiO₂) (8), titanium (4), poly(methyl methacrylate) (PMMA) (3), zinc oxide (ZnO) (2), and gold (2).

2.3.2 Effective dimensions of bactericidal nanopatterns

Nanopatterns with a wide range of dimensions were reported in the included studies to be bactericidal (Figure 2.2). The dimensions of the nanopatterns were usually presented in terms of height/length (H/L), diameter/width (D/W), and spacing (S).

Nanopillar arrays with $100 \text{ nm} < H < 900 \text{ nm}$, $20 \text{ nm} < D < 207 \text{ nm}$, and $9 \text{ nm} < S < 380 \text{ nm}$ have been found to be effective in killing bacteria. Similar effects were observed for nanocolumns with $250 \text{ nm} < H < 478 \text{ nm}$, $33 \text{ nm} < D < 300 \text{ nm}$, and $100 \text{ nm} < S < 200 \text{ nm}$. Nanocones with the following dimensions were also found to be bactericidal: $100 \text{ nm} < H < 350 \text{ nm}$, $10 \text{ nm} < D < 80 \text{ nm}$, and $175 \text{ nm} < S < 250 \text{ nm}$.

These ranges are somewhat wider when considering nanopatterns in the shape of spikes or spinules. Spikes with $S \approx 220 \text{ nm}$, $20 \text{ nm} < D < 200 \text{ nm}$, and $H > 200 \text{ nm}$ (up to $11 \mu\text{m}$) have been shown to display bactericidal characteristics. Natural spinules (mostly found on gecko's skin) and their synthetic replicas have a height in the microscale ($1\text{-}4 \mu\text{m}$) range but their diameters and spacing are in the nano and submicron scales ($10\text{-}85 \text{ nm}$ and $500\text{-}1000 \text{ nm}$, respectively).

As for nanowires, the reported dimensions are $298 \text{ nm} < H < 350 \text{ nm}$, $30 \text{ nm} < D < 143 \text{ nm}$, and $S \approx 77 \text{ nm}$. The few studies on nanopores, nanopits, and nanogrooves show that a depth of as small as 2.3 nm may be sufficient for inducing bactericidal behavior provided that it is combined with a diameter of $40\text{-}99 \text{ nm}$ and a spacing of $70\text{-}300 \text{ nm}$.

In summary, most studies report the bactericidal behavior for nanopatterns whose dimensions lie in the following ranges: $100 \text{ nm} < H < 1000 \text{ nm}$, $10 \text{ nm} < D < 300 \text{ nm}$, and $S < 500 \text{ nm}$.

2.3.3 Cytocompatibility of nanopatterns

Among the studies (12) that examined the cytocompatibility of surface nanopatterns, the majority (11) found no adverse effects on mammalian cells. For instance, the morphology of human mesenchymal stem cells (hMSCs) remained unchanged and osteoblasts proliferated on Ti nanocolumns ($250 \text{ nm} < H < 500 \text{ nm}$ and $30 \text{ nm} < W < 60 \text{ nm}$). Growth and proliferation of other cell types such as keratinocyte, fibroblast, and human dental pulp stem cells on different types of nanopatterns have been also reported in the literature⁴³⁻⁴⁵. The dimensions of the nanopatterns were in most cases as follows: diameter of 10 to 100 nm and heights of 200 to 650 nm . One study⁴⁶ reports that nanopatterns with extremely high aspect ratios (> 200) may kill mammalian cells in addition to bacteria.

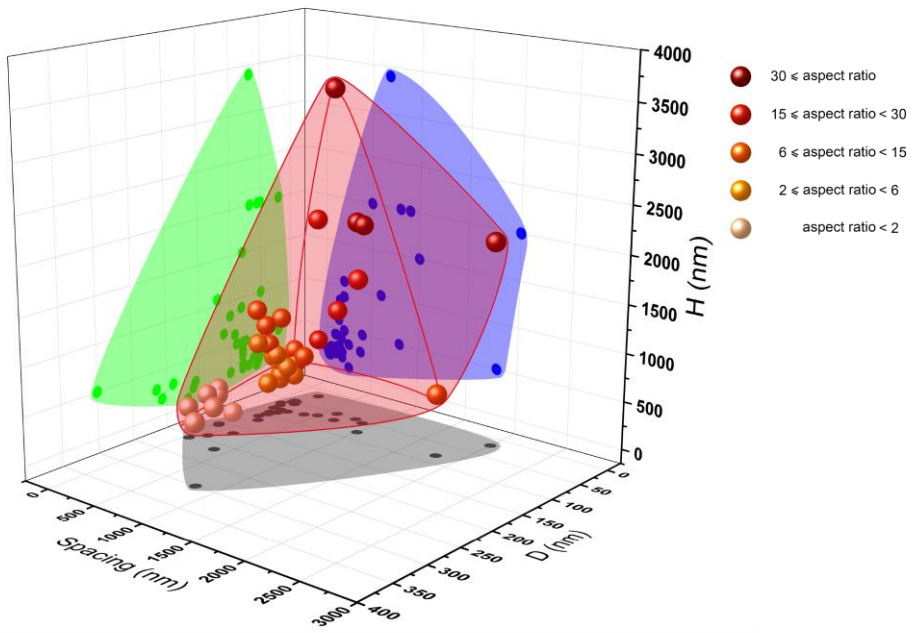


Figure 2.2. Effective dimensions for bactericidal nanopatterns. The red area indicates the range of dimensions in which the nanopatterns show bactericidal activity. The majority of bactericidal nanopatterns reported in the literature (colored bullets) have a height of 100-500 nm, a diameter of 10-300 nm, and a spacing of 10-380 nm. Different colors of bullets show the aspect ratio of nanopatterns reported in each study. The green, blue, and grey projections enable comparison between those three parameters.

2.4 Discussion

The results of this systematic review show that nanopatterns with a relatively wide range of design parameters could exhibit bactericidal behavior. The included studies have, in many cases, investigated the bactericidal properties of the surfaces using scanning electron microscopy (SEM) to observe any drastic changes or deformations in the morphology of the bacteria, the disruption of the cell, and any other signs of damaged or dead bacteria. To quantify the bactericidal efficiency, most studies count the colony-forming units (CFU) and use live/dead staining. The former determines the number of viable bacterial cells able to form a colony after being exposed to the nanopatterns, and the latter distinguishes between the viable and dead bacterial cells based on the integrity of the membrane^{47, 48}. As most studies found no adverse effects of nanopatterns on mammalian cells, there seems to be a large window within which bactericidal

nanopatterns could be designed without negatively influencing the attachment and proliferation of host cells that are required for tissue regeneration and integration of the implant in the human body. Nevertheless, most of the included studies investigated the bactericidal activity within the first 24 hours *in vitro*. It is, therefore, not completely clear what happens to the bacteria after they are killed and what will happen if the surfaces are constantly exposed to subsequent bacteria. Unlike the “kill and release” surfaces⁴⁹, the remnant components of the dead bacteria may negate the long-term functionality of the nanopatterns. Further *in vivo* studies are, thus, required to understand if the immune cells can effectively clean up the surface and whether the surface will maintain its bactericidal activity in the long term⁵⁰. On the other hand, the antibacterial properties of the biomaterials surfaces may be most crucial in the first few hours after implantation where the “race for the surface”⁵⁰ is ongoing. If bactericidal surfaces deter the bacteria in those first few hours, the host cells are more likely to win that race after which there will be less need for antibacterial protection. Indeed, it has been shown that mammalian cells can win the race and dominate the surface in long term. For example, Pham *et al.* have shown that eukaryotic cells could grow and proliferate on a pre-infected nanopatterned surface right after that surface had inhibited bacterial growth on it⁴⁵. The fact that mechanosensing pathways could be different in eukaryotic and prokaryotic cells^{28, 51}, opens the way to design nanopatterned surfaces which selectively allow eukaryotic cells to survive⁴⁵. Nanopatterns which initially eliminate the bacteria and subsequently promote host cells to attach and proliferate on the surface may, therefore, be able to deliver long-term benefits.

Despite the advances in micro/nanofabrication techniques, it is very challenging to create nanopatterns on 3D-shaped devices as the current patterning techniques are mostly only applicable to flat surfaces. Novel strategies have been, therefore, proposed to create 3D structures from flat sheets that are first ornamented with nanopatterns and are then (self-) folded into complex 3D shapes using origami-based approaches³¹. This could be promising for translating bactericidal and osteogenic nanopatterns to clinical use.

2.4.1 Bactericidal mechanisms of nanopatterns

The interactions between surface nanopatterns and bacteria are multi-faceted, making it difficult to fully delineate the role of various influencing factors. As a consequence, the exact killing mechanism and the role of various factors in regulating the bactericidal behavior of nanopatterns remain controversial^{35, 52}. Notwithstanding the

disagreements, most researchers agree that mechanical deformation in general and the rupture of cellular components such as cell wall due to large deformations and the penetration of high aspect ratio nanofeatures play a key role in this regard (Figure 2.3)^{36, 43, 53-56}. The optimum shape and dimensions of nanopatterns for maximizing the bactericidal behavior are, nevertheless, unknown (Figure 2.2).

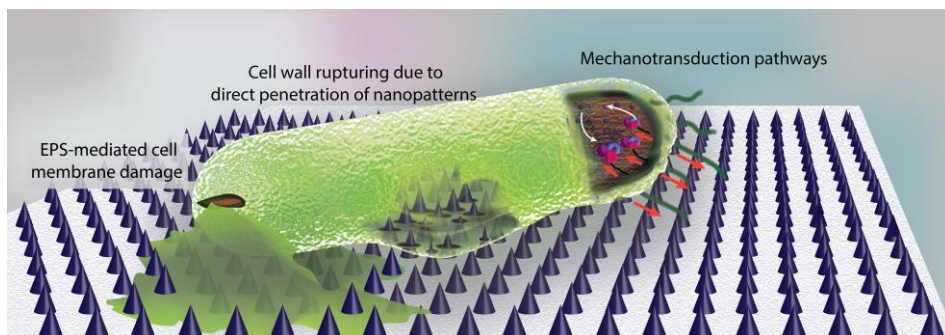


Figure 2.3. The main bactericidal mechanisms of nanopatterns. While the commonly believed theory is that bacterial cell wall is ruptured by penetration of high aspect ratio nanopatterns, there are a few studies suggesting that EPS plays a key role in this regard. It has been shown that the strong attachment of EPS to the nanopatterns and the attempts of bacteria to move away from the unfavorable surface leads to cell membrane damage. Moreover, mechanotransduction pathways in which the mechanical forces affect the metabolomics and the genomics of bacteria could be possible mechanisms of bacteria death on the surface.

When trying to understand the antibacterial behavior of nanopatterns, it is important to separate the effects of surface chemistry from those of nanopatterns. For example, naturally occurring bactericidal surfaces are often hydrophobic in nature and exhibit low surface energy, which varies with the dimensions of the nanopatterns⁵⁷. To isolate the effects of nanopatterns and eliminate the effect of surface chemistry, nanopatterned surfaces have been coated with gold⁵⁸. The coated surfaces exhibited similar antibacterial behavior, suggesting that the bactericidal behavior is physical in nature. Moreover, hydrophilic surfaces are shown to exhibit bactericidal properties as well⁵⁸. In the cases where the nanopatterns are made from materials that possess intrinsic antibacterial activity, *e.g.*, TiO₂ or ZnO, it may be challenging to isolate the effects of nanopatterns from those of the material itself. Moreover, the material and nanopatterns may work synergistically to kill bacteria. A number of studies that satisfied the inclusions criteria and are, therefore, included in this review have used nanopatterns based on TiO₂ or ZnO. Given the fact that many studies that use TiO₂ nanopatterns coat them with gold,

the intrinsic antibacterial effects of the material are not expected to have played a major role in those studies. However, further systematic studies are needed to fully understand the isolated and synergistic effects of nanopatterns and TiO₂ on bacteria, as not enough control surfaces have been used in most of the included studies. Concerning ZnO, it has been shown that the ZnO nanopillars produced on different types of substrates kill the adhered bacteria by mechanical rupturing with no significant difference in the killing efficiency⁵⁹. Unlike other substrates, however, the ZnO nanopillars made on a zinc substrate were also capable of killing non-adhered bacteria through the release of high concentrations of superoxide radicals, which were generated by electron donation from zinc⁵⁹. Other studies in the literature have also suggested that the antibacterial activity of ZnO nanowires could be partially attributed to the release of zinc ions^{60, 61}. Taken together, these results suggest that when TiO₂, ZnO, or other types of materials that possess intrinsic antibacterial properties are used for creating nanopatterns, multiple control surfaces should be included in the study to enable separating the effects of nanopatterns from those of the material itself and to quantify any synergistic effects that may be present.

2.4.2 The role of surface affinity and surface adhesion

The high aspect ratio features found in nanopatterns could also influence the affinity of microorganisms to the surface⁶². Interestingly, the level of bactericidal behavior is found to increase with the level of adherence of the microorganism to the surface⁶². Another study has shown that the susceptibility of different types of bacteria to mechanical rupturing by nanopattern varies with their stage of maturity⁵⁵. For example, the nanopillars found on the wing of *Calopteryx haemorrhoidalis* damselfly were deadliest against young *Staphylococcus aureus* and mature *Pseudomonas aeruginosa* cells⁵⁵. This behavior was explained to be related to the higher affinity of the bacteria to the surface in those specific stages of their life⁶³. These studies suggest that a high degree of adherence to the nanopatterned surface is the first necessary step to have the bacteria killed on the nanopatterns. In contrast to these findings, nanocolumns produced on titanium surface were found to decrease the surface covered by bacteria, as well as biofilm formation³⁷. Further studies revealed that the dimensions of nanopatterns⁶⁴ and the contact time⁶⁵ both affect the number of bacteria attached to the surface. More importantly, nanopatterns mainly affect the adhesion forces and not necessarily the number of adhered bacteria⁶⁶.

2.4.3 The effects of other nanopattern design parameters

In addition to the design parameters considered here (*i.e.*, height, diameter, interspacing), there are a number of other parameters that may influence the bactericidal behavior of nanopatterns. Fisher *et al.* found that a surface patterned non-uniformly (with more varying dimensions) is more lethal to the bacteria⁶⁷. There is, however, a need for more conclusive data with a wider range of studied parameters (shapes, dimensions, *etc.*), as other studies have shown that disorganized nanopatterns are not as effective as the organized ones⁶¹. A few studies have also investigated the effects of compaction and density of nanopatterns on the bactericidal activity. Linklater *et al.* showed that smaller and more compact nanopillars on black silicon surface are more effective in killing both Gram-negative and Gram-positive bacteria as compared to larger and more separated nanopillars on the same surface⁶⁸. Furthermore, it has been recently shown that optimizing the density of nanofeatures could play a crucial role in the killing efficiency of nanopatterns against *Staphylococcus aureus*⁶⁹.

2.4.4 The effects of bacterial-dependent characteristics

The intrinsic characteristics of bacteria could also influence the interactions between bacteria and nanopatterns^{17, 70}. For instance, the bactericidal behavior of nanopatterns has been shown to be dependent on the motility of the bacteria with highly motile bacteria being killed more efficiently⁷¹. Hasan *et al.* demonstrated that nanopatterns hold on to the bacterial membrane of *Escherichia coli* and the cell wall of *Staphylococcus aureus*. Due to bacterial motility, the membrane/cell wall is being increasingly stretched and eventually permanently deformed, thereby leading to cell death⁴⁶. Moreover, bacteria with different morphologies exhibit different degrees of adhesion to the nanopatterns, as observed for *Staphylococcus aureus* (coccoid-shaped) and *Pseudomonas aeruginosa* (rod-shaped) when cultured on the same nanopatterned surface⁷².

There may be additional effects associated with the size of the bacteria^{67, 73}. According to a theory presented by Li *et al.*⁷³, larger bacterial cells (*i.e.*, larger than the spacing between the nanopatterns) may get penetrated and ruptured, whereas those that are smaller than this dimension, interact with the side edges of the nanofeatures. They may be, therefore, either stretched due to the gravity and adhesion forces or compressed between the bases of the nanopatterns. In the case of spinule-like structures, there may be

different stiffness values along the height of a single nanofeature. Those stiffness variations may further affect the viability of the bacteria⁷³.

2.4.5 The role of extracellular polymeric substance (EPS)

The role of EPS in regulating the bactericidal effects of nanopatterns has been highlighted in some recent studies⁵². It has been, for example, shown that at least some bacterial strains secrete strongly adherent EPS when subjected to the nanopillars of the dragonfly wing⁵². Once the bacteria find the surface unfavorable and try to move away, EPS anchorage causes cell wall rupture and cell death⁵². The findings of this study have highlighted the role of EPS in the bactericidal behavior of nanopatterns⁵². Linklater *et al.* performed a study on the bactericidal mechanism of black silicon, which has been shown to be comparable to the dragonfly wing in terms of killing efficiency against Gram-negative and Gram-positive bacteria³⁵. The results showed that the bacteria are killed within 3-5 minutes of contact with the nanopatterns, which is not enough for bacteria to produce and secrete EPS³⁵. Moreover, neither the affinity of cells with the surface nor the motility of the bacteria influenced the killing efficiency of the nanopatterned surface³⁵. The key factor in determining the bactericidal behavior was the height of the nanopatterns³⁵.

Even though only one study has so far demonstrated the role of EPS in regulating the bactericidal behavior of nanopatterns, it may have more far-reaching effects than currently thought. Previous studies have shown that pressure-induced EPS production leads to higher levels of bacterial death since the membrane efflux pumps open during this process and impair the membrane barrier function⁶⁶. Bacterial EPS mainly consists of proteins, extracellular DNA, and polysaccharides, which all play various crucial roles in the development of the biofilm including forming the 3D architecture of the biofilm, protecting it against environmental factors, and facilitating cell-cell signaling^{74, 75}. For instance, studies on the EPS composition in *Pseudomonas aeruginosa*, widely studied as the model biofilm-forming organism, have shown that it is mainly composed of two polysaccharides, namely Pel and Psl. Pel is highly involved in the adhesion of bacteria to the surface and maintaining the cell-cell interactions in the bacterial biofilm, as well as providing a level of protection against aminoglycoside antibiotics^{74, 76, 77}. Manipulating the Pel secretion is proposed to be effective in disrupting the biofilm⁷⁶. Moreover, Pel is associated with making the adhesion forces short-ranged and symmetric⁷⁸. Therefore, it is plausible to hypothesize that mechanical forces which disrupt the function of Pel,

eventually kill the bacteria through a direct mechanotransduction pathway. The indirect mechanotransduction pathways could also be responsible for the bacterial death, as nanoscale topography may affect the genomics and proteomics of the bacterium⁷⁹. Further studies are, therefore, required to determine the exact mechanisms through which nanopatterns kill bacteria and the role of EPS.

2.4.6 Interactions of mammalian cells with the nanopatterns

There are differences in the ways bacteria and mammalian cells attach to surfaces and sense them. While bacteria form a community within the EPS to live on the surface, eukaryotic cells are able to adhere to the surface as single cells²⁹. Unlike bacteria, this adhesion is always mediated through the extracellular matrix (ECM)²⁹. Cellular features to probe the surface also differ between these two types of cells. The adhesion of mammalian cells to the ECM or other nanotopographical structures is mediated by integrins, which form dynamic adhesion structures known as focal adhesions³⁴. It has been shown that nanotopography could alter the expression of integrins and focal adhesions signaling, which finally influences the cytoskeletal structure⁸⁰ indicating activation of mechanotransduction pathways. Moreover, the design parameters of nanopatterns (*e.g.*, height) have been shown to affect the size and density of the focal adhesions in MSCs^{81,82}. Bacterial cells are much smaller than mammalian cells and due to their more rigid cell wall, they are less deformable. These differences affect the sensing mechanisms and the following mechanotransduction pathways induced by nanotopographical features whose dimensions are comparable with the size of the bacteria²⁹. Therefore, those nanopatterns, which are lethal to the bacteria, could possibly trigger direct or indirect mechanotransduction pathways within mammalian cells affecting their function. For instance, it has been shown that the osteogenic differentiation of MSCs is sensitive to a variety of factors including the spatial arrangement of the nanopatterns and their shapes^{83,84}. Moreover, an optimum height of nanopillars could be identified yielding the highest osteogenic marker expression in MSCs²⁸. Thus, using nanopatterns with specific designs could be a promising tool in directing stem cell fate.

Although more studies on nanotopography-induced cellular responses and mechanotransduction pathways have been carried out on mammalian cells than bacterial cells, the exact molecular mechanisms and outcomes are yet to be discovered, as these pathways are complex and involve a large number of biomolecules and signals³⁴.

2.5 Conclusions

We systematically reviewed the studies on the bactericidal effects of nanopatterned surfaces. Different types of nanopatterns with heights of 100 nm to > 900 nm, diameters between 10 and 300 nm, and interspacings of < 500 nm have been reported in the literature to exhibit bactericidal properties. Most of the studies that also examined the impact of nanopatterns on the mammalian cells found no evidence of adverse effects with the only exception being nanopatterns with extremely high aspect ratios.

Controversy exists over the exact killing mechanism of nanopatterns and the factors controlling the bactericidal efficiency. While the main mechanism is thought to be mechanical in nature and associated with the rupturing of the bacterial cell wall by high aspect ratio nanopatterns, some studies suggest that the EPS produced by the bacteria and the intrinsic properties of bacteria such as motility and size play a role as well. Overall, high aspect ratio nanopatterns could be considered as an effective tool for killing bacteria, especially because they achieve this goal without any need for chemical agents or antibiotics, thereby offering an alternative route for the design of the next generation of implantable medical devices.

2.6 Supplementary information

Table S2.1. Bactericidal nanopatterns found in the literature search.

Surface Nanopattern	Patterns Characteristics	Material	Fabrication Method	Microorganism	Microorganism Type	Results	Ref
Spinule	h < 4 μm d: 10-30 nm s: sub-micron density: 500/ μm^2	Gecko (<i>Lucasium steindachneri</i>) skin	Naturally occurring	<i>P. gingivalis</i>	Gram-negative	Death of bacteria due to cell wall stretching on the nanopatterns Compatible for growth of human dental pulp stem cells	43
Spinule	d: similar to gecko skin s: 500 nm density: 2-4/ μm^2	Epoxy resin (acrylic)	Biotemplating	<i>S. mutans</i> <i>P. gingivalis</i>	Gram-positive Gram-negative	Nanopatterns killed both types of bacteria with different mechanisms which could be determined by the size of bacteria.	73
Spinule	h: 1-1.5 μm w: 350-400 nm s: 600 nm-1 μm density: 8/ μm^2 d (tip): 50-80 nm h: 2 μm w: 350-400 nm s: 800 nm-1 μm density: 4/ μm^2 d (tip): 50-60 nm h: 2 μm w: 350-450 nm s: 500 nm-1 μm density: 8/ μm^2 d (tip): 50 nm h: 2 μm w: 300-400 nm	Polystyrene Alginate/Chitosan Chitosan Silk fibroin	Biotemplating using negative and positive molds	A co-culture of 7 gut bacteria	Gram-positive	The method is promising in replicating gecko skin nanopatterns for studying bactericidal properties.	85

	s: 500 nm density: 8/ μm^2 d (tip): 50-85 nm h: 3.4 μm w: 350-450 nm	Chitosan/Keratin					
Needle	s: 500-750 nm density: 8/ μm^2 d (tip): 50-85 nm h: 500-1000 nm	Boron-doped diamond (BDD) coated black silicon	Plasma etching	<i>P. aeruginosa</i>	Gram-negative	The Nanopattern damaged the membrane and killed the bacteria.	53
Dagger	h > 1 (with sharp nanotips)	ZIF-coated PMMA, ZIF-coated glass, ZIF-coated silicon rubber, ZIF-coated filter paper	Coating by a solution	<i>S. aureus</i> <i>E. coli</i> <i>C. albicans</i>	Gram-positive Gram-negative Yeast	ZIF-coated PMMA decreased the CFU compared to control for all types of bacteria. Other coated materials were tested against <i>E. coli</i> and reduced the CFU.	86
Micropatterns containing nanopatterns	10-20 μm with 100 nm features	Ti	Femtosecond laser ablation technique	<i>P. aeruginosa</i> <i>S. aureus</i>	Gram-negative Gram-positive	The attachment of bacteria is dependent on the cellular morphology.	72
Pin	h: 4 μm d: 220 nm w (tip): 10-20 nm	Si	DRIE (SPTS) technique	<i>E. coli</i> <i>S. aureus</i>	Gram-negative Gram-positive	The motility of bacteria attached to the nanopillars led to mechanical stretch in their wall. The membranes of mouse osteoblasts were also disrupted and showed low viability on the surface.	46
Groove	depth: 40 nm w: 1.6 μm	Methyl-functionalized maleic anhydride plasma polymer	Pulsed plasma polymerization and UV-irradiation	<i>E. coli</i>	Gram-negative	<i>E. coli</i> was not able to align with the nanopatterns, which could be associated with the small depth of nanogrooves that bacteria cannot sense.	87

Wire	L: 298 nm d: 52 nm	TiO ₂	Hydrothermal synthesis	<i>S. aureus</i>	Gram-positive	Nanopatterns were cytocompatible toward human osteoprogenitor cells. • The nanopatterns were effective in killing the bacteria and increasing the metabolic activity of human osteoblast cells.	88
Brush type Wire	h: 3 μm d: 100 nm	TiO ₂	Alkaline hydrothermal treatment	High motility <i>S. aureus</i> <i>E. faecalis</i> <i>K. pneumoniae</i>	Gram-positive Gram-negative Gram-negative	The bactericidal property was shown to be dependent on the motility of bacteria. The surface supports cell growth and proliferation.	71
Niche type Wire	h: 3 μm d: 10-15 μm			Low motility <i>S. aureus</i> <i>E. faecalis</i> <i>K. pneumoniae</i>	Gram-negative Gram-positive Gram-positive		
Wire	d: 143 nm Thickness: 11.3 μm s: 77 nm	Si	Two-step metal-assisted chemical etching (MACE) process	<i>E. coli</i> <i>S. aureus</i>	Gram-negative Gram-positive	The surface displayed a relatively low, but measurable, antibacterial activity.	89
Rod-shaped wire	A) Organized d: 30 nm h: 350 nm B) Disorganized d: 150 nm	ZnO nanowires on stainless steel	Custom-made hydrothermal approach	<i>S. aureus</i> <i>P. aeruginosa</i> <i>E. coli</i>	Gram-positive Gram-negative Gram-negative	Both samples are effective in killing bacterial cells, however, surface B is less effective in killing <i>S. aureus</i> in comparison with surface A. The cytocompatibility toward mouse preosteoblast was also proven.	61
Wire	h: 1 μm d: 25 nm	TiO ₂	Alkaline hydrothermal process	<i>P. aeruginosa</i>	Gram-negative	Nanowires were highly bactericidal toward the Gram-negative and motile bacterium <i>P. aeruginosa</i> .	90

Pit	d: 99 nm depth: 70 nm s: 300 nm	Polycarbonate	E-beam lithography	<i>S. aureus</i>	Gram-positive	<i>In vitro</i> co-culture demonstrated the osteogenic properties of TiO ₂ nanowires without an unwanted osteoclastic response. Reduced the risk of infection and facilitated tissue integration without using antibiotics. Both contact time and surface nanopatterns affect the adhesion of <i>S. aureus</i> to the surface.	65
Channel	h: 90 nm w: 900 nm	Cu Au	Electrodeposition	<i>P. fluorescens</i>	Gram-negative	When the parameters that characterize topography and roughness were in the order of bacteria dimension, bacteria easily adhered and less amount of EPS was produced.	20
Tube	d: 30 nm d: 100 nm d: 200 nm	TiO ₂	Electrochemical anodizing	<i>S. aureus</i>	Gram-positive	Bacterial attachment decreased by increasing the diameter. Nanotubes with diameters of 100 and 200 nm significantly inhibited bacterial cell attachment in comparison with samples of 30 nm diameter. Nanopatterns with a diameter of 100 nm could improve osteogenic differentiation of hMSCs.	64
Cone	h: 350 nm w (cap): 80 nm s: 250 nm	PMMA	Nanoimprint lithography	<i>E. coli</i> <i>P. aeruginosa</i> <i>S. aureus</i>	Gram-negative Gram-negative Gram-positive	Nanopatterns mechanically ruptured the bacteria and were also cytocompatible toward human keratinocyte cells.	44
Cone	A) h: 800 nm-2.5 μm w: 350-750 nm d: 10-40 nm B) h: < 100 nm or 3-5 μm	Diamond nanocone on a silicon wafer	Microwave plasma chemical vapor deposition	<i>P. aeruginosa</i>	Gram-negative	Both surfaces are bactericidal but B with more varying dimensions, decreased density, and the non-uniform pattern is more effective.	67

Column	w: < 100 nm or 1.2 μm d: 10-40 nm s: B > A h: 478 nm w: 33 nm	Ti	(MPCVD) followed by RIE Glancing angle sputter deposition	<i>S. aureus</i> <i>E. coli</i>	Gram-positive Gram-negative	<i>E. coli</i> showed an irregular and damaged morphology. In contrast, <i>S. aureus</i> morphology and viability were not affected. hMSCs morphology and distribution were similar on the nanopatterned and control surfaces.	91
Column	h: 250-350 nm d: 40-60 nm s: 100-200 nm	Ti	Glancing angle deposition by magnetron sputtering	<i>S. aureus</i> and 6 clinical strains of it	Gram-positive	Compared to non-patterned Ti, adhesion of all strains and biofilm formation were decreased on the nanopatterned surface. Nanopatterned surface supported osteoblast proliferation.	97
Column Spike	d: 200-300 nm d: 20 nm	TiO ₂	Thermal oxidation	<i>E. coli</i>	Gram-negative	Nanostructures significantly reduced the number of live bacterial cells.	92
Spike	h: 200 nm-11 μm d: 20-200 nm (avg. 100 nm) s: 220 nm	Silicon	Metal-assisted chemical etching (MacEtch)	<i>E. coli</i>	Gram-negative	Nanostructures reduced the number of CFU and live cells.	93
Pore	d: 20-25 nm Thickness: 40-50 nm	Ti	Oxidative nanopatterning	<i>S. aureus</i> <i>E. coli</i> <i>C. albicans</i>	Gram-positive Gram-negative Yeast	The mesoporous surface significantly inhibited the bacterial adhesion and also changed the structural parameters of <i>C. albicans</i> that determines its invasiveness.	94
Pore	d (external): 110.9 nm d (internal): 51.2 nm h (rim): 4.3 nm depth: 2.3 nm pitch between the nanopores: 200 nm	poly(hydroxymethylsiloxane) (PHMS)	Colloidal template- assisted method.	<i>P. aeruginosa</i>	Gram-negative	A general increase in the number of adhered cells was observed compared to unmodified PHMS surfaces. For the nanostructured surfaces, a moderate occurrence of patchy biofilm-like structures has been observed.	95

Hemisphere	h: 83.5 nm w: 167 nm s: 252 nm	<i>Magicicada septendecim</i> (brood II periodical cicada) wings	Naturally occurring	<i>Saccharomyces cerevisiae</i> : W303 SK1-CAN1	Yeast	The more adherent strain (SK1) showed greater death on all nanopatterns. Cellular affinity to the surface is associated with bactericidal efficacy.	62
Spherically capped cones	h: 183 nm w (base): 104 nm w (cap): 57 nm s: 175 nm	<i>Tibicen tibicen</i> (dog day annual cicada) wings	Naturally occurring				
Spherically capped cylinders	h: 241 nm w: 53 nm s: 123 nm	<i>Progomphus obscurus</i> (common sanddragon) wings	Naturally occurring				
Pillar (bundled)	d (tip): 10-30 nm h: 2 μm s: 2 μm	TiO ₂	Electrochemical anodizing	<i>S. aureus</i>	Gram-positive	Coating with tannic acid/gentamicin had a synergistic effect on the bactericidal property of the nanopatterns.	96
Pore	d: 40-55 nm depth: 1 μm s: 70 nm						
Pillar	h: 100 nm d: 50 nm density: 100 / μm^2	Au	Electrodeposition on nanoporous alumina templates	<i>S. aureus</i>	Gram-positive	Using Au nanostructures significantly increased the bactericidal activity of the Al through cell deformation.	97
Ring	h: 100 nm d: 100-200 nm density: 30 / μm^2					There was no significant difference between bactericidal effects of different shapes of Au nanostructures.	
Nugget	h: 100 nm d: 100-200 nm density: 30 / μm^2					Pillars with a height around 50 nm cannot kill the bacterial cells.	
Pillar	h: 890 \pm 130 nm d: 82 \pm 18 nm s: 200 nm	Black silicon	Reactive ion etching	Dormant and germinated	Gram-positive	Nanopatterns were effective in rupturing and killing the growing bacteria but not the dormant spores.	36

Pillar	h: 500 nm d: 20-80 nm s: 200-1800 nm	Black silicon	Reactive ion etching	spores of <i>B. subtilis</i> Dormant spores of <i>B. cereus</i> Dormant spores of <i>B. megaterium</i> <i>P. aeruginosa</i> <i>S. aureus</i> <i>B. subtilis</i> (vegetatives and spores)	Gram-negative Gram-positive Gram-positive	Effective in killing different types of bacteria. Black silicon is comparable to the cicada wing.	58
Pillar	h: 280 nm d: 62.7 nm s: 62.1 nm density: 86.7/ μm^2 h: 430 nm d: 80.3 nm s: 99.5 nm density: 26.6/ μm^2 h: 610 nm d: 92.7 nm s: 139.7 nm density: 23.7/ μm^2	Black silicon	Inductively coupled plasma (ICP) assisted RIE	<i>S. aureus</i> <i>P. aeruginosa</i>	Gram-positive Gram-negative	Nanopillars with shorter height, smaller tip diameter, and reduced spacing were more effective in killing the bacteria.	68
Pillar	h: 210 nm w: 70 nm s: 100 nm h: 300 nm w: 190 nm s: 130 nm h: 300 nm	PMMA	Nanoimprint lithography	<i>E. coli</i>	Gram-negative	The optimal spacing for bactericidal nanopattern was reported to be 130-380 nm.	42

Pillar	w: 215 nm s: 380 nm h: 652 ± 10.3 nm d: 100 ± 1.8 nm density: 12.2/μm ²	Black silicon	Reactive ion etching	<i>P. aeruginosa</i> <i>S. aureus</i>	Gram-negative Gram-positive	Nanopatterned surface inhibited bacterial colonization. Nanopatterned surface supported fibroblast cells growth on the pre-infected surface. Nanopatterned surface reduced the inflammatory response in vivo.	45
Pillar	h: 200-300 nm d: 80 ± 20 nm s: 180 ± 30 nm	Wings of <i>Hemianax papuensis</i> , <i>Austroaeschna multipunctata</i> , and <i>Diplacodes bipunctata</i> dragonflies	Naturally occurring	<i>P. aeruginosa</i> <i>S. aureus</i> <i>B. subtilis</i>	Gram-negative Gram-positive Gram-positive	The killing rate is dependent on the species and it is significantly higher for <i>D. bipunctata</i> in killing Gram-positive bacterial cells.	98
Pillar	d: 150–200 nm s: 100–250 nm	Si	Low-density capacitively-coupled plasma RIE	<i>E. coli</i> <i>S. aureus</i> <i>B. cereus</i>	Gram-negative Gram-positive Gram-positive	Even though <i>B. cereus</i> is more resistant than the other two bacteria, the nanopatterns mechanically ruptured the cell membrane and killed them.	54
Pillar	h: 311 nm d: 57 nm h: 187 nm d: 37nm	Dragonfly wings	Naturally occurring	<i>E. coli</i>	Gram-negative	The bacteria adhered to the pillars through a strong attachment of their EPS which leads to a rupture in the bacterial cell wall when it attempts to move away from the surface.	52
Pillar	<i>Megapomponia intermedia</i> : h: 241 nm d: 156 nm s: 9 nm <i>Cryptotympana</i>	Three different <i>Psaltoda claripennis</i> cicada wings	Naturally occurring	<i>P. fluorescens</i>	Gram-negative	Dimensions of the nanostructure are directly responsible for the hydrophobic characteristics and low surface energies of the wings.	57

	<p><i>aguila:</i> h: 182 nm d: 159 nm s: 28 nm</p> <p><i>Ayuthia spectabile:</i> h: 182 nm d: 207 nm s: 44 nm</p>					Greater bactericidal activity was observed when a higher number of nanopillars came into contact with the bacterial cell.	
Pillar	<p>h: 213 nm Cap d: 21.04 nm h: 475 nm Cap d: 93.4 nm h: 612 nm Cap d: 72 nm</p>	Black silicon	Plasma etching	<p><i>P. aeruginosa</i> <i>S. aureus</i></p>	<p>Gram-negative Gram.positive</p>	<p>The killing efficacy, as well as the bacterial attachment to the surface, are dependent on nanopillars' height. Cellular affinity for the surface or the motility of bacterial cells does not determine the bactericidal efficacy. Also, EPS does not play a role in mechanobactericidal pathways.</p>	35
Pillar	N/A	<p><i>Psaltoda claripennis</i> cicada wings</p>	Naturally occurring	<p><i>B. subtilis</i> <i>B. catarrhalis</i> <i>E. coli</i> <i>P. maritimus</i> <i>P. aeruginosa</i> <i>P. fluorescens</i> <i>S. aureus</i> <i>S. aureus</i></p>	<p>Gram-positive Gram-negative Gram-negative Gram-positive Gram-negative Gram-negative Gram-positive Gram-positive</p>	<p>Gram-negative cells were all found to be sensitive to the wing surface, while all Gram-positive cells were resistant.</p>	41
Pillar	<p>h: 500 nm d: 90 nm s: 200 nm h: 500 nm d: 75nm s: 400 nm h: 500 nm d: 300 nm s: 800 nm</p>	Si	Laser interference lithography followed by RIE	<p><i>S. aureus</i></p>	Gram-positive	<p>Nanopatterns reduced bacterial adhesion The adhesion force on nanopillars of the surface is significantly lower than that on a smooth surface.</p>	66

Pillar	h: 433 nm d: 47.7 nm s: 116 nm	<i>Caloptery haemorrhoidalis</i> damsel fly wings	Naturally occurring	<i>P. aeruginosa</i> <i>S. aureus</i>	Gram-negative Gram-positive	The nanopatterns mechanically ruptured both types of bacteria in their early and late stationary phases of growth.	55
Pillar	h: 200 or 400 nm d: 80 nm s: 170 nm density: 40/ μm^2	Ormostamp polymer	Nano-replication technology	<i>S. aureus</i>	Gram-positive	An optimized range of spacing was revealed to be effective in killing the bacteria.	69
Pillar	N/A	ZnO	Growing nanopillars in an aqueous solution of zinc salts	<i>E. coli</i> <i>P. aeruginosa</i> <i>S. aureus</i> <i>C. albicans</i>	Gram-negative Gram-negative Gram-positive Yeast	Nanopillars grown on zinc showed strong bactericidal activity.	59
Pillar	d :100 nm	TiO ₂	Hydrothermal treatment	<i>S. epidermidis</i>	Gram-positive	The nanopatterns increased the killing rate and delayed the biofilm formation.	56
Pillar	h: 836.8 nm w (tip): 100.1 nm s: 153.1 nm density: 11/ μm^2 h: 657.9 nm w (tip): 110.3 nm s: 135.6 nm density: 10/ μm^2 h: 1063.2 nm w (tip): 120.5 nm s: 197.4 nm density: 8/ μm^2	Black silicon	Reactive ion etching	<i>P. aeruginosa</i> <i>S. aureus</i>	Gram-negative Gram-positive	The pillars larger than 1 μm and less dense were not much effective in killing the bacteria.	99
Pillar	h: 90 nm	TiO ₂	Through-mask anodization	<i>S. mitis</i> <i>F. nucleatum</i>	Gram-positive Gram-negative	Effective in killing the bacteria but the effect disappears by saliva coating.	100
Pillar	h: 200 nm d (base): 100 nm d (tip): 60 nm s: 170 nm	<i>Psaltoda claripennis</i> cicada wings	Naturally occurring	<i>P. aeruginosa</i>	Gram-negative	Nanopatterns are able to rapidly kill the bacteria (within 3 min).	101

Bibliography

- [1] W. Zimmerli, A. Trampuz, P.E. Ochsner, Prosthetic-joint infections, *New England Journal of Medicine*, 351(16), 1645-1654, 2004.
- [2] J.M. Steckelberg, D.R. Osmon, *Prosthetic joint infections*, in *Infections Associated with Indwelling Medical Devices, Third Edition*. 2000, American Society of Microbiology. p. 173-209.
- [3] T. Peel, *Introduction to Prosthetic Joint Infection*, in *Prosthetic Joint Infections*. 2018, Springer. p. 1-4.
- [4] J. Hasan, R.J. Crawford, E.P. Ivanova, Antibacterial surfaces: the quest for a new generation of biomaterials, *Trends in Biotechnology*, 31(5), 295-304, 2013.
- [5] Y. Wang, G. Subbiahdoss, J. Swartjes, H.C. van der Mei, H.J. Busscher, M. Libera, Length-Scale Mediated Differential Adhesion of Mammalian Cells and Microbes, *Advanced Functional Materials*, 21(20), 3916-3923, 2011.
- [6] S. Bakhshandeh, Z. Gorgin Karaji, K. Lietaert, A.C. Fluit, C.E. Boel, H.C. Vogely, T. Vermonden, W.E. Hennink, H. Weinans, A.A. Zadpoor, Simultaneous Delivery of Multiple Antibacterial Agents from Additively Manufactured Porous Biomaterials to Fully Eradicate Planktonic and Adherent Staphylococcus aureus, *ACS Applied Materials & Interfaces*, 9(31), 25691-25699, 2017.
- [7] B. Wang, H. Liu, Z. Wang, S. Shi, K. Nan, Q. Xu, Z. Ye, H. Chen, A self-defensive antibacterial coating acting through the bacteria-triggered release of a hydrophobic antibiotic from layer-by-layer films, *Journal of Materials Chemistry B*, 5(7), 1498-1506, 2017.
- [8] J. Hirschfeld, E.M. Akinoglu, D.C. Wirtz, A. Hoerauf, I. Bekeredjian-Ding, S. Jepsen, E.-M. Haddouti, A. Limmer, M. Giersig, Long-term release of antibiotics by carbon nanotube-coated titanium alloy surfaces diminish biofilm formation by Staphylococcus epidermidis, *Nanomedicine: Nanotechnology, Biology and Medicine*, 13(4), 1587-1593, 2017.
- [9] S. Amin Yavari, L. Loozen, F.L. Paganelli, S. Bakhshandeh, K. Lietaert, J.A. Groot, A.C. Fluit, C. Boel, J. Alblas, H.C. Vogely, Antibacterial behavior of additively manufactured porous titanium with nanotubular surfaces releasing silver ions, *ACS Applied Materials & Interfaces*, 8(27), 17080-17089, 2016.
- [10] I.A. van Hengel, M. Riool, L.E. Fratila-Apachitei, J. Witte-Bouma, E. Farrell, A.A. Zadpoor, S.A. Zaat, I. Apachitei, Selective laser melting porous metallic implants with immobilized silver nanoparticles kill and prevent biofilm formation by methicillin-resistant Staphylococcus aureus, *Biomaterials*, 140, 1-15, 2017.
- [11] Z. Jia, P. Xiu, P. Xiong, W. Zhou, Y. Cheng, S. Wei, Y. Zheng, T. Xi, H. Cai, Z. Liu, Additively manufactured macroporous titanium with silver-releasing micro-/nanoporous surface for multipurpose infection control and bone repair—a proof of concept, *ACS Applied Materials & Interfaces*, 8(42), 28495-28510, 2016.
- [12] B.S. Necula, L.E. Fratila-Apachitei, S.A. Zaat, I. Apachitei, J. Duszczyk, In vitro antibacterial activity of porous TiO₂-Ag composite layers against methicillin-resistant Staphylococcus aureus, *Acta Biomaterialia*, 5(9), 3573-3580, 2009.

-
- [13] B. Necula, J. Van Leeuwen, L. Fratila-Apachitei, S. Zaat, I. Apachitei, J. Duszczuk, In vitro cytotoxicity evaluation of porous TiO₂-Ag antibacterial coatings for human fetal osteoblasts, *Acta Biomaterialia*, 8(11), 4191-4197, 2012.
- [14] R.P. Singh, P. Ramarao, Cellular uptake, intracellular trafficking and cytotoxicity of silver nanoparticles, *Toxicology Letters*, 213(2), 249-259, 2012.
- [15] L.Q. Chen, L. Fang, J. Ling, C.Z. Ding, B. Kang, C.Z. Huang, Nanotoxicity of silver nanoparticles to red blood cells: size dependent adsorption, uptake, and hemolytic activity, *Chemical Research in Toxicology*, 28(3), 501-509, 2015.
- [16] A. Gallardo-Godoy, C. Muldoon, B. Becker, A.G. Elliott, L.H. Lash, J.X. Huang, M.S. Butler, R. Pelington, A.M. Kavanagh, S. Ramu, Activity and predicted nephrotoxicity of synthetic antibiotics based on polymyxin B, *Journal of Medicinal Chemistry*, 59(3), 1068-1077, 2016.
- [17] A. Elbourne, R.J. Crawford, E.P. Ivanova, Nano-structured antimicrobial surfaces: From nature to synthetic analogues, *Journal of Colloid and Interface Science*, 508, 603-616, 2017.
- [18] A. Panáček, L. Kvítek, M. Smékalová, R. Večeřová, M. Kolář, M. Röderová, F. Dyčka, M. Šebela, R. Prucek, O. Tomanec, Bacterial resistance to silver nanoparticles and how to overcome it, *Nature Nanotechnology*, 13(1), 65-71, 2018.
- [19] F. Song, M.E. Brasch, H. Wang, J.H. Henderson, K. Sauer, D. Ren, How bacteria respond to material stiffness during attachment: a role of Escherichia coli flagellar motility, *ACS Applied Materials & Interfaces*, 9(27), 22176-22184, 2017.
- [20] C. Díaz, M.C. Cortizo, P.L. Schilardi, S.G.G.d. Saravia, M.A.F.L.d. Mele, Influence of the nano-micro structure of the surface on bacterial adhesion, *Materials Research*, 10(1), 11-14, 2007.
- [21] R.J. Crawford, H.K. Webb, V.K. Truong, J. Hasan, E.P. Ivanova, Surface topographical factors influencing bacterial attachment, *Advances in Colloid and Interface Science*, 179, 142-149, 2012.
- [22] H. Gu, A. Chen, X. Song, M.E. Brasch, J.H. Henderson, D. Ren, How Escherichia coli lands and forms cell clusters on a surface: A new role of surface topography, *Scientific Reports*, 6, 29516, 2016.
- [23] D.E. Discher, P. Janmey, Y.-I. Wang, Tissue cells feel and respond to the stiffness of their substrate, *Science*, 310(5751), 1139-1143, 2005.
- [24] M.M. Stevens, J.H. George, Exploring and engineering the cell surface interface, *Science*, 310(5751), 1135-1138, 2005.
- [25] M.J. Dalby, N. Gadegaard, R.O. Oreffo, Harnessing nanotopography and integrin-matrix interactions to influence stem cell fate, *Nature Materials*, 13(6), 558-569, 2014.
- [26] S. Oh, K.S. Brammer, Y.J. Li, D. Teng, A.J. Engler, S. Chien, S. Jin, Stem cell fate dictated solely by altered nanotube dimension, *Proceedings of the National Academy of Sciences*, 106(7), 2130-2135, 2009.
- [27] W.L. Murphy, T.C. McDevitt, A.J. Engler, Materials as stem cell regulators, *Nature Materials*, 13(6), 547, 2014.
- [28] S. Dobbenga, L.E. Fratila-Apachitei, A.A. Zadpoor, Nanopattern-induced osteogenic differentiation of stem cells—A systematic review, *Acta Biomaterialia*, 46, 3-14, 2016.
- [29] K. Anselme, P. Davidson, A. Popa, M. Giazzon, M. Liley, L. Ploux, The interaction of cells and bacteria with surfaces structured at the nanometre scale, *Acta Biomaterialia*, 6(10), 3824-3846, 2010.

- [30] K.K. Chung, J.F. Schumacher, E.M. Sampson, R.A. Burne, P.J. Antonelli, A.B. Brennan, Impact of engineered surface microtopography on biofilm formation of *Staphylococcus aureus*, *Biointerphases*, 2(2), 89-94, 2007.
- [31] S. Janbaz, N. Noordzij, D.S. Widyaratih, C.W. Hagen, L.E. Fratila-Apachitei, A.A. Zadpoor, Origami lattices with free-form surface ornaments, *Science Advances*, 3(11), eaao1595, 2017.
- [32] A. Tripathy, P. Sen, B. Su, W.H. Briscoe, Natural and bioinspired nanostructured bactericidal surfaces, *Advances in Colloid and Interface Science*, 248, 85-104, 2017.
- [33] B.D. Gates, Q. Xu, M. Stewart, D. Ryan, C.G. Willson, G.M. Whitesides, New approaches to nanofabrication: molding, printing, and other techniques, *Chemical Reviews*, 105(4), 1171-1196, 2005.
- [34] Y. Sun, C.S. Chen, J. Fu, Forcing stem cells to behave: a biophysical perspective of the cellular microenvironment, *Annual Review of Biophysics*, 41, 519-542, 2012.
- [35] D.P. Linklater, S. Juodkazis, S. Rubanov, E.P. Ivanova, Comment on "Bactericidal Effects of Natural Nanotopography of Dragonfly Wing on *Escherichia coli*", *ACS Applied Materials & Interfaces*, 9(35), 29387-29393, 2017.
- [36] S. Ghosh, S. Niu, M. Yankova, M. Mecklenburg, S.M. King, J. Ravichandran, R.K. Kalia, A. Nakano, P. Vashishta, P. Setlow, Analysis of killing of growing cells and dormant and germinated spores of *Bacillus* species by black silicon nanopillars, *Scientific Reports*, 7(1), 17768, 2017.
- [37] I. Izquierdo-Barba, J.M. García-Martín, R. Álvarez, A. Palmero, J. Esteban, C. Pérez-Jorge, D. Arcos, M. Vallet-Regí, Nanocolumnar coatings with selective behavior towards osteoblast and *Staphylococcus aureus* proliferation, *Acta Biomaterialia*, 15, 20-28, 2015.
- [38] L. Feng, S. Li, Y. Li, H. Li, L. Zhang, J. Zhai, Y. Song, B. Liu, L. Jiang, D. Zhu, Superhydrophobic surfaces: from natural to artificial, *Advanced Materials*, 14(24), 1857-1860, 2002.
- [39] K. Liu, L. Jiang, Bio-inspired design of multiscale structures for function integration, *Nano Today*, 6(2), 155-175, 2011.
- [40] K. Modaresifar, S. Azizian, A. Hadjizadeh, Nano/biomimetic tissue adhesives development: from research to clinical application, *Polymer Reviews*, 56(2), 329-361, 2016.
- [41] J. Hasan, H.K. Webb, V.K. Truong, S. Pogodin, V.A. Baulin, G.S. Watson, J.A. Watson, R.J. Crawford, E.P. Ivanova, Selective bactericidal activity of nanopatterned superhydrophobic cicada *Psaltoda claripennis* wing surfaces, *Applied Microbiology and Biotechnology*, 97(20), 9257-9262, 2013.
- [42] M.N. Dickson, E.I. Liang, L.A. Rodriguez, N. Vollereaux, A.F. Yee, Nanopatterned polymer surfaces with bactericidal properties, *Biointerphases*, 10(2), 021010, 2015.
- [43] G.S. Watson, D.W. Green, L. Schwarzkopf, X. Li, B.W. Cribb, S. Myhra, J.A. Watson, A gecko skin micro/nano structure—A low adhesion, superhydrophobic, anti-wetting, self-cleaning, biocompatible, antibacterial surface, *Acta Biomaterialia*, 21, 109-122, 2015.
- [44] F. Viela, I. Navarro-Baena, J.J. Hernández, M.R. Osorio, I. Rodriguez, Moth eye mimetic cytocompatible bactericidal nanotopography: A convergent design, *Bioinspiration & Biomimetics*, 2018.

- [45] V.T. Pham, V.K. Truong, A. Orłowska, S. Ghanaati, M. Barbeck, P. Booms, A.J. Fulcher, C.M. Bhadra, R. Buividas, V. Baulin, "Race for the surface": eukaryotic cells can win, *ACS Applied Materials & Interfaces*, 8(34), 22025-22031, 2016.
- [46] J. Hasan, S. Raj, L. Yadav, K. Chatterjee, Engineering a nanostructured "super surface" with superhydrophobic and superkilling properties, *RSC Advances*, 5(56), 44953-44959, 2015.
- [47] P. Stiefel, S. Schmidt-Emrich, K. Maniura-Weber, Q. Ren, Critical aspects of using bacterial cell viability assays with the fluorophores SYTO9 and propidium iodide, *BMC Microbiology*, 15(1), 36, 2015.
- [48] J. Sjollema, S.A. Zaat, V. Fontaine, M. Ramstedt, R. Luginbuehl, K. Thevissen, J. Li, H.C. van der Mei, H.J. Busscher, In vitro methods for the evaluation of antimicrobial surface designs, *Acta Biomaterialia*, 2018.
- [49] Q. Yu, Z. Wu, H. Chen, Dual-function antibacterial surfaces for biomedical applications, *Acta Biomaterialia*, 16, 1-13, 2015.
- [50] H.J. Busscher, H.C. Van Der Mei, G. Subbiahdoss, P.C. Jutte, J.J. Van Den Dungen, S.A. Zaat, M.J. Schultz, D.W. Grainger, Biomaterial-associated infection: locating the finish line in the race for the surface, *Science Translational Medicine*, 4(153), 153rv110-153rv110, 2012.
- [51] A. Persat, Bacterial mechanotransduction, *Current Opinion in Microbiology*, 36, 1-6, 2017.
- [52] C.D. Bandara, S. Singh, I.O. Afara, A. Wolff, T. Tesfamichael, K. Ostrikov, A. Oloyede, Bactericidal effects of natural nanotopography of dragonfly wing on Escherichia coli, *ACS Applied Materials & Interfaces*, 9(8), 6746-6760, 2017.
- [53] P. May, M. Clegg, T. Silva, H. Zanin, O. Fatibello-Filho, V. Celorrio, D. Fermin, C. Welch, G. Hazell, L. Fisher, Diamond-coated 'black silicon' as a promising material for high-surface-area electrochemical electrodes and antibacterial surfaces, *Journal of Materials Chemistry B*, 4(34), 5737-5746, 2016.
- [54] E. Vassallo, M. Pedroni, T. Silveti, S. Morandi, S. Toffolatti, G. Angella, M. Brasca, Bactericidal performance of nanostructured surfaces by fluorocarbon plasma, *Materials Science and Engineering: C*, 2017.
- [55] V.K. Truong, N.M. Geeganagamage, V.A. Baulin, J. Vongsvivut, M.J. Tobin, P. Luque, R.J. Crawford, E.P. Ivanova, The susceptibility of Staphylococcus aureus CIP 65.8 and Pseudomonas aeruginosa ATCC 9721 cells to the bactericidal action of nanostructured Calopteryx haemorrhoidalis damselfly wing surfaces, *Applied Microbiology and Biotechnology*, 101(11), 4683-4690, 2017.
- [56] Y. Cao, B. Su, S. Chinnaraj, S. Jana, L. Bowen, S. Charlton, P. Duan, N.S. Jakubovics, J. Chen, Nanostructured titanium surfaces exhibit recalcitrance towards Staphylococcus epidermidis biofilm formation, *Scientific Reports*, 8(1), 1071, 2018.
- [57] S.M. Kelleher, O. Habimana, J. Lawler, B. O'Reilly, S. Daniels, E. Casey, A. Cowley, Cicada wing surface topography: an investigation into the bactericidal properties of nanostructural features, *ACS Applied Materials & Interfaces*, 8(24), 14966-14974, 2015.
- [58] E.P. Ivanova, J. Hasan, H.K. Webb, G. Gervinskas, S. Juodkazis, V.K. Truong, A.H. Wu, R.N. Lamb, V.A. Baulin, G.S. Watson, Bactericidal activity of black silicon, *Nature Communications*, 4, 2013.

- [59] G. Yi, Y. Yuan, X. Li, Y. Zhang, ZnO Nanopillar Coated Surfaces with Substrate-Dependent Superbactericidal Property, *Small*, 14(14), 1703159, 2018.
- [60] G. Jin, H. Qin, H. Cao, S. Qian, Y. Zhao, X. Peng, X. Zhang, X. Liu, P.K. Chu, Synergistic effects of dual Zn/Ag ion implantation in osteogenic activity and antibacterial ability of titanium, *Biomaterials*, 35(27), 7699-7713, 2014.
- [61] W. Wang, T.L. Li, H.M. Wong, P.K. Chu, R.Y. Kao, S. Wu, F.K. Leung, T.M. Wong, M.K. To, K.M. Cheung, Development of novel implants with self-antibacterial performance through in-situ growth of 1D ZnO nanowire, *Colloids and Surfaces B: Biointerfaces*, 141, 623-633, 2016.
- [62] K. Nowlin, A. Boseman, A. Covell, D. LaJeunesse, Adhesion-dependent rupturing of *Saccharomyces cerevisiae* on biological antimicrobial nanostructured surfaces, *Journal of the Royal Society Interface*, 12(102), 20140999, 2015.
- [63] S.L. Walker, J.E. Hill, J.A. Redman, M. Elimelech, Influence of growth phase on adhesion kinetics of *Escherichia coli* D21g, *Applied and Environmental Microbiology*, 71(6), 3093-3099, 2005.
- [64] Z. Xu, Y. Lai, D. Wu, W. Huang, S. Huang, L. Zhou, J. Chen, Increased mesenchymal stem cell response and decreased staphylococcus aureus adhesion on titania nanotubes without pharmaceuticals, *BioMed Research International*, 2015, 2015.
- [65] S. Aguayo, A. Strange, N. Gadegaard, M. Dalby, L. Bozec, Influence of biomaterial nanotopography on the adhesive and elastic properties of *Staphylococcus aureus* cells, *RSC Advances*, 6(92), 89347-89355, 2016.
- [66] F. Hizal, C.-H. Choi, H.J. Busscher, H.C. van der Mei, Staphylococcal adhesion, detachment and transmission on nanopillared si surfaces, *ACS Applied Materials & Interfaces*, 8(44), 30430-30439, 2016.
- [67] L.E. Fisher, Y. Yang, M.-F. Yuen, W. Zhang, A.H. Nobbs, B. Su, Bactericidal activity of biomimetic diamond nanocone surfaces, *Biointerphases*, 11(1), 011014, 2016.
- [68] D.P. Linklater, H.K.D. Nguyen, C.M. Bhadra, S. Juodkakis, E.P. Ivanova, Influence of nanoscale topology on bactericidal efficiency of black silicon surfaces, *Nanotechnology*, 28(24), 245301, 2017.
- [69] S. Wu, F. Zuber, K. Maniura-Weber, J. Brugger, Q. Ren, Nanostructured surface topographies have an effect on bactericidal activity, *Journal of Nanobiotechnology*, 16(1), 20, 2018.
- [70] S. Pogodin, J. Hasan, V.A. Baulin, H.K. Webb, V.K. Truong, V. Boshkovikj, C.J. Fluke, G.S. Watson, J.A. Watson, R.J. Crawford, Biophysical model of bacterial cell interactions with nanopatterned cicada wing surfaces, *Biophysical Journal*, 104(4), 835-840, 2013.
- [71] T. Diu, N. Faruqui, T. Sjöström, B. Lamarre, H.F. Jenkinson, B. Su, M.G. Ryadnov, Cicada-inspired cell-instructive nanopatterned arrays, *Scientific Reports*, 4, 2014.
- [72] E. Fadeeva, V.K. Truong, M. Stiesch, B.N. Chichkov, R.J. Crawford, J. Wang, E.P. Ivanova, Bacterial retention on superhydrophobic titanium surfaces fabricated by femtosecond laser ablation, *Langmuir*, 27(6), 3012-3019, 2011.
- [73] X. Li, G. Cheung, G.S. Watson, J.A. Watson, S. Lin, L. Schwarzkopf, D. Green, The nanotipped hairs of gecko skin and biotemplated replicas impair and/or kill pathogenic bacteria with high efficiency, *Nanoscale*, 8(45), 18860-18869, 2016.

- [74] M.G. Mazza, The physics of biofilms—an introduction, *Journal of Physics D: Applied Physics*, 49(20), 203001, 2016.
- [75] D.H. Limoli, C.J. Jones, D.J. Wozniak, Bacterial extracellular polysaccharides in biofilm formation and function, *Microbiology Spectrum*, 3(3), 2015.
- [76] K.M. Colvin, V.D. Gordon, K. Murakami, B.R. Borlee, D.J. Wozniak, G.C. Wong, M.R. Parsek, The pel polysaccharide can serve a structural and protective role in the biofilm matrix of *Pseudomonas aeruginosa*, *PLOS Pathogens*, 7(1), e1001264, 2011.
- [77] A. Dragoš, Á.T. Kovács, The peculiar functions of the bacterial extracellular matrix, *Trends in Microbiology*, 25(4), 257-266, 2017.
- [78] B.J. Cooley, T.W. Thatcher, S.M. Hashmi, G. L'Her, H.H. Le, D.A. Hurwitz, D. Provenzano, A. Touhami, V.D. Gordon, The extracellular polysaccharide Pel makes the attachment of *P. aeruginosa* to surfaces symmetric and short-ranged, *Soft Matter*, 9(14), 3871-3876, 2013.
- [79] L. Rizzello, B. Sorce, S. Sabella, G. Vecchio, A. Galeone, V. Brunetti, R. Cingolani, P.P. Pompa, Impact of nanoscale topography on genomics and proteomics of adherent bacteria, *ACS Nano*, 5(3), 1865-1876, 2011.
- [80] E.K. Yim, E.M. Darling, K. Kulangara, F. Guilak, K.W. Leong, Nanotopography-induced changes in focal adhesions, cytoskeletal organization, and mechanical properties of human mesenchymal stem cells, *Biomaterials*, 31(6), 1299-1306, 2010.
- [81] T. Sjöström, L.E. McNamara, R.D. Meek, M.J. Dalby, B. Su, 2D and 3D nanopatterning of titanium for enhancing osteoinduction of stem cells at implant surfaces, *Advanced Healthcare Materials*, 2(9), 1285-1293, 2013.
- [82] L.E. McNamara, T. Sjöström, K.E. Burgess, J.J. Kim, E. Liu, S. Gordonov, P.V. Moghe, R.D. Meek, R.O. Oreffo, B. Su, Skeletal stem cell physiology on functionally distinct titania nanotopographies, *Biomaterials*, 32(30), 7403-7410, 2011.
- [83] S. Guvendik, L. Trabzon, M. Ramazanoglu, The effect of Si nano-columns in 2-D and 3-D on cellular behaviour: nanotopography-induced CaP deposition from differentiating mesenchymal stem cells, *Journal of Nanoscience and Nanotechnology*, 11(10), 8896-8902, 2011.
- [84] R.K. Silverwood, P.G. Fairhurst, T. Sjöström, F. Welsh, Y. Sun, G. Li, B. Yu, P.S. Young, B. Su, R.M. Meek, Analysis of osteoclastogenesis/osteoblastogenesis on nanotopographical titania surfaces, *Advanced Healthcare Materials*, 5(8), 947-955, 2016.
- [85] D.W. Green, K.K.-H. Lee, J.A. Watson, H.-Y. Kim, K.-S. Yoon, E.-J. Kim, J.-M. Lee, G.S. Watson, H.-S. Jung, High Quality Bioreplication of Intricate Nanostructures from a Fragile Gecko Skin Surface with Bactericidal Properties, *Scientific Reports*, 7, 2017.
- [86] Y. Yuan, Y. Zhang, Enhanced Biomimic Bactericidal Surfaces by Coating with Positively-Charged ZIF Nano-Dagger Arrays, *Nanomedicine: Nanotechnology, Biology and Medicine*, 2017.
- [87] L. Ploux, K. Anselme, A. Dirani, A. Ponche, O. Soppera, V. Roucoules, Opposite responses of cells and bacteria to micro/nanopatterned surfaces prepared by pulsed plasma polymerization and UV-irradiation, *Langmuir*, 25(14), 8161-8169, 2009.
- [88] A. Jaggessar, A. Mathew, H. Wang, T. Tesfamichael, C. Yan, P.K. Yarlagadda, Mechanical, bactericidal and osteogenic behaviours of hydrothermally synthesised TiO₂ nanowire arrays, *Journal of the Mechanical Behavior of Biomedical Materials*, 80, 311-319, 2018.

- [89] A. Susarrey-Arce, I. Sorzabal-Bellido, A. Oknianska, F. McBride, A. Beckett, J. Gardeniers, R. Raval, R. Tiggelaar, Y.D. Fernandez, Bacterial viability on chemically modified silicon nanowire arrays, *Journal of Materials Chemistry B*, 4(18), 3104-3112, 2016.
- [90] P. Tsimbouri, L. Fisher, N. Holloway, T. Sjostrom, A. Nobbs, R.D. Meek, B. Su, M. Dalby, Osteogenic and bactericidal surfaces from hydrothermal titania nanowires on titanium substrates, *Scientific Reports*, 6, 2016.
- [91] C. Sengstock, M. Lopian, Y. Motemani, A. Borgmann, C. Khare, P.J.S. Buenconsejo, T.A. Schildhauer, A. Ludwig, M. Köller, Structure-related antibacterial activity of a titanium nanostructured surface fabricated by glancing angle sputter deposition, *Nanotechnology*, 25(19), 195101, 2014.
- [92] T. Sjöström, A.H. Nobbs, B. Su, Bactericidal nanospike surfaces via thermal oxidation of Ti alloy substrates, *Materials Letters*, 167, 22-26, 2016.
- [93] H. Hu, V.S. Siu, S.M. Gifford, S. Kim, M. Lu, P. Meyer, G.A. Stolovitzky, Bio-inspired silicon nanospikes fabricated by metal-assisted chemical etching for antibacterial surfaces, *Applied Physics Letters*, 111(25), 253701, 2017.
- [94] F. Variola, S.F. Zalzal, A. Leduc, J. Barbeau, A. Nanci, Oxidative nanopatterning of titanium generates mesoporous surfaces with antimicrobial properties, *International Journal of Nanomedicine*, 9, 2319, 2014.
- [95] C. Satriano, G. Messina, S. Carnazza, S. Guglielmino, G. Marletta, Bacterial adhesion onto nanopatterned polymer surfaces, *Materials Science and Engineering: C*, 26(5), 942-946, 2006.
- [96] F. Hizal, I. Zhuk, S. Sukhishvili, H.J. Busscher, H.C. van der Mei, C.-H. Choi, Impact of 3D hierarchical nanostructures on the antibacterial efficacy of a bacteria-triggered self-defensive antibiotic coating, *ACS Applied Materials & Interfaces*, 7(36), 20304-20313, 2015.
- [97] S. Wu, F. Zuber, J. Brugger, K. Maniura-Weber, Q. Ren, Antibacterial Au nanostructured surfaces, *Nanoscale*, 8(5), 2620-2625, 2016.
- [98] D.E. Mainwaring, S.H. Nguyen, H. Webb, T. Jakubov, M. Tobin, R.N. Lamb, A.H.-F. Wu, R. Marchant, R.J. Crawford, E.P. Ivanova, The nature of inherent bactericidal activity: insights from the nanotopology of three species of dragonfly, *Nanoscale*, 8(12), 6527-6534, 2016.
- [99] C.M. Bhadra, M. Werner, V.A. Baulin, V.K. Truong, M. Al Kobaisi, S.H. Nguyen, A. Balcytis, S. Juodkazis, J.Y. Wang, D.E. Mainwaring, Subtle Variations in Surface Properties of Black Silicon Surfaces Influence the Degree of Bactericidal Efficiency, *Nano-Micro Letters*, 10(2), 36, 2018.
- [100] J. Pang, T. Sjöström, D. Dymock, B. Su, Adhesion of *Streptococcus mitis* and *Fusobacterium nucleatum* on nanopatterned titanium surfaces, *Bioinspired, Biomimetic and Nanobiomaterials*, 2(3), 117-122, 2013.
- [101] E.P. Ivanova, J. Hasan, H.K. Webb, V.K. Truong, G.S. Watson, J.A. Watson, V.A. Baulin, S. Pogodin, J.Y. Wang, M.J. Tobin, Natural bactericidal surfaces: mechanical rupture of *Pseudomonas aeruginosa* cells by cicada wings, *Small*, 8(16), 2489-2494, 2012.

Toward bioinspired bactericidal nanopatterns

Developing synthetic bactericidal surfaces is a drug-free route to the prevention of implant-associated infections. Surface nanotopographies with specific dimensions and order (also known as surface nanopatterns) have been shown to kill various types of bacterial strains through a mechanical mechanism, while regulating stem cell differentiation and tissue regeneration. The effective ranges of dimensions required to simultaneously achieve both aims are outside the operational range of the vast majority of surface bio-functionalization techniques. Here, a nanoscale additive manufacturing (= 3D printing) technique called electron beam-induced deposition (EBID) is used to fabricate nanopillars with reproducible and precisely controlled dimensions and arrangements that are within those effective ranges (*i.e.*, a height of 190 nm, a diameter of 80 nm, and an interspacing of 170 nm). When compared to the flat surface, the nanopatterned surfaces showed significant bactericidal activity against both *Escherichia coli* and *Staphylococcus aureus* (with respective killing efficiencies of $97 \pm 1\%$ and $36 \pm 5\%$). The difference in the measured killing efficiencies might be related to the more rigid cell wall of *S. aureus* that makes it more resistant to the cell wall disruption caused by the direct penetration of nanopatterns. Nevertheless, assessing the potential of such bactericidal nanopatterns in inducing osteogenic differentiation in mammalian cells requires overcoming the challenges associated with upscaling the area patterned with EBID.

M. Ganjian, K. Modaresifar, M. R. O. Ligeon, L. B. Kunkels, N. Tümer, L. Angeloni, C. W. Hagen, L. G. Otten, P-L. Hagedoorn, I. Apachitei, L. E. Fratila-Apachitei, A. A. Zadpoor, Nature helps: toward bioinspired bactericidal nanopatterns, *Advanced Materials Interfaces*, 2019.

3.1 Introduction

While the increased life expectancy is leading to increased numbers of surgical replacements of orthopedic implants, further increasing risk of implant-associated infections (IAIs) is among the main causes of the failure of those implants¹. Opportunistic pathogens including different types of bacteria are able to attach to and grow on the implant surface, eventually forming a biofilm, which is less susceptible to antibiotics and cannot be easily cleared by the host immune system². This phenomenon hinders the function of the implant and results in significant morbidity and/or mortality³.

Different techniques have been proposed for the prevention of bacterial attachment to the implant surface and/or for killing the bacteria upon contact with the surface⁴. While the majority of non-adherent surfaces are unfavorable for the attachment of both bacterial and host cells, they are not of much utility in this case. That is because attachment and growth of host cells on the implant surface is a crucial step in the osseointegration process. One, therefore, needs surfaces that can selectively kill bacteria while supporting the growth and proliferation of host cells⁵. Consequently, there has been a surge in the efforts aimed at developing contact-killing surfaces with such properties. Non-cytotoxic bactericidal surfaces primarily work based on a chemical or physical killing mechanism. As chemical methods usually deliver antibiotics^{6, 7}, bactericidal metallic nanoparticles such as silver⁸⁻¹⁰, or other antibacterial agents¹¹, their long-term widespread use may lead to the development of bacterial resistance against the delivered agents¹²⁻¹⁴.

On the other hand, surface topographies at the nano/submicron scales have been shown to be capable of killing bacteria through mechanical pathways^{15, 16}. Indeed, several nanotopographical features found in nature, exhibit bactericidal behavior and have inspired the development of an alternative approach to common chemical methods^{17, 18}. A great number of these surface nanotopographies are distinguished by the highly controlled spatial arrangements of their nanoscale features¹⁹. Recent advances in micro- and nano-fabrication techniques have enabled researchers to replicate some of these naturally occurring nanopatterns (*e.g.*, spinules of gecko skin) on synthetic materials or to develop new nanopatterns with desired design parameters such as height (depth), diameter, and interspacing^{20, 21}.

Reactive ion etching (RIE), hydrothermal treatment, anodizing, electron beam lithography (EBL), and nanoimprint lithography (NIL) can be considered as the most

commonly used methods to create nanopatterns. However, the size range that these methods are able to produce and the controllability of the process highly differs from one technique to another¹⁹. In order to systematically investigate the effects of nanopattern design parameters on the bactericidal properties, it is crucial to use a technique that allows the user to control each single design parameter independently of all others while being able to precisely and reproducibly fabricate feature sizes below 100 nm²². Electron beam-induced deposition (EBID) is a nanoscale additive manufacturing (= 3D printing) method, which enables the user to approach feature sizes in the range of a few nanometers²³ by dissociating precursor molecules using a focused electron beam (Figure 3.1a). Precursor molecules dissociate into two parts, a volatile and a nonvolatile part²². The nonvolatile part remains on the substrate and creates a deposited layer, while the volatile part desorbs and is evacuated²⁴. Some studies have shown the EBID potential to create arrays of nanopillars with dimensions of a single nanometer²² as well as complex 2D and 3D shapes²⁵⁻³².

The effective range for the design parameters of surface nanopatterns (in the shape of pillars) in which the bacteria could be mechanically killed in the absence of any antibacterial agents (*i.e.*, the range between 100 nm and 900 nm for the height; 20 nm and 207 nm for the diameter; 9 nm and 380 nm for the interspacing; and the aspect ratio higher than 2) has been recently reported¹⁹. In the specific cases of *Escherichia coli* and *Staphylococcus aureus* as model organisms representing Gram-negative and Gram-positive bacteria, respectively, the reported ranges of dimensions of nanopillars that induce bactericidal behavior are as follows: diameters of 70-100 nm for *S. aureus* and 70-80 nm for *E. coli*, heights of 100-900 nm for *S. aureus* and 180-300 nm for *E. coli*, and interspaces of 60-200 nm for *S. aureus* and 60-380 nm for *E. coli*¹⁹. To simultaneously target both Gram-positive and Gram-negative bacteria, we chose the following approximate dimensions: height = 190 nm, diameter = 80 nm, and interspace = 170 nm. It is, nevertheless, worth noting that the bactericidal behavior of nanopatterns is not only dependent on their dimensions but also on the type of the bacterial strains and their initial attachment to the surface^{19, 33, 34}. A bacterial cell is likely to deform or sink into the nanopatterns due to the penetration of the nanopillars into the bacterial cell wall (Figure 3.1c). To the best of our knowledge, the present study is the first to use EBID as a powerful tool to fabricate nanopatterns with precisely controlled dimensions chosen from the

above-mentioned range in order to have a nanopatterned surface with high killing efficiency against both Gram-negative and Gram-positive bacteria.

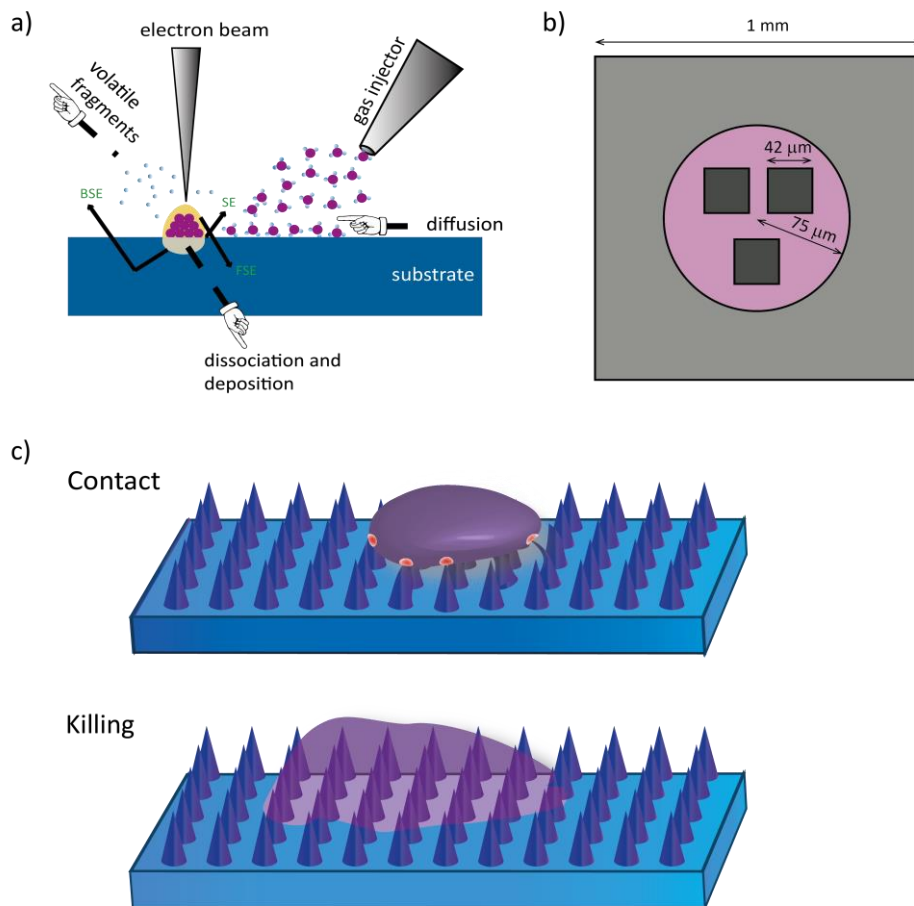


Figure 3.1. a) Schematic representation of the EBID method. b) sample design: dark gray indicates the patterned area, the pink area is close to the patterns, and the light gray area is far from the patterns. c) a schematic drawing demonstrating the fate of bacteria residing on nanopatterns including their deformation on the nanopatterns upon contact and sinking in the nanopatterns due to the penetration of nanopillars into the bacterial cell wall.

3.2 Materials and Methods

3.2.1 Nanopatterns design, fabrication, and characterization

Double-sided polished 4-inch (diameter = 10.16 cm) silicon wafers (thickness = $525 \pm 25 \mu\text{m}$, p-type) were diced into $1 \times 1 \text{ cm}^2$ samples and cleaned with nitric acid. A stream

file was designed to create nanopillars with a square arrangement possessing the approximate dimensions of 190 nm, 80 nm, and 170 nm for their height, base diameter, and center-to-center spacing, respectively. A Nova Nano Lab 650 Dual Beam system (FEI, US) equipped with EBID and scanning electron microscopy (SEM) was used to create three nanopatterned areas of $42 \times 42 \mu\text{m}^2$ on each sample (Figure 3.1b). Trimethyl(methylcyclopentadienyl)-platinum(IV) (chemical formula: $\text{C}_9\text{H}_{18}\text{Pt}$) was used as the precursor gas, and EBID was performed in the electron limited regime and at a working distance of 5 mm with 17.8 kV as the electron beam voltage and 0.6 nA as the beam current. The background vacuum of the system was 8.82 e^{-7} mbar and the EBID process started at 2.33 e^{-6} mbar (as the minimum reachable chamber pressure after opening the gas injection system and leaving the sample for two hours inside the chamber). The writing strategy was single dot exposure, using stream files generated by a MATLAB (MathWorks, US) code. The resulting nanopatterns were characterized by SEM. The height, base diameter, and tip diameter were measured for sixty different pillars per sample by using 35° tilted SEM images. The center-to-center spacing was also measured from the top view images. The mean and standard deviation of the measurements were calculated. The chemical composition of the specimens was characterized using an energy-dispersive X-ray spectroscopy (EDS) analysis performed inside an SEM (Helios NanoLab 600i Dual Beam, FEI, US) on a Pt-C deposited structure with 1000 nm as the diameter and 192 nm as the height, using an image with $\times 16000$ magnification acquired with an accelerating voltage of 5 kV. Nanopatterns were also imaged using atomic force microscopy (AFM) with a Dimension FastScan AFM (Bruker, Germany) in the ScanAsyst mode with a scan rate of 0.96 Hz and a FastScan-A probe having a nominal spring constant of 18 N/m and nominal tip radius of 5 nm. To measure the water contact angle of the nanopatterns, a thin layer of Pt-C was initially deposited on a set of silicon wafers to identify the static contact angle of Pt-C material (θ_0) by a drop shape analyzer (DSA 100, Krüss, Germany) using deionized water. A volume of 2 μl liquid with a falling rate of 1667 $\mu\text{l}/\text{min}$ was placed on the surface using a syringe. The contact angle figure was recorded 5 seconds after the droplet had rested on the surface. The reported value for the measurement is the average contact angle within 30 seconds after the whole volume of the droplet touched the substrate. Since the nanopatterned area is too small compared to the water droplet, its contact angle was measured indirectly using

the Cassie-Baxter wettability model, assuming that air was trapped between the nanopillars^{35,36}. The following equation gives the Cassie-Baxter contact angle (θ_c):

$$\cos(\theta_c) = \varphi (\cos(\theta_0) + 1) - 1$$

Here, φ and θ_0 are the solid fraction (the ratio between the tip area of the nanopillar and the projected surface area) and the contact angle of the flat Pt-C surface, respectively. The solid fraction was calculated as follows:

$$\varphi = \frac{\pi d^2}{4i^2}$$

Where d represents the tip diameter of the nanopillar and i is the interspacing of the nanopillars.

3.2.2 Bacterial growth conditions

Gram-negative bacteria *E. coli* (K12 strain) (BEI Resources, US) and Gram-positive bacteria *S. aureus* (RN0450 strain) (BEI Resources, US) were used to investigate the bactericidal activity of nanopatterned surfaces. *E. coli* and *S. aureus* were grown on Lysogeny broth (LB) (BD Life Sciences, US) and Brain Heart Infusion (BHI) (Sigma-Aldrich, US) agar plates, respectively, at 37 °C overnight. Pre-cultures of both bacterial cells were prepared by inoculating a single colony in 100 ml autoclaved LB/BHI liquid medium, shaken at 140 rpm at 37 °C. The bacterial cells were collected at their logarithmic stage of growth and their optical density at 600 nm wavelength (OD_{600}) in the medium solution was adjusted at a value of 0.05 (55.1×10^6 CFU/ml) and 0.1 (61.6×10^6 CFU/ml) for *E. coli* and *S. aureus*, respectively.

3.2.3 Evaluation of bactericidal properties

The nanopatterned areas of the surface and the surrounding non-patterned areas (75 μm) (Figure 3.1b) were considered as the study (triplicate) and control groups in the bacterial studies, respectively. A thin layer of Pt-C was also deposited on a set of silicon wafers to distinguish the bactericidal effect of nanopatterns from those of the deposition material itself. Samples were immersed in 70% ethanol and subsequently dried exposed to UV light for 20 minutes in a sterile flow cabinet prior to the addition of the bacterial culture. For each type of bacteria, a sample containing three nanopatterned areas was inoculated with 1 ml of bacterial suspension in a 24-well plate (Cell Star, Germany). The samples were then incubated at 37 °C for 18 hours. Subsequently, the adhered bacteria were fixed for SEM imaging using a fixation solution containing 4% formaldehyde

(Sigma-Aldrich, US) and 1% glutaraldehyde (Sigma-Aldrich, US) in 10 mM phosphate buffer. The samples were then washed with MilliQ water and dehydrated using 50%, 70%, and 96% ethanol, respectively, and eventually, soaked in hexamethyldisilazane (Sigma-Aldrich, US) for 30 minutes and air-dried.

A thin layer of gold was sputtered on the samples and SEM images were acquired at various magnifications and tilt angles for each sample. The total number of bacteria adhered to the surface was counted manually from the SEM images. Due to the small patterned area on the surface, it was not feasible to use other assessment methods like live/dead staining or colony-forming unit (CFU) counting. The damaged/dead bacteria were distinguished by a drastic change in their morphology compared to a normal live cell or by observing disruption of their cell wall. The bactericidal efficiency of nanopatterned and non-patterned areas was determined by dividing the number of damaged/dead bacteria by the total number of bacteria in those regions.

3.2.4 Statistical analysis

To assess if there is a significant difference between the killing efficiency of different surfaces (*i.e.*, silicon surface, Pt-C surface, and nanopatterned surface), an analysis of variance was conducted using the one-way ANOVA test followed by *post hoc* analysis. Depending on the results of the Levene's test for the equality of variance, we made a decision about applying the Bonferroni's test (in case that the resultant *p*-value of the Levene's test is higher than 0.05), or the Games-Howell's test (in case that the resultant *p*-value of the Levene's test is less than 0.05). Mean \pm standard deviation for the bactericidal measurements were provided. The statistical analysis was conducted using IBM SPSS Statistics 23 Software and a *p*-value less than 0.05 was considered to be statistically significant.

3.3 Results

3.3.1 Characterization of nanopatterns

Three patterned areas ($42 \times 42 \mu\text{m}^2$) were fabricated on each sample (Figure 3.1b) under the previously mentioned conditions. Nanopatterns were produced in the shape of pillars (similar to a droplet-shaped structure) (Figure 3.2f). The nanopillars had a mean height of 186 nm (SD 8 nm), a base diameter of 75 nm (SD 5 nm), a tip diameter of 21 nm (SD 3 nm), and an interpillar spacing of 170 nm (Figure 3.2). The nanopillar density

was 36 pillars per μm^2 (Figure 3.2c,h). The chemical composition of the EBID deposited material included $\approx 15.5\%$ Pt, $\approx 73.4\%$ C, and $\approx 8.7\%$ O (Figure 3.2g). The result of the water contact angle measurement on the surface of Pt-C showed the hydrophilicity of the surface with a contact angle of $59 \pm 2^\circ$ (inset of Figure 3.2g). Applying the Cassie-Baxter wettability model showed a hydrophobic contact angle of $169 \pm 0.1^\circ$ for the nanopatterned surface.

3.3.2 Bactericidal activity of nanopatterns

E. coli cells exhibited their normal rod-shaped morphology on flat silicon samples (Figure 3.3a,b) and the mean percentage of damaged/dead cells was 8.0% (SD 6.4%) on the control surfaces (Figure 3.5). Similar to previous studies³⁷, the live cells had an average length of 2.6 μm (SD 0.7 μm) and a width of 808 nm (SD 107 nm) (Figure 3.3a,b). On the other hand, *E. coli* cells were found extremely deformed on the nanopatterned surfaces (Figure 3.3e,f) with substantial amounts of the disrupted bacterial cell wall and remnant cellular fragments on the nanopatterned areas (Figure 3.3c-e). The killing efficiency was $97.0 \pm 1.2\%$ for *E. coli* cells on the nanopatterned surfaces. The length and width of the cells on the nanopatterned surfaces could not be determined due to the drastic deformations and disruptions of the bacterial cells (Figure 3.3f).

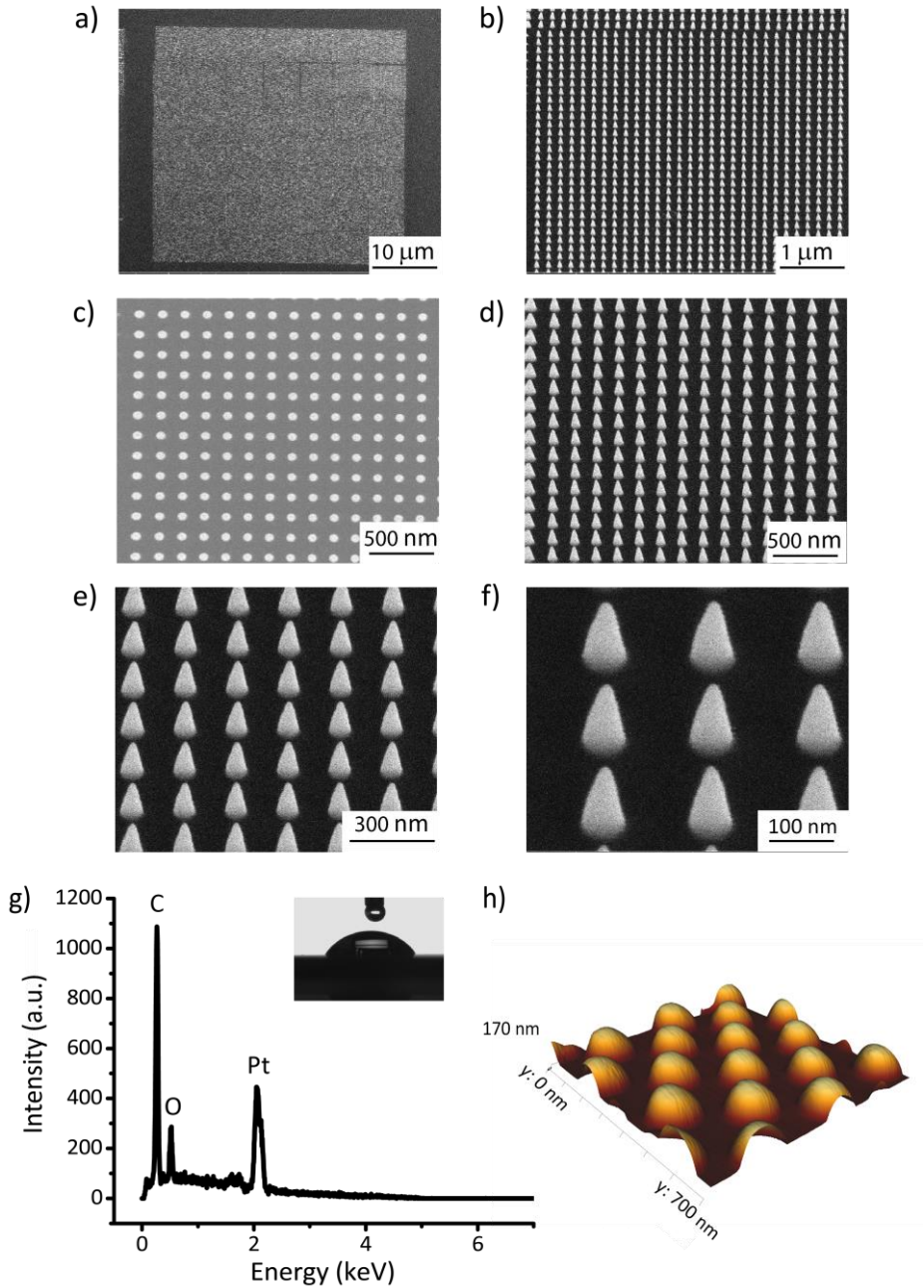


Figure 3.2. a–f) SEM images of nanopillars produced by EBID at different magnifications: a,c) top view and b,d,e,f) 35° tilted view. g) EDS characterization of Pt-C deposited structure. The inset shows the water contact angle on the flat Pt-C surface. h) AFM imaging showing a 3D overview of the nanopillars.

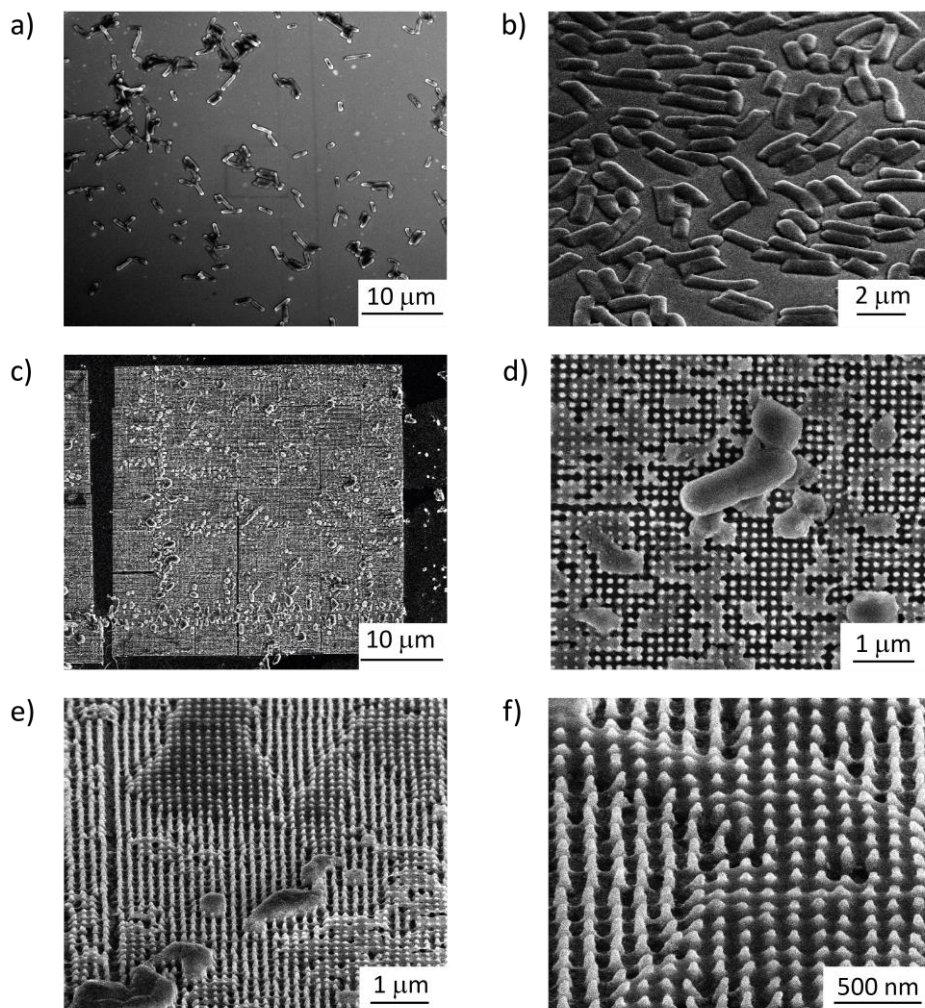


Figure 3.3. SEM images of *E. coli* bacteria on the control Si surface: a) top overview and b) 50° tilted view. SEM images of *E. coli* bacteria on the nanopatterned surface after 18 hours incubation: c) top overview, d) damaged bacteria from the top view, e) damaged bacteria from 50° tilted view, and f) bacteria totally sunk into the nanopatterns (50° tilted view).

Similarly, *S. aureus* cells had a normal coccoid-shaped morphology and size³⁸ on the Si control surfaces with an average diameter of ≈ 790 nm (SD 66 nm), and no bacterial cell was found damaged or dead (Figure 3.4a,b). The damaged cells, mostly sunk on the nanopillars, showed a squashed morphology and the penetration of the nanopillars into the bacterial cell wall could be clearly seen (Figure 3.4d,f). Additionally, bending of the nanopillars underneath the bacterial cells was observed and leftovers of bacterial

components were also found on some of the nanopillars (Figure 3.4e,f). The killing efficiency of the nanopatterns for *S. aureus* cells was $36.5 \pm 4.7\%$ (Figure 3.5). Furthermore, the bactericidal efficiency of Pt-C surface against *E. coli* and *S. aureus* was significantly lower than the nanopatterned surface ($p < 0.0001$ and $p < 0.01$, respectively) (Figure 3.5).

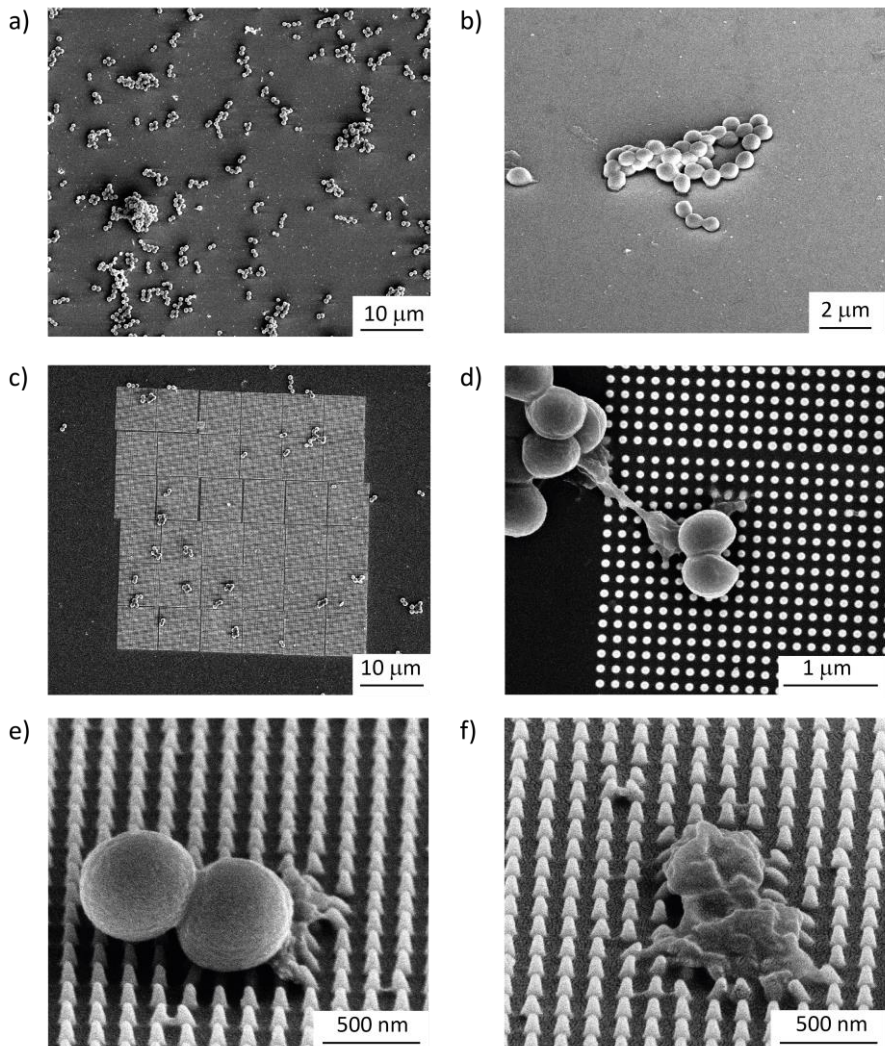


Figure 3.4. SEM images of *S. aureus* bacteria on the control Si surface: a) top overview and b) 50° tilted view. SEM images of *S. aureus* bacteria on the nanopatterned surface: c) top overview, d) two healthy and one dead bacteria on the pattern from the top view, e) the remnant fragments of the bacteria on the nanopillars, and f) two dead bacteria on the nanopatterns from 50° tilted view.

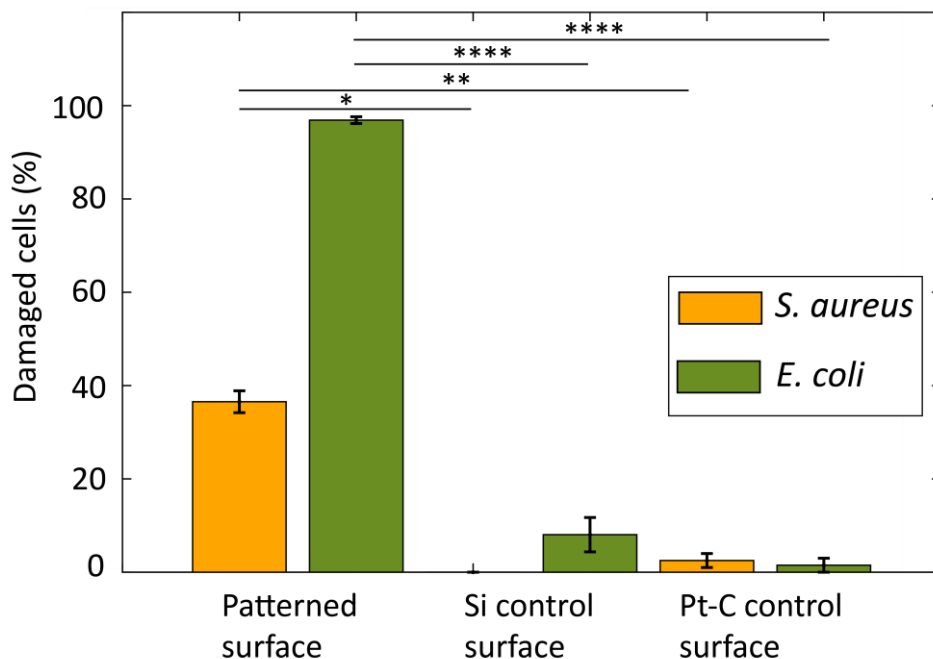


Figure 3.5. Quantitative characterization of the percentage of damaged *E. coli* and *S. aureus* bacterial cells on nanopatterned, Si control, and Pt-C control surfaces ($n = 3$ per group, One-way ANOVA followed by Games-Howell's test, * $p < 0.05$, ** $p < 0.01$, and **** $p < 0.0001$). The killing efficiency was not affected by the chemical composition of the surface, and the number of damaged/dead cells was significantly higher on the nanopatterned surface.

3.4 Discussion

Designing multi-biofunctional surfaces to selectively influence the behavior of mammalian cells and bacteria is of high current interest and importance for the development of implant materials as well as being a formidable challenge given the substantial differences between mammalian cells and bacteria in sensing and responding to surfaces³⁹. Some of the naturally occurring nanopatterned surfaces (*e.g.*, gecko skin, cicada wings, dragonfly wings) have shown bactericidal properties while they are not cytotoxic (Figure 3.6)^{17, 33, 40-44}.

When it comes to designing orthopedic implants, the holy grail would be having surfaces that simultaneously kill bacteria and promote osteogenesis (or osteogenic differentiation of stem cells). The main contribution of this study was the application of an ultra-fine nanoscale 3D printing process with a resolution of a few nanometers to create nanopatterns with reproducible and precisely controlled dimensions that exhibit

bactericidal behavior against both Gram-negative and Gram-positive bacteria. The dimensions of the nanopatterns produced in this study are within the bactericidal range found in literature and close to some of the naturally occurring bactericidal surfaces (Figure 3.6)¹⁹. The vast majority of commonly used nano-fabrication techniques do not allow control over individual dimensions of such nanostructures independently of the other dimensions. EBID makes it feasible to produce specific controllable dimensions at the nanoscale, with a resolution comparable or better than EBL²². Additionally, there is no need for a mask or other chemical wet processes. These characteristics make EBID an ideal method for producing a variety of nanopatterns that are required for performing systematic studies to determine which exact dimensions of the nanopatterns result in maximum bactericidal activity while promoting osteogenic differentiation of the host cells. EBID uses a precursor gas (trimethyl(methylcyclopentadienyl)-platinum(IV) in this study) to write directly on the substrate. In the EBID process, the precursor gas molecules dissociate on the substrate under the electron beam⁴⁵. The main components of the deposited material in this study were platinum and carbon. The platinum percentage can vary from 8.9 % to 16.8 % depending on the beam current, deposition time, and electron dosage⁴⁶.

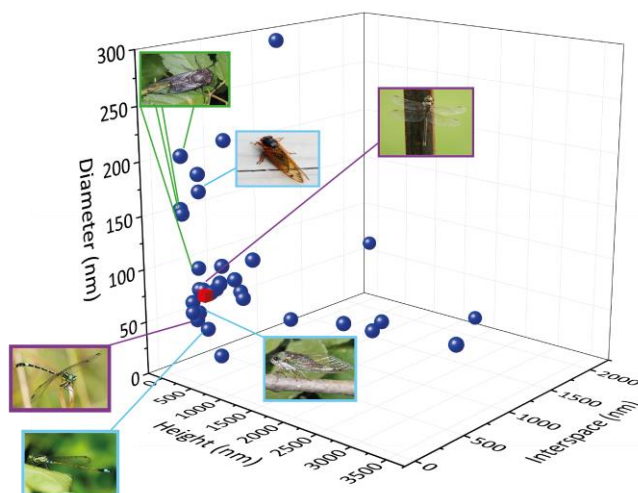


Figure 3.6. The dimensions of the bactericidal nanopatterns found in the literature. The nanopattern produced for this study (represented as the red cube) had dimensions close to the dimension range of naturally occurring nanopatterns. The images of insects with green and blue frames are reprinted from wikipedia.org and stock.adobe.com, respectively, with permission. The images with purple frames are taken by Roos Coy (www.therebedragonflies.com.au) and reprinted with permission.

The nanopatterned surface showed a high bactericidal efficiency against *E. coli* where almost all the bacterial cells were sunk on the nanopillars with the cell components leaked out and a distorted morphology. However, the nanopatterns could not kill *S. aureus* as efficiently as *E. coli*. Considering that the bactericidal activity of the nanopatterns is physical in nature, (corroborated by the results of Pt-C flat surface), the difference between the bactericidal efficiency against *E. coli* and *S. aureus* could be explained by the more rigid and thicker cell wall of *S. aureus* which requires higher forces to be ruptured^{17,40,47}. Bending of the nanopillars beneath the bacteria is consistent with this hypothesis (Figure 3.4e,f). Other differences between Gram-negative and Gram-positive bacteria such as the size and morphology could also affect the bactericidal efficiency⁴⁸. Moreover, as remnant fragments of *S. aureus* were observed on the nanopatterns (Figure 3.4e), one could speculate that the bacteria had found the surface unfavorable for adhesion and moved away from the surface. This hypothesis has been previously introduced in the literature⁴³. If a number of bacteria have moved away from the surface, the antibacterial activity that includes the bactericidal effects and prevention of bacterial adhesion to the surface might have been stronger than what could be concluded from the SEM images alone. Due to the small size of the patterned areas (compared to the whole samples' surface) which could be fabricated by EBID, other methods of antibacterial activity assessment such as live/dead staining and CFU enumeration⁴⁹ were not applicable. Nevertheless, previous studies have shown that bacteria with similar irregular/damaged morphologies are equivalent to the dead bacteria in those mentioned methods^{50,51}.

While the direct penetration of high aspect ratio nanopatterns into the bacterial cell wall and their consequent disruption is considered the main bactericidal mechanism of nanopatterned surfaces, many other factors have been proposed to play important roles in the bactericidal potential of nanopatterned surfaces¹⁹. For instance, the uniformity of the nanopatterns⁵², their compaction⁵³ and density⁵⁴ on the surface, and surface wettability¹⁹ have been shown to affect the bactericidal activity. In this regard, theoretical studies with a mechanistic point of view have previously shown that the interspace and the diameter of the nanopillars could be the determining factors for applying the highest force and imposing the highest degree of stretching and deformation, and ultimately, leading to death of bacteria⁵⁵. Therefore, more systematic studies are needed to improve the bactericidal efficiency of nanopatterns against more resistant bacteria such as methicillin-resistant *S. aureus*. Moreover, studying the behavior of mammalian cells on

such nanopatterns is required to better visualize and tag the exact overlapping range of bactericidal and osteogenic nanopatterns. So far, an overlap between the bactericidal and osteogenic ranges can already be pictured based on the data available in the literature (Figure 3.7) ^{19, 56-61}. The nanopatterns produced in this study are positioned inside the overlap area of these two important types of behavior, implying that they are likely to exhibit osteogenic properties as well. It is, therefore, important to further assess their osteogenic properties in future studies. Indeed, more studies on the osteogenic behavior of nanopatterned surfaces are required to more accurately define the boundaries of the osteogenic range.

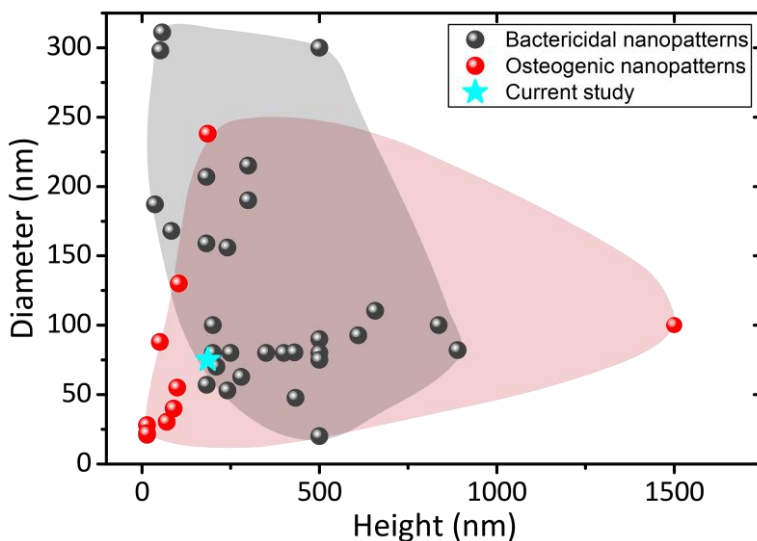


Figure 3.7. Comparison of the dimensions (diameter and height) of nanopillars found in the literature displaying bactericidal and osteogenic activities. This graph illustrates that the nanopattern studied here is within the area where nanopatterns possess both bactericidal and osteogenic properties.

Although EBID enables the fabrication of nanopatterns with arbitrary shapes and accurate controllable dimensions, which is ideal for systematic studies, upscaling the patterned area is still challenging. It took 6.5 hours to produce each of the $42 \times 42 \mu\text{m}^2$ patterned areas, check the dimensions, and refocus again to have exactly the same nanostructures. To create surfaces that are suitable for further experiments with mammalian cells such as mesenchymal stem cells (MSCs) culture, it is necessary to enlarge the patterned area, for example to $3 \times 3 \text{mm}^2$ which could be achieved by further developments of the process. One approach would be to use parallel electron beam-

induced deposition using a multi-beam scanning electron microscope, which enables patterning the desired area using several parallel beams (e.g., 14×14 beams to expose a larger area and reduce the required deposition time to a few hours⁶²). Another method, which has a comparably higher throughput, higher resolution, and lower cost is using EBID patterns as a mask stamp for step and repeat NIL. There are two major NIL methods: UV NIL and thermal NIL. For the UV step and repeat NIL, one needs to deposit the desired nanopatterns on a substrate that is highly transmissive to deep UV (e.g., fused silica⁶³ or glass substrate⁶⁴). The thermal step and repeat NIL is another technique to enlarge the nanopatterned area. Si is the preferred stamp material for thermal NIL due to its high elastic modulus, mechanical strength, and thermal expansion coefficient⁶⁵. Transferring EBID nanopatterns composed of the precursor molecules into Si substrate as the NIL stamp is the first step for this technique, which needs to be done by RIE^{66,67}. In both NIL methods, the following step after preparing a nanopatterned stamp is bringing the stamp in contact with the desired substrate that should have been covered by imprint polymer inside a nanoimprint machine and applying a constant pressure. After the required time, the pressure is released and the user can separate the stamp from the polymer and move it to pattern the next desired area. The final step is etching the residual layer of the imprint polymer and the substrate using RIE. Regardless of the chosen upscaling technique, the underlying EBID technology is the key to achieving reproducible and precisely controlled nanopatterns and is, therefore, recommended for future studies.

3.5 Conclusions

In order to develop a bactericidal surface suitable for the fabrication of orthopedic implants, we used EBID to create nanopatterns with dimensions within the bactericidal range and comparable to nanopatterns found in nature in terms of height and diameter. The nanopatterns were produced in the shape of pillars with a height of ≈ 190 nm, a diameter of 80 nm, and an interspacing of 170 nm. The nanopillars were found to mechanically rupture the cell wall of *E. coli* and *S. aureus* and showed a significantly higher bactericidal activity as compared to the non-patterned surfaces and flat surfaces coated with the same material as the pillars. However, the bactericidal efficiency for *S. aureus* was significantly lower than *E. coli*, which could be explained by the differences in the characteristics of Gram-negative and Gram-positive bacteria such as the cell wall thickness and stiffness. Further investigations are required to determine the exact killing

mechanism, the role of different factors involved in that process, and the possible osteogenic activity, as the dimensions of the current nanopatterns are within the osteogenic range. Although EBID is a very powerful technique to have control over all of the dimensions of the nanopatterns in the fabrication process, the challenge of upscaling the patterned area while reducing the writing time is yet to be overcome. This is crucial for further experiments on mammalian cells, which are larger in size than bacterial cells. Such an approach would open the way for the development of nanopatterns with simultaneous bactericidal and osteogenic potential that could be translated to clinical use in the future.

Bibliography

- [1] W. Zimmerli, A. Trampuz, P.E. Ochsner, Prosthetic-joint infections, *New England Journal of Medicine*, 351(16), 1645-1654, 2004.
- [2] C.R. Arciola, D. Campoccia, L. Montanaro, Implant infections: adhesion, biofilm formation and immune evasion, *Nature Reviews Microbiology*, 1, 2018.
- [3] J.M. Steckelberg, D.R. Osmon, *Prosthetic joint infections*, in *Infections Associated with Indwelling Medical Devices, Third Edition*. 2000, American Society of Microbiology. p. 173-209.
- [4] J. Hasan, R.J. Crawford, E.P. Ivanova, Antibacterial surfaces: the quest for a new generation of biomaterials, *Trends in Biotechnology*, 31(5), 295-304, 2013.
- [5] Y. Wang, G. Subbiahdoss, J. Swartjes, H.C. van der Mei, H.J. Busscher, M. Libera, Length-Scale Mediated Differential Adhesion of Mammalian Cells and Microbes, *Advanced Functional Materials*, 21(20), 3916-3923, 2011.
- [6] S. Bakhshandeh, Z. Gorgin Karaji, K. Lietaert, A.C. Fluit, C.E. Boel, H.C. Vogely, T. Vermonden, W.E. Hennink, H. Weinans, A.A. Zadpoor, Simultaneous Delivery of Multiple Antibacterial Agents from Additively Manufactured Porous Biomaterials to Fully Eradicate Planktonic and Adherent Staphylococcus aureus, *ACS Applied Materials & Interfaces*, 9(31), 25691-25699, 2017.
- [7] J. Hirschfeld, E.M. Akinoglu, D.C. Wirtz, A. Hoerauf, I. Bekereldjian-Ding, S. Jepsen, E.-M. Haddouti, A. Limmer, M. Giersig, Long-term release of antibiotics by carbon nanotube-coated titanium alloy surfaces diminish biofilm formation by Staphylococcus epidermidis, *Nanomedicine: Nanotechnology, Biology and Medicine*, 13(4), 1587-1593, 2017.
- [8] M. Croes, S. Bakhshandeh, I. van Hengel, K. Lietaert, K. van Kessel, B. Pouran, B. van der Wal, H. Vogely, W. Van Hecke, A. Fluit, Antibacterial and immunogenic behavior of silver coatings on additively manufactured porous titanium, *Acta Biomaterialia*, 81, 315-327, 2018.
- [9] I.A. van Hengel, M. Riool, L.E. Fratila-Apachitei, J. Witte-Bouma, E. Farrell, A.A. Zadpoor, S.A. Zaat, I. Apachitei, Selective laser melting porous metallic implants with immobilized silver nanoparticles kill and prevent biofilm formation by methicillin-resistant Staphylococcus aureus, *Biomaterials*, 140, 1-15, 2017.
- [10] S. Amin Yavari, L. Loozen, F.L. Paganelli, S. Bakhshandeh, K. Lietaert, J.A. Groot, A.C. Fluit, C. Boel, J. Alblas, H.C. Vogely, Antibacterial behavior of additively manufactured porous titanium with nanotubular surfaces releasing silver ions, *ACS Applied Materials & Interfaces*, 8(27), 17080-17089, 2016.
- [11] X.J. Loh, Latest advances in antibacterial materials, *Journal of Molecular and Engineering Materials*, 5(01), 1740001, 2017.
- [12] A. Elbourne, R.J. Crawford, E.P. Ivanova, Nano-structured antimicrobial surfaces: From nature to synthetic analogues, *Journal of Colloid and Interface Science*, 508, 603-616, 2017.
- [13] A. Panáček, L. Kvítek, M. Smékalová, R. Večeřová, M. Kolář, M. Röderová, F. Dyčka, M. Šebela, R. Prucek, O. Tomanec, Bacterial resistance to silver nanoparticles and how to overcome it, *Nature Nanotechnology*, 13(1), 65-71, 2018.

-
- [14] M.C. Enright, D.A. Robinson, G. Randle, E.J. Feil, H. Grundmann, B.G. Spratt, The evolutionary history of methicillin-resistant *Staphylococcus aureus* (MRSA), *Proceedings of the National Academy of Sciences*, 99(11), 7687-7692, 2002.
- [15] S. Ghosh, S. Niu, M. Yankova, M. Mecklenburg, S.M. King, J. Ravichandran, R.K. Kalia, A. Nakano, P. Vashishta, P. Setlow, Analysis of killing of growing cells and dormant and germinated spores of *Bacillus* species by black silicon nanopillars, *Scientific Reports*, 7(1), 17768, 2017.
- [16] D.P. Linklater, S. Juodkazis, S. Rubanov, E.P. Ivanova, Comment on “Bactericidal Effects of Natural Nanotopography of Dragonfly Wing on *Escherichia coli*”, *ACS Applied Materials & Interfaces*, 9(35), 29387-29393, 2017.
- [17] J. Hasan, H.K. Webb, V.K. Truong, S. Pogodin, V.A. Baulin, G.S. Watson, J.A. Watson, R.J. Crawford, E.P. Ivanova, Selective bactericidal activity of nanopatterned superhydrophobic cicada *Psaltoda claripennis* wing surfaces, *Applied Microbiology and Biotechnology*, 97(20), 9257-9262, 2013.
- [18] I. Izquierdo-Barba, J.M. García-Martín, R. Álvarez, A. Palmero, J. Esteban, C. Pérez-Jorge, D. Arcos, M. Vallet-Regí, Nanocolumnar coatings with selective behavior towards osteoblast and *Staphylococcus aureus* proliferation, *Acta Biomaterialia*, 15, 20-28, 2015.
- [19] K. Modaresifar, S. Azizian, M. Ganjian, L.E. Fratila-Apachitei, A.A. Zadpoor, Bactericidal effects of nanopatterns: a systematic review, *Acta Biomaterialia*, 2018.
- [20] D.W. Green, K.K.-H. Lee, J.A. Watson, H.-Y. Kim, K.-S. Yoon, E.-J. Kim, J.-M. Lee, G.S. Watson, H.-S. Jung, High Quality Bioreplication of Intricate Nanostructures from a Fragile Gecko Skin Surface with Bactericidal Properties, *Scientific Reports*, 7, 2017.
- [21] M.N. Dickson, E.I. Liang, L.A. Rodriguez, N. Vollereaux, A.F. Yee, Nanopatterned polymer surfaces with bactericidal properties, *Biointerphases*, 10(2), 021010, 2015.
- [22] W.F. Van Dorp, B. Van Someren, C.W. Hagen, P. Kruit, P.A. Crozier, Approaching the resolution limit of nanometer-scale electron beam-induced deposition, *Nano Letters*, 5(7), 1303-1307, 2005.
- [23] M.-K. Seo, H.-G. Park, J.-K. Yang, J.-Y. Kim, S.-H. Kim, Y.-H. Lee, Controlled sub-nanometer tuning of photonic crystal resonator by carbonaceous nano-dots, *Optics Express*, 16(13), 9829-9837, 2008.
- [24] G. Gazzadi, S. Frabboni, C. Menozzi, L. Incerti, Electrical characterization of suspended Pt nanowires grown by EBID with water vapour assistance, *Microelectronic Engineering*, 85(5-6), 1166-1169, 2008.
- [25] W. Van Dorp, C.W. Hagen, A critical literature review of focused electron beam induced deposition, *Journal of Applied Physics*, 104(8), 10, 2008.
- [26] S. Janbaz, N. Noordzij, D.S. Widyaratih, C.W. Hagen, L.E. Fratila-Apachitei, A.A. Zadpoor, Origami lattices with free-form surface ornaments, *Science Advances*, 3(11), eaao1595, 2017.
- [27] T. Bret, I. Utke, P. Hoffmann, Influence of the beam scan direction during focused electron beam induced deposition of 3D nanostructures, *Microelectronic Engineering*, 78, 307-313, 2005.
- [28] T. Bret, I. Utke, P. Hoffmann, M. Abourida, P. Doppelt, Electron range effects in focused electron beam induced deposition of 3D nanostructures, *Microelectronic Engineering*, 83(4-9), 1482-1486, 2006.

-
- [29] R. Winkler, F.-P. Schmidt, U. Haselmann, J.D. Fowlkes, B.B. Lewis, G. Kothleitner, P.D. Rack, H. Plank, Direct-write 3d nanoprinting of plasmonic structures, *ACS Applied Materials & Interfaces*, 9(9), 8233-8240, 2016.
- [30] J.D. Fowlkes, R. Winkler, B.B. Lewis, A. Fernandez-Pacheco, L. Skoric, D. Sanz-Hernandez, M.G. Stanford, E. Mutunga, P.D. Rack, H. Plank, High-Fidelity 3D-Nanoprinting via Focused Electron Beams: Computer-Aided Design (3BID), *ACS Applied Nano Materials*, 1(3), 1028-1041, 2018.
- [31] J.D. Fowlkes, R. Winkler, B.B. Lewis, M.G. Stanford, H. Plank, P.D. Rack, Simulation-guided 3D nanomanufacturing via focused electron beam induced deposition, *ACS Nano*, 10(6), 6163-6172, 2016.
- [32] L. Keller, M. Huth, Pattern generation for direct-write three-dimensional nanoscale structures via focused electron beam induced deposition, *Beilstein Journal of Nanotechnology*, 9(1), 2581-2598, 2018.
- [33] K. Nowlin, A. Boseman, A. Covell, D. LaJeunesse, Adhesion-dependent rupturing of *Saccharomyces cerevisiae* on biological antimicrobial nanostructured surfaces, *Journal of The Royal Society Interface*, 12(102), 20140999, 2015.
- [34] T. Diu, N. Faruqui, T. Sjöström, B. Lamarre, H.F. Jenkinson, B. Su, M.G. Ryadnov, Cicada-inspired cell-instructive nanopatterned arrays, *Scientific Reports*, 4, 2014.
- [35] B. Bhushan, M. Nosonovsky, The rose petal effect and the modes of superhydrophobicity, *Philosophical Transactions of the Royal Society A: Mathematical, Physical and Engineering Sciences*, 368(1929), 4713-4728, 2010.
- [36] M. Sun, G.S. Watson, Y. Zheng, J.A. Watson, A. Liang, Wetting properties on nanostructured surfaces of cicada wings, *Journal of Experimental Biology*, 212(19), 3148-3155, 2009.
- [37] O. Pierucci, Dimensions of *Escherichia coli* at various growth rates: model for envelope growth, *Journal of Bacteriology*, 135(2), 559-574, 1978.
- [38] L. Harris, S. Foster, R. Richards, An introduction to *Staphylococcus aureus*, and techniques for identifying and quantifying *S. aureus* adhesins in relation to adhesion to biomaterials: review, *European Cells & Materials*, 4(3), 2002.
- [39] K. Anselme, P. Davidson, A. Popa, M. Giazzon, M. Liley, L. Ploux, The interaction of cells and bacteria with surfaces structured at the nanometre scale, *Acta Biomaterialia*, 6(10), 3824-3846, 2010.
- [40] E.P. Ivanova, J. Hasan, H.K. Webb, V.K. Truong, G.S. Watson, J.A. Watson, V.A. Baulin, S. Pogodin, J.Y. Wang, M.J. Tobin, Natural bactericidal surfaces: mechanical rupture of *Pseudomonas aeruginosa* cells by cicada wings, *Small*, 8(16), 2489-2494, 2012.
- [41] V.K. Truong, N.M. Geeganagamage, V.A. Baulin, J. Vongsvivut, M.J. Tobin, P. Luque, R.J. Crawford, E.P. Ivanova, The susceptibility of *Staphylococcus aureus* CIP 65.8 and *Pseudomonas aeruginosa* ATCC 9721 cells to the bactericidal action of nanostructured *Calopteryx haemorrhoidalis* damselfly wing surfaces, *Applied Microbiology and Biotechnology*, 101(11), 4683-4690, 2017.
- [42] S.M. Kelleher, O. Habimana, J. Lawler, B. O'Reilly, S. Daniels, E. Casey, A. Cowley, Cicada wing surface topography: an investigation into the bactericidal properties of nanostructural features, *ACS Applied Materials & Interfaces*, 8(24), 14966-14974, 2015.

- [43] C.D. Bandara, S. Singh, I.O. Afara, A. Wolff, T. Tesfamichael, K. Ostrikov, A. Oloyede, Bactericidal effects of natural nanotopography of dragonfly wing on *Escherichia coli*, *ACS Applied Materials & Interfaces*, 9(8), 6746-6760, 2017.
- [44] G.S. Watson, D.W. Green, L. Schwarzkopf, X. Li, B.W. Cribb, S. Myhra, J.A. Watson, A gecko skin micro/nano structure—A low adhesion, superhydrophobic, anti-wetting, self-cleaning, biocompatible, antibacterial surface, *Acta Biomaterialia*, 21, 109-122, 2015.
- [45] J. Wnuk, S. Rosenberg, J. Gorham, W. Van Dorp, C. Hagen, D. Fairbrother, Electron beam deposition for nanofabrication: Insights from surface science, *Surface Science*, 605(3-4), 257-266, 2011.
- [46] A. Botman, M. Hesselberth, J. Mulders, Improving the conductivity of platinum-containing nano-structures created by electron-beam-induced deposition, *Microelectronic Engineering*, 85(5-6), 1139-1142, 2008.
- [47] S. Pogodin, J. Hasan, V.A. Baulin, H.K. Webb, V.K. Truong, V. Boshkovikj, C.J. Fluke, G.S. Watson, J.A. Watson, R.J. Crawford, Biophysical model of bacterial cell interactions with nanopatterned cicada wing surfaces, *Biophysical Journal*, 104(4), 835-840, 2013.
- [48] E. Fadeeva, V.K. Truong, M. Stiesch, B.N. Chichkov, R.J. Crawford, J. Wang, E.P. Ivanova, Bacterial retention on superhydrophobic titanium surfaces fabricated by femtosecond laser ablation, *Langmuir*, 27(6), 3012-3019, 2011.
- [49] J. Sjollem, S.A. Zaat, V. Fontaine, M. Ramstedt, R. Luginbuehl, K. Thevissen, J. Li, H.C. van der Mei, H.J. Busscher, In vitro methods for the evaluation of antimicrobial surface designs, *Acta Biomaterialia*, 2018.
- [50] E.P. Ivanova, J. Hasan, H.K. Webb, G. Gervinskas, S. Juodkazis, V.K. Truong, A.H. Wu, R.N. Lamb, V.A. Baulin, G.S. Watson, Bactericidal activity of black silicon, *Nature Communications*, 4, 2013.
- [51] D. Widayatih, P.-L. Hagedoorn, L. Otten, M. Ganjian, N. Tümer, I. Apachitei, C.W.K. Hagen, L. Fratila-Apachitei, A.A. Zadpoor, Towards osteogenic and bactericidal nanopatterns?, *Nanotechnology*, 2019.
- [52] L.E. Fisher, Y. Yang, M.-F. Yuen, W. Zhang, A.H. Nobbs, B. Su, Bactericidal activity of biomimetic diamond nanocone surfaces, *Biointerphases*, 11(1), 011014, 2016.
- [53] D.P. Linklater, H.K.D. Nguyen, C.M. Bhadra, S. Juodkazis, E.P. Ivanova, Influence of nanoscale topology on bactericidal efficiency of black silicon surfaces, *Nanotechnology*, 28(24), 245301, 2017.
- [54] S. Wu, F. Zuber, K. Maniura-Weber, J. Brugger, Q. Ren, Nanostructured surface topographies have an effect on bactericidal activity, *Journal of Nanobiotechnology*, 16(1), 20, 2018.
- [55] M. Mirzaali, I. Van Dongen, N. Tümer, H. Weinans, S.A. Yavari, A. Zadpoor, In-silico quest for bactericidal but non-cytotoxic nanopatterns, *Nanotechnology*, 29(43), 43LT02, 2018.
- [56] J.-H. Hwang, D.-H. Lee, M.R. Byun, A.R. Kim, K.M. Kim, J.I. Park, H.T. Oh, E.S. Hwang, K.B. Lee, J.-H. Hong, Nanotopological plate stimulates osteogenic differentiation through TAZ activation, *Scientific Reports*, 7(1), 3632, 2017.
- [57] T. Sjöström, L.E. McNamara, R.D. Meek, M.J. Dalby, B. Su, 2D and 3D nanopatterning of titanium for enhancing osteoinduction of stem cells at implant surfaces, *Advanced Healthcare Materials*, 2(9), 1285-1293, 2013.

-
- [58] Z. Li, J. Qiu, L.Q. Du, L. Jia, H. Liu, S. Ge, TiO₂ nanorod arrays modified Ti substrates promote the adhesion, proliferation and osteogenic differentiation of human periodontal ligament stem cells, *Materials Science and Engineering: C*, 76, 684-691, 2017.
- [59] L.E. McNamara, T. Sjöström, K.E. Burgess, J.J. Kim, E. Liu, S. Gordonov, P.V. Moghe, R.D. Meek, R.O. Oreffo, B. Su, Skeletal stem cell physiology on functionally distinct titania nanotopographies, *Biomaterials*, 32(30), 7403-7410, 2011.
- [60] T. Sjöström, M.J. Dalby, A. Hart, R. Tare, R.O. Oreffo, B. Su, Fabrication of pillar-like titania nanostructures on titanium and their interactions with human skeletal stem cells, *Acta Biomaterialia*, 5(5), 1433-1441, 2009.
- [61] G.M. de Peppo, H. Agheli, C. Karlsson, K. Ekström, H. Brisby, M. Lennerås, S. Gustafsson, P. Sjövall, A. Johansson, E. Olsson, Osteogenic response of human mesenchymal stem cells to well-defined nanoscale topography in vitro, *International Journal of Nanomedicine*, 9, 2499, 2014.
- [62] P. Post, A. Mohammadi-Gheidari, C. Hagen, P. Kruit, Parallel electron-beam-induced deposition using a multi-beam scanning electron microscope, *Journal of Vacuum Science & Technology B, Nanotechnology and Microelectronics: Materials, Processing, Measurement, and Phenomena*, 29(6), 06F310, 2011.
- [63] Y. Zhao, E. Berenschot, M. De Boer, H. Jansen, N. Tas, J. Huskens, M. Elwenspoek, Fabrication of a silicon oxide stamp by edge lithography reinforced with silicon nitride for nanoimprint lithography, *Journal of Micromechanics and Microengineering*, 18(6), 064013, 2008.
- [64] D.J. Resnick, S. Sreenivasan, C.G. Willson, Step & flash imprint lithography, *Materials Today*, 8(2), 34-42, 2005.
- [65] L.J. Guo, Nanoimprint lithography: methods and material requirements, *Advanced Materials*, 19(4), 495-513, 2007.
- [66] H. Cao, Z. Yu, J. Wang, J.O. Tegenfeldt, R.H. Austin, E. Chen, W. Wu, S.Y. Chou, Fabrication of 10 nm enclosed nanofluidic channels, *Applied Physics Letters*, 81(1), 174-176, 2002.
- [67] A. Notargiacomo, E. Giovine, L. Di Gaspare, Ion and electron beam deposited masks for pattern transfer by reactive ion etching, *Microelectronic Engineering*, 88(8), 2710-2713, 2011.

The effects of geometry on bactericidal properties

Recent progress in nano-/micro-fabrication techniques has paved the way for the emergence of synthetic bactericidal patterned surfaces that are capable of killing the bacteria via mechanical mechanisms. Different design parameters are known to affect the bactericidal activity of nanopatterns. Evaluating the effects of each parameter, isolated from the others, requires systematic studies. Here, we systematically assess the effects of the interspacing and disordered arrangement of nanopillars on the bactericidal properties of nanopatterned surfaces. Electron beam-induced deposition (EBID) was used to additively manufacture nanopatterns with precisely controlled dimensions (*i.e.*, a height of 190 nm, a diameter of 80 nm, and interspaces of 100, 170, 300, and 500 nm) as well as disordered versions of them. The killing efficiency of the nanopatterns against *Staphylococcus aureus* bacteria increased by decreasing the interspace, achieving the highest efficiency of $62 \pm 23\%$ on the nanopatterns with 100 nm interspacing. By comparison, the disordered nanopatterns did not influence the killing efficiency significantly, as compared to their ordered correspondents. Direct penetration of nanopatterns into the bacterial cell wall was identified as the killing mechanism according to cross-sectional views, which is consistent with previous studies. These findings indicate that future studies aimed at optimizing the design of bactericidal nanopatterns should focus on interspacing as an important parameter affecting the bactericidal properties.

K. Modaresifar, L. B. Kunkels, M. Ganjian, N. Tümer, C. W. Hagen, L. G. Otten, P-L. Hagedoorn, L. Angeloni, M. K. Ghatkesar, L. E. Fratila-Apachitei, A. A. Zadpoor, Deciphering the roles of interspace and controlled disorder in the bactericidal properties of nanopatterns against *Staphylococcus aureus*, *Nanomaterials*, 2020.

4.1 Introduction

An increasing number of orthopedic implants are being implanted every year ¹, resulting in a growing number of implant-associated infections (IAIs). Despite all efforts in preventing infections in clinical settings, IAIs still occur and are recognized as one of the most prevalent causes of the failure of orthopedic implants ^{2,3}. Such infections usually necessitate either revision surgeries or the prolonged administration of antibiotics, which diminishes the patients' quality of life, causes major side effects, significantly increases the healthcare costs, and could lead to patient morbidity or even mortality ^{3,4}. *Staphylococci* bacteria are the most widespread infectious pathogens involved in IAIs ⁵. While *Staphylococcus aureus* accounts for 20%-30% of IAIs following fracture fixation and prosthetic joint infections ⁵⁻⁷, antibiotic treatment could act as a double-edged sword particularly given the growing crisis of antibacterial resistance leading to the evolution of antibiotic-resistant species like methicillin-resistant *Staphylococcus aureus* (MRSA) ⁸. Moreover, recent reports have shown that in addition to antibiotics, bacteria can develop resistance against other types of killing agents, such as silver nanoparticles ⁹. Therefore, alternative approaches to the prevention of IAIs including those based on physical forces should be more seriously considered. In such approaches, specifically-designed surface features kill the bacteria that reach the implant surface ¹⁰.

The recent progress in nano-/micro-fabrication techniques has made it feasible to develop surfaces ornamented with geometrical features (*e.g.*, pillars) whose arbitrary shapes, sizes, and arrangements are precisely controlled ¹¹. Eukaryotic and prokaryotic cells are known to interact with these patterns in different ways ending up with distinct, and even contrary, cellular responses ^{12, 13}. There are pieces of evidence suggesting that mechanobiological pathways trigger and control these responses ^{12, 14, 15}. At the same time, nature offers great examples of surfaces with nanoscale features (nanopatterns) that leave bacterial cells with no choice of response but death ^{10, 16, 17}. Therefore, studying the interactions between different types of cells and surface nanopatterns is of high interest, because, unlike larger length scales, nanopatterns can affect individual cell receptors, which stand first in the line for the transduction of mechanical signals ^{14, 18}.

Inspired by nature, many synthetic replicas of naturally occurring bactericidal nanopatterns have been designed, fabricated, and tested against a wide variety of bacterial strains ^{17, 19}. Several design parameters such as the shape, dimensions (height, diameter, and the interspace between them), and arrangement highly influence the response of

bacterial cells to surface nanopatterns^{12,20}. For example, a specific range of dimensions is known to induce bactericidal properties (*i.e.*, 100 nm < height < 900 nm; 20 nm < diameter < 207 nm; 9 nm < interspacing < 380 nm)²⁰.

The limited number of systematic studies has made it difficult to draw concrete conclusions regarding the isolated effects of each design parameter (*i.e.*, height, diameter, or interspacing) on the bactericidal properties of surfaces. Similarly, while extensive data is available regarding the effects of disordered nanopatterns on the response of mammalian cells²¹⁻²³, a limited number of reports can be found on how disordered arrangement can affect the bactericidal properties of nanopatterns²⁴.

In the present study, we aimed to study the isolated effects of one specific design parameter (*i.e.*, interspacing) as well as the controlled disorder on the functionality of a bactericidal nanopattern. Pillar-shaped nanopatterns with an approximate height of 190 nm, a diameter of 80 nm, and an interspacing of 170 nm were chosen as the reference bactericidal nanopattern, which has been shown to be effective against both Gram-positive and Gram-negative bacteria²⁵. Keeping the height and diameter constant, the interspacing of the nanopillars was changed to 100, 300, and 500 nm to create new nanopatterns. These values cover the full range of possible interspacing including one that was larger than all previously reported ones (*i.e.*, 500 nm), one close to the maximum value reported before (*i.e.*, 300 nm), and one smaller than the majority of the previous studies (*i.e.*, 100 nm)²⁰. The controlled disorder was the other studied parameter, creating a variant to each of the four above-mentioned nanopatterns. Furthermore, *S. aureus* was used as the study organism because of its prevalence in IAI. We used electron beam-induced deposition (EBID) as a nanoscale additive manufacturing (= 3D printing) technique to fabricate the nanopatterns due to its high precision and controllability that make it an unrivaled single-step method for the direct printing of 3D surface physical features at the sub-10 nm nanoscale²⁵⁻²⁷.

4.2 Materials and Methods

4.2.1 Nanopatterns design, fabrication, and characterization

To introduce controlled disorder to the nanopatterns, the maximum distance at which nanopillars did not intersect when displaced toward each other was set as the maximum disorder distance. Having set the diameter of nanopatterns to 80 nm, the maximum disorder distance was defined for each nanopattern to be half of the difference

between the interspacing and the diameter. Since such a small level of disorder does not substantially change the arrangement of the nanopatterns with an interspacing of 100 nm, the effects of disorder were not studied for that particular level of interspacing. The following nanopatterns were, therefore, included in the study: ordered nanopatterns with interspacings of 100, 170, 300, and 500 nm as well as disordered nanopatterns with interspacings of 170, 300, and 500 nm. We will call those patterns 100 *O*, 170 *O*, 170 *D*, 300 *O*, 300 *D*, 500 *O*, and 500 *D* where the first number corresponds to the interspacing of the nanopillars followed by a letter indicating whether the arrangement of nanopillars has been fully ordered (*O*) or included controlled disorder (*D*).

EBID was used to fabricate the desired nanopatterns on silicon substrates as described before²⁵. Briefly, 1×1 cm² samples were prepared by cutting double-sided polished 4-inch (diameter = 10.16 cm) silicon wafers (thickness = 525 ± 25 μm , p-type), cleaning with nitric acid, and rinsing with deionized water subsequently.

A Helios Nano Lab 650 scanning electron microscope (SEM) (FEI, US) equipped with the apparatus required for EBID was used to create three nanopatterned areas of 20×20 μm^2 per specimen (Figure 4.1d). The precursor gas was Trimethyl(methylcyclopentadienyl)-platinum(IV) (chemical formula: $\text{C}_9\text{H}_{18}\text{Pt}$). The EBID process was performed using a working distance of 5 mm, an electron voltage of 17.8 kV, and a beam current of 0.4 nA. The background vacuum of the system was 8.82×10^{-7} mbar and the precursor gas flux was adjusted such that the total pressure was 2.33×10^{-6} mbar, after which the EBID process was started. Single-dot exposure was used as the writing strategy, using stream files generated through MATLAB (MathWorks, US) scripts.

The resulting nanopatterns were characterized by scanning electron microscopy (SEM) performing using the same equipment. The height and the base diameter were measured for thirty different pillars per sample using 52° tilted SEM images. The center-to-center spacing was also measured from top view images. The dimensions of the produced nanopatterns are reported as mean \pm standard deviation (Table 4.1).

Given that the static water contact angles could not be measured directly (due to the small size of the patterned areas), we used the Cassie-Baxter wettability model to estimate the values corresponding to different designs^{28,29}. To this aim, the contact angle of an EBID-fabricated Pt-C layer was measured by a DSA 100 drop shape analyzer (Krüss, Germany) using deionized water. A volume of 2 μL liquid with a falling rate of 1667

$\mu\text{l}/\text{min}$ was placed on the surface and the average contact angle was recorded within 30 seconds after the droplet touched the surface. The measured contact angle was further used to calculate the Cassie-Baxter contact angle (Table 4.1) ²⁵.

Furthermore, topography images of the nanopatterns were acquired in Quantitative Imaging (QI) mode using an atomic force microscope (AFM, JPK Nanowizard 4, Bruker, Germany) and a high aspect ratio probe (TESPA-HAR, Bruker, Germany). A setpoint of 20 nN, a Z length of 300 nm, and a pixel time of 10 ms were used as scanning parameters. The images were analyzed by the JPK SPM data processing software (JPK instruments, version 6.1, Germany) to obtain 3D images of the surface and the average roughness.

4.2.2 Preparation of bacterial cultures

Gram-positive bacteria *Staphylococcus aureus* (RN0450 strain) (BEI Resources, US) was grown on brain heart infusion (BHI) (Sigma-Aldrich, US) agar plates at 37 °C overnight. A pre-culture of bacteria was prepared by inoculating a single colony in 10 ml autoclaved BHI, shaken at 140 rpm at 37 °C. The bacterial cells were collected at their logarithmic stage of growth and their optical density at 600 nm wavelength (OD_{600}) in the medium solution was adjusted to a value of 0.1 to be finally cultured on the specimens. Such OD is equivalent to 148×10^6 colony-forming units (CFU) per milliliter.

4.2.3 Investigation of bactericidal properties

Two independent sets of experiments were performed to evaluate the bactericidal properties of the nanopatterns. In each set of experiments, the nanopatterned areas of each specimen and the surrounding flat areas (Figure 4.1d) were considered as the study and control groups (all in triplicates) in the bacterial studies, respectively. The specimens were initially sterilized through immersion in 70% ethanol and were exposed to UV light for 20 minutes prior to inoculation with 1 ml of the bacterial suspension in a 24-well plate (Cell Star, Germany). The specimens were then incubated at 37 °C for 18 hours.

As previously explained ²⁵, fabricating large areas of nanopatterned surfaces using EBID is not time-efficient yet, but patterning a small area would suffice for systematically studying the bactericidal effects of highly controlled nanopatterns. However, it hinders the use of certain assessment methods such as live/dead staining and CFU counting. We, therefore, exploited a method applied previously in several other studies ^{25, 30-33} in which morphological evaluation of bacterial cells through SEM imaging is used to distinguish between disrupted and healthy bacterial cells. The validity of this technique has been

demonstrated before in studies that have used and compared different evaluation techniques in determining the bactericidal properties of nanopatterned surfaces^{30, 33}. Therefore, to determine the killing efficiency of the nanopatterns, we first washed our specimens with phosphate-buffered saline (PBS) to remove any non-adherent bacteria. The adhered bacterial cells were then fixed by immersion in a PBS solution containing 4% formaldehyde (Sigma-Aldrich, US) and 1% glutaraldehyde (Sigma-Aldrich, US) at 4 °C for 1 hour. Subsequently, the samples were dehydrated by a series of ethanol washing (50%, 70%, and 96% ethanol, respectively) and finally with hexamethyldisilazane (Sigma-Aldrich, US) for 30 minutes. After being air-dried, a thin layer of gold was sputtered on the specimens prior to being imaged by SEM at different magnifications and tilt angles of 0° and 52°. The killing efficiency was defined as the ratio of damaged cells to the total number of cells on the intended areas. Moreover, counting the total number of the bacterial cells attached to the nanopatterned and flat areas of each specimen enabled a comparison between the cell adhesion within the flat and nanopatterned surfaces.

4.2.4 Investigation of nanopattern-bacteria interface

In order to further investigate the interactions between the bacterial cells and the nanopillars, and to analyze the possible killing mechanism of the nanopattern with the highest killing efficiency, focused ion beam scanning electron microscopy (FIB-SEM, Helios Nano Lab 650, FEI, US) was performed to acquire a cross-sectional view of the interface between cells and patterns. The specimen was tilted to 52° at which angle the surface was milled using Gallium ions with a 7.7 pA ion beam ($Z = 1.5 \mu\text{m}$, operating voltage = 30 kV).

4.2.5 Statistical analysis

To determine the statistical significance of the differences between the means of different experimental groups in terms of their bacterial cells attachment, a two-way ANOVA test was performed, followed by a Šídák's multiple comparisons test, which was performed using Prism version 8.0.1 (GraphPad, US). Similarly, the killing efficiency of different nanopatterns was statistically analyzed using the Mann-Whitney test. A p -value below 0.05 was considered to indicate statistical significance.

4.3 Results

4.3.1 Characteristics of the fabricated nanopatterns

Nanopillar arrays with different types of arrangements and interspacing values were successfully fabricated in $20 \times 20 \mu\text{m}^2$ areas on each sample (Figure 4.1).

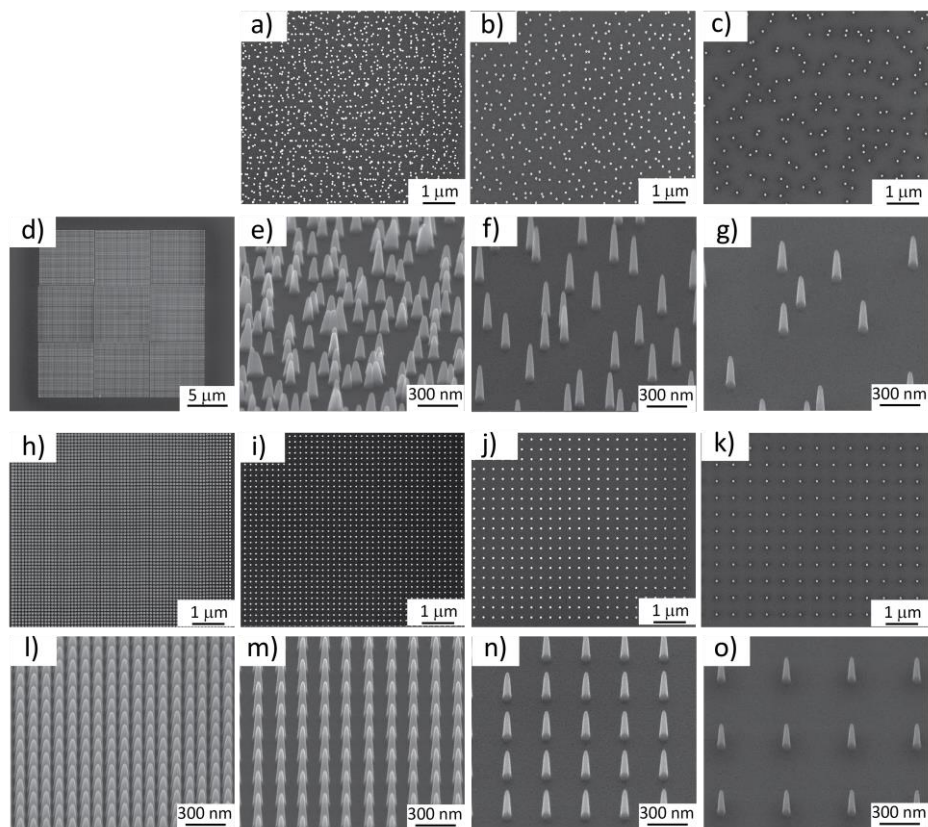


Figure 4.1. The scanning electron microscope (SEM) images of a) the top view of the nanopillars with a height of 190 nm, a diameter of 80 nm, and an interspacing of 170 nm with 45 nm disorder distance (170 *D*), b) the top view of the nanopillars with an interspacing of 300 nm and 110 nm disorder distance (300 *D*), c) the top view of the nanopillars with an interspacing of 500 nm and 210 nm disorder distance (500 *D*), d) $20 \times 20 \mu\text{m}^2$ nanopatterned areas on a Si substrate, e) the tilted view of 170 *D*, f) the tilted view of 300 *D*, g) the tilted view of 500 *D*, h) the top view of the ordered nanopillars with an interspacing of 100 nm (100 *O*), i) the top view of the ordered nanopillars with an interspacing of 170 nm (170 *O*), j) the top view of the ordered nanopillars with an interspacing of 300 nm (300 *O*), k) the top view of the ordered nanopillars with an interspacing of 500 nm (500 *O*), l) the tilted view of 100 *O*, m) the tilted view of 170 *O*, n) the tilted view of 300 *O*, o) the tilted view of 500 *O*.

Notwithstanding some slight variations, the intended dimensions were achieved for all the experimental groups (Table 4.1). The differences in the dimensions and arrangements of the nanopillars were clearly observed in SEM images (Figure 4.1) and AFM images (Figure 4.2). The average roughness decreased by increasing the interspacing of both ordered nanopillars (from 46.8 ± 4.9 nm for 100 *O* to 39.1 ± 1.8 nm for 500 *O*) and disordered nanopillars (from 68.3 ± 4.9 nm for 170 *D* to 24.8 ± 2.3 nm for 500 *D*). The density of the nanopillars decreased by increasing the interspacing, from 100.6 pillars per μm^2 for 100 *O* to 4.5 pillars per μm^2 for 500 *O* and 500 *D*. The nanopatterned surfaces were hydrophobic, as estimated by using the Cassie-Baxter model, with water contact angles ranging from 154° to 176° .

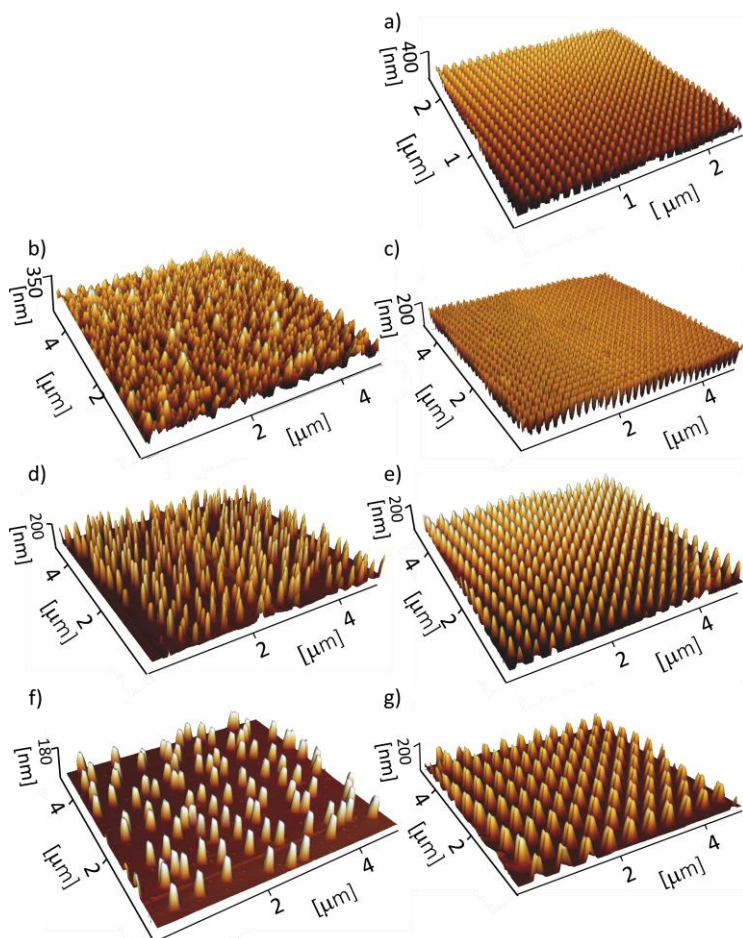


Figure 4.2. 3D AFM images of a) 100 *O*, b) 170 *D*, c) 170 *O*, d) 300 *D*, e) 300 *O*, f) 500 *D*, and g) 500 *O* nanopillars.

Table 4.1. Characteristics of the nanopatterns produced by EBID.

Interspacing (nm)	Disorder distance (nm)	Height (nm)	Base diameter (nm)	Aspect ratio	Pillar density (number/ μm^2)
100	0	197.9 \pm 7.3	88.9 \pm 4.2	2.2 \pm 0.0	100.6
170	45	199.8 \pm 12.7	72.9 \pm 9.3	2.7 \pm 0.2	35.5
170	0	187.8 \pm 21.8	67.4 \pm 12.6	2.8 \pm 0.2	35.5
300	110	177.2 \pm 13.5	72.6 \pm 3.1	2.4 \pm 0.1	11.9
300	0	189.5 \pm 28.2	71.3 \pm 1.9	2.7 \pm 0.3	11.9
500	210	200.8 \pm 14.8	75.9 \pm 3.8	2.6 \pm 0.1	4.5
500	0	184.3 \pm 15.9	72.3 \pm 2.8	2.6 \pm 0.1	4.5

4.3.2 Effect of interspacing on bactericidal properties

Before analyzing the effects of the selected parameters on the bactericidal activity of the nanopatterns, the bacterial adhesion to the specimens was studied to see whether any of the fabricated nanopatterns impair the attachment of bacterial cells. Although care was taken to ensure seeding was as homogeneous as possible, there might be local differences in the number of bacteria attached to the specimens. However, the ratio of the number of cells attached to the nanopatterned surfaces to those attached to a similar-sized flat area did not significantly vary between the specimens, meaning that bacterial cell adhesion was similar between all experimental groups (Figure 4.3a).

S. aureus cells showed their typical coccoid-shaped morphology on the flat areas with no significant sign of irregularity, disruption, or death (Figure 4.3b). On the contrary, ruptured bacterial cells with squashed morphologies were identified on the nanopatterned areas and were marked as damaged/dead cells (Figures 4.3f-i). The ordered nanopatterns with larger interspacing values (*i.e.*, 300 *O* and 500 *O*) displayed significantly lower bactericidal efficiencies against *S. aureus* (8.6 \pm 4.2% and 3.7 \pm 2.3%, respectively) as compared to 100 *O* and 170 *O* ($p < 0.01$) (Figure 4.4a). While there was a significant difference in the killing efficiency between 300 *O* and 500 *O* ($p < 0.05$), no significant differences were observed between 100 *O* and 170 *O*.

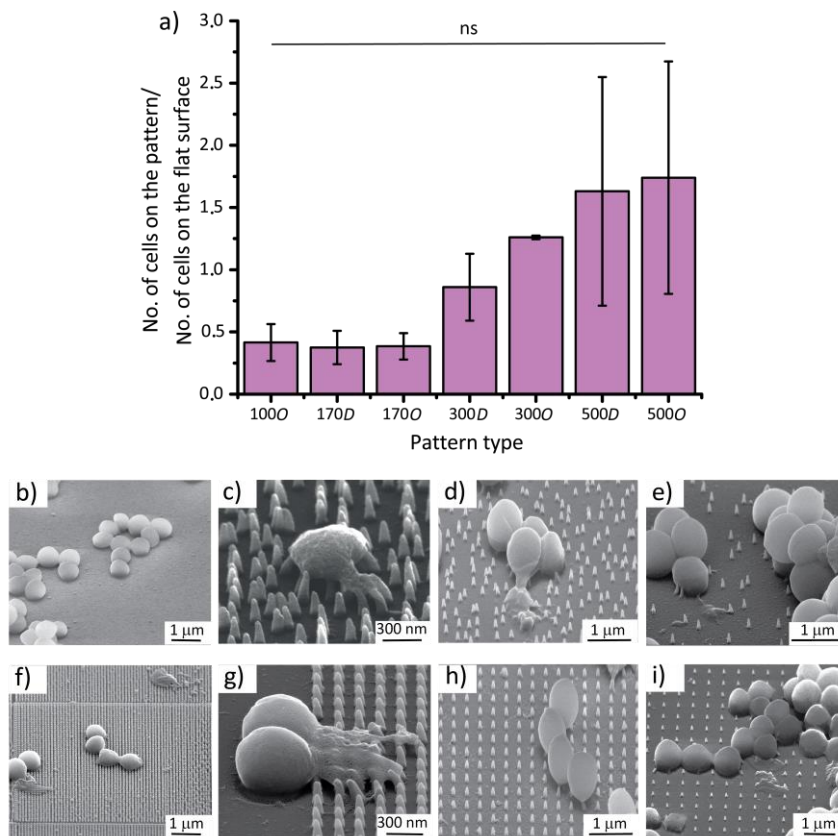


Figure 4.3. a) The ratio of the bacterial cells attached to the nanopatterns to those attached to similar flat areas. No significant difference in that ratio for different types of nanopattern indicates that bacterial adhesion is similar between different groups ($n = 3$ per group, Two-way ANOVA followed by Šidák's test). The SEM images of *S. aureus* bacteria on b) the control Si surface, c) 170 D, d) 300 D, e) 500 D, f) 100 O, g) 170 O, h) 300 O, and i) 500 O at 52° tilted view. The damaged bacterial cells can be identified with irregular and unrecognizable morphologies as compared to normal cells on flat surfaces.

4.3.3 The effects of controlled disorder on bactericidal properties

The effects of controlled disorder on the bactericidal activity of the nanopatterned surfaces were evaluated by comparing the killing efficiency of the ordered and disordered nanopatterns with the same interspacing (Figures 4.3c-e). Although somewhat higher values of killing efficiencies were observed for the disordered nanopatterns with larger interspacing values (*i.e.*, 300 D and 500 D) as compared to their ordered counterparts, the differences were not statistically significant (Figure 4.3b). The disordered nanopattern

with the lower interspacing (*i.e.*, 170 *D*) showed the same bactericidal efficiency as the ordered counterpart (Figure 4.4b).

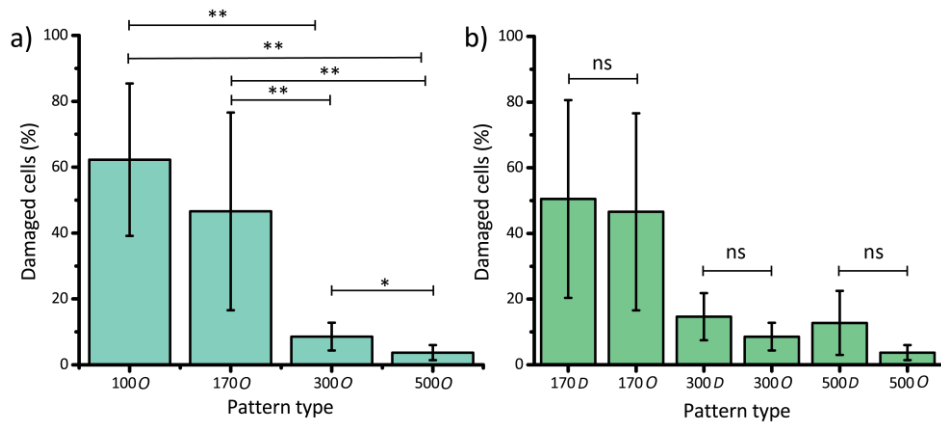


Figure 4.4. a) The effects of interspacing on the bactericidal efficiency of nanopatterns ($n = 3$ per group, Mann-Whitney test, * $p < 0.05$ and ** $p < 0.01$). b) The effects of controlled disorder on the bactericidal efficiency of nanopatterns. No significant differences were observed between the ordered and disordered nanopatterns but the value of interspacing.

4.3.4 Nanopattern-bacteria interface

Cross-sectional views showed that nanopatterns could penetrate the bacterial cell wall and cause their death by disrupting it (Figure 4.5). Moreover, the bending of the nanopillars underneath the bacterial cells (Figures 4.3 and 4.5) suggested significant amounts of reciprocal forces that cells and pillars exert on each other.

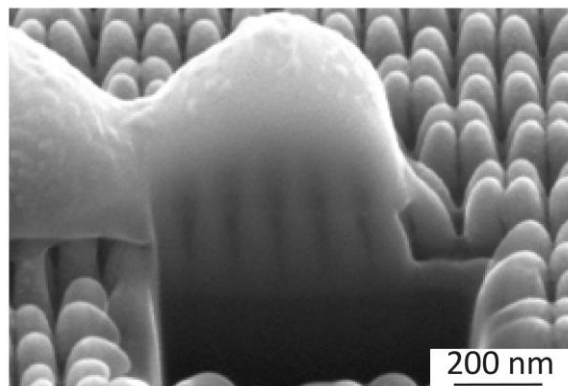


Figure 4.5. The SEM image of the interface between bacteria and the 100 *O* nanopattern. The depth of direct penetration of the nanopillars into the bacterial cell wall (about 100 nm) far exceeds the average cell wall thickness of *S. aureus* (*i.e.*, 10–20 nm).

4.4 Discussion

The main contribution of this study was shedding light on how interspacing and controlled disorder could affect the bactericidal properties of nanopatterns. The height and diameter of the fabricated nanopatterns were, therefore, kept constant while the interspacing and the arrangement of nanopillars were systematically altered in seven different study groups.

In order to elucidate the effects of these two parameters on the bactericidal properties of nanopatterns, it is crucial to first consider their killing mechanisms. The main killing mechanism of nanopatterns is widely believed to be the direct penetration of high aspect ratio nanopatterns into the bacterial cell wall and disrupting it by exerting a high enough force^{20,31}. Since the thickness and composition of cell walls are different in Gram-negative and Gram-positive bacteria³⁴, the same force will not rupture different cell walls equally^{16,35}. Moreover, other factors such as hydrostatic and gravitational forces should be also considered when studying the interactions between bacteria and nanopatterns³⁶.

The results of this study showed that the cell wall of *S. aureus* could be mechanically penetrated by nanopatterns (Figure 4.5) and be severely damaged with an unrecognizable morphology (Figure 4.3), as reported previously^{25, 30, 37}. However, changing the interspacing of nanopatterns drastically affected the percentage of the damaged cells. Although aspect ratio is a crucial design parameter of bactericidal nanopatterns, interspacing seems to overshadow the effects of the nanopatterns aspect ratio, which is corroborated by other studies in the literature. Linklater *et al.* showed that nanopillars with a diameter of 80.3 nm, an interspacing of 99.5 nm (similar to 100 O in the present study), and a height of around 430 nm (much higher than 100 O), exhibited a comparable level of bactericidal activity against *S. aureus*³⁸. Similarly, another study³⁹ showed that naturally occurring nanopillars with the approximate height of 430 nm, the approximate tip diameter of 48 nm, and an interspacing of around 116 nm (*i.e.*, larger height than 100 O but comparable interspacing), exhibit a killing efficiency of $39.4 \pm 20.3\%$ against *S. aureus* after 18 hours. Computational simulations have also demonstrated that, as compared to the height, the interspacing has a substantially greater effect on the bactericidal properties of nanopillars⁴⁰. It is plausible that a smaller interspacing and thus a higher density of nanopatterns result in more contact points between the bacteria and nanopatterns. This, in turn, leads to more physicochemical interactions and higher

chances of bacteria being ruptured⁴¹, however, further studies are required to determine the minimum number of contact points that exert enough force to rupture the cell wall of different types of bacteria. According to the literature, the majority of bactericidal nanopatterns have an interspacing below 300 nm²⁰. The reported values make more sense when it comes to bactericidal activity against *S. aureus*, which has a coccoid shape with a diameter larger than 500 nm⁴². For an interspacing exceeding the diameter of *S. aureus*, it is likely that bacterial cells may land in between the nanopillars, thereby escaping the deadly spikes (Figures 4.3h and i).

An increased number of contact points for the lower values of interspacing could also contribute to some other proposed killing mechanisms. Bandara *et al.*⁴³ have argued that nanopillars do not directly interact with the bacterial cell membrane and showed that bacterial cells attach to surface nanopatterns via the expression of extracellular polymeric substances (EPS). Further movement of the bacteria on the surface on the one hand and strong EPS-mediated adhesion forces on the other lead to the stretching of the cell membrane beyond its rupture point. Considering this theory, an increased number of adhesion sites between surface features and expressed EPS could potentially amplify such a stretching mechanism. Although the bending of the nanopillars underneath the bacterial cells could be due to that movement rather than the bacteria weight only, further evaluations such as live imaging for real-time tracking of the bacteria on the surface, are required to confirm such a mechanism. Additionally, AFM measurements in another study have shown that the adhesion force of an EPS-producing *S. aureus* strain attached to nanopatterns does not significantly change by differences in interspacing⁴⁴. Altogether, the results of the present study are more consistent with the direct penetration theory, as it can be seen that nanopatterns have actually intruded about 101 nm (SD 9 nm) (Figure 4.5) into the bacterial cells which is much larger than the cell wall thickness of *S. aureus* (*i.e.*, 10-20 nm)⁴⁵.

Deviation from an ordered arrangement in nanopatterns has been shown to effectively influence the differentiation of the human mesenchymal stem cells²² and the response of osteoblast cells²¹. Biochemical mechanotransduction pathways have been shown to be involved in translating mechanical cues (*e.g.*, disordered nanopatterns) into biochemical responses (proteomic changes)⁴⁶. An intricate network of cellular components is associated with receiving, transducing, and interpreting the mechanical cues¹⁴. In contrast, the bacterial mechanotransduction mechanisms seem to be simpler as

the structure and components of bacterial cells are not as complex as those of mammalian cells¹⁵. Moreover, the information over the influence of nanopatterns disorder on bacterial mechanotransduction is scarcely available in the literature. Further studies are, therefore, needed to elucidate the possible mechanobiological pathways pertaining to the interactions of bacteria and nanopatterns. Similar to another study that used *Escherichia coli*²⁴, our results showed no significant difference between the bactericidal efficiencies of ordered and disordered nanopatterns against *S. aureus* as long as the interspacing is kept constant. Given the killing mechanism observed in this study, it can be concluded that introducing controlled disorder either does not change the mechanical force that bacteria experience or does not increase it beyond the threshold required for cell wall rupture. The findings of this study indicate that interspacing is a highly promising design parameter that should be further optimized to achieve nanopatterned surfaces with the highest potential of bactericidal activity. In combination with controlled disorder, nanopatterns with contrary effects on bacterial and mammalian cells may be developed in order to achieve selective biocidal activity.

4.5 Conclusions

The effects of the interspacing and controlled disorder, as two design parameters, on the bactericidal properties of nanopatterns were systematically studied. Nanopatterns with constant heights and diameters of 190 nm and 80 nm, respectively, and different values of interspacing (*i.e.*, 100, 170, 300, and 500 nm) were fabricated using EBID. A controlled disordered version of the nanopatterns with interspacings of 170, 300, and 500 nm was also fabricated. Quantifying the number of damaged *S. aureus* cells cultured on the nanopatterns for 18 hours, showed that decreasing the interspacing significantly increased the bactericidal efficiency, and the nanopatterns with 100 nm interspacing exhibited the highest efficiency ($62.3 \pm 23.1\%$). The nanopatterns with controlled disorder did not enhance the bactericidal efficiency compared with the ordered counterparts. Moreover, the direct penetration of nanopatterns into the bacterial cell wall and its eventual rupture due to the forces applied to it was shown to be the dominant killing mechanism of these nanopatterns which is consistent with the majority of the previous studies. Further research is required to elucidate whether interspacing and controlled disorder could affect the biochemical mechanotransduction pathways in bacteria.

Bibliography

- [1] S. Kurtz, K. Ong, E. Lau, F. Mowat, M. Halpern, Projections of primary and revision hip and knee arthroplasty in the United States from 2005 to 2030, *JBJS*, 89(4), 780-785, 2007.
- [2] W. Zimmerli, A. Trampuz, P.E. Ochsner, Prosthetic-joint infections, *New England Journal of Medicine*, 351(16), 1645-1654, 2004.
- [3] T.F. Moriarty, R. Kuehl, T. Coenye, W.-J. Metssemakers, M. Morgenstern, E.M. Schwarz, M. Riool, S.A. Zaat, N. Khana, S.L. Kates, Orthopaedic device-related infection: current and future interventions for improved prevention and treatment, *EFORT open reviews*, 1(4), 89-99, 2016.
- [4] J.M. Steckelberg, D.R. Osmon, *Prosthetic joint infections*, in *Infections Associated with Indwelling Medical Devices, Third Edition*. 2000, American Society of Microbiology. p. 173-209.
- [5] L. Montanaro, P. Speziale, D. Campoccia, S. Ravaioli, I. Cangini, G. Pietrocola, S. Giannini, C.R. Arciola, Scenery of Staphylococcus implant infections in orthopedics, *Future Microbiology*, 6(11), 1329-1349, 2011.
- [6] A. Trampuz, W. Zimmerli, Diagnosis and treatment of infections associated with fracture-fixation devices, *Injury*, 37(2), S59-S66, 2006.
- [7] S. Corvec, M.E. Portillo, B.M. Pasticci, O. Borens, A. Trampuz, Epidemiology and new developments in the diagnosis of prosthetic joint infection, *The International Journal of Artificial Organs*, 35(10), 923-934, 2012.
- [8] N.A. Turner, B.K. Sharma-Kuinkel, S.A. Maskarinec, E.M. Eichenberger, P.P. Shah, M. Carugati, T.L. Holland, V.G. Fowler, Methicillin-resistant Staphylococcus aureus: an overview of basic and clinical research, *Nature Reviews Microbiology*, 17(4), 203-218, 2019.
- [9] A. Panáček, L. Kvítek, M. Smékalová, R. Večeřová, M. Kolář, M. Röderová, F. Dyčka, M. Šebela, R. Prucek, O. Tomanec, Bacterial resistance to silver nanoparticles and how to overcome it, *Nature Nanotechnology*, 13(1), 65-71, 2018.
- [10] J. Hasan, R.J. Crawford, E.P. Ivanova, Antibacterial surfaces: the quest for a new generation of biomaterials, *Trends in Biotechnology*, 31(5), 295-304, 2013.
- [11] B.D. Gates, Q. Xu, M. Stewart, D. Ryan, C.G. Willson, G.M. Whitesides, New approaches to nanofabrication: molding, printing, and other techniques, *Chemical Reviews*, 105(4), 1171-1196, 2005.
- [12] K. Anselme, P. Davidson, A. Popa, M. Giazson, M. Liley, L. Ploux, The interaction of cells and bacteria with surfaces structured at the nanometre scale, *Acta Biomaterialia*, 6(10), 3824-3846, 2010.
- [13] L. Ploux, K. Anselme, A. Dirani, A. Ponche, O. Soppera, V. Roucoules, Opposite responses of cells and bacteria to micro/nanopatterned surfaces prepared by pulsed plasma polymerization and UV-irradiation, *Langmuir*, 25(14), 8161-8169, 2009.
- [14] Y. Sun, C.S. Chen, J. Fu, Forcing stem cells to behave: a biophysical perspective of the cellular microenvironment, *Annual Review of Biophysics*, 41, 519-542, 2012.
- [15] A. Persat, Bacterial mechanotransduction, *Current Opinion in Microbiology*, 36, 1-6, 2017.

- [16] J. Hasan, H.K. Webb, V.K. Truong, S. Pogodin, V.A. Baulin, G.S. Watson, J.A. Watson, R.J. Crawford, E.P. Ivanova, Selective bactericidal activity of nanopatterned superhydrophobic cicada *Psaltoda claripennis* wing surfaces, *Applied Microbiology and Biotechnology*, 97(20), 9257-9262, 2013.
- [17] A. Elbourne, R.J. Crawford, E.P. Ivanova, Nano-structured antimicrobial surfaces: From nature to synthetic analogues, *Journal of Colloid and Interface Science*, 508, 603-616, 2017.
- [18] M.J. Dalby, N. Gadegaard, R.O. Oreffo, Harnessing nanotopography and integrin–matrix interactions to influence stem cell fate, *Nature Materials*, 13(6), 558-569, 2014.
- [19] J. Hasan, A. Roy, K. Chatterjee, P.K. Yarlagadda, Mimicking Insect Wings: The Roadmap to Bioinspiration, *ACS Biomaterials Science & Engineering*, 5(7), 3139-3160, 2019.
- [20] K. Modaresifar, S. Azizian, M. Ganjian, L.E. Fratila-Apachitei, A.A. Zadpoor, Bactericidal effects of nanopatterns: a systematic review, *Acta Biomaterialia*, 2018.
- [21] C. Allan, A. Ker, C.-A. Smith, P.M. Tsimbouri, J. Borsoi, S. O’Neill, N. Gadegaard, M.J. Dalby, R. Dominic Meek, Osteoblast response to disordered nanotopography, *Journal of Tissue Engineering*, 9, 2041731418784098, 2018.
- [22] M.J. Dalby, N. Gadegaard, R. Tare, A. Andar, M.O. Riehle, P. Herzyk, C.D. Wilkinson, R.O. Oreffo, The control of human mesenchymal cell differentiation using nanoscale symmetry and disorder, *Nature Materials*, 6(12), 997-1003, 2007.
- [23] S. Dobbenga, L.E. Fratila-Apachitei, A.A. Zadpoor, Nanopattern-induced osteogenic differentiation of stem cells—A systematic review, *Acta Biomaterialia*, 46, 3-14, 2016.
- [24] D. Widayatih, P.-L. Hagedoorn, L. Otten, M. Ganjian, N. Tümer, I. Apachitei, C.W.K. Hagen, L. Fratila-Apachitei, A.A. Zadpoor, Towards osteogenic and bactericidal nanopatterns?, *Nanotechnology*, 2019.
- [25] M. Ganjian, K. Modaresifar, M.R. Ligeon, L.B. Kunkels, N. Tümer, L. Angeloni, C.W. Hagen, L.G. Otten, P.L. Hagedoorn, I. Apachitei, Nature Helps: Toward Bioinspired Bactericidal Nanopatterns, *Advanced Materials Interfaces*, 1900640, 2019.
- [26] W.F. Van Dorp, B. Van Someren, C.W. Hagen, P. Kruit, P.A. Crozier, Approaching the resolution limit of nanometer-scale electron beam-induced deposition, *Nano Letters*, 5(7), 1303-1307, 2005.
- [27] L. van Kouwen, A. Botman, C.W. Hagen, Focused electron-beam-induced deposition of 3 nm dots in a scanning electron microscope, *Nano Letters*, 9(5), 2149-2152, 2009.
- [28] B. Bhushan, M. Nosonovsky, The rose petal effect and the modes of superhydrophobicity, *Philosophical Transactions of the Royal Society A: Mathematical, Physical and Engineering Sciences*, 368(1929), 4713-4728, 2010.
- [29] M. Sun, G.S. Watson, Y. Zheng, J.A. Watson, A. Liang, Wetting properties on nanostructured surfaces of cicada wings, *Journal of Experimental Biology*, 212(19), 3148-3155, 2009.
- [30] E.P. Ivanova, J. Hasan, H.K. Webb, G. Gervinskas, S. Juodkazis, V.K. Truong, A.H. Wu, R.N. Lamb, V.A. Baulin, G.S. Watson, Bactericidal activity of black silicon, *Nature Communications*, 4, 2013.
- [31] D.P. Linklater, S. Juodkazis, S. Rubanov, E.P. Ivanova, Comment on “Bactericidal Effects of Natural Nanotopography of Dragonfly Wing on *Escherichia coli*”, *ACS Applied Materials & Interfaces*, 9(35), 29387-29393, 2017.

- [32] D.P. Linklater, M. De Volder, V.A. Baulin, M. Werner, S. Jessl, M. Golozar, L. Maggini, S. Rubanov, E. Hanssen, S. Juodkazis, High aspect ratio nanostructures kill bacteria via storage and release of mechanical energy, *ACS Nano*, 12(7), 6657-6667, 2018.
- [33] D.P. Linklater, S. Juodkazis, R. Crawford, E. Ivanova, Mechanical inactivation of *Staphylococcus aureus* and *Pseudomonas aeruginosa* by titanium substrata with hierarchical surface structures, *Materialia*, 5, 100197, 2019.
- [34] L. Brown, J.M. Wolf, R. Prados-Rosales, A. Casadevall, Through the wall: extracellular vesicles in Gram-positive bacteria, mycobacteria and fungi, *Nature Reviews Microbiology*, 13(10), 620-630, 2015.
- [35] S. Pogodin, J. Hasan, V.A. Baulin, H.K. Webb, V.K. Truong, V. Boshkovikj, C.J. Fluke, G.S. Watson, J.A. Watson, R.J. Crawford, Biophysical model of bacterial cell interactions with nanopatterned cicada wing surfaces, *Biophysical Journal*, 104(4), 835-840, 2013.
- [36] F. Xue, J. Liu, L. Guo, L. Zhang, Q. Li, Theoretical study on the bactericidal nature of nanopatterned surfaces, *Journal of Theoretical Biology*, 385, 1-7, 2015.
- [37] A. Jaggessar, P.K. Yarlagadda, Modelling the growth of hydrothermally synthesised bactericidal nanostructures, as a function of process conditions, *Materials Science and Engineering: C*, 110434, 2019.
- [38] D.P. Linklater, H.K.D. Nguyen, C.M. Bhadra, S. Juodkazis, E.P. Ivanova, Influence of nanoscale topology on bactericidal efficiency of black silicon surfaces, *Nanotechnology*, 28(24), 245301, 2017.
- [39] V.K. Truong, N.M. Geeganagamage, V.A. Baulin, J. Vongsvivut, M.J. Tobin, P. Luque, R.J. Crawford, E.P. Ivanova, The susceptibility of *Staphylococcus aureus* CIP 65.8 and *Pseudomonas aeruginosa* ATCC 9721 cells to the bactericidal action of nanostructured *Calopteryx haemorrhoidalis* damselfly wing surfaces, *Applied Microbiology and Biotechnology*, 101(11), 4683-4690, 2017.
- [40] M. Mirzaali, I. Van Dongen, N. Tümer, H. Weinans, S.A. Yavari, A. Zadpoor, In-silico quest for bactericidal but non-cytotoxic nanopatterns, *Nanotechnology*, 29(43), 43LT02, 2018.
- [41] G. Hazell, L.E. Fisher, W.A. Murray, A.H. Nobbs, B. Su, Bioinspired bactericidal surfaces with polymer nanocone arrays, *Journal of Colloid and Interface Science*, 528, 389-399, 2018.
- [42] L. Harris, S. Foster, R. Richards, An introduction to *Staphylococcus aureus*, and techniques for identifying and quantifying *S. aureus* adhesins in relation to adhesion to biomaterials: review, *European Cells & Materials*, 4(3), 2002.
- [43] C.D. Bandara, S. Singh, I.O. Afara, A. Wolff, T. Tesfamichael, K. Ostrikov, A. Oloyede, Bactericidal effects of natural nanotopography of dragonfly wing on *Escherichia coli*, *ACS Applied Materials & Interfaces*, 9(8), 6746-6760, 2017.
- [44] F. Hizal, C.-H. Choi, H.J. Busscher, H.C. van der Mei, Staphylococcal adhesion, detachment and transmission on nanopillared si surfaces, *ACS Applied Materials & Interfaces*, 8(44), 30430-30439, 2016.
- [45] P.J. Wyatt, Cell wall thickness, size distribution, refractive index ratio and dry weight content of living bacteria (*staphylococcus aureus*), *Nature*, 226(5242), 277, 1970.
- [46] F. Kantawong, K.E. Burgess, K. Jayawardena, A. Hart, R.J. Burchmore, N. Gadegaard, R.O. Oreffo, M.J. Dalby, Whole proteome analysis of osteoprogenitor differentiation

induced by disordered nanotopography and mediated by ERK signalling, *Biomaterials*, 30(27), 4723-4731, 2009.

Cell adhesion, mechanics, and osteogenesis

The surface topography of implantable devices greatly affects the interactions of the host cells/tissue with the implant and its ultimate function. Due to the limited quantitative information available regarding those effects, we used direct laser writing to 3D print submicron pillars with precisely controlled dimensions and spatial arrangements to perform a systematic study of such interactions. Using single-cell force spectroscopy, we quantified the adhesion parameters of the preosteoblast cells residing on the different types of surfaces. Not only the adhesion parameters but also the formation of focal adhesions (FAs) was strongly dependent on the geometry and arrangement of the pillars. Sufficiently tall and dense pillars enhanced both adhesion parameters and the formation of FAs, and induced possibly higher internal stresses. Furthermore, cells with highly organized cytoskeletal networks exhibited greater values of elastic modulus. The early response of these cells was associated with a “top state” settling state on the pillars and also correlated with upregulated expression of osteopontin after 21 days of culture under both osteogenic and non-osteogenic conditions. These findings paint a detailed picture of at least one possible cascade of events that starts from initial cell adhesion and continues to subsequent cellular functions and eventual matrix mineralization.

M. Nouri-Goushki, L. Angeloni, K. Modaresifar, M. Minneboo, P. E. Boukany, M. J. Mirzaali, M. K. Ghatkesar, L. E. Fratila-Apachitei, A. A. Zadpoor, 3D-printed submicron patterns reveal the interrelation between cell adhesion, cell mechanics, and osteogenesis, *ACS Applied Materials & Interfaces*, 2021.

5.1 Introduction

The micro- and nanotopographical features of a biomaterial surface influence cellular responses, including cell adhesion¹, bactericidal activity², and immunoregulatory effects³. The roles of a wide range of topographical characteristics in eliciting specific cellular responses have been previously investigated. These include surface roughness⁴, the aspect ratio of the surface features⁵, their shape and dimensions⁶, which could be exploited to improve the treatment of bony defects. For example, micro- and nanostructured surfaces with certain characteristics have been found to promote osteogenic response⁷ of stem cells, thereby expediting osseointegration and potentially improving the service life of implants.

While the isolated effects of surface micro- and nanofeatures on bone tissue regeneration remain mainly elusive, some trends have already been identified. At the microscale (*i.e.*, feature size $> 1 \mu\text{m}$), for example, surface micropillars with greater heights (*i.e.*, $\geq 1.6 \mu\text{m}$) and smaller diameters and interspacing (*i.e.*, 1, 2, 4, and 6 μm) have been found to enhance the expression of osteogenic markers (*e.g.*, osteopontin (OPN))⁸. At the nanoscale (*i.e.*, feature size $< 100 \text{ nm}$), previous studies^{9,10} have reported a decreased level of OPN and osteocalcin (OCN) expression for nanopillars with greater heights. Despite the presence of these individual studies, the landscape of how the design parameters of surface patterns affect the osteogenic response remains largely unknown: (i) how the cell adhesion properties (*e.g.*, cell adhesion work and force) are regulated via interactions with patterns at different scales (from nano to microscale) and (ii) whether the initial cell adhesion force promotes the osteogenic differentiation of the cells.

It is becoming increasingly clear that cellular receptors, such as integrins, can sense small topographical features during the adhesion phase and activate topography-induced mechanotransduction pathways¹¹. These involve integrin clustering, the formation of focal adhesions (FAs), and the reorganization of the cytoskeleton and nucleus^{11,12}. There are, therefore, many mechanobiological pathways that are directly or indirectly involved in how surface features influence cell response. Quantification of the adhesion force of the cell during its early interactions with patterned surfaces could enhance our understanding of how mechanics-related factors influence cell-surface interactions. However, most of the previous studies have used qualitative approaches, such as flow shear stress assays^{13,14}, stretching devices^{11,15}, and microscopy techniques¹⁶ to evaluate the adhesion of cells to the substrate.

Among experimental force-sensitive techniques for mechanical probing of cells¹⁷, single-cell force spectroscopy (SCFS) can quantitatively measure the early stage¹⁸ of cellular adhesion force in the range of a few to tens of nanoNewton¹⁹ while precisely manipulating the cell attachment positions. To date, few studies have applied SCFS to measure the initial cellular adhesion force of osteoblasts^{18, 20-22} and mesenchymal stem cells (MSCs)^{19, 23} on various surfaces. Quantitative SCFS analyses have revealed that the adhesion force of the human osteoblasts increases with the surface roughness on selected laser melted titanium surfaces, reaching a value of 8.5 nN on the roughest surface relative to surfaces treated with different blasting agents²⁰. This finding was associated with a higher degree of osteoblast colonization. In another SCFS study, partially denatured collagen surfaces were found to increase the initial cellular adhesion relative to native collagen and promote spreading, migration, and osteogenic differentiation of preosteoblasts¹⁸.

SCFS has not yet been applied to surfaces decorated with precisely controlled micro- and nanopatterns. Understanding the impact of the design parameters of surface micro- and nanopatterns and their length scale on cell adhesion and the interrelation between the adhesion forces and subsequent cell function necessitates systematic studies of such effects²⁴. One of the main factors that limit such systematic investigations has been the unavailability of fabrication methods to create precisely controlled surface patterns. Direct laser writing via two-photon polymerization (2PP) has been recently shown to be a powerful technique for generating submicron patterns with high degrees of reproducibility and geometric fidelity^{25, 26}. Moreover, this technique facilitates the surface engineering of implantable devices, since it is capable of printing structures with a wide range of length scales (*i.e.*, 200 nm-100 μ m) in a single-step process. In our previous studies^{25, 26}, we have demonstrated the 3D printing of highly controllable submicron patterns over a large area and the cytocompatibility of the applied materials (IP-DIP and IP-L780) for the human mesenchymal stem cells (hMSCs) and MC3T3-E1 preosteoblast cells using this technique.

To reveal the relationships between the various steps of cell-surface interactions and to identify the early markers of the osteogenic potential of surface-decorated biomaterials, we studied the effects of height and interspace of submicron pillars on the response of MC3T3-E1 cells from the adhesion phase up to matrix mineralization under both osteogenic and non-osteogenic conditions. Toward that aim, we applied quantitative

methods, such as SCFS and atomic force microscopy (AFM), as well as a host of biological assays. Particular attention was paid to the spatiotemporal changes in cell morphology, cytoskeletal organization, the formation of FAs, and the mechanical characterization of living cells during the adhesion phase (from a few seconds to 24 hours). Moreover, the relevant properties of the patterns (dimensions, wettability, and roughness) and the cell-pattern interface were assessed to better elucidate the underlying mechanisms.

5.2 Materials and Methods

5.2.1 Fabrication of the patterns

Submicron pillars with a diameter of 250 nm, different heights (*i.e.*, 250, 500, and 1000 nm), and different interspaces (*i.e.*, center-to-center distances of 700 and 1000 nm) were designed and printed using a Photonic Professional GT machine (Nanoscribe, Germany) following our previously described protocol²⁵. Briefly, six different patterns were designed and imported into a job preparation program (Describe, Nanoscribe, Germany). Arrays (1 mm²) of pillars were manufactured with a laser power of 14% and a scanning speed of 1200 $\mu\text{m/s}$ using the conventional configuration and the Galvo writing strategy. A droplet of IP-L780 resin (Nanoscribe, Germany) was placed on a glass coverslip and then exposed to a femtosecond infrared laser beam (wavelength of 780 nm) to fabricate the patterns. After printing, the specimens were developed in propylene glycol monomethyl ether acetate (PGMEA) (Sigma-Aldrich, Germany) and rinsed in isopropanol (Sigma-Aldrich, Germany) for 25 and 5 minutes, respectively, followed by blow-drying.

We refer to the patterns with a “small” interspace (designed value = 700 nm) with the letter “S” and the patterns with a “large” interspace (designed value = 1000 nm) with the letter “L”. The lowest height (designed value = 250 nm) will be identified with the number “1”, the intermediate height (designed value = 500 nm) with the number “2”, and the highest height (designed value = 1000 nm) with the number “3”. Thus, groups S1, S2, and S3 were patterned using a “small” (*i.e.*, 700 nm) interspace and the designed heights of 250, 500, and 1000 nm, respectively. Similarly, groups L1, L2, and L3 were patterned with a “large” (*i.e.*, 1000 nm) interspace and the designed heights of 250, 500, and 1000 nm, respectively. For all groups, the flat substrate (glass) was considered as the control group.

5.2.2 Characterization of the patterns

Morphological analysis

The morphology of the patterns was characterized using scanning electron microscopy (SEM) (Helios Nano Lab 650, FEI, US). The specimens were coated with gold (coating thickness ≈ 5 nm) using a sputter coater (JFC-1300, JEOL, Japan) and then imaged by SEM. To acquire the height of the pillars, the samples were tilted 30° during imaging. The average diameter and height of 100 pillars from the different areas of each sample were quantified using ImageJ (NIH, US). The reported height values of the pillars were corrected for the measurement tilt angle.

3D topographical images of the patterns were acquired in the tapping mode using an AFM (JPK Nanowizard 4, Germany) and a high aspect ratio probe (TESPA-HAR, Bruker, Germany). Three images of $10 \times 10 \mu\text{m}^2$ for each sample were recorded and analyzed. The average surface roughness (R_a) was determined using the JPK SPM data processing software (JPK instruments, version 6.1, Germany).

Wettability

The wettability of the patterned surfaces was measured using a drop shape analyzer (DSA100, Krüss, Germany). Briefly, deionized water droplets (2 μl) were placed on the flat (glass without patterns) and patterned surfaces (with an area of 9 mm^2) in triplicate, and the contact angle was recorded after 5 seconds at room temperature.

Surface chemistry analysis

Fourier transform infrared spectroscopy (FTIR, Thermo Fisher Scientific Nicolet FTIR Spectrometer 6700, US) was performed to identify the functional groups of the IP-L780 photoresist and the submicron pillars. Four scans in the range of $4000\text{--}650 \text{ cm}^{-1}$ were performed to acquire each spectrum using the attenuated total reflection (ATR) element.

X-ray photoelectron spectroscopy (XPS, Thermo Fisher K-Alpha, US) was performed to analyze the chemical composition of the 3D printed submicron pillars on the glass substrate. Ten scans were acquired with an energy step of 0.2 eV using an Al K_α source gun with a spot size of $400 \mu\text{m}^2$ in the standard lens mode. Due to the small size of the pillars and the space between the individual pillars, XPS measured both the pillars and the substrate. The apparent disturbance of the potassium (K 2p) signal within a carbon

(C 1s) scan was used to calculate and subtract the amount of the carbon signal that originated from the substrate.

5.2.3 Cell experiments

Cell culture conditions

The specimens were first sterilized by immersion in 70% ethanol (Sigma-Aldrich, Germany), followed by UV light exposure for 20 minutes. Then, 5×10^4 preosteoblast cells (MC3T3-E1, passage 11, Sigma-Aldrich, Germany) were seeded on each sample in a 6-well plate (Greiner Bio-One, The Netherlands) and incubated at 37 °C, 5% CO₂ (Life Technologies, US) in an alpha minimum essential medium (α -MEM) (Thermo Fisher, US) supplemented with 10% (v/v) fetal bovine serum (Thermo Fisher, US) and 1% (v/v) penicillin-streptomycin (Thermo Fisher, US). For the long-term experiments (*i.e.*, 21 days of culture), the medium was refreshed every 2 days. For the cases where osteogenic conditions were desired, 50 μ g/ml ascorbic acid and 4 mM β -glycerophosphate (both from Sigma-Aldrich, Germany) were added to α -MEM from day 2 onward.

Cell adhesion measurements by SCFS

SCFS experiments were performed using a JPK Nanowizard 4 AFM (JPK Instruments, Germany) mounted on a Zeiss Axio Observer optical microscope (Carl Zeiss AG, Germany) and equipped with the JPK CellHesion module (JPK Instruments, Germany), which allows for an extended 100 μ m Z-range. The specimens were glued to petri dishes (TPP, Switzerland), which were compatible with the JPK petri dish heater (JPK Instruments, Germany) that maintained the temperature constant at 37 °C during the experiments.

Arrow TL-tipless cantilevers (NanoWorld, Switzerland) with a nominal spring constant of 0.03 N/m were incubated in phosphate-buffered saline (PBS, Thermo Fisher, US) containing 10 μ g/mL fibronectin (Sigma-Aldrich, Germany) for 30 minutes at room temperature. After functionalization, the cantilevers were rinsed twice in PBS and were calibrated using the thermal noise method.

For the SCFS experiments, 5×10^4 MC3T3-E1 cells were pre-cultured in a standard 6-well plate. When the cells reached confluence, the culture medium was removed, and the cells were rinsed twice with 2 ml of PBS and were detached from the well using 100 μ l of 0.5% trypsin-EDTA (Thermo Fisher, US) solution (37 °C, 3 minutes). The trypsinized cells were suspended in 1 mL of culture medium and were used for the SCFS experiments.

100 μl of the cell suspension was directly injected in a petri dish containing the sample and 2 ml of culture medium, relatively far from the patterned area. Single rounded cells were identified by the optical microscope and individually picked up by the functionalized probe. To pick the cells, the free end of the cantilever was carefully aligned with the cell, and a force-distance cycle was performed using the following parameters: i) a setpoint force of 3 nN, a Z length of 50 μm , the approach and retract speed of 2 $\mu\text{m/s}$, and a contact time of 10 seconds. The cantilever with a cell attached to the tip is referred to as the “cell probe”. The cell adhesion measurements with surfaces were then performed by acquiring force-distance curves with the “cell probe” using the following parameters: i) a setpoint force of 1 nN, a Z length of 80 μm , and the approach and retract speed of 5 $\mu\text{m/s}$. Since the first phase of cell adhesion, characterized by single-integrin adhesion events, takes place during the first 60 seconds of contact with a surface²⁷⁻²⁹, 2 and 60 seconds contact times were tested.

Since immunostaining analysis showed that cells interacting with L1 and S1 patterns did not have different behaviors (in terms of cell area, cell morphology, and FAs) as compared to the control samples, SCFS experiments were performed only on S2, S3, L2, L3 and on the control (flat glass) surfaces. Three force-distance curves on the pattern and three force-distance curves on the glass control surface were acquired with each “cell probe”. Between seven and nine cells were tested on each specimen. The reported normalized values of the adhesion force and the work of adhesion were obtained by normalizing the values from each cell on the patterns to the values obtained for the same cell on the glass control surface.

Immunocytochemical analyses

The actin filaments, nucleus, and FAs of the cells were stained after 4 hours and 1 day. As previously described²⁵, the specimens were first rinsed with PBS, and the cells were fixed using a 4% (v/v) formaldehyde solution (Sigma-Aldrich, Germany). After permeabilization with 0.5% Triton X-100/PBS (Sigma-Aldrich, US) at 4 °C for 5 minutes, the cells were incubated in 1% BSA/PBS (Sigma-Aldrich, Germany) at 37 °C for 5 minutes. Then, the specimens were incubated in the rhodamine-conjugated phalloidin (1:1000 in 1% BSA/PBS, Thermo Fisher, US) and anti-vinculin mouse monoclonal primary antibody (1:100 in 1% BSA/PBS, Sigma-Aldrich, Germany) for 1 hour at 37 °C. The cells were then rinsed thrice with 0.5% Tween-20/PBS (Sigma-Aldrich, US) and incubated in Alexa Fluor 488, donkey anti-mouse polyclonal secondary antibody (1:200

in BSA/PBS, Thermo Fisher, US) for 1 hour at room temperature. The specimens were again rinsed thrice with 0.5% Tween-20/PBS for 5 minutes each time, followed by 5 minutes rinsing with 1X PBS. Afterward, a droplet of 10 μ l of Prolong gold (containing 4',6-diamidino-2-phenylindole (DAPI), Thermo Fisher, US) was laid on the cells, and the specimens were flipped over on microscopic glass slides and were imaged using a fluorescence microscope (ZOE fluorescent cell imager, Bio-Rad, The Netherlands).

For SEM observations, the stained specimens were rinsed twice with distilled water for 5 minutes and then dehydrated in 50%, 70%, and 96% ethanol solutions for 15, 20, and 20 minutes, respectively. Finally, the samples were dried overnight at room temperature and were coated with gold by sputtering prior to being imaged by SEM.

The cell matrix mineralization was analyzed on day 21 in both non-osteogenic and osteogenic media. The cells were washed with PBS and were fixed with a 4% (v/v) formaldehyde solution for 15 minutes. Next, the samples were prepared for staining by a process similar to cytoskeleton staining (see above). The cells were incubated with the OPN antibody conjugated to Alexa Fluor 488 (1:100 in BSA/PBS, Santa Cruz Biotechnology, US) for 1 hour at 37 °C. Then, the cells were rinsed thrice with 0.5% Tween-20/PBS for 5 minutes, followed by a subsequent 5 minutes rinsing with 1X PBS. Prolong gold was added to the specimens, and they were mounted on glass slides to be imaged using the fluorescence microscope.

Mechanics of living cells by AFM

Mechanical mapping of living cells after 1 day of culture was performed using an AFM (JPK Nanowizard 3, JPK Instruments, Germany) in the quantitative imaging (QI) mode and a qp-BioAC-CB3 probe (Nanosensors, Switzerland) with a nominal spring constant of 0.06 N/m. The instrument allowed for a maximum scan area of 30 \times 30 μ m². During the experiments, the temperature was maintained at 37 °C using the JPK petri dish heater (JPK Instruments, Germany). The probe was calibrated using the thermal noise method³⁰. The applied setpoint force was 1 nN, which corresponded to an indentation depth in the range of 300-900 nm. The cells were evaluated using a pixel time of 20 ms and a Z length of 2 μ m. The maps of the elastic modulus were obtained by fitting the force-distance curves measured at each point of the scanned area to the Hertz-Sneddon model³¹ considering a paraboloid tip with a nominal tip radius of 10 nm. The reported values of the elastic modulus were calculated as the average elastic modulus value in a certain area of interest (*e.g.*, the periphery or center of the cells).

Image analysis

ImageJ was used to process the fluorescence images. First, the image overlay was split into channels to separate the nucleus, F-actin, and other proteins (*i.e.*, vinculin and OPN). The grayscale images of F-actin and OPN were thresholded. The cell area, the degree of anisotropy (DA, $DA \approx 1$ presents polarization in cells and $DA \approx 0$ indicates the fully isotropic cells) of 20 cells per sample ($n = 4$), and the OPN area ($n = 4$) were then quantified through the Analyze Particles command²⁵.

To count and measure the FA area, a previously described method was used³². Briefly, the background was subtracted from the grayscale images under the Sliding Paraboloid option with a rolling ball radius of 50 pixels. The local contrast of the image was then enhanced by running the CLAHE plugin with a block size of 19, histogram bins of 256, and a maximum slope of 6. To further minimize the background, the mathematical exponential (EXP) was applied through the process menu. Next, the brightness, contrast, and threshold were automatically adjusted. Finally, the area and number of FAs were measured using the Analyze Particles command³². The measurements were performed only on fully separated focal points.

Statistical analysis

To determine whether there were significant differences between the means of different experimental groups, one-way ANOVA followed by Tukey's multiple comparisons *post hoc* test was performed using Prism (version 8.0.1, GraphPad, US). The nonparametric Kruskal-Wallis test was used to compare the measurements of cell adhesion parameters on different patterns. A *p*-value below 0.05 was considered to indicate statistical significance.

5.2.4 Computational models

We used a commercial nonlinear finite element code (Abaqus, version 6.21) for our computational simulations to study the mechanics of the submicron pillars interacting with cells. We used isotropic linear elastic material properties for the modeling of the submicron pillars ($E = 3.35$ GPa, $\nu = 0.4$) and the glass substrates ($E = 63$ GPa, $\nu = 0.2$). Using a tie-constraint, the pillar and the substrate were attached. Two pillars with different heights ($h = 500$ and 1000 nm) and similar boundary conditions were modeled. A reference point was defined at the center of the top surface of the pillars. This reference point was kinematically coupled to the nodes on the top surface of the pillars. A

displacement boundary condition along the x-axis (U_x) was applied to the reference point. The magnitude of the displacement of the tip of the bent pillars was extracted from SEM images of the cells on different patterns using ImageJ. The displacements of the pillars were applied to the pillars present in each computational model (*i.e.*, $U_x = 0-70$ nm for $h = 500$ nm, and $U_x = 0-190$ nm for $h = 1000$ nm). Clamped boundary conditions were applied to the glass substrate. 3D quadratic hexahedral elements (C3D20) with a minimum mesh size of 20 nm were used in all of our models. A standard nonlinear analysis was used for the simulations. The average local traction forces were calculated from the experimental displacement observations.

5.3 Results and discussion

5.3.1 Characterization of the patterns

The diameter and the interspacing of the pillars were generally very controllable (Table 5.1 and Figure 5.1a). The deviations observed in the height of the pillars could be attributed to the fluctuations of the laser intensity during the printing process, as previously reported^{25,26}. The printing time varied between 4.5 and 11.5 h/mm² depending on the height and areal density of the pillars (Table 5.1). The average roughness (R_a) of the series S and L was measured by AFM and varied between 79-236 nm and 29-213 nm, respectively (Table 5.1). As expected, the surface roughness increased with the height of the pillars, while increasing the interspacing of the pillars reduced the measured roughness of the patterned surface, particularly for the pillars with the smaller heights (Table 5.1 and Figure 5.1b). The hydrophilicity of the substrate increased with the height of the pillars (Figure 5.1c). This behavior is in agreement with the previous studies^{33, 34} that have shown that rougher surfaces tend to increase the wettability of the surface if the contact angle of the initial surface (48° in our study) is below 60°.

We have analyzed the functional groups of photoresists before and after polymerization via the FTIR test. C=C stretch bonds were found in the region of 1680 cm⁻¹ in the resin but disappeared in the polymer spectrum, indicating no signs of monomer after polymerization (Figure 5.1d). Peaks at 1720 cm⁻¹ showed the ester groups in IP-L780 before and after polymerization (Figure 5.1d). Since the polymerized nanopillars are printed over a small area, the absorbance value of the ester peak in the polymer is less than the one appearing in the monomer. Furthermore, we have quantified the binding energy and percentage of carbon bonds in the polymerized IP-L (Table 5.2). C-C, C=O, and C-

O bonds were present in the XPS spectra of nanopillars showing the presence of acrylic structures in the polymer (Figure 5.1e).

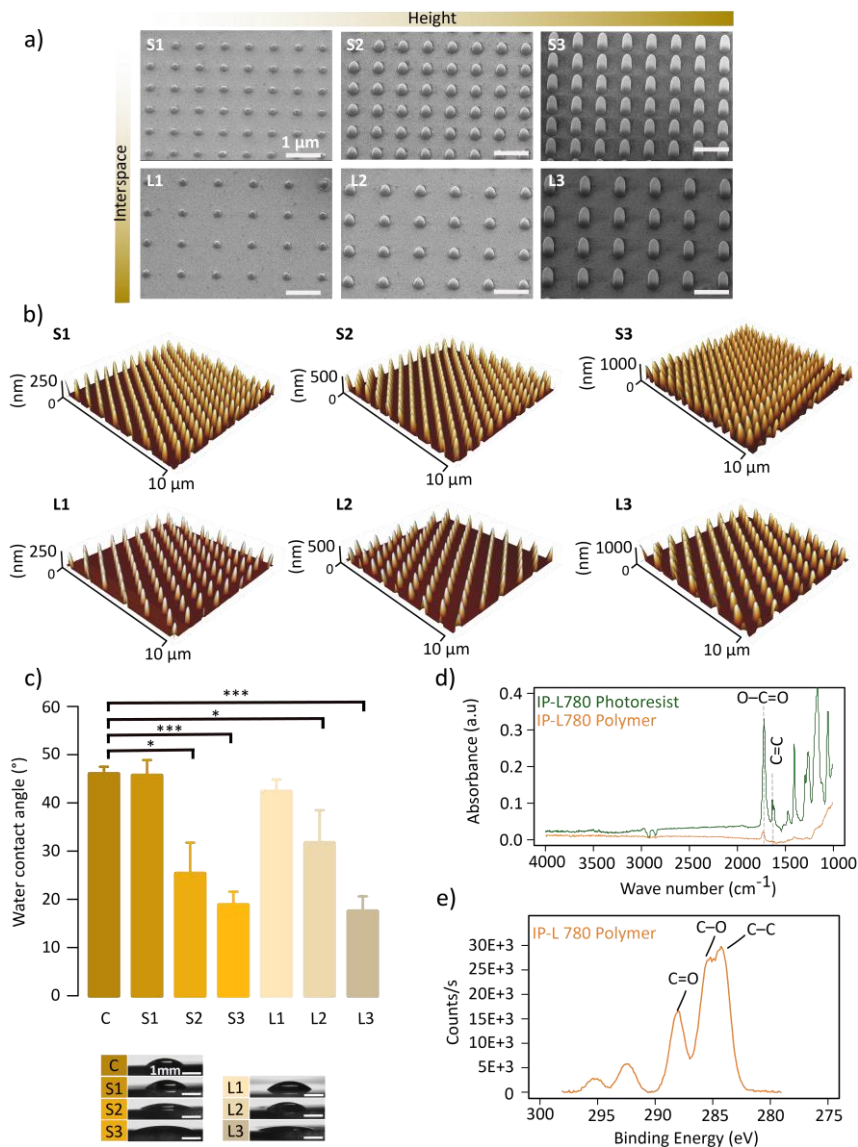


Figure 5.1. Characterization of the submicron pillars. a) SEM and b) AFM images of submicron pillars 3D printed using 2PP. c) Comparison of the wettability of the patterned and control (glass) (C) specimens characterized through water contact angle measurement ($n = 3$ per group, One-way ANOVA followed by Tukey's test, * $p < 0.05$, ** $p < 0.01$, and *** $p < 0.001$). d) FTIR spectra in the ATR mode of the IP-L780 photoresist and polymer (after 2PP). e) XPS spectra of C 1s peaks in IP-L780 after polymerization.

Table 5.1. Characteristics of the submicron pillars, the printing times, and the average roughness of the patterned surfaces.

Groups	Diameter [nm]		Interspacing [nm]		Height [nm]		Aspect ratio	Density [/ $100\mu\text{m}^2$]	Print time [h/ mm^2]	Roughness (R_a) [nm]
	design	measured	design	measured	design	measured				
S1	250	235 \pm 16	700	716 \pm 12	250	251 \pm 24	1	205	5.5	79 \pm 13
S2	250	288 \pm 9	700	714 \pm 9	500	540 \pm 46	2	205	7.5	114 \pm 2
S3	250	305 \pm 14	700	706 \pm 9	1000	928 \pm 32	4	205	11.5	236 \pm 11
L1	250	211 \pm 21	1000	1012 \pm 13	250	253 \pm 30	1	100	4.5	29 \pm 2
L2	250	265 \pm 17	1000	1010 \pm 14	500	498 \pm 28	2	100	5.5	91 \pm 8
L3	250	297 \pm 4	1000	1012 \pm 15	1000	973 \pm 44	4	100	7.5	213 \pm 13

Table 5.2. Energy binding of C 1s species in the 3D printed submicron pillars (made of IP-L780).

Chemical bond	Energy binding [eV]	Atomic %
C-C	284.9	33.1
C-O	286.2	43.4
C=O	288.8	23.5

5.3.2 Differential effects of the patterns on cell adhesion, morphology, and elastic modulus

Cell adhesion

The representative force-distance (F-D) curves acquired at 2 and 60 seconds on the S2, S3, L2, and L3 patterns (Figure 5.2a) showed the typical shape observed when a cell interacts with a surface, indicating the proper functioning of our “cell probes” in terms of cell viability and the positioning of the cantilever. The maximum force peak on the retrace curve, indicating the cell detachment force (*i.e.*, F_{adh}), was followed by step-like events,

which were preceded either by a ramp-like change in force (jumps) or by a plateau region (tethers)^{27,35,36}.

The adhesion force (F_{adh}) and the work of adhesion (W_{adh}) increased for all groups after 60 seconds of contact time as compared to the values recorded after 2 seconds of contact. This can be explained by the fact that a longer contact time enables the formation of more and possibly stronger (more mature) adhesion sites between the cellular receptors and the surface. The type of pattern also influenced the cellular adhesion (Figure 5.2b,c). After both 2 and 60 seconds of contact time, the patterns with the tallest pillars (*i.e.*, S3 and L3) exhibited significantly higher F_{adh} as compared to the patterns with the shorter pillars (*i.e.*, S2 and L2) and the control surface (Figure 5.2b). The F_{adh} values measured for the S2 and L2 groups were not significantly different from those of the control surface (Figure 5.2b).

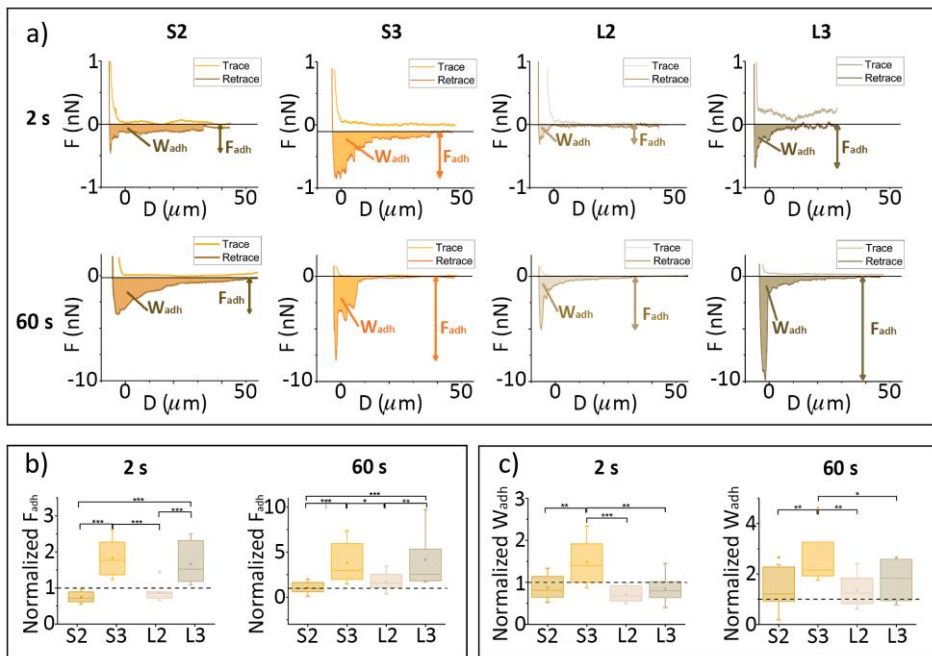


Figure 5.2. Characterization of cell adhesion. a) representative F-D curves obtained by SCFS on S2, S3, L2, and L3 patterns after 2 (first line) and 60 seconds (second line) of contact. b) The adhesion force (normalized with respect to that of the control surface) was measured by SCFS on the patterned surfaces after 2 (left) and 60 seconds (right) of contact. c) Work of adhesion (normalized with respect to that of the control surface) measured by SCFS on the patterned surfaces after 2 (left) and 60 seconds (right) of contact (Kruskal-Wallis test, * $p < 0.1$, ** $p < 0.05$, and *** $p < 0.01$).

Furthermore, the patterns with the highest areal density of pillars (*i.e.*, S3 and S2) exhibited a higher W_{adh} as compared to the patterns having similar heights but lower areal densities (*i.e.*, L3 and L2). S3 exhibited higher W_{adh} as compared to L3 (Figure 5.2c). A less clear difference was observed between S2 and L2 where S2 exhibited slightly (but not significantly) higher W_{adh} as compared to L2 after both 2 and 60 seconds of contact time.

The curves acquired for the patterns with similar heights (and comparable roughness and contact angle) indicated similar values of F_{adh} after 60 seconds (*e.g.*, 3.8 nN for S2, 4.8 nN for L2, 8.1 nN for S3, and 9.8 nN for L3 in the examples reported in Figure 5.2a). The adhesion force increased almost linearly with the height of the pillars. For example, the adhesion force corresponding to a pillar height of 1000 nm was around two times higher than the one corresponding to a pillar height of 500 nm. The work of adhesion, W_{adh} , was higher on the surfaces decorated with the denser patterns (*e.g.*, 47.5 fJ for S2 vs. 20.6 fJ for L2 and 43.5 fJ for S3 vs. 33.8 fJ for L3 in the examples reported in Figure 5.2a).

In summary, the pattern with the tallest and densest pillars (S3) exhibited the highest values of the adhesion parameters (*i.e.*, adhesion force and adhesion work). The L3 pattern, which has a similar height of pillars but a lower pillar density, exhibited an adhesion force that was similar to S3 but a lower work of adhesion. By comparison, the adhesion characteristics of the shorter S2 and L2 patterns were close to the control surface with S2 showing a slightly higher work of adhesion as compared to L2 and the control group.

Hydrophilicity and roughness are known to impact the initial attachment of cells to various kinds of non-patterned surfaces^{18, 20, 37, 38}. We found that the patterns with the tallest pillars (S3 and L3), which are also the most hydrophilic and roughest patterns (Figure 5.1c), result in the highest values of the adhesion force.

The interspacing between the pillars affected the mechanism of the early adhesion of cells to the analyzed submicron patterns. Lower interspacing resulted in a greater work of adhesion. The work of adhesion depends, among such factors as the adhesion force and the characteristics of the cell type, on the number of the anchoring points (*i.e.*, detachment events) of the cell to the surface³⁶. Our results, therefore, suggest that the number of cellular anchoring points on the patterns increases with the areal density of the pillars. This increase was particularly clear for the patterns with the tallest pillars (*i.e.*, S3 as compared to L3).

Cell morphology and cytoskeleton organization

After 4 hours of culture, round cells with an average area of $1900 \pm 719 \mu\text{m}^2$ and diameters around $49 \mu\text{m}$ were visible on all the patterns and the control specimens (Figure 5.3a,c). Nevertheless, the cells on the S3 pattern developed clearly visible membrane extensions rich in vinculin, indicating their ability to more easily spread and interact with the pillars on this pattern. Therefore, the largest variation in the cell area was encountered for this pattern (Figure 5.3c). The presence of relatively well-developed membrane extensions (mainly lamellipodia) around the periphery of the cells (Figure 5.3a) suggests the start of FA maturation, followed by the formation of actin bundles, indicating that the cells are in the contractile spreading phase³⁹. On the contrary, the cells cultured on the control specimens and the specimens from other groups had nascent vinculin sites around the periphery of the cells, and the protrusive activity had not yet started (Figure 5.3a), indicating that the cells were not yet in the contractile spreading phase³⁹ but rather in an earlier phase of the development of FAs³⁹.

The faster development of FAs on the substrates exhibiting both high hydrophilicity and higher initial adhesion force (measured by SCFS experiments) has been observed in studies performed on non-patterned surfaces as well¹⁸. In our case, the formation of FAs on the S3 pattern was promoted not only by enhanced hydrophilicity but also by a higher areal density of pillars relative to the other patterns (*e.g.*, L3) that could favor integrin clustering³⁷. This was also supported by our SCFS experiments (Figure 5.1), which indicated that a high areal density of the pillars results in the formation of more discrete attachment sites already after 2 seconds and 1 minute of contact with these patterned surfaces. Furthermore, integrin clustering may have been further favored by the lower stiffness of the taller pillars in the case of the S3 pattern. Indeed, taller pillars could undergo enhanced bending, thereby further approaching each other when subjected to the interaction forces with the cells⁴⁰.

After the first day of culture, the cells significantly grew in size regardless of the experimental group (Figure 5.3b,c). The cells cultured on the patterned surfaces were, however, smaller than those residing on the control surface. In both S and L series, the cell area decreased with the height of the pillar from $\approx 2800\text{-}2900 \mu\text{m}^2$ for the shorter pillars (S2 and L2) to $\approx 2100\text{-}2200 \mu\text{m}^2$ for the taller pillars (L3 and S3). By comparison, the pillar interspacing did not affect the area of the cells (Figure 5.3b,c). This observation

is in line with the previous studies that have reported a decrease in the cell area for an increased roughness in the submicron range ⁴.

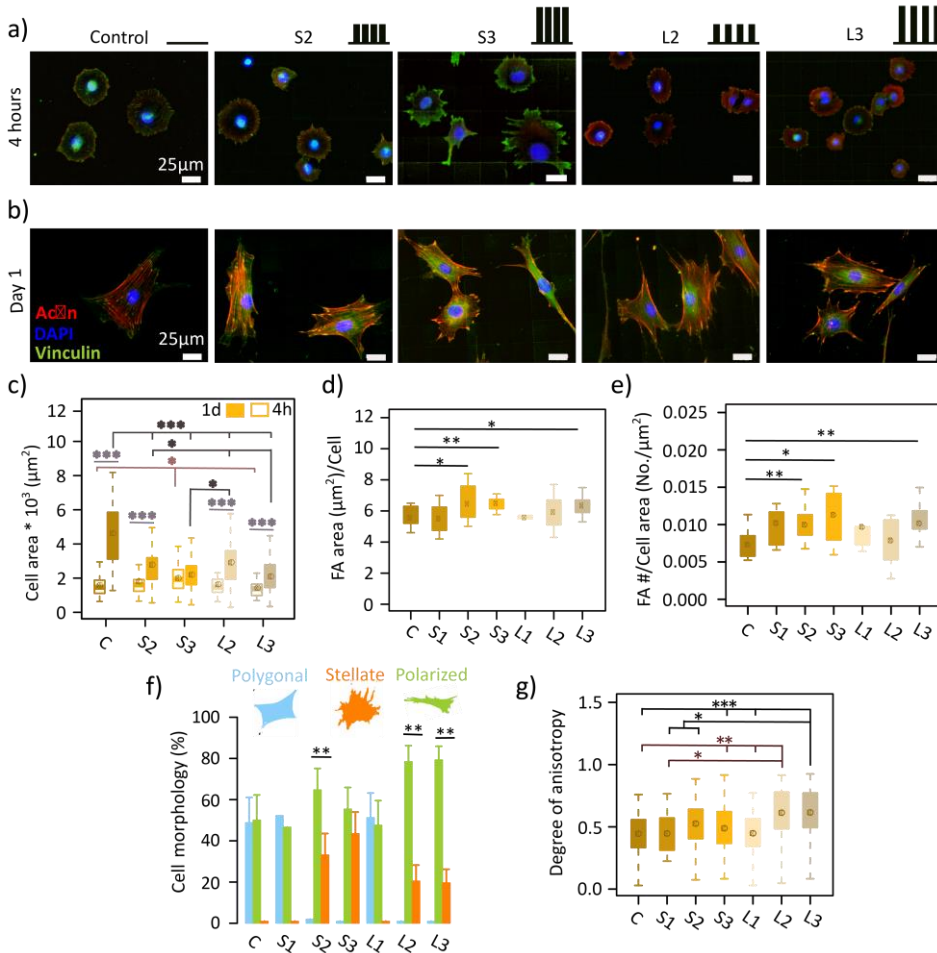


Figure 5.3. Cells spreading and the early response of the MC3T3-E1 cells cultured on the patterned and control surfaces at different time points. a) F-actin, vinculin, and nucleus of the cells cultured on the control and different patterned surfaces after 4 hours and b) 1 day. c) The cell area was measured on the patterned and control samples after 4 hours and 1 day. d) FA area and e) FA density of the cells residing on the patterned and control surfaces on day 1. f) Different types of cell morphology and g) the DA of the cells residing on the patterned and control surfaces on day 1 (One-way ANOVA followed by Tukey's test, * $p < 0.05$, ** $p < 0.01$, and *** $p < 0.001$).

On day 1, the area and density of FAs per cell increased with the height of the pillars (Figure 5.3d,e). However, the pillar interspacing did not significantly influence the area and density of vinculin-rich plaques. The cells cultured on the S2, S3, and L3 specimens

formed the largest FA areas with an average area of $6.5 \pm 0.03 \mu\text{m}^2$, which was significantly higher than the one found on the control sample (*i.e.*, $5.5 \pm 0.7 \mu\text{m}^2$) (Figure 5.3d,e). Furthermore, the cells residing on taller patterns (S3 and L3) exhibited the highest FA density (Figure 5.3e).

After 1 day of culture, three different cell shapes with different cytoskeletal organizations were visible on the specimens (Figure 5.3b,f): 1) polygonal cells with peripherally organized actin fibers, 2) polarized cells with perinuclear actin cap fibers, and 3) stellate cells characterized by the presence of actin fibers in the perinuclear region and multidirectional membrane extensions (mostly filopodia). The polygonal cells were isotropic ($DA \approx 0.4$) and were found on the control specimens as well as on the specimens from the S1 and L1 groups (Figure 5.3b,f,g). The majority of the cells residing on the S2, L2, and L3 specimens were polarized ($DA \approx 0.7$) with wider leading edges showing the motile behavior of the cells (Figure 3b, f, g). The cells grown on the S3 pattern adopted a half-polarized, half-stellate morphology and had a DA value close to 0.5 (Figure 3b,f,g). In the stellate cells, F-actin stress fibers were stretched toward the protrusions and FA sites. Taken together, the DA and the number of polarized cells were enhanced as the height and interspacing of the pillars increased. However, the influence of the pillar interspacing on the shape and the DA of the cells was more pronounced than that of the height (Figure 5.3f,g).

Cells with different morphologies exhibited qualitatively different spatial organizations of the FAs and F-actin bundles (Figure 5.3b). A coupling between the FAs and the F-actin bundles was more visible for the cells with multidirectional protrusions (*e.g.*, stellate cells on S3 and L3 in Figure 5.3b), which exhibited mature and long-lasting FA sites mainly at the proximity of the cell edge (mostly present in the S3 group) (Figure 5.3b). The coupling of F-actin with FAs around the periphery of cells tends to enhance cellular adhesion⁴¹. The coupling of vinculin with the actin bundles was less visible on the polarized cells than on the stellate cells, and they were mainly located in the front and rear of the cells (Figure 5.3b). In the polarized cells, the actin stress fibers were aligned and stretched along the direction of the protrusions, suggesting that the cells were migrating and indicating a higher destabilization of the cell adhesion as well as presumably short-lasting FA points⁴².

Furthermore, we observed three different settling states of the cells on the patterned surfaces (Figure 5.4a,b) that we categorized as follows: 1) a “top state”⁴³ in which the

entire cell body resides on top of the submicron pillars, 2) a “bottom state”⁴³ in which the submicron pillars fully penetrate the cell body, and 3) a “mixed state”⁴³ where some areas of the cell sink into the submicron pillars (bottom state), whereas other areas reside on top of the pillars (top state) (Figure 5.4a,b).

On the shortest pillars (*i.e.*, S1 and L1), the bottom state was observed. The cells fully engulfed the pillars and came into contact with the entire available surface of the pillars (top and lateral) and the substrate (Figure 5.4a,b). The body of the cells appeared very thin as the tip of the pillars was almost visible through the entire cell (Figure 5.4a,b). The pillar interspacing did not influence the settling state on those two patterns.

On the taller pillars, the effects of the pillar interspacing on the cell settling state were more pronounced. The cells cultured on the S2 patterns exhibited a mixed state, with a dominant top state. Indeed, the bottom state was observed only in some regions at the periphery of the cell. Moving toward the nucleus, the cell body appeared thicker, resulting in a top state (Figure 5.4a,b). On the L2 patterns, the bottom state was dominant and was observed almost for the entire body of the cells (Figure 5.4a,b). This may have been caused by the larger pillar interspacing, which helps the cells to easily fill the space between the submicron pillars.

In the case of the S3 patterns characterized by the maximum height and the minimum interspacing, the top state was always observed, suggesting that the cells come into contact only with the top of the pillars without touching the substrate (Figure 5.4a,b). On the L3 patterns, with the maximum height and interspacing, the mixed state was observed. The bottom state was observed only in very small regions around the cell periphery, especially at the rear and front ends of the cells, while the top state was dominant for the rest of the cell body (Figure 5.4a,b).

Previous studies have already shown the effects of the density of nanostructures on how cells “settle” onto a patterned surface and have demonstrated that a high areal density of nanostructures ($\geq 80/\mu\text{m}^2$) and a large diameter of nanopillars (≥ 200 nm) energetically promote the top state⁴³⁻⁴⁵. The small interspacing between the nanopillars leads to intense stretching and unfolding deformation of the cell membranes while they adhere to the sidewalls⁴³. Consequently, the cells adhere to the tip of the pillars. Here, we observed a combined effect of both the density and height of the pillars with a diameter of 250 nm. Indeed, both the height and interspacing in the range investigated in this study had an impact on the interactions between the cells and the underlying pillars. The cells that were

cultured on the pillars with smaller heights and large interspacing distances (*i.e.*, S1, L1, and L2) came into contact with both pillars and substrate (the dominant bottom state), while increasing the height of the pillars and decreasing their interspacing (*i.e.*, S2, L3, and S3 patterns) caused the cells to mostly interact with the top of the pillars without touching the substrate, hence the dominant top state.

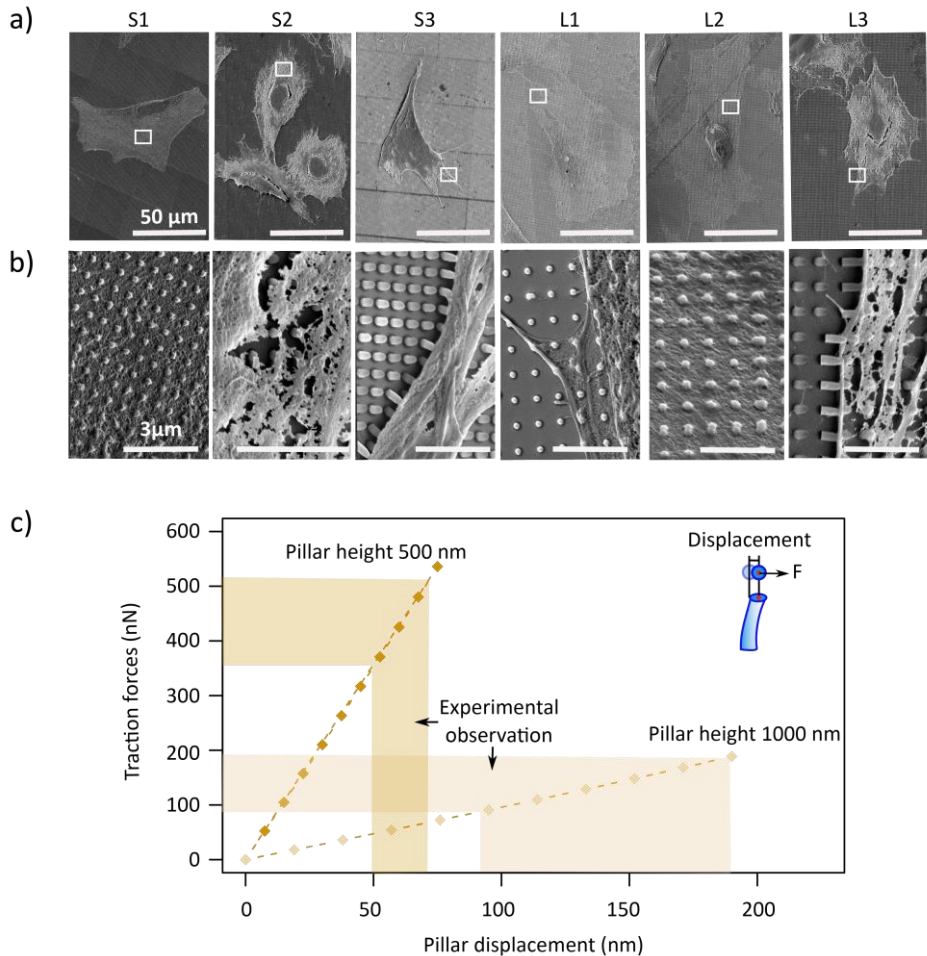


Figure 5.4. Visualization of the cell interactions with the patterned surfaces using SEM and computational modeling. a) Low- and b) high-magnification SEM images of the cells on the patterned surfaces. c) Reaction force (applied by cells to the pillars) and von Mises stress in the submicron pillars calculated using the computational models. Lateral displacements of 58, 140, and 289 nm were applied to the pillars with the heights of 250, 500, and 1000 nm, respectively.

Interestingly, the cells were able to bend the pillars locally after 1 day of residing on the substrate. The bending was more prominent in the vicinity of the edge of the cells settled in the top state (S2, S3, and L3 in Figure 5.4a,b). The pillars were deflected toward the center of the cells (S2, S3, and L3 in Figure 5.4a,b). The lateral displacement of the pillar tips was measured by analyzing the SEM images of the dehydrated cells on the patterns (Figure 5.4c). The corresponding local traction forces in the proximity of the cell border were estimated through computational modeling (Figure 5.4c). The cells applied average local traction forces of 144 ± 38 nN to the pillars with a height of 1000 nm. A higher force value (429 ± 62 nN) was calculated for the pillars with a height of 500 nm. As the traction forces are exerted to the extracellular matrix by FAs⁴⁶, we further assessed the relationship between the traction forces and the FA area. Although we observed no significant differences between the area of FAs on the pillars with the heights of 1000 and 500 nm, the estimated local traction forces were different on those pillars. These findings suggest that mature FAs with the same area can withstand a wide range of force values (100-429 nN estimated in Figure 5.4c), and the results of refs⁴⁶ and⁴⁷ support our findings. These observations were made for preosteoblasts and are in line with the previous studies that have found direct correlations between the FA size and the traction forces only during the initial growth phase of FAs and not for mature FAs^{46,47}. It is, nevertheless, important to realize that the fixation protocol might affect the deformation of the pillars and thus the estimated forces.

The elastic modulus of the cells

The different shapes and cytoskeletal organizations found on the different patterns together with the observations on the cell-pattern interfaces indicated that cells residing on different patterns may also have different mechanical properties. Therefore, the elastic moduli of the living cells interacting with the patterned (S2, S3, L2, and L3) and control surfaces were analyzed by acquiring AFM mechanical maps of the cells after 1 day of culture (Figure 5.5). Exploiting the capability of AFM-based stiffness measurements to perform subsurface imaging of soft biological samples up to a depth of 900 nm^{48,49} also allows for a more detailed analysis of the organization of cortical actin, especially in the perinuclear region.

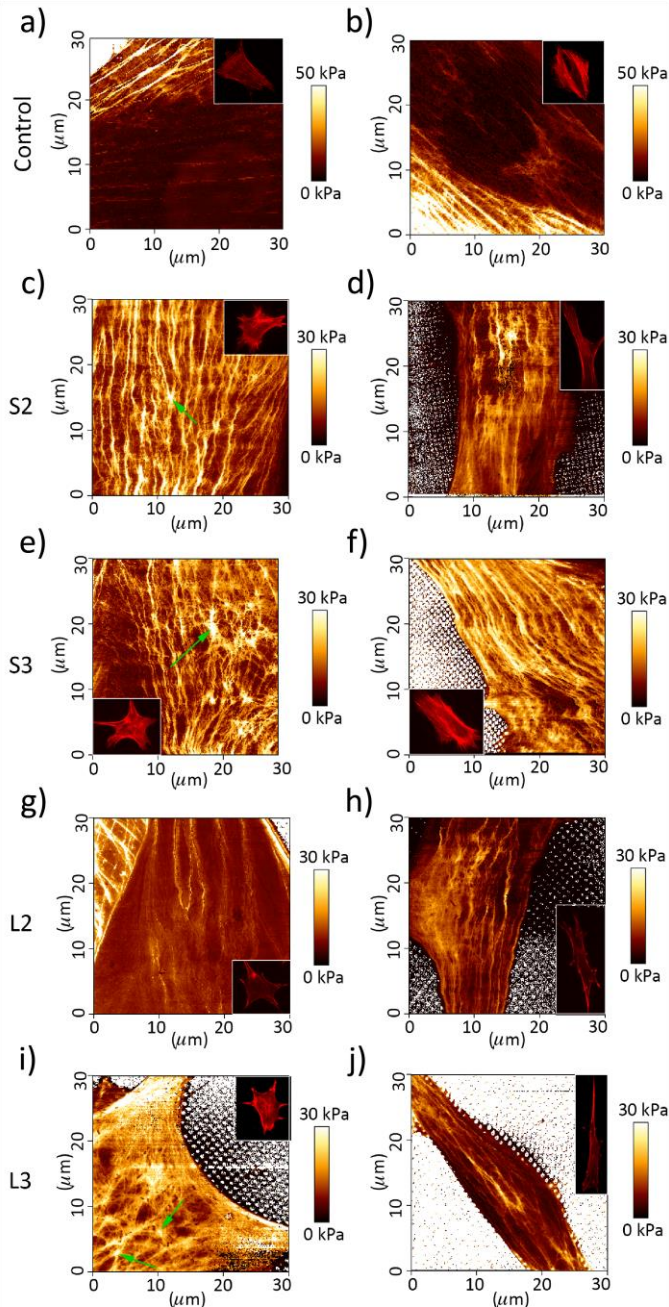


Figure 5.5. AFM-based mechanical characterization of the cells cultured on the patterned and control surfaces on day 1. Some examples of the maps of the elastic modulus obtained for a) a polygonal cell on the control surface, b) a polarized cell on the control surface, c,e,g,i) stellate cells on the S2, S3, L2, and L3 patterns, and d,f,h,j) polarized cells on the S2, S3, L2, and L3 patterns.

On the control surfaces (Figure 5.5a,b), the presence of thick peripheral actin fibers was observed in the cells with both polygonal and polarized shapes, while no or few perinuclear actin fibers were detected. This type of cytoskeletal organization resulted in a high elastic modulus at the periphery of the cells ($E = 25.8$ kPa for the polygonal cell in Figure 5.5a and $E = 42.5$ kPa for the polarized cell shown in Figure 5.5b) and a low elastic modulus at the center of the cells, corresponding to the perinuclear region ($E = 6.1$ kPa in the case of the polygonal cell in Figure 5.5a and $E = 4.9$ kPa for the polarized cell in Figure 5.5b).

On all the patterned surfaces, the cells with the polarized shape presented aligned (almost parallel) fibers crossing the perinuclear region of the cells from the leading edge to the cell rear, suggesting a motile state where, in general, actin fibers tend to align in the direction of cell movement. This type of cytoskeletal organization can be ascribed to the actin cap formation⁵⁰ and gave rise to an elastic modulus, in the perinuclear region, in the range of 6-8 kPa for the cells cultured on the S2, L2, and L3 patterns (*i.e.*, $E = 7.6$, 6.1, and 6.2 kPa for the cells shown in Figure 5.5d,h,j, respectively). A significantly higher elastic modulus in the perinuclear region was observed for the elongated cells residing on the S3 pattern (*e.g.*, $E = 14.45$ kPa for the region shown in Figure 5.5f), which may be due to a more organized cytoskeleton formed by the thick bundles of actin fibers. This organization can be the result of a faster formation of perinuclear stress fibers in the polarized cells grown on the S3 pattern and suggests higher cell contractility and tension.

Stellate cells exhibited a different type of cytoskeletal organization in the perinuclear region, which in the case of the specimens from the S2, S3, and L3 groups resulted in a branched network of thick bundles of actin fibers and thus higher values of the elastic modulus ($E = 14.6$, 13.9, and 14.5 kPa, respectively for the cells residing on the S2, S3, and L3 patterns, Figure 5.5c,e,i). This type of organization indicates that the stress fibers in these cells were stretched in different directions. The presence of actin star sites (*e.g.*, the small green arrows in Figure 5.5c,e,i) were associated with the highest values of the elastic modulus and suggested the entanglement of several actin bundles coming from different directions^{51,52}. The formation of these actin patterns, such as asters or stars, has been hypothesized to be associated with high levels of intrinsic mechanical stress within the cortical network^{53,54}. They may, therefore, indicate a high-tension state for the stellate cells residing on the S2, S3, and L3 patterns.

The stellate cells cultured on the L2 patterns exhibited a different type of cytoskeletal organization as compared to the stellate cells grown on other patterns. Large peripheral actin stress fibers were observed, while the nuclear region was characterized by a very limited presence of actin fibers or filaments and thus a low value of the elastic modulus (*i.e.*, 8.5 kPa for the sample cell shown in Figure 5.5g). This suggests lower contractility and tension of the stellate cells on the L2 pattern as compared to the other patterns. Interestingly, the cells residing on the L2 patterns, in contrast with those cultured on the other patterns (S2, S3, and L3), exhibited mostly a “bottom settling state” (*i.e.*, contact not only with the top of the pillars but also with the substrate between them) (Figure 5.4a,b). This observation suggests a correlation between the way cells adhere to and settle onto the patterns (*i.e.*, top state or bottom state) and their response in terms of cytoskeletal organization and mechanical properties.

Summary of the early cellular responses on submicron pillars

We found a correlation between the initial phase of cell adhesion and the settling state of the cells on the patterned surfaces. While the cells residing on the S2, S3, and L3 surfaces generally only interacted with the tip of the pillars (*i.e.*, exhibited a dominant top settling state), those on the L2 surface interacted with both the pillars and the substrate (*i.e.*, exhibited a dominant bottom settling state) (Figure 5.4a,b). This is most likely caused by the spatial organization of these pillars, which enables the cells to partially occupy the space between them. Our SCFS results suggest that a similar type of cell-pattern interaction may occur during the initial adhesion phase. Assuming that cells come into contact only with the tip of the pillars when interacting with the S3 and L3 patterns, the significant increase in the work of adhesion observed in the case of S3 as compared to L3 can be explained by the increase in the available surface caused by a higher areal density of the pillars. The increased density of the initial anchoring points could result in a higher density of integrin binding sites, which could give rise, during the later adhesion phases, to a different, potentially faster FA development process^{40, 55, 56}. We did not observe a significant difference in the work of adhesion of the S2 and L2 patterns. This observation, in combination with the results of the SEM analysis, indicates that there is no direct relationship between the density of the pillars and the binding sites in the case of the S2 and L2 patterns. This is because the cells settle differently onto the surface (*i.e.*, dominant top state in the case of S2 and dominant bottom state in the case of L2).

Interestingly, the effects of topography on the initial adhesion force, FA area, and density were visible only on those patterns that exhibited a dominant top state (S2, S3, and L3). No significant difference in the FA area and density as compared to the control surface was observed for the patterns with a dominant bottom state. Therefore, the patterns influenced the adhesion process and FA development only when the contact between the cells and the pillars was concentrated around the tip of the pillars.

We also found a direct relationship between cell adhesion, surface wettability, and surface roughness. S3 and L3 were the roughest and most hydrophilic surfaces, and the cells on those patterns exhibited the highest initial adhesion force and the most abundant FA sites after 1 day. Our results are in line with the previous studies showing the positive impact of hydrophilicity²⁵ and intermediate roughness (*i.e.*, $R_a \approx 200$ nm) in the submicron range on cell adhesion^{4, 57, 58}.

Furthermore, our results suggest a faster FA formation process on the S3 pattern (Figure 5.3a). The faster formation of vinculin-rich sites may have been caused not only by the high initial adhesion force on such surfaces but also by the geometry of the pillars (height and interspace). Tall and dense pillars provide a large number of anchoring points (higher work of adhesion), as observed in our SCFS experiments. The high density of the anchoring points could result in a high density of integrin binding sites, which could more easily cluster and develop mature FAs⁵⁶.

The morphology and cytoskeletal organization of the cells on day 1 support the statement regarding the faster formation of mature FAs. The S3 patterns exhibited the highest numbers of stellate cells at day 1, implying the greater coupling of the focal points with F-actin, which normally form in the presence of mature FAs^{42, 59} and, thus, indicate a more advanced state of the FA formation process.

The cells cultured on the S3 surfaces with both elongated and stellate morphologies exhibited the highest values of the elastic modulus and the highest degree of cytoskeletal organization, characterized by the presence of thick and dense actin stress fibers in the perinuclear region. This observation suggests higher contractility and higher tension as compared to the cells interacting with the other patterns, which may be attributed to the different adhesion behavior of the cells residing on this type of surface, as indicated by the initial force and work of adhesion as well as the development and distribution of FAs. This may lead to a higher level of nuclear tension^{4, 60} and affect subsequent cellular functions. Indeed, previous studies have shown that the presence of dense actin cap fibers

is associated with elevated levels of nuclear tension, high chromatin condensation, and Yes-associated protein (YAP) nuclear accumulation, resulting in the osteogenic differentiation of MSCs on catecholic polyglycerol coatings with roughness values (R_a) in the range of 150-300 nm⁴.

The next question was whether our findings regarding the early adhesion, morphology, and mechanical properties of preosteoblasts affect the subsequent cellular functions. Therefore, a long-term experiment was performed to investigate the ECM formation by preosteoblast cells.

5.3.3 Effects of the patterns on the ECM

One of the essential ECM proteins expressed by mature osteoblasts is OPN⁶¹, which is further enhanced by applying mechanical stress⁶². We, therefore, analyzed the level of OPN expression for the specimens from different experimental groups using both osteogenic and non-osteogenic media after 21 days of cell culture. On flat controls, OPN was expressed only in the osteogenic medium (Figure 5.6b). In the osteogenic condition, the surfaces patterned with the tallest pillars (*i.e.*, S3 and L3) significantly upregulated the expression of OPN as compared to the other patterns and the control group (Figure 5.6a,c). In addition, a slight (not significant) increase in the OPN expression compared to the control surface was observed for the S2 group, while the other patterns did not show any difference as compared to the control group (Figure 5.6c). A difference in the OPN expression after 21 days was observed only on those patterns (S2, S3, and L3) for which an increased area and density of FAs were observed after 1 day (Figure 5.6f) and where cells mostly interacted with the top region of the pillars (dominant top state). This finding supports the presence of a relationship between the capability of the cells to rapidly form mature FAs and the subsequent matrix mineralization process. The S3 pattern, for which we found the strongest cell adhesion and the highest elastic modulus values in the perinuclear areas, also exhibited the highest level of OPN expression, further supporting the hypothesis that a direct relationship exists between the early cell adhesion behavior and the late matrix mineralization process. We did not, however, detect a significant difference between S3 and L3 (pillars with a larger interspacing of 1000 nm) under the osteogenic conditions (Figure 5.6a,c).

To isolate the effects of the surface patterns from those of the osteogenic supplements, we repeated the experiments for the S3, L3, and control groups under non-

osteogenic conditions. The difference between the OPN expression of the S3 and L3 groups was statistically significant when using a non-osteogenic medium (Figure 5.6d,e). The differential effects of the patterns with different geometries on the OPN expression could, therefore, be more easily detected when the influence of the osteogenic supplements was removed. These findings reveal possible osteoinductive properties of the S3 pattern.

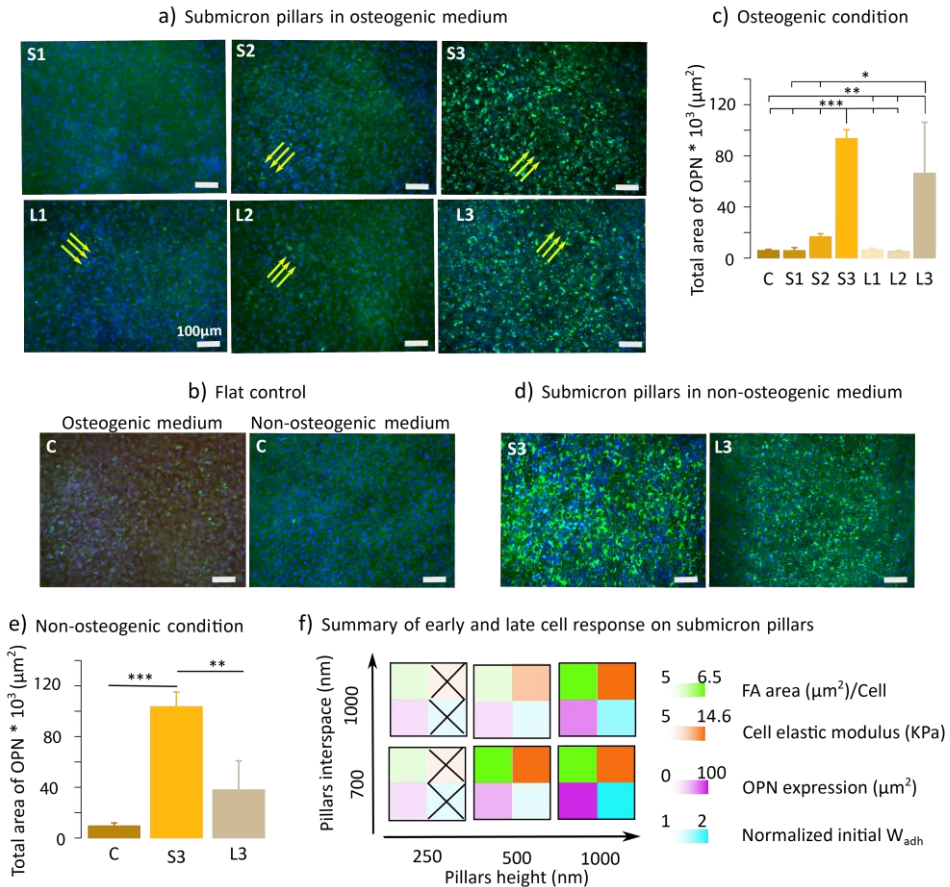


Figure 5.6. a) Representative images of OPN expression in the MC3T3-E1 matrix after 21 days of culture on patterned surfaces under osteogenic condition. b) Representative images of OPN expression on flat control under both osteogenic and non-osteogenic conditions. c) Total area of OPN expressed on patterned and flat surfaces under osteogenic condition. d) Representative images of OPN expression on patterned surfaces under non-osteogenic condition. e) Total area of OPN expressed on patterned and flat surfaces under non-osteogenic conditions. f) Response of the preosteoblast cells as a function of the height and interspacing of the pillars (One-way ANOVA followed by Tukey’s test, * $p < 0.05$, ** $p < 0.01$, and *** $p < 0.001$).

The combined use of different techniques allowed us to unravel the relationships between the early and late indicators of the response of preosteoblasts to submicron surface patterns. On the most potent pattern, *i.e.*, the S3 pattern, the initial work of adhesion and the area of FA sites (vinculin) were upregulated, which in turn increased the elastic modulus of the cells, resulting in stretched actin stress fibers in all directions (Figure 5.6f). As a result, the highest amount of OPN expression was observed (Figure 5.6e). Thus, the quantitative and systematic approach used in our study suggests that the earlier markers related to the adhesion phase (*e.g.*, adhesion strength and cell mechanical properties) may be useful for predicting the osteogenic potential of patterned biomaterials.

The geometry and spacing of the submicron and nanopillars are known to influence the extracellular proteins expressed by preosteoblasts⁶³. At the nanoscale, shorter pillars enhanced the bone matrix nodules in hMCSs⁹. While at the submicron scale, we observed an opposite trend. The tall and dense submicron pillars were the most potent physical stimuli to alter the response and function of preosteoblast cells. Furthermore, the roughness of the osteogenic pattern identified in our study is in the range of the roughness values (150-450 nm) that have been found in the literature to enhance the osteogenic differentiation of osteoblasts and MSCs^{4,64}.

In addition to the surface design, the substrate stiffness can influence the response of cells. It is known that in soft materials such as hydrogels, a higher stiffness is needed to favor osteogenic differentiation in hMSCs and preosteoblasts^{65,66}. On the other hand, the scale of surface topographies affects osteogenic differentiation on very stiff substrates, such as titanium. For example, at the nanoscale, short titania pillars (around 15 nm in height) have been found to be effective for ECM mineralization by MSCs⁹. At the submicron scale, roughness values of around 150-450 nm have been shown to stimulate the adhesion and osteogenesis of osteoblasts and MSCs^{4,64}. By comparison, microscale roughness (1050 nm) tends to attenuate the osteogenic mineralization by MSCs⁴ and the formation of FAs in osteoblasts ($R_a = 2.19\text{-}3.4\ \mu\text{m}$)⁶⁷.

Substrate stiffness and topographies can induce intracellular tension by promoting the polymerization of actin and increasing actomyosin forces^{68,69}. Increasing the stiffness of the substrate activates RhoA/ROCK signaling pathway, leading to the enhanced osteogenesis of hMSCs^{68,70}. The presence of stretch and tension in the osteoblast cytoskeleton leads to the activation of the mechanocoupling phase and is a messenger of

the mechanotransduction process⁶². A direct mechanotransduction pathway may be activated by the S3 pattern via integrin clustering, followed by the signal transduction through the cytoskeleton elements toward the nucleus where mechanoactuators activate the mechanosensitive genes. These mechanotransduction pathways include kinase pathways that involve the phosphorylation of kinase proteins, such as focal adhesion kinase (FAK) and subsequent upregulation of late osteogenic markers, such as the OPN gene in preosteoblasts^{12, 62}. Further research is required to gain insights into the mechanotransduction pathways activated by such a patterned surface.

5.4 Conclusions

We performed a systematic study on the effects of the design parameters of 3D printed submicron pillars on the response of preosteoblasts from initial adhesion to the formation of the extracellular matrix. This included the single-cell measurement of the adhesion parameters (*i.e.*, adhesion force and work of adhesion), a study of cell morphology and cytoskeletal organization, mapping of the elastic modulus within individual cells, and expression of late osteogenic markers (*i.e.*, OPN). The adhesion of cells and the subsequent formation of FAs were positively modulated by the surface topography only when the pillars were tall and dense enough, in which case the cells settled onto the surface in the “top state”. Furthermore, the cells interacting with tall and dense pillars were characterized by numerous thick actin stress fibers in the perinuclear region and the upregulation of OPN. These findings reveal previously undocumented mechanistic pathways through which submicron pillars with specific geometries and spatial organizations initiate a cascade of events that regulate the cell response starting from initial adhesion and continuing all the way to matrix mineralization. These findings pave the way toward the discovery of early and quantifiable markers capable of predicting the osteogenic potential of biomaterials. This improved understanding of how the design parameters of submicron pillars influence the bone tissue regeneration process could inform the future designs of instructive surfaces, thereby enhancing the osseointegration of future orthopedic implants.

Bibliography

- [1] D. Khang, J. Lu, C. Yao, K.M. Haberstroh, T.J. Webster, The Role of Nanometer and Sub-micron Surface Features on Vascular and Bone Cell Adhesion on Titanium, *Biomaterials*, 29(8), 970-983, 2008.
- [2] M. Mirzaali, I. Van Dongen, N. Tümer, H. Weinans, S.A. Yavari, A. Zadpoor, In-silico quest for bactericidal but non-cytotoxic nanopatterns, *Nanotechnology*, 29(43), 43LT02, 2018.
- [3] F.Y. McWhorter, T. Wang, P. Nguyen, T. Chung, W.F. Liu, Modulation of Macrophage Phenotype by Cell Shape, *Proceedings of the National Academy of Sciences*, 110(43), 17253-17258, 2013.
- [4] Y. Hou, W. Xie, L. Yu, L.C. Camacho, C. Nie, M. Zhang, R. Haag, Q. Wei, Surface Roughness Gradients Reveal Topography-Specific Mechanosensitive Responses in Human Mesenchymal Stem Cells, *Small*, 16(10), 1905422, 2020.
- [5] S.G. Higgins, M. Becce, A. Belessiotis-Richards, H. Seong, J.E. Sero, M.M. Stevens, High-Aspect-Ratio Nanostructured Surfaces as Biological Metamaterials, *Advanced Materials*, 1903862, 2020.
- [6] M.J. Dalby, N. Gadegaard, R. Tare, A. Andar, M.O. Riehle, P. Herzyk, C.D. Wilkinson, R.O. Oreffo, The Control of Human Mesenchymal Cell Differentiation Using Nanoscale Symmetry and Disorder, *Nature Materials*, 6(12), 997-1003, 2007.
- [7] S. Dobbenga, L.E. Fratila-Apachitei, A.A. Zadpoor, Nanopattern-Induced Osteogenic Differentiation of Stem Cells—A Systematic Review, *Acta Biomaterialia*, 46, 3-14, 2016.
- [8] J. Lovmand, J. Justesen, M. Foss, R.H. Lauridsen, M. Lovmand, C. Modin, F. Besenbacher, F.S. Pedersen, M. Duch, The Use of Combinatorial Topographical Libraries for the Screening of Enhanced Osteogenic Expression and Mineralization, *Biomaterials*, 30(11), 2015-2022, 2009.
- [9] T. Sjöström, M.J. Dalby, A. Hart, R. Tare, R.O. Oreffo, B. Su, Fabrication of Pillar-Like Titania Nanostructures on Titanium and their Interactions with Human Skeletal Stem Cells, *Acta Biomaterialia*, 5(5), 1433-1441, 2009.
- [10] L.E. McNamara, T. Sjöström, K.E.V. Burgess, J.J.W. Kim, E. Liu, S. Gordonov, P.V. Moghe, R.M.D. Meek, R.O.C. Oreffo, B. Su, M.J. Dalby, Skeletal Stem Cell Physiology on Functionally Distinct Titania Nanotopographies, *Biomaterials*, 32(30), 7403-7410, 2011.
- [11] J.L. Tan, J. Tien, D.M. Pirone, D.S. Gray, K. Bhadriraju, C.S. Chen, Cells Lying on a Bed of Microneedles: an Approach to Isolate Mechanical Force, *Proceedings of the National Academy of Sciences*, 100(4), 1484-1489, 2003.
- [12] J.E. Gautrot, J. Malmström, M. Sundh, C. Margadant, A. Sonnenberg, D.S. Sutherland, The Nanoscale Geometrical Maturation of Focal Adhesions Controls Stem Cell Differentiation and Mechanotransduction, *Nano Letters*, 14(7), 3945-3952, 2014.
- [13] K.W. Kwon, S.S. Choi, B. Kim, S.N. Lee, M.C. Park, P. Kim, S.H. Lee, S.H. Park, K.Y. Suh. A Microfluidic Flow Sensor for Measuring Cell Adhesion. in *Sensors*, IEEE, 2006.
- [14] P. Zorlutuna, Z. Rong, P. Vадgama, V. Hasirci, Influence of Nanopatterns on Endothelial Cell Adhesion: Enhanced Cell Retention under Shear Stress, *Acta Biomaterialia*, 5(7), 2451-2459, 2009.

- [15] C.G. Galbraith, M.P. Sheetz, A Micromachined Device Provides a New Bend on Fibroblast Traction Forces, *Proceedings of the National Academy of Sciences*, 94(17), 9114-9118, 1997.
- [16] P. Roy, Z. Rajfur, P. Pomorski, K. Jacobson, Microscope-Based Techniques to Study Cell Adhesion and Migration, *Nature Cell Biology*, 4(4), E91-E96, 2002.
- [17] G. Bao, S. Suresh, Cell and Molecular Mechanics of Biological Materials, *Nature Materials*, 2(11), 715-725, 2003.
- [18] A.V. Taubenberger, M.A. Woodruff, H. Bai, D.J. Muller, D.W. Huttmacher, The Effect of Unlocking RGD-motifs in Collagen I on Pre-osteoblast Adhesion and Differentiation, *Biomaterials*, 31(10), 2827-2835, 2010.
- [19] L. Jiang, Z. Sun, X. Chen, J. Li, Y. Xu, Y. Zu, J. Hu, D. Han, C. Yang, Cells Sensing Mechanical Cues: Stiffness Influences the Lifetime of Cell-Extracellular Matrix Interactions by Affecting the Loading Rate, *ACS Nano*, 10(1), 207-217, 2016.
- [20] J. Markwardt, J. Friedrichs, C. Werner, A. Davids, H. Weise, R. Lesche, A. Weber, U. Range, H. Meißner, G. Lauer, B. Reitemeier, Experimental Study on the Behavior of Primary Human Osteoblasts on Laser-Cused Pure Titanium Surfaces, *Journal of Biomedical Materials Research Part A*, 102(5), 1422-1430, 2014.
- [21] T. Naganuma, The Relationship Between Cell Adhesion Force Activation on Nano/Micro-Topographical Surfaces and Temporal Dependence of Cell Morphology, *Nanoscale*, 9(35), 13171-13186, 2017.
- [22] M. Grau, J. Matena, M. Teske, S. Petersen, P. Aliuos, L. Roland, N. Grabow, H. Murua Escobar, N.-C. Gellrich, H. Haferkamp, In Vitro Evaluation of PCL and P (3HB) as Coating Materials for Selective Laser Melted Porous Titanium Implants, *Materials*, 10(12), 1344, 2017.
- [23] P. Bertoncini, S. Le Chevalier, S. Lavenus, P. Layrolle, G. Louarn, Early Adhesion of Human Mesenchymal Stem Cells on TiO₂ Surfaces Studied by Single-Cell Force Spectroscopy Measurements, *Journal of Molecular Recognition*, 25(5), 262-269, 2012.
- [24] C. Cimmino, L. Rossano, P.A. Netti, M. Ventre, Spatio-Temporal Control of Cell Adhesion: Toward Programmable Platforms to Manipulate Cell Functions and Fate, *Frontiers in Bioengineering and Biotechnology*, 6(190), 2018.
- [25] M. Nouri-Goushki, M.J. Mirzaali, L. Angeloni, D. Fan, M. Minneboo, M.K. Ghatkesar, U. Staufer, L.E. Fratila-Apachitei, A.A. Zadpoor, 3D Printing of Large Areas of Highly Ordered Submicron Patterns for Modulating Cell Behavior, *ACS Applied Materials & Interfaces*, 12(1), 200-208, 2020.
- [26] M. Nouri-Goushki, A. Sharma, L. Sasso, S. Zhang, B.C. Van der Eerden, U. Staufer, L.E. Fratila-Apachitei, A.A. Zadpoor, Submicron Patterns-on-a-Chip: Fabrication of a Microfluidic Device Incorporating 3D Printed Surface Ornaments, *ACS Biomaterials Science & Engineering*, 5(11), 6127-6136, 2019.
- [27] A. Taubenberger, D.A. Cisneros, J. Friedrichs, P.-H. Puech, D.J. Muller, C.M. Franz, Revealing Early Steps of $\alpha 2\beta 1$ Integrin-mediated Adhesion to Collagen Type I by Using Single-Cell Force Spectroscopy, *Molecular Biology of the Cell*, 18(5), 1634-1644, 2007.
- [28] N. Strohmeyer, M. Bharadwaj, M. Costell, R. Fässler, D.J. Müller, Fibronectin-Bound $\alpha 5\beta 1$ Integrins Sense Load and Signal to Reinforce Adhesion in Less than a Second, *Nature Materials*, 16(12), 1262-1270, 2017.

- [29] R. Changede, X. Xu, F. Margadant, Michael P. Sheetz, Nascent Integrin Adhesions Form on All Matrix Rigidities after Integrin Activation, *Developmental Cell*, 35(5), 614-621, 2015.
- [30] S. Belikov, J. Alexander, C. Wall, I. Yermolenko, S. Magonov, I. Malovichko. Thermal Tune Method for AFM Oscillatory Resonant Imaging in Air and Liquid. in *American Control Conference*, 2014.
- [31] I.N. Sneddon, The Relation Between Load and Penetration in the Axisymmetric Boussinesq Problem for a Punch of Arbitrary Profile, *International Journal of Engineering Science*, 3(1), 47-57, 1965.
- [32] U. Horzum, B. Ozdil, D. Pesen-Okvur, Step-by-step quantitative analysis of focal adhesions, *MethodsX*, 1, 56-59, 2014.
- [33] H. Busscher, A. Van Pelt, P. De Boer, H. De Jong, J. Arends, The Effect of Surface Roughening of Polymers on Measured Contact Angles of Liquids, *Colloids and Surfaces*, 9(4), 319-331, 1984.
- [34] M. Lampin, R. Warocquier-Clérout, C. Legris, M. Degrange, M. Sigot-Luizard, Correlation between Substratum Roughness and Wettability, Cell Adhesion, and Cell Migration, *Journal of Biomedical Materials Research*, 36(1), 99-108, 1997.
- [35] M. Benoit, H.E. Gaub, Measuring Cell Adhesion Forces with the Atomic Force Microscope at the Molecular Level, *Cells Tissues Organs*, 172(3), 174-189, 2002.
- [36] J. Friedrichs, K.R. Legate, R. Schubert, M. Bharadwaj, C. Werner, D.J. Müller, M. Benoit, A Practical Guide to Quantify Cell Adhesion Using Single-Cell Force Spectroscopy, *Methods*, 60(2), 169-178, 2013.
- [37] M. Ferrari, F. Cirisano, M.C. Morán, Mammalian Cell Behavior on Hydrophobic Substrates: Influence of Surface Properties, *Colloids and Interfaces*, 3(2), 48, 2019.
- [38] M.N. Goushki, S.A. Mousavi, M.J. Abdekhodaie, M. Sadeghi, Free Radical Graft Polymerization of 2-Hydroxyethyl Methacrylate and Acrylic Acid on the Polysulfone Membrane Surface Through Circulation of Reaction Media to Improve its Performance and Hemocompatibility Properties, *Journal of Membrane Science*, 564, 762-772, 2018.
- [39] N.C. Gauthier, T.A. Masters, M.P. Sheetz, Mechanical Feedback between Membrane Tension and Dynamics, *Trends in Cell Biology*, 22(10), 527-535, 2012.
- [40] C.W. Kuo, D.-Y. Chueh, P. Chen, Investigation of Size-Dependent Cell Adhesion on Nanostructured Interfaces, *Journal of Nanobiotechnology*, 12(1), 54, 2014.
- [41] R. Zaidel-Bar, M. Cohen, L. Addadi, B. Geiger, Hierarchical Assembly of Cell-Matrix Adhesion Complexes, *Biochemical Society Transactions*, 32(3), 416-420, 2004.
- [42] Y. Zhukova, C. Hiepen, P. Knaus, M. Osterland, S. Prohaska, J.W.C. Dunlop, P. Fratzl, E.V. Skorb, The Role of Titanium Surface Nanostructuring on Preosteoblast Morphology, Adhesion, and Migration, *Advanced Healthcare Materials*, 6(15), 1601244, 2017.
- [43] J. Zhou, X. Zhang, J. Sun, Z. Dang, J. Li, X. Li, T. Chen, The Effects of Surface Topography of Nanostructure Arrays on Cell Adhesion, *Physical Chemistry Chemical Physics*, 20(35), 22946-22951, 2018.
- [44] M.A. Bucaro, Y. Vasquez, B.D. Hatton, J. Aizenberg, Fine-Tuning the Degree of Stem Cell Polarization and Alignment on Ordered Arrays of High-Aspect-Ratio Nanopillars, *ACS Nano*, 6(7), 6222-6230, 2012.

-
- [45] N. Buch-Månson, D.-H. Kang, D. Kim, K.E. Lee, M.-H. Yoon, K.L. Martinez, Mapping Cell Behavior Across a Wide Range of Vertical Silicon Nanocolumn Densities, *Nanoscale*, 9(17), 5517-5527, 2017.
- [46] J. Stricker, Y. Aratyn-Schaus, P.W. Oakes, M.L. Gardel, Spatiotemporal constraints on the force-dependent growth of focal adhesions, *Biophysical Journal*, 100(12), 2883-2893, 2011.
- [47] L. Trichet, J. Le Digabel, R.J. Hawkins, S.R.K. Vedula, M. Gupta, C. Ribault, P. Hersen, R. Voituriez, B. Ladoux, Evidence of a large-scale mechanosensing mechanism for cellular adaptation to substrate stiffness, *Proceedings of the National Academy of Sciences*, 109(18), 6933-6938, 2012.
- [48] C. Roduit, S. Sekatski, G. Dietler, S. Catsicas, F. Lafont, S. Kasas, Stiffness Tomography by Atomic Force Microscopy, *Biophysical Journal*, 97(2), 674-677, 2009.
- [49] L. Angeloni, M. Reggente, D. Passeri, M. Natali, M. Rossi, Identification of Nanoparticles and Nanosystems in Biological Matrices with Scanning Probe Microscopy, *WIREs Nanomedicine and Nanobiotechnology*, 10(6), e1521, 2018.
- [50] M. Maninova, J. Caslavsky, T. Vomastek, The Assembly and Function of Perinuclear Actin Cap in Migrating Cells, *Protoplasma*, 254(3), 1207-1218, 2017.
- [51] M. Fritzsche, D. Li, H. Colin-York, V.T. Chang, E. Moeendarbary, J.H. Felce, E. Sezgin, G. Charras, E. Betzig, C. Eggeling, Self-Organizing Actin Patterns Shape Membrane Architecture but not Cell Mechanics, *Nature Communications*, 8(1), 14347, 2017.
- [52] C.R. Guerrero, P.D. Garcia, R. Garcia, Subsurface Imaging of Cell Organelles by Force Microscopy, *ACS Nano*, 13(8), 9629-9637, 2019.
- [53] L. Haviv, Y. Brill-Karniely, R. Mahaffy, F. Backouche, A. Ben-Shaul, T.D. Pollard, A. Bernheim-Groswasser, Reconstitution of the Transition from Lamellipodium to Filopodium in a Membrane-Free System, *Proceedings of the National Academy of Sciences*, 103(13), 4906, 2006.
- [54] M. Soares e Silva, M. Depken, B. Stuhmann, M. Korsten, F.C. MacKintosh, G.H. Koenderink, Active Multistage Coarsening of Actin Networks Driven by Myosin Motors, *Proceedings of the National Academy of Sciences*, 108(23), 9408, 2011.
- [55] E.A. Cavalcanti-Adam, T. Volberg, A. Micoulet, H. Kessler, B. Geiger, J.P. Spatz, Cell Spreading and Focal Adhesion Dynamics Are Regulated by Spacing of Integrin Ligands, *Biophysical Journal*, 92(8), 2964-2974, 2007.
- [56] K.A. Jansen, D.M. Donato, H.E. Balcioğlu, T. Schmidt, E.H.J. Danen, G.H. Koenderink, A Guide to Mechanobiology: Where Biology and Physics Meet, *Biochimica et Biophysica Acta Molecular Cell Research*, 1853(11, Part B), 3043-3052, 2015.
- [57] A. Lerebours, P. Vigneron, S. Bouvier, A. Rassineux, M. Bigerelle, C. Egles, Additive manufacturing process creates local surface roughness modifications leading to variation in cell adhesion on multifaceted TiAl6V4 samples, *Bioprinting*, 16, e00054, 2019.
- [58] C. Wu, M. Chen, T. Zheng, X. Yang, Effect of Surface Roughness on the Initial Response of MC3T3-E1 Cells Cultured on Polished Titanium Alloy, *Bio-Medical Materials and Engineering*, 26(s1), S155-S164, 2015.
- [59] K. Kulangara, K.W. Leong, Substrate Topography Shapes Cell Function, *Soft Matter*, 5(21), 4072-4076, 2009.
- [60] A. Buxboim, J. Irianto, J. Swift, A. Athirasala, J.-W. Shin, F. Rehfeldt, D.E. Discher, Coordinated Increase of Nuclear Tension and Lamin-A with Matrix Stiffness

- Outcompetes Lamin-B Receptor that Favors Soft Tissue Phenotypes, *Molecular Biology of the Cell*, 28(23), 3333-3348, 2017.
- [61] M. Zhu, H. Ye, J. Fang, C. Zhong, J. Yao, J. Park, X. Lu, F. Ren, Engineering High-Resolution Micropatterns Directly onto Titanium with Optimized Contact Guidance to Promote Osteogenic Differentiation and Bone Regeneration, *ACS Applied Materials & Interfaces*, 11(47), 43888-43901, 2019.
- [62] S. Stewart, A. Darwood, S. Masouros, C. Higgins, A. Ramasamy, Mechanotransduction in Osteogenesis, *Bone & Joint Research*, 9(1), 1-14, 2020.
- [63] B. Ghezzi, P. Lagonegro, N. Fukata, L. Parisi, D. Calestani, C. Galli, G. Salviati, G.M. Macaluso, F. Rossi, Sub-Micropillar Spacing Modulates the Spatial Arrangement of Mouse MC3T3-E1 Osteoblastic Cells, *Nanomaterials*, 9(12), 1701, 2019.
- [64] D. Khang, J. Choi, Y.-M. Im, Y.-J. Kim, J.-H. Jang, S.S. Kang, T.-H. Nam, J. Song, J.-W. Park, Role of Subnano-, Nano- and Submicron-Surface Features on Osteoblast Differentiation of Bone Marrow Mesenchymal Stem Cells, *Biomaterials*, 33(26), 5997-6007, 2012.
- [65] M. Sun, G. Chi, J. Xu, Y. Tan, J. Xu, S. Lv, Z. Xu, Y. Xia, L. Li, Y. Li, Extracellular Matrix Stiffness Controls Osteogenic Differentiation of Mesenchymal Stem Cells Mediated by Integrin $\alpha 5$, *Stem Cell Research & Therapy*, 9(1), 52, 2018.
- [66] H.-S. Lee, J.-I. Kang, W.-J. Chung, D.H. Lee, B.Y. Lee, S.-W. Lee, S.Y. Yoo, Engineered Phage Matrix Stiffness-Modulating Osteogenic Differentiation, *ACS Applied Materials & Interfaces*, 10(5), 4349-4358, 2018.
- [67] K. Anselme, M. Bigerelle, B. Noel, E. Dufresne, D. Judas, A. Iost, P. Hardouin, Qualitative and Quantitative Study of Human Osteoblast Adhesion on Materials with Various Surface Roughnesses, *Journal of Biomedical Materials Research*, 49(2), 155-166, 2000.
- [68] Y. Yang, K. Wang, X. Gu, K.W. Leong, Biophysical Regulation of Cell Behavior—Cross Talk between Substrate Stiffness and Nanotopography, *Engineering*, 3(1), 36-54, 2017.
- [69] M. Ghibaudo, A. Saez, L. Trichet, A. Xayaphoummine, J. Browaeys, P. Silberzan, A. Buguin, B. Ladoux, Traction Forces and Rigidity Sensing Regulate Cell Functions, *Soft Matter*, 4(9), 1836-1843, 2008.
- [70] A.J. Keung, E.M. de Juan-Pardo, D.V. Schaffer, S. Kumar, Rho GTPases Mediate the Mechanosensitive Lineage Commitment of Neural Stem Cells, *Stem Cells*, 29(11), 1886-1897, 2011.

Nanoimprinting for upscaling the osteogenic nanopatterns

Developing high-throughput nanopatterning techniques that also allow for precise control over the dimensions of the fabricated features is essential for the study of cell-nanopattern interactions. Here, we developed a process that fulfills both criteria. Firstly, we used electron-beam lithography (EBL) to fabricate precisely controlled arrays of submicron pillars with varying values of interspacing on a large area of fused silica. Two types of etching procedures with two different systems were developed to etch the fused silica and create the final desired height. We then studied the interactions of preosteoblasts with these pillars. Varying interspacing was observed to significantly affect the morphological characteristics of the cell, the organization of actin fibers, and the formation of focal adhesions. The expression of osteopontin significantly increased on the patterns, indicating the potential of the pillars for inducing osteogenic differentiation. The EBL pillars were thereafter used as master molds in two subsequent processing steps, namely soft lithography and thermal nanoimprint lithography for high-fidelity replication of pillars on the substrates of interest. The method proposed in this chapter, therefore, enables the precise fabrication of submicron- and nanopatterns on a wide variety of materials that are relevant for systematic cell studies.

M. Ganjian, K. Modaresifar, D. Rompolas, L. E. Fratila-Apachitei, A. A. Zadpoor, Nanoimprinting for high-throughput replication of geometrically precise pillars in fused silica to regulate cell behavior, *Acta Biomaterialia*, 2021.

6.1 Introduction

The rapid expansion of cell-based therapies in a variety of pathological circumstances¹⁻³ along with the emergence of recent generations of cell-instructive biomaterials⁴ has underscored the importance of directing the (stem) cell fate. While stem cells demonstrate an extensive capacity for commitment to certain lineages in response to many biochemical and/or biophysical exogenous stimuli^{5,6}, the complications associated with the use of biochemical agents, such as the high cost of growth factors and their potential adverse effects⁷⁻⁹, have motivated researchers to investigate the physical interactions of cells and biomaterials to a deeper extent.

Among such physical stimuli, submicron and nanoscale topographies have been demonstrated to be particularly effective in controlling such cell behaviors as proliferation, migration, and differentiation¹⁰⁻¹². While many studies have been carried out to elucidate the biological effects of surface patterns at the nanoscale (< 100 nm)¹³⁻¹⁶, less is known about the optimum dimensions at the submicron scale (100-1000 nm)^{6,17-19} for inducing specific cell responses.

Despite many efforts dedicated to understanding the effects of surface topography on the various types of cell behavior, many aspects of such interactions remain poorly understood. One of the main reasons underlying this lack of understanding is the large number of design parameters that define the geometry and arrangement of such topographies. Each of those design parameters may influence the cell response in a unique way both in isolation and in combination with other design parameters. Moreover, the intracellular pathways by which the cells sense and respond to their microenvironment are highly complex^{7,13,20}. There is, therefore, a need for extensive systematic studies to understand the effects of different design parameters on the interactions between submicron and nanoscale surface patterns and cell behavior. Such systematic studies are, however, hampered by practical considerations regarding nanofabrication techniques. The currently available techniques for the fabrication of precisely controlled submicron and nanoscale patterns include electron beam-induced deposition (EBID)²¹⁻²³, electron beam lithography (EBL)^{24,25}, two-photon polymerization²⁶, *etc.* All of these techniques suffer from a major limitation, namely low throughput. A low throughput means that it is not feasible to pattern large surface areas. Some other techniques are available for high-throughput patterning of surfaces at the nanoscale and submicron scales, including reactive ion etching^{27,28}, anodizing²⁹, and hydrothermal treatment³⁰⁻³². These high-

throughput techniques, however, offer limited geometrical precision and usually lack the capability to change each design parameter independent of the others. There is, therefore, an urgent need for a high-throughput yet precise nanofabrication technique for the patterning of bio-instructive surfaces at the submicron and nanoscales. Nanoimprint lithography (NIL) is a facile fabrication technique that offers a number of unique advantages, including high throughput and scalability^{33, 34}, the ability to pattern a large variety of geometrical features and materials with ultrahigh resolutions³⁵, simplicity, and low cost³⁶. Given these favorable properties, NIL is widely used for the fabrication of biosensors^{37, 38}, photovoltaics^{39, 40}, bactericidal^{7, 41} and osteogenic nanopatterns^{13, 19, 42, 43}, and flexible electronics⁴⁴⁻⁴⁶.

Here, we use a combination of EBL and NIL for high-throughput patterning of bio-instructive surfaces with geometrically precise submicron pillars. Variations in the interspacing of submicron pillars fabricated by two-photon polymerization have been recently shown to induce osteogenic differentiation in preosteoblasts⁶. The settling state of the cells on the pillars and traction forces applied to the pillars resulting in their tips being displaced were hypothesized to determine the long-term osteogenic response of the cells. Nevertheless, the relatively low stiffness of the pillars could be a reason why they were bent underneath the cells, thus, it is still an unanswered question whether the same pillar geometry and dimensions would induce the same biological response if there is no tip displacement and bending. Moreover, these pillars were fabricated on a very small area (1 mm²) which limits practicing certain biological assays. Here, to show the potential of the fabrication process developed in this study, we used EBL to pattern a large area (3 × 5 mm²) of fused silica substrates (significantly stiffer than the polymeric resin used in two-photon polymerization) with submicron pillars whose dimensions were similar to those of the above-mentioned study. The EBL parameters, including resist type, resist thickness, exposure parameters (*e.g.*, beam current, spot size, and electron dosage), and mask thickness, were optimized to generate submicron pillars with the highly precise dimensions in as short of a processing time as possible. We then, for the first time, cultured preosteoblasts on a fused silica substrate containing submicron pillars that were made of the same material to study the interaction of the preosteoblasts with the submicron features of fused silica and verify that the effects of the submicron pillars on those cells are independent of the chemical properties and stiffness of the material. Moreover, we created hybrid polydimethylsiloxane (PDMS) molds (replica of the master

mold) that enabled us to replicate the patterns multiple times, thereby substantially decreasing the costs and time associated with the proposed nanofabrication process and making it possible to economically produce a large enough number of specimens. Fused silica was chosen as the final substrate and by finding the appropriate hard mask, thermoplastic resist, etching gases, and nanoimprint parameters, the desired submicron patterns were successfully replicated from the hybrid PDMS replica mold into the fused silica substrate. The high transparency and mechanical properties of fused silica make it a proper candidate for both UV and thermal NIL. Although there are some studies on transferring the nano/submicron features into the different types of polymers using the NIL technique, to the best of our knowledge, there is no study on transferring them into fused silica which has more relevant properties for the intended research and clinical applications.

6.2 Materials and Methods

6.2.1 Master mold fabrication by EBL

The process steps involved in the fabrication of the master mold are illustrated in Figure 6.1a. Double side polished 4-inch (diameter = 10.16 cm) fused silica wafers (thickness = $525 \pm 25 \mu\text{m}$) (University Wafers Inc., US) were cleaned in the Piranha solution (a mixture of 3:1 (v/v) H_2SO_4 (Honeywell, Romania) and H_2O_2 (VWR international, The Netherlands)) at room temperature for 12 minutes, were rinsed with deionized (DI) water, and were dried with a nitrogen gun. The wafer was then covered with a thin layer of photoresist to protect its surface from damage. Subsequently, the wafer was diced into $1 \times 1 \text{ cm}^2$ specimens using a dicing saw (DAD3220, Disco Hi-Tec Europe GmbH, Germany). After dicing, the photoresist layer was removed by placing the pieces into acetone (Sigma-Aldrich, The Netherlands) combined with ultrasonication for 20 minutes. The cleaning process was followed by immersing the specimens in isopropanol (IPA, Sigma-Aldrich, The Netherlands) and DI water, respectively, and drying them with a nitrogen gun.

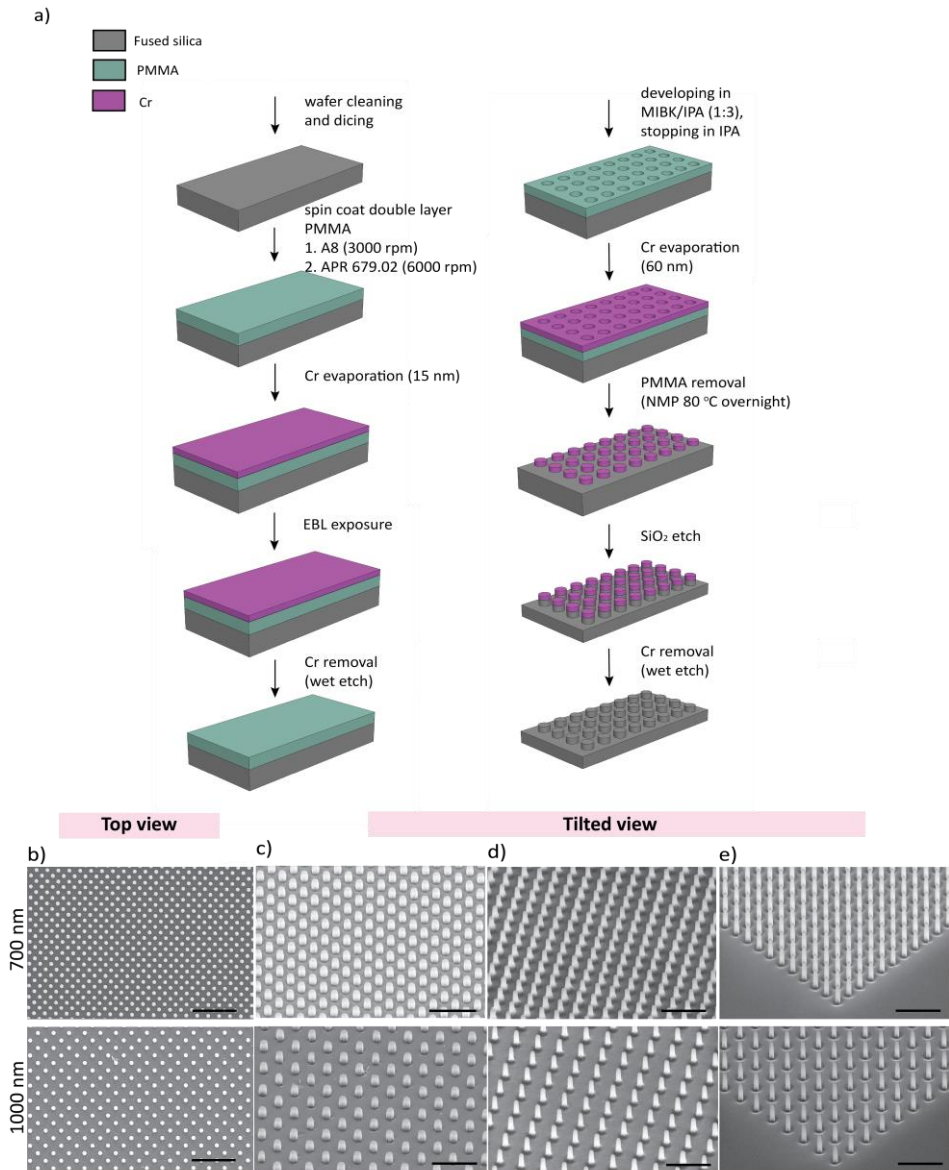


Figure 6.1. a) A schematic drawing of the procedure of fabricating submicron pillars on the fused silica master mold using electron beam lithography. b) Top- and c-e) tilted-view SEM images of the submicron pillars with the interspacing values of 700 and 1000 nm formed on the fused silica substrate. Scale bar = 2 μ m. c) Submicron pillars after 255 seconds of etching using ICP RIE. d) Submicron pillars after 8 minutes of etching using ICP RIE. e) Submicron pillars after 90 minutes of etching using ICP RIE.

Polymethyl methacrylate (PMMA) resist (495, A8) (495 K molecular weight, 8 wt% in anisole, Microchem Corp, US) was spun coat on the fused silica substrate at 3000 rpm and was baked at 185 °C on a hotplate for 20 minutes. Once it cooled down, PMMA AR-P 679.02 (950 K, Allresist GmbH, Germany) was spun coat on the specimens at 6000 rpm. The specimens were then baked at 185 °C for 10 minutes. A multilayer resist was used to make the lift-off process easier. The resist thickness was measured using a Dektak profilometer (Bruker, Germany). Then, 15 nm of chromium (Cr) with a rate of 0.5 °A/sec was evaporated on the specimens using an e-beam evaporator (Temescal FC-2000, Ferrotec, Germany) to make them conductive before e-beam exposure. The PMMA resist was directly patterned using EBL (Raith EBPG 5200) operated at an acceleration voltage of 100 kV and a beam current of 364 pA. The designed file included circular features with a diameter of 250 nm and two different values of interspacing, namely 700 and 1000 nm.

As the optimized electron dosage had to be determined for each dimension, a broad range dose test was performed from 500 $\mu\text{C}/\text{cm}^2$ to 2000 $\mu\text{C}/\text{cm}^2$. After exposure, the Cr layer was removed by immersing the specimens in a Cr etchant (Chromium Etchant N1, MicroChemicals, Germany) for 20 seconds. The specimens were then rinsed in DI water for 5 minutes and were dried with a nitrogen gun. The PMMA resist was developed using a methyl isobutyl ketone (MIBK, Sigma-Aldrich, The Netherlands)/IPA 1:3 solution for 75 seconds, rinsing in IPA for 30 seconds, and drying with a nitrogen gun. To remove the resist residues from the holes, the specimens were exposed to an oxygen plasma (PVA Tepla M4L Gas Plasma System, US) with an oxygen gas flow rate of 200 sccm and a power of 100 W for 20 seconds. After the plasma treatment, 60 nm Cr was deposited on the specimens as a mask using an e-beam evaporator (evaporation rate = 0.5 °A/sec, chamber pressure = 1.5×10^{-6} mbar). A lift-off process was performed to remove the resist from the area around the features. To do so, N-Methyl-2-pyrrolidone (NMP, Sigma-Aldrich, The Netherlands) was heated up to 80 °C and was used for soaking the specimens for 2 hours. To transfer the patterns into the substrate and create the submicron pillars, two different etching methods of the fused silica were investigated: ICP RIE (Adixen AMS 100 I-speeder, Alcatel, France) or RIE (Sentech Etchlab 200, Sentech Instruments, Germany). In the case of ICP RIE, a gas mixture of $\text{C}_4\text{F}_8/\text{CH}_4/\text{He}$ (flow rates: 15/15/150 sccm) was used for different durations to reach the desired height. The other etching parameters were as follows: a source power of 2500 W, a bias voltage of 23 V, and a temperature of 0 °C. In the case of RIE, a gas mixture of CHF_3/O_2 (flow rates: 68/5 sccm) with an RF power of 102 W, a bias voltage of 340 V, and a chamber pressure of 15 μbar were used. As the

submicron pillars were formed on the fused silica substrate, the Cr mask was removed by immersing the specimens into the Cr etchant for 20 seconds. This process was followed by rinsing the specimens with DI water for 5 minutes. The final step before scanning electron microscopy (SEM) inspection was cleaning the specimens with the Piranha solution for 12 minutes to remove the organic and polymeric contaminants which had been formed on the substrate during the etching process, followed by rinsing with DI water for 5 minutes and drying with a nitrogen gun.

Top and tilted SEM images of the resultant master mold were taken using a Helios Nano Lab 650 (FEI, US) SEM, with an acceleration voltage of 10 kV and a beam current of 50 pA. The diameter and height of the submicron pillars were measured from the tilted SEM images, while the interspacing values were measured from the top view SEM images.

6.2.2 Interactions of MC3T3-E1 preosteoblast cells with the patterned surfaces

All the fused silica specimens were sterilized prior to cell seeding by immersing them in 70% ethanol and exposing them to UV light for 20 minutes. The specimens were rinsed twice with 10X phosphate-buffered saline (PBS, Sigma-Aldrich, Germany), were submerged in a solution of 50 $\mu\text{g}/\text{ml}$ bovine fibronectin (Sigma-Aldrich, US), and were incubated at 37 °C and 5% CO₂ for 30 minutes to improve the cell adhesion⁴⁷. MC3T3-E1 preosteoblast cells (Sigma-Aldrich, Germany) cultured in the alpha minimum essential medium (α -MEM) supplemented with 10% (v/v) fetal bovine serum and 1% (v/v) penicillin-streptomycin (all from Thermo Fisher Scientific, US) were seeded on the specimens (1×10^4 cells per sample) in a 24 well-plate (Greiner, Bio-One, The Netherlands) and were incubated at 37 °C and 5% CO₂.

After 1 day of culture, the samples ($n = 3$) were washed twice with 10X PBS and the cells were fixed using a 4% (v/v) formaldehyde solution (Sigma-Aldrich, Germany). Following the cell membrane permeabilization using 0.5% Triton X-100/PBS (Sigma-Aldrich, US) at 4 °C for 5 minutes, the samples were incubated in 1% BSA/PBS (Sigma-Aldrich, Germany) at 37 °C for 5 minutes. The specimens were then incubated in anti-vinculin mouse monoclonal primary antibody (1:100 in 1% BSA/PBS, Sigma-Aldrich, Germany) and rhodamine-conjugated phalloidin (1:1000 in 1% BSA/PBS, Thermo Fisher Scientific, US) for 1 hour at 37 °C. The cells were then washed three times with 0.5% Tween-20/PBS (Sigma-Aldrich, US) and were incubated in Alexa Fluor 488 (*i.e.*, donkey

anti-mouse polyclonal secondary antibody, 1:200 in 1% BSA/PBS, Thermo Fisher Scientific, US) for 1 hour at room temperature. After washing with 0.5% Tween-20/PBS and 1X PBS, the samples were mounted on microscopic glass slides using 10 μ l of the Prolong gold antifade reagent containing DAPI (4',6-diamidino-2-phenylindole) (Thermo Fisher Scientific, US). Finally, the specimens were imaged using a fluorescence microscope (ZOE fluorescent cell imager, Bio-Rad, The Netherlands). For the SEM observations, the stained samples ($n = 3$) were washed twice with distilled water for 5 minutes and were then dehydrated in 50%, 70%, and 96% ethanol solutions for 15, 20, and 20 minutes, respectively. After air-drying overnight at room temperature, the samples were gold-sputtered before SEM imaging.

To evaluate the osteogenic properties of the patterned surfaces, the cells were stained for osteopontin (OPN) after 21 days of culture in an osteogenic medium (the above-mentioned α -MEM medium supplemented with 50 μ g/ml ascorbic acid and 4 mM β -glycerophosphate, both from Sigma-Aldrich, Germany). Following the fixation and permeabilization of cells, they were incubated with OPN antibody conjugated to Alexa fluor 488 (1:100 in BSA/PBS, Santa Cruz Biotechnology, US) for 1 hour at 37 °C ($n = 3$). The same assay was also performed under the non-osteogenic culture condition.

ImageJ 1.53c (NIH, US) was used to quantify the morphological characteristics of the cells as well as the area of focal adhesions (FAs) and OPN according to methods described before^{48,49}.

6.2.3 Contact angle measurements

A drop shape analyzer (DSA100, Krüss, Germany) was used to evaluate the wettability of the surfaces used for cell culture (*i.e.*, the flat and patterned surfaces, $n = 3$). A droplet of DI water with a volume of 3 μ l was placed on the surface. The images were recorded after 5 seconds.

6.2.4 Fabrication of the hybrid PDMS replica molds

A schematic drawing illustrating the process steps of soft lithography is presented in Figure 6.2a. Prior to performing hybrid PDMS molding, the fused silica master mold was first placed, for 30 minutes, in a vacuum desiccator close enough to a glass petri dish containing a droplet of octyltrichlorosilane (OTS, Gelest Inc., Germany) to coat the surface of the master mold with a hydrophobic layer, thereby preventing the cured hybrid PDMS layer from sticking to the master mold. The hybrid PDMS mold consisted of two

layers: a thin layer of hard-PDMS (hPDMS) (a 30-40 μm stiff layer), that was in direct contact with the patterns during the molding process, and a PDMS (a 3-5 mm flexible layer) that formed the bulk of the replica mold. The hPDMS was made by mixing 0.85 g of 7-8% (vinylmethylsiloxane)-dimethylsiloxane copolymer (trimethylsiloxy terminated) (Gelest Inc., Germany), 2 μl of 2,4,6,8-Tetramethyl-2,4,6,8-tetravinylcyclotetrasiloxane (Sigma-Aldrich, Germany), and 3 μl of platinum-divinyltetramethyldisiloxane complex in xylene (Gelest Inc., Germany) for 5 minutes. This combination was left in a vacuum desiccator for 30 minutes to remove the air bubbles present in the mixture. After this step, 0.25 g of 25-35% (methylhydrosiloxane)-dimethylsiloxane (PDMS copolymer, 25-35 cSt, Gelest Inc., Germany) was added to the previous mixture, was mixed for 3 minutes, was poured, and was spun coat on the fused silica master mold for 40 seconds using a spinning rate of 1000 rpm, followed by curing in an oven at 60 $^{\circ}\text{C}$ for 20 minutes. PDMS (Sylgard 184, Dow Inc., US) combined with the curing agent at a weight ratio of 10:1 was mixed thoroughly, cast on the master mold, and desiccated in vacuum for 30 minutes to remove the air bubbles. The fused silica master mold (with the hybrid PDMS on top) was then cured in an oven at 40 $^{\circ}\text{C}$ for 16 hours. After curing, the hybrid PDMS was carefully peeled off from the substrate. The master and the replica molds were finally sterilized by IPA. We verified that the same master mold could be used at least 5 times to apply the patterns into PDMS without a significant loss of fidelity.

The quality of the patterns replicated into the hybrid PDMS was evaluated using SEM. Prior to SEM imaging, the PDMS substrates were gold-sputtered.

6.2.5 Cross-sectional characterization using FIB milling

In order to measure the depth of the replicated patterns (submicron pits) on the hybrid PDMS mold, focused ion beam scanning electron microscopy (FIB-SEM) was performed in a FIB microscope (Helios G4 CX dual beam workstation, FEI, US). The specimens were tilted to 52 $^{\circ}$ and the surface was milled using Gallium ions with a 7 pA ion beam (acceleration voltage = 30 kV).

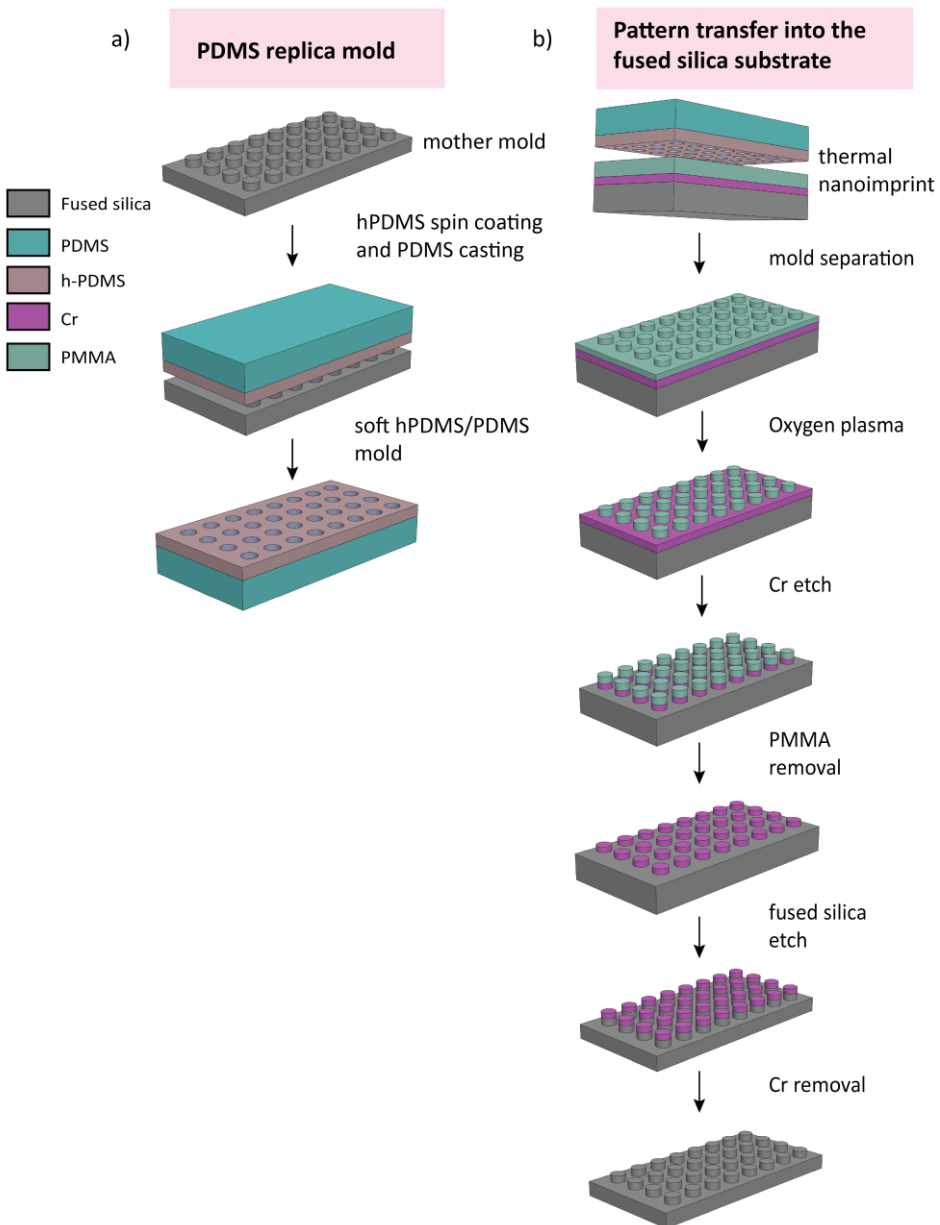


Figure 6.2. A schematic drawing of a) the steps involved in the preparation of the hPDMS/PDMS daughter molds and b) the thermal nanoimprint process used to transfer the submicron pits from the hPDMS/PDMS mold to the fused silica substrate.

6.2.6 Pattern transfer from the hybrid PDMS replica mold to the substrate of interest by thermal nanoimprint

The details of the process steps involved in NIL are presented in Figure 6.2b. Firstly, Cr (30 nm) was evaporated on the $1 \times 1 \text{ cm}^2$ fused silica specimens. PMMA (950 A3) (950 K molecular weight, 3 wt% in anisole, Microchem Corp., US) was then spun coat on the specimens at 4250 rpm, and baked on a hotplate at 185 °C for 20 minutes. The nanoimprinting was carried out using a commercial thermal nanoimprinting EVG bonder (EVG 520, EVgroup, Austria). The hybrid PDMS replica mold containing submicron pits and the fused silica specimens were brought into contact with each other (hybrid PDMS on top and fused silica at the bottom). The temperature was then increased to above the glass transition temperature (T_g) of PMMA (140 °C) (T_g of PMMA = 105 °C). The hybrid PDMS mold was then pressed into the PMMA layer with a set force of 1250 N for 3 minutes at the embossing temperature. After imprinting, the chamber was cooled down below T_g (80 °C in this study) with a rate of 2 °C/min. The slow cooling rate was chosen to reduce the thermal stress caused by cooling in the material. To prevent the polymeric microstructures from flattening and rounding of the edges, the embossing force was maintained during the cooling down process. The force was released one minute after reaching 80 °C (de-embossing temperature). The cooling down process was continued to reach 40 °C, and then the hybrid PDMS mold and the fused silica specimen were separated gently and taken out from the chamber afterward.

To transfer the submicron pillars formed on the PMMA into the fused silica substrate underneath, we first used oxygen plasma to remove the residues of the PMMA that rest in between the pillars (Figure 6.2b) in a process called descum. The descum process was performed using 20 sccm O_2 plasma, with a power of 20 W, and at a chamber pressure of 40 μbar in a plasma etcher (RIE Etchlab 200, Sentech Instruments, Germany) for 2 minutes.

To have access to the surface of the fused silica specimens, the Cr layer was etched using a Chlorine-based ICP RIE machine (PlasmaLab System 100, Oxford Instruments, UK) while employing PMMA as the mask. The etching process was conducted under the following conditions: RF power = 50 W, Cl_2 = 50 sccm, O_2 = 5 sccm, temperature = 40 °C, chamber pressure = 12.5 μbar , and etching time = 90 seconds. Once the patterns were transferred into the Cr layer, the PMMA mask could be removed. To do so, the specimens were soaked in NMP at 80 °C overnight. This step was followed by transferring the

submicron pillars into the fused silica substrate, by using the Cr layer as the mask during the etching step. The fused silica was etched using ICP RIE (Adixen AMS100 I-speeder, Alcatel, France), by $C_4F_8/CH_4/He$ (flow rates: 15/15/150 sccm) as the etching gases for 4 minutes and 15 seconds, and with a source power of 2500 W, an RF power of 250 W, a bias voltage of 23 V, and at 0 °C. The Cr mask was then etched away using the Cr etchant and the specimens were dried using a nitrogen gun and were gold-sputtered before SEM imaging.

6.2.7 Statistical analysis

To statistically analyze the results of cell culture experiments, the raw data were first tested for normal distribution using the D'Agostino-Pearson omnibus normality test in Prism version 9.1.2 (GraphPad, US). For normally distributed datasets, the Brown-Forsythe and Welch ANOVA test was performed, followed by Dunnett's T3 multiple comparisons test to determine the statistical significance of the differences between the means of the different experimental groups. For the datasets which did not pass the normality test, the nonparametric Kruskal-Wallis test was performed, followed by Dunn's multiple comparisons test. All data are presented as mean \pm standard deviation and a *p*-value below 0.05 was considered to indicate statistical significance.

6.3 Results

6.3.1 Fabrication and characterization of the master mold

In the case of ICP RIE and after 255 seconds of etching, the submicron pillars with an interspacing of 700 nm had a height of 508 ± 24 nm and a diameter of 269 ± 19 nm while the submicron pillars with an interspacing of 1000 nm had a height of 523 ± 25 nm and a diameter of 275 ± 22 nm (Figure 6.1c). After 8 minutes of ICP RIE etching, the submicron pillars with an interspacing of 700 nm had a height of 990 ± 37 nm and a diameter of 245 ± 22 nm while the submicron pillars with an interspacing of 1000 nm had a height of 1046 ± 31 nm and a diameter of 255 ± 31 nm (Figure 6.1d). In the case of RIE, after 90 minutes of etching, a height of 973 ± 43 nm and a diameter of 206 ± 14 nm was reached for the submicron pillars with an interspacing of 700 nm while the submicron pillars with an interspacing of 1000 nm had a height of 1068 ± 41 nm and a diameter of 222 ± 13 nm (Figure 6.1e).

6.3.2 Adaptation of preosteoblasts to the patterned surfaces

MC3T3-E1 preosteoblast cells presented different morphologies on the flat and patterned surfaces (the ones etched using ICP RIE for 8 minutes) after 1 day of culture (Figures 6.3a-c and S6.1). While the majority of the cells had a polygonal shape on the flat surfaces, more cells with a stellate or polarized shape ⁶ could be recognized on the patterned surfaces (Figure 6.3a). The actin fibers in most of the cells residing on the flat areas were oriented toward the vertices of the polygonal shape of the cell body (Figure 6.3b). Interestingly, actin fibers were collectively organized more homogeneously along the whole cell body in the polarized cells residing on the submicron pillars with an interspacing of 700 nm. Nevertheless, the cytoskeleton was less organized in the cells cultured on the submicron pillars with an interspacing of 1000 nm as compared to the last two surfaces. Further SEM observations revealed different settling states for the cells residing on submicron pillars with different values of interspacing. A “top state” was identified for the cells residing on the submicron pillars with an interspacing of 700 nm, meaning that the cell body was on top of the pillars (Figures 6.3c,d and S6.2). The cells on the submicron pillars with an interspacing of 1000 nm, however, presented a “mixed state” in which the areas of the cell closer to the cell nucleus seemed to be in a “top state” while farther from these regions (*i.e.*, at the cell periphery), showed a “bottom state”. At these regions, the cell was not only in contact with both the tip and lateral sides of the pillars but also with the substrate.

The cell area decreased as the interspacing of the submicron pillars increased (Figure 6.4a). An opposite trend was observed for the cell aspect ratio (*i.e.*, more polarization for the larger interspacing value). However, the cell shape index (*i.e.*, the roundness of the cells) was not significantly different between the flat and patterned surfaces. Despite the differences in the cell nucleus area and shape index between the flat controls and the patterned surfaces with an interspacing of 700 nm, a discernible trend was not observed regarding the effects of interspacing on the morphological characteristics of the nucleus (Figure 6.4b).

The average FA area was found to be significantly affected by the surface topography. The cells residing on the submicron pillars with an interspacing of 700 nm formed significantly smaller FAs as compared to the flat controls and patterned surfaces with an interspacing of 1000 nm (Figure 6.4c). Finally, the expression of OPN in the matrix was significantly upregulated on the patterned surfaces (Figures 6.3c and 6.4d).

The pillars with an interspacing of 1000 nm were found to have a significantly higher potential for promoting OPN expression as compared to the pillars with an interspacing of 700 nm. However, the patterned surfaces did not enhance OPN expression as compared to the flat controls under the non-osteogenic culture condition (Figure S6.1).

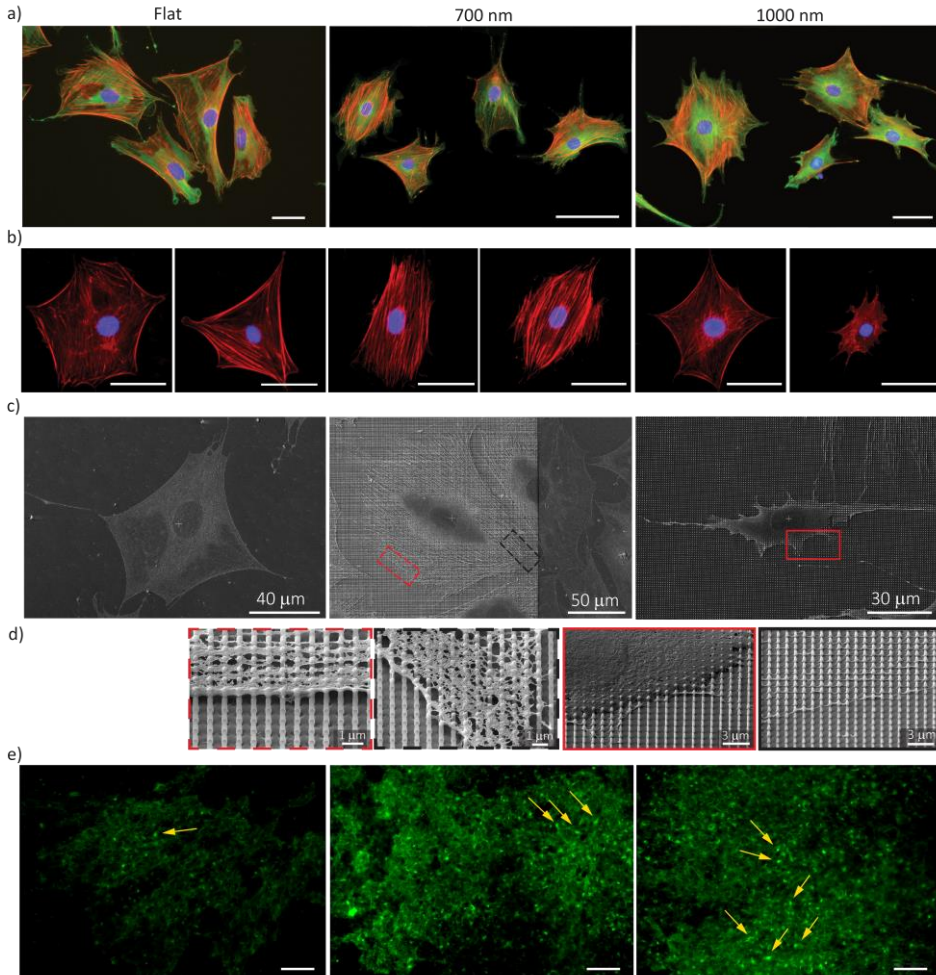


Figure 6.3. a) Immunofluorescence staining of vinculin (green), actin (red), and nucleus (blue) of MC3T3-E1 preosteoblast cells cultured on the flat and patterned specimens for 1 day. Scale bar = 100 μm . b) Representative images of the cytoskeletal organization of the cells residing on the flat and patterned specimens (red: actin and blue: nucleus). Scale bar = 20 μm . c) Top-view SEM images of the representative cell morphology on the flat and patterned specimens. d) Highly magnified tilted-view SEM images of the settlement state of the cells on the patterned specimens and their interactions with the single pillars at cell periphery. e) The expression of OPN visualized using immunostaining after 21 days. Scale bar = 100 μm .

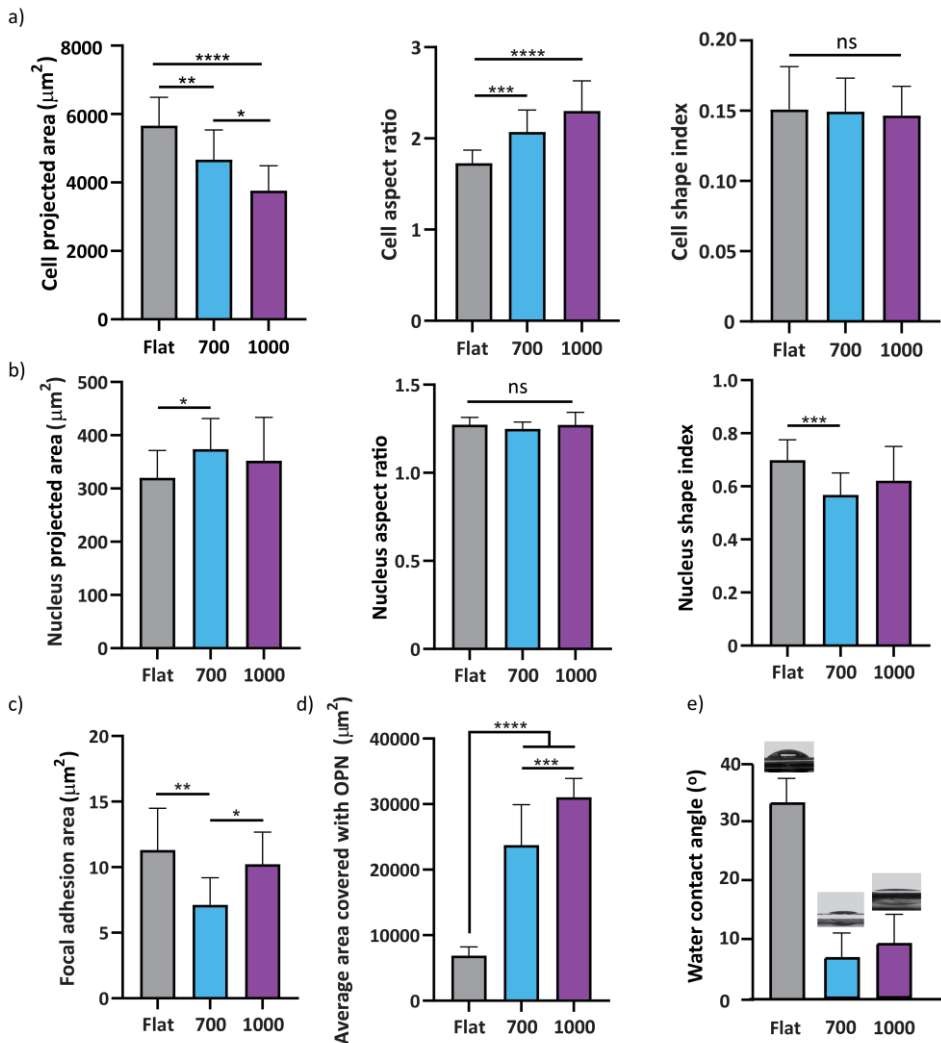


Figure 6.4. a) The morphological characteristics of preosteoblasts (*i.e.*, cell area, aspect ratio, and shape index) cultured on the flat and patterned specimens after 1 day. b) The morphological characteristics of the cell nucleus (*i.e.*, nucleus area, aspect ratio, and shape index) cultured on the flat and patterned specimens after 1 day. At least 250 cells were analyzed for each geometrical parameter. c) The average FA area of the cells residing on the flat and patterned specimens. At least 10 cells were analyzed per study group. d) The average area covered with OPN after 21 days. At least 8 images were taken from each sample of each study group for quantification of OPN area. e) Water contact angle on the flat and patterned specimens. (Brown-Forsythe and Welch ANOVA followed by Dunnett's T3 test for a, c, d, and e, Kruskal-Wallis test followed by Dunn's test for b excluding nucleus aspect ratio which follows the former test, * $p < 0.05$, ** $p < 0.01$, *** $p < 0.001$, and **** $p < 0.0001$).

6.3.3 Water contact angle

While the contact angle for the flat fused silica was $34.0 \pm 3.3^\circ$ ($n = 3$), it was significantly decreased to $7.0 \pm 4.3^\circ$ ($n = 3$) on the patterned fused silica specimens with an interspacing of 700 nm and to $9.0 \pm 6.3^\circ$ ($n = 3$) on the patterned fused silica specimens with an interspacing of 1000 nm, indicating the superhydrophilicity of the patterned surfaces (Figure 6.4e).

6.3.4 Fabrication and characterization of the replica mold

The hybrid PDMS mold, containing two sets of submicron pit arrays, was successfully replicated from the fused silica master mold with the shorter submicron pillars (the one illustrated in Figure 6.1c and Table 6.1).

Table 6.1. Characteristics of the submicron patterns produced/replicated after the application of every fabrication technique.

Mold	Pattern type	Design interspacing = 700 nm				Design interspacing = 1000 nm			
		Diameter (nm)	Interspacing (nm)	Height (nm)	Aspect ratio	Diameter (nm)	Interspacing (nm)	Height (nm)	Aspect ratio
Master mold (fused silica) before molding	Submicron pillars	269 ± 19	712 ± 13	509 ± 25	1.9 ± 0.2	275 ± 22	1013 ± 21	523 ± 25	1.9 ± 0.2
Replica mold (hybrid PDMS)	Submicron pits	293 ± 20	685 ± 24	---	---	245 ± 28	980 ± 33	---	---
Master mold (fused silica) after molding	Submicron pillars	275 ± 19	702 ± 14	516 ± 20	1.9 ± 0.2	291 ± 16	1003 ± 15	517 ± 25	1.7 ± 0.1
Final patterns (fused silica)	Submicron pillars	235 ± 19	720 ± 12	501 ± 27	2.1 ± 0.2	221 ± 13	1022 ± 18	492 ± 30	2.2 ± 0.2

The patterns replicated into the PDMS were geometrically similar to the original patterns (Figure 6.5a). SEM images indicated no irregularity, clogging, or any other artifacts or signs of incomplete replication of the submicron pits or any damaging of the imprinted substrate (Figure 6.5a,b). The average diameter and interspacing of the replicated submicron pits, measured on SEM images, confirm the precision of the imprinted patterns (Table 6.1). To quantify the submicron pits, FIB milling of the submicron pits was performed. The depths measured were 428 ± 55 nm and 402 ± 25 nm for the submicron pits with the interspacing values of 700 nm and 1000 nm, respectively (Figure 6.5c).

The SEM images of the fused silica master mold, after gently peeling off the hybrid PDMS from it, revealed that the morphology of the submicron pillars had not changed and that there were no significant differences between the dimension of the submicron pillars before and after PDMS molding (Figure 6.5d and Table 6.1). Furthermore, only negligible amounts of PDMS residues remained in between the submicron pillars, confirming that the fused silica master mold can be used for several rounds of molding without being damaged.

6.3.5 Characterization of the patterns transferred into the fused silica substrate through thermal nanoimprinting

After 255 seconds of etching of fused silica using Cr mask, the heights of the transferred submicron pillars with the interspacing values of 700 and 1000 nm, were respectively 501 ± 27 nm and 492 ± 30 nm (Table 6.1 and Figure 6.5e).

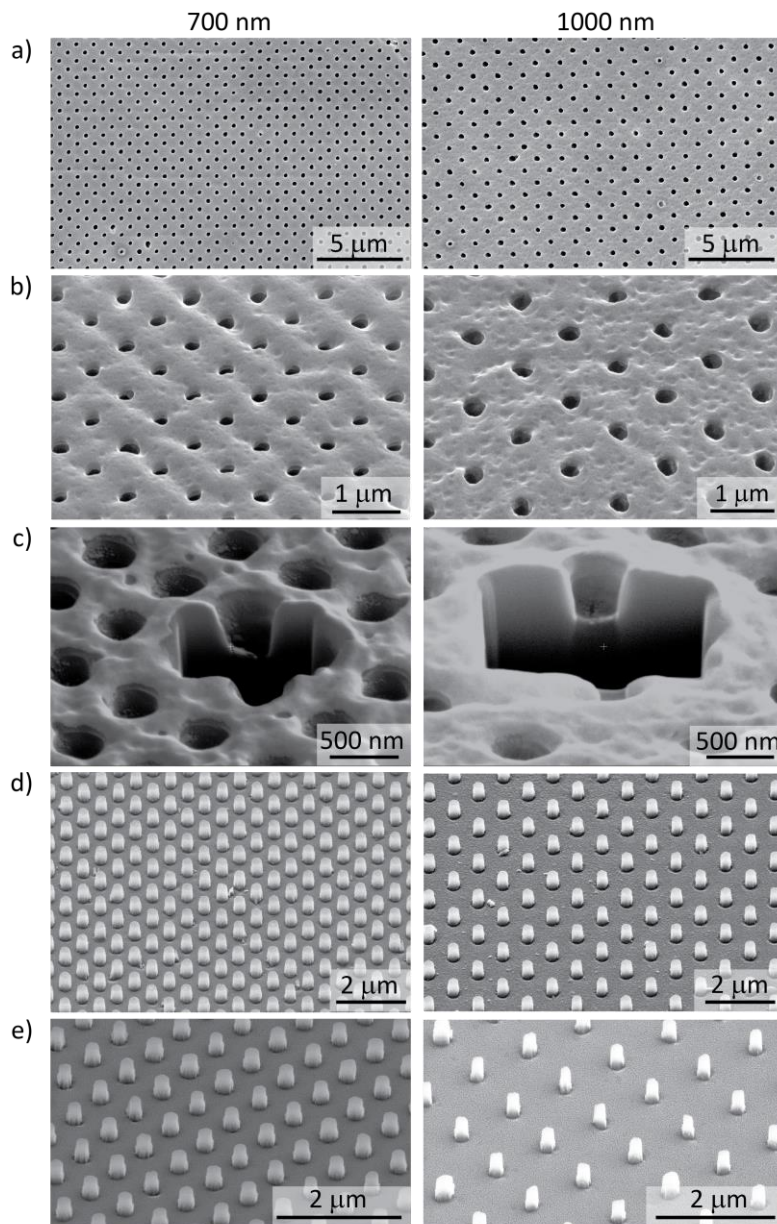


Figure 6.5. a) Top- and b) tilted-view SEM images of the replica patterns (*i.e.*, submicron pits) that were successfully transferred into the hybrid PDMS mold. c) SEM images of the hybrid PDMS replica mold after FIB milling, showing the depth of the submicron pits. d) SEM images of submicron pillars present on the master mold after peeling off the PDMS that confirm the patterns were nicely transferred into the PDMS without damaging or destroying the master mold e) SEM images of the successfully transferred submicron pillars into the fused silica substrate.

6.4 Discussion

The design and fabrication of bioinspired and/or rationally designed nanoscale and submicron patterns on the surface of biomaterials could enhance their functionality by eliciting certain cell responses and guiding cells toward the desired lineages. The development of high-throughput and highly precise fabrication processes that make it feasible to fabricate large areas of patterned surfaces on a variety of substrates regardless of their composition and geometry (*i.e.*, flat or curved) is of importance. The main challenge here lies in simultaneously achieving high geometrical precision and high throughput. There has hardly been any nanofabrication technique that can satisfy both requirements. For instance, such techniques as ICP RIE and hydrothermal treatment enable the rapid production of nano/submicron patterns over a large area but are limited in their geometrical precision when compared with low-throughput techniques, such as EBID, EBL, or FIB, while also not being able to adjust every single design parameter independently of the others^{21, 22}. The main contribution of this study, therefore, is the development of a rapid and accurate fabrication process to overcome the above-mentioned challenges. Nanoimprint lithography offers geometrical precision and high resolutions on the one hand and high throughput on the other. Moreover, it provides the opportunity to transfer the patterns into the flat and curved substrates as well⁵⁰⁻⁵². The availability of such techniques is expected to enable more extensive studies of the interactions between cells and nanopatterns, thereby broadening our knowledge of how cells interact with surface topography and how topographical cues can be exploited to promote tissue regeneration. While other materials, such as titanium alloys, may be more suitable as bone substitutes, we used fused silica in the current study to benefit from its high transparency that makes it an ideal material for both thermal and UV nanoimprint lithography, as well as for imaging purposes during cell studies.

6.4.1 Interactions of MC3T3-E1 cells with patterns

The early-stage adaptation of the cells to the surface and their interactions with the topographical cues of the surface largely determine the long-term response of cells, including their osteogenic differentiation^{6, 48}. It has been shown that cell shape and area affect the cytoskeletal organization, as well as the formation and distribution of FAs, which together modulate the stem cell fate⁵³⁻⁵⁵. Cell shape can also regulate the phenotype independently of tension-based mechanisms⁵⁶. Moreover, in the case of high aspect ratio

pillars, direct nuclear mechanotransduction pathways could determine the cell fate⁵⁷. In our study, the submicron pillars significantly affected the morphological characteristics of the cells in terms of area and aspect ratio. In agreement with a number of reports available in the literature, the presence of the pillars on the biomaterial surface decreased the cell spreading area^{48, 58, 59}. The spreading area decreased further as the pillar interspacing increased^{48, 58, 59}. It seems that as the pillars become more separated, the cells tend to confine their area to secure their initial adhesion points as well as an optimized membrane trafficking^{58, 60}. The differences in the cytoskeletal organization and FA area between the 700 and 1000 nm submicron pillars could be interpreted within this context. The cells residing on the 1000 nm submicron pillars likely undergo a slower adaptation as their actin fibers are not yet well-oriented (as compared to the cells residing on the 700 nm submicron pillars). On the other hand, a larger FA area on the 1000 nm submicron pillars may be indicative of the fact that the cells are still attempting to form stronger adhesions to the surface.

The increased cell aspect ratio (*i.e.*, elongation) is believed to be beneficial for osteogenic differentiation^{18, 61}. The increase in the cell aspect ratio has been shown to increase the anisotropy of FAs^{53, 62}. Similarly, we observed that the FAs are preferentially formed at the periphery of smaller and more elongated cells, especially on the 1000 nm submicron pillars. The increased expression of OPN on the 1000 nm pillars suggests that the elongation of the cells and the differential distribution of FAs at the early stages of adaptation to the surface may favorably promote osteogenic differentiation.

Different settling states in the cells residing on the submicron pillars with different interspacing values could be another factor and/or indicator of the varied cytoskeletal organization. The “top state” observed on the submicron pillars with an interspacing of 700 nm ensures that the cells maintain a global convex geometry (from the cell periphery toward the nucleus), which is shown to be associated with higher forces exerted on the nucleus and eventually lead to higher levels of osteogenic differentiation⁶³. The “mixed state” observed on the submicron pillars with an interspacing of 1000 nm, on the other hand, imposes a different geometry on the cells at some regions as there is a significant difference in the height between the nuclear area (the thickest part of the cell body) and the cell periphery (deeply sunk into the submicron pillars). This might hinder or delay the global cytoskeletal organization. In a previous study involving pillars with the same dimensions made of a commercial polymer, the pillars with an interspacing of 700 nm,

which induced a “top state” to the cells, showed the highest expression of OPN⁶. Since the pillars in that study were bent underneath the cells, the traction forces were, therefore, assumed to have been transferred all the way to the nucleus via a direct mechanotransduction pathway, affecting the long-term osteogenic response of the cells. In the present study, however, the pillars were stiff enough to not be bent. There may, therefore, be some differences in the cell traction forces observed in these two studies.

In the current study, the pillars inducing the “mixed state” maximized the expression of OPN. It could, therefore, be postulated that engulfing the high aspect ratio pillars by cells in a “mixed state” of the settlement could also trigger direct or indirect mechanotransduction pathways that eventually increase the expression of osteogenic markers, such as OPN⁶⁰. Given that a higher substrate stiffness and a reduced cell area lead to the exertion of larger traction forces⁵⁸, further studies using traction force microscopy might shed some light on the origins of the observed differences in the OPN expression between the pillars with different interspacing values. Nevertheless, the results of this study show that submicron pillars with specific geometry and dimensions have a significant effect on the osteogenic differentiation of cells regardless of their material. Therefore, having the possibility to produce such submicron pillars using high-throughput methods that enable the generation of a large number of samples with acceptable reproducibility on various substrates is essential for further research.

6.4.2 Water contact angle

The superhydrophilicity of the patterned surfaces is in good agreement with the predictions of the Wenzel model^{64, 65}. In this model, it is assumed that the liquid penetrates in between the pillars. The contact angle of a rough surface (θ_w) can then be estimated using the following equation:

$$\cos(\theta_w) = r \cos(\theta)$$

where θ_w and θ are respectively the contact angles of the droplet on the patterned and flat substrates and r is the ratio of the real surface area to the projected surface area, called the roughness factor. Assuming the pillars to be cylindrical in shape with a diameter of d , a height of h , and a pitch of p , r can be calculated as²⁶:

$$r = \frac{A_{real}}{A_{projected}} = \frac{p^2 + 4\left(\frac{\pi dh}{4}\right)}{p^2} = 1 + \frac{\pi dh}{p^2}$$

Based on the Wenzel equation, a hydrophilic surface ($\theta < 90^\circ$) becomes more hydrophilic after patterning ($\theta_w < \theta$)⁶⁴. Substituting the dimensions of the submicron pillars ($d = 245$ nm, $h = 990$ nm for $p = 700$ nm and $d = 255$ nm, $h = 1046$ nm for $p = 1000$ nm) and $\theta = 34^\circ$ into the above-mentioned equations yields $r = 2.14$ and $\cos(\theta_w) > 1$ for $p = 700$ nm, and $r = 1.54$ and $\cos(\theta_w) > 1$ for $p = 1000$ nm. $\cos(\theta_w) > 1$ in both cases indicates that the surface becomes completely wet (*i.e.*, the surface is superhydrophilic), which is in a good agreement with the results of our experiments, where the measured contact angles were $7 \pm 4^\circ$ and $9 \pm 6^\circ$ for $p = 700$ nm and $p = 1000$ nm, respectively (Figure 6.4e).

6.4.3 Hybrid PDMS molding

The PDMS molds suffer from some limitations. First, due to the low elastic modulus of PDMS, patterns with very high or very low aspect ratio deform, collapse, or buckle and create some defects on the patterned areas during the molding process, meaning that the patterns cannot be fully transferred during the PDMS molding⁶⁶. On the other hand, the low elastic modulus of PDMS (≈ 1.5 MPa) also limits the minimum feature size of the transferable patterns (*i.e.*, ≈ 500 nm)^{67,68}. In order to improve the accuracy and resolution, Schmid *et al.*⁶⁹, have developed hPDMS that offers enhanced mechanical properties⁷⁰. Having hybrid PDMS molds allows for reaching a resolution of 10 nm³⁵, which is the resolution that can be reached by rigid molds. We, therefore, applied hPDMS to the substrate prior to PDMS casting to precisely imprint the submicron pillars from the master mold into the hybrid PDMS replica mold. This hybrid mold was then used in the thermal nanoimprint process thanks to its low deformation and high flexibility. Comparing the dimension of the patterns present on the hybrid PDMS substrate with the original submicron pillars (*i.e.*, those of the master mold) indicated that the deviations in the diameter of the pillars are only 9-10% while deviations of 3-4% were observed for the interspacing values.

6.4.4 Thermal nanoimprint lithography

As PDMS is inert and hydrophobic, there is no need to perform any post-processing on it prior to bringing it into contact with PMMA, and the poor adhesion between PDMS and PMMA is an advantage during the nanoimprint process. After nanoimprinting, optimizing the etching parameters to properly transfer the patterns from PMMA to the final substrate is the key step that affects the feature sizes. Although Pandey *et al.*³⁵ have previously shown the potential of PDMS as the master mold in thermal nanoimprint

processes, they did not continue the process to transfer the patterns into the final substrate. In other words, while they transferred the patterns of the PDMS mold to the PMMA layer, which was coated on the final substrate, they did not use the PMMA or any hard mask to etch the final substrate and transfer the patterns into the final substrate. Here, the nanoimprinting process was followed by the proper etching steps to have the desired patterns transferred into the substrate of interest.

The nanoimprinting process parameters, including the applied force, thermoplastic material, embossing temperature, time, and chamber pressure determine the resolution and quality of the transferred patterns. The values reported in the literature for the embossing temperature, while using PMMA as the resist, vary between 120 and 180 °C⁷¹. At very low temperatures, PMMA is not formable enough to follow the height of the pattern on the master mold, resulting in incomplete pattern transfer or in features that possess a lower aspect ratio than desired. On the contrary, embossing at a very high temperature may crush or destroy the master mold⁷². In our study, the embossing temperature was set to 140 °C. However, PMMA was used as the mask to transfer the submicron pillars first to Cr. Then, the Cr mask was employed to transfer the submicron pillars into the fused silica substrate. Therefore, as long as the height of the submicron pillars formed on PMMA is high enough to etch the unwanted Cr layer, the embossing temperature is not the critical parameter. The applied force and its uniformity are the other crucial parameters to achieve homogeneous and high-resolution patterns throughout the substrate surface and to prevent the mold and its underlying substrate from being damaged. Applying very high forces will damage the hybrid PDMS mold with the degree of mold deformation increasing with the applied force³⁵. On the other hand, very low forces result in the nanopatterns not being thoroughly transferred. Achieving full imprinting with high fidelity of the transferred patterns is, therefore, challenging and requires proper optimization of the involved parameters. In our study, 250 N was high enough to fully transfer the submicron pillars into the PMMA without damaging the hybrid PDMS master mold.

Following the above-mentioned process steps led to the realization of high-quality replicas from a single master mold. Inspecting the dimensions and quality of the final patterns transferred into the fused silica substrates (Figure 6.5e) and comparing it with the master mold (Figure 6.1c) indicates that there are only minor deviations in the diameter and interspacing of the submicron pillars (Table 6.1). In the case of the

submicron pillars with an interspacing of 700 nm, the deviations were around 12% for the diameter and 1% for the interspacing. As for the submicron pillars with an interspacing of 1000 nm, the deviations were around 19% for the diameter and 1% for the interspacing. Considering the fact that the patterned area was relatively large, the effects of such deviations on the patterned area, in its entirety, are not significant. In other words, optimized processing parameters lead to high-fidelity replica molds despite the large number of steps involved. These results confirm that pattern replication by thermal nanoimprinting produces precisely formed submicron patterns with minimal surface defects.

The primary limitation of the thermal nanoimprint lithography is the processing temperature of the master mold, which should be lower than the embossing temperature. Even with this limitation, nanoimprint lithography appears to be the best candidate for decorating the surface of biomaterials with cell-instructive nano/submicron pillars⁷³.

6.5 Conclusions

In summary, we developed a precise and facile method for high-throughput patterning of various types of surfaces with nanoscale and submicron patterns whose geometries are precisely controlled. First, we used electron beam lithography to fabricate two arrays of submicron pillars with precise dimensions and controlled shape over a large area ($3 \times 5 \text{ mm}^2$) of a fused silica substrate. Assessing the adaptation of MC3T3-E1 preosteoblast cells to the fabricated patterns showed that varying the interspacing of the submicron pillars significantly influences the cytoskeletal organization, cell area, cell elongation, and formation of FAs. The interactions of the cells with the submicron pillars were found to be subordinate to the settling state of the cells. The “top state” observed on submicron pillars with an interspacing of 700 nm shifted to a “mixed state” on submicron pillars with an interspacing of 1000 nm, meaning that in the latter, the cells not only interacted with the top of the pillars but also engulfed the whole pillar and came into contact with its lateral sides as well as the substrate. Both types of pillars significantly increased the expression of OPN as compared to a flat control surface. Afterward, to overcome the restrictions of many fabrication techniques, namely being expensive and time-consuming, we used soft lithography to replicate the submicron pillars present on the original mold into the hybrid PDMS mold. The shape, morphology, and depth of the replicated patterns were analyzed with SEM and FIB, and the results confirmed the geometric fidelity of the hybrid replica. As PDMS is not the material of choice for cell

studies, we used hybrid PDMS molds as the master mold in thermal nanoimprint lithography to transfer the patterns to the thermoplastic resist coated on the desired final substrate (fused silica in our study). The results of this study clearly show the advantages of nanoimprint lithography as a unique high-throughput yet precise technique for the patterning of large areas of bio-instructive surfaces, while guarantying the quality and resolution of the nanopatterns required for further biological assessments. The height/depth of the final patterns can be adjusted by optimizing the applied force and embossing temperature as well as through the application of specific etching steps.

6.6 Supplementary information

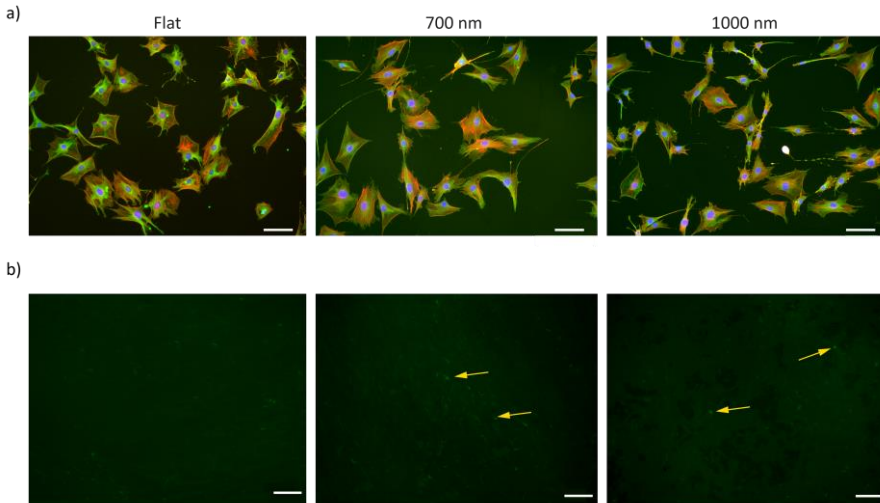


Figure S6.1. a) Low magnification overview of MC3T3-E1 preosteoblast cells cultured on the flat and patterned surfaces for 1 day and stained for vinculin (green), actin (red), and nucleus (blue). Scale bar = 100 μm . b) OPN could hardly be detected on the flat and patterned surfaces under non-osteogenic culture conditions after 21 days.

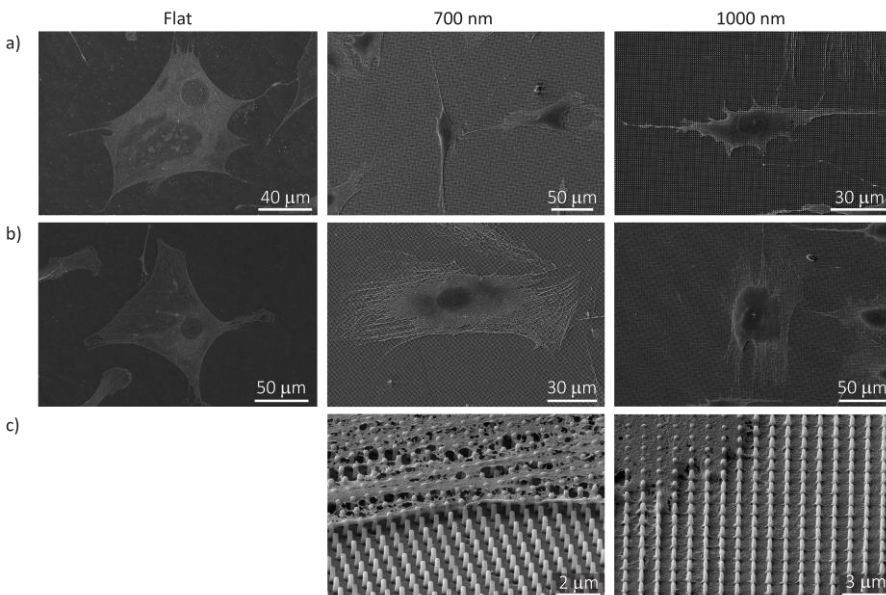


Figure S6.2. a) Top and b) tilted view SEM images of the representative cell morphology on the flat and patterned surfaces. c) Highly magnified tilted SEM views of the settlement state of the cells on the patterned specimens and their interactions with the single pillars at the cell periphery.

Bibliography

- [1] Å. Ekblad-Nordberg, L. Walther-Jallow, M. Westgren, C. Götherström, Prenatal stem cell therapy for inherited diseases: Past, present, and future treatment strategies: Concise Review, *Stem Cells Translational Medicine*, 2019.
- [2] J. Ng, C.B. Little, S. Woods, S. Whittle, F.Y. Lee, S. Gronthos, S. Mukherjee, D.J. Hunter, D.L. Worthley, Stem Cell Directed Therapies for Osteoarthritis: the promise and the practice: Concise Review, *Stem Cells*, 2019.
- [3] L. Zhao, A.D. Kaye, A.J. Kaye, A. Abd-Elseyed, Stem Cell Therapy for Osteonecrosis of the Femoral Head: Current Trends and Comprehensive Review, *Current Pain and Headache Reports*, 22(6), 41, 2018.
- [4] M. Ventre, P.A. Netti, Engineering cell instructive materials to control cell fate and functions through material cues and surface patterning, *ACS Applied Materials & Interfaces*, 8(24), 14896-14908, 2016.
- [5] A. Augello, C. De Bari, The regulation of differentiation in mesenchymal stem cells, *Human Gene Therapy*, 21(10), 1226-1238, 2010.
- [6] M. Nouri-Goushki, L. Angeloni, K. Modaresifar, M. Minneboo, P.E. Boukany, M.J. Mirzaali, M.K. Ghatkesar, L.E. Fratila-Apachitei, A.A. Zadpoor, 3D-Printed Submicron Patterns Reveal the Interrelation between Cell Adhesion, Cell Mechanics, and Osteogenesis, *ACS Applied Materials & Interfaces*, 13(29), 33767-33781, 2021.
- [7] K. Modaresifar, S. Azizian, M. Ganjian, L.E. Fratila-Apachitei, A.A.J.A.b. Zadpoor, Bactericidal effects of nanopatterns: A systematic review, *Acta Biomaterialia*, 83, 29-36, 2019.
- [8] M. Salandova, I.A.J. van Hengel, I. Apachitei, A.A. Zadpoor, B.C.J. van der Eerden, L.E. Fratila-Apachitei, Inorganic Agents for Enhanced Angiogenesis of Orthopedic Biomaterials, *Advanced Healthcare Materials*, 10(12), e2002254, 2021.
- [9] M. Fazel, H.R. Salimijazi, M. Shamanian, M. Minneboo, K. Modaresifar, I.A.J. van Hengel, L.E. Fratila-Apachitei, I. Apachitei, A.A. Zadpoor, Osteogenic and antibacterial surfaces on additively manufactured porous Ti-6Al-4V implants: Combining silver nanoparticles with hydrothermally synthesized HA nanocrystals, *Materials Science and Engineering: C*, 120, 111745, 2021.
- [10] H.N. Kim, A. Jiao, N.S. Hwang, M.S. Kim, D.-H. Kim, K.-Y. Suh, Nanotopography-guided tissue engineering and regenerative medicine, *Advanced Drug Delivery Reviews*, 65(4), 536-558, 2013.
- [11] C.R. Pedrosa, D. Arl, P. Grysan, I. Khan, S.p. Durrieu, S. Krishnamoorthy, M.-C. Durrieu, Controlled Nanoscale Topographies for Osteogenic Differentiation of Mesenchymal Stem Cells, *ACS Applied Materials & Interfaces*, 11(9), 8858-8866, 2019.
- [12] M.J. Dalby, N. Gadegaard, R.O. Oreffo, Harnessing nanotopography and integrin–matrix interactions to influence stem cell fate, *Nature Materials*, 13(6), 558-569, 2014.
- [13] S. Dobbenga, L.E. Fratila-Apachitei, A.A. Zadpoor, Nanopattern-induced osteogenic differentiation of stem cells—A systematic review, *Acta Biomaterialia*, 46, 3-14, 2016.
- [14] K. von der Mark, J. Park, S. Bauer, P. Schmuki, Nanoscale engineering of biomimetic surfaces: cues from the extracellular matrix, *Cell and Tissue Research*, 339(1), 131, 2010.

- [15] T. Sjoström, M.J. Dalby, A. Hart, R. Tare, R.O. Oreffo, B. Su, Fabrication of pillar-like titania nanostructures on titanium and their interactions with human skeletal stem cells, *Acta Biomaterialia*, 5(5), 1433-1441, 2009.
- [16] L.E. McNamara, T. Sjoström, K.E. Burgess, J.J. Kim, E. Liu, S. Gordonov, P.V. Moghe, R.M. Meek, R.O. Oreffo, B. Su, M.J. Dalby, Skeletal stem cell physiology on functionally distinct titania nanotopographies, *Biomaterials*, 32(30), 7403-7410, 2011.
- [17] C.-H. Chen, C.-C. Tsai, P.-T. Wu, I.-K. Wang, J. Yu, W.-B. Tsai, Modulation of Neural Differentiation through Submicron-Grooved Topography Surface with Modified Polydopamine, *ACS Applied Bio Materials*, 2(1), 205-216, 2018.
- [18] S. Watari, K. Hayashi, J.A. Wood, P. Russell, P.F. Nealey, C.J. Murphy, D.C. Genetos, Modulation of osteogenic differentiation in hMSCs cells by submicron topographically-patterned ridges and grooves, *Biomaterials*, 33(1), 128-136, 2012.
- [19] M.J. Dalby, N. Gadegaard, R. Tare, A. Andar, M.O. Riehle, P. Herzyk, C.D. Wilkinson, R.O. Oreffo, The control of human mesenchymal cell differentiation using nanoscale symmetry and disorder, *Nature Materials*, 6(12), 997-1003, 2007.
- [20] Y. Sun, C.S. Chen, J. Fu, Forcing stem cells to behave: a biophysical perspective of the cellular microenvironment, *Annual Review of Biophysics*, 41, 519-542, 2012.
- [21] M. Ganjian, K. Modaresifar, M.R. Ligeon, L.B. Kunkels, N. Tümer, L. Angeloni, C.W. Hagen, L.G. Otten, P.L. Hagedoorn, I.J.A.M.I. Apachitei, Nature helps: toward bioinspired bactericidal nanopatterns, *Advanced Materials Interfaces*, 6(16), 1900640, 2019.
- [22] K. Modaresifar, L.B. Kunkels, M. Ganjian, N. Tümer, C.W. Hagen, L.G. Otten, P.-L. Hagedoorn, L. Angeloni, M.K. Ghatkesar, L.E.J.N. Fratila-Apachitei, Deciphering the roles of interspace and controlled disorder in the bactericidal properties of nanopatterns against *Staphylococcus aureus*, *Nanomaterials*, 10(2), 347, 2020.
- [23] D.S. Widyaratih, P.L. Hagedoorn, L.G. Otten, M. Ganjian, N. Tümer, I. Apachitei, C.W. Hagen, L.E. Fratila-Apachitei, A.A. Zadpoor, Towards osteogenic and bactericidal nanopatterns?, *Nanotechnology*, 30(20), 20LT01, 2019.
- [24] D.K. Oh, H. Jeong, J. Kim, Y. Kim, I. Kim, J.G. Ok, J. Rho, Top-down nanofabrication approaches toward single-digit-nanometer scale structures, *Journal of Mechanical Science and Technology*, 35(3), 837-859, 2021.
- [25] M.N. M. N, U. Hashim, M. Md Arshad, A.R. Ruslinda, S. Rahman, M. Fathil, M.H.J.P.O. Ismail, Top-down nanofabrication and characterization of 20 nm silicon nanowires for biosensing applications, *PLOS One*, 11(3), e0152318, 2016.
- [26] M. Nouri-Goushki, M. Mirzaali, L. Angeloni, D. Fan, M. Minneboo, M. Ghatkesar, U. Staufer, L. Fratila-Apachitei, A.J.A.a.m. Zadpoor, interfaces. 3d printing of large areas of highly ordered submicron patterns for modulating cell behavior, *ACS Applied Materials & Interfaces*, 12(1), 200-208, 2019.
- [27] M. Ganjian, K. Modaresifar, H. Zhang, P.-L. Hagedoorn, L.E. Fratila-Apachitei, A.A.J.S.r. Zadpoor, Reactive ion etching for fabrication of biofunctional titanium nanostructures, *Scientific Reports*, 9(1), 1-20, 2019.
- [28] E.P. Ivanova, J. Hasan, H.K. Webb, G. Gervinskas, S. Juodkazis, V.K. Truong, A.H. Wu, R.N. Lamb, V.A. Baulin, G.S.J.N.c. Watson, Bactericidal activity of black silicon, *Nature Communications*, 4(1), 1-7, 2013.

- [29] F. Hizal, I. Zhuk, S. Sukhishvili, H.J. Busscher, H.C. van der Mei, C.-H.J.A.a.m. Choi, interfaces, Impact of 3D hierarchical nanostructures on the antibacterial efficacy of a bacteria-triggered self-defensive antibiotic coating, *ACS Applied Materials & Interfaces*, 7(36), 20304-20313, 2015.
- [30] G. Yi, Y. Yuan, X. Li, Y.J.S. Zhang, ZnO Nanopillar Coated Surfaces with Substrate-Dependent Superbactericidal Property, *Small*, 14(14), 1703159, 2018.
- [31] P.M. Tsimbouri, L. Fisher, N. Holloway, T. Sjoström, A. Nobbs, R.D. Meek, B. Su, M.J.J.S.r. Dalby, Osteogenic and bactericidal surfaces from hydrothermal titania nanowires on titanium substrates, *Scientific Reports*, 6(1), 1-12, 2016.
- [32] A. Jaggesar, A. Mathew, H. Wang, T. Tesfamichael, C. Yan, P.K.J.J.o.t.m.b.o.b.m. Yarlagadda, Mechanical, bactericidal and osteogenic behaviours of hydrothermally synthesised TiO₂ nanowire arrays, *Journal of the Mechanical Behavior of Biomedical Materials*, 80, 311-319, 2018.
- [33] S.H. Ahn, L.J. Guo, Large-area roll-to-roll and roll-to-plate nanoimprint lithography: a step toward high-throughput application of continuous nanoimprinting, *ACS Nano*, 3(8), 2304-2310, 2009.
- [34] S.H. Ahn, L.J. Guo, High-speed roll-to-roll nanoimprint lithography on flexible plastic substrates, *Advanced Materials*, 20(11), 2044-2049, 2008.
- [35] A. Pandey, S. Tzadka, D. Yehuda, M.J.S.M. Schwartzman, Soft thermal nanoimprint with a 10 nm feature size, *Soft Matter*, 15(13), 2897-2904, 2019.
- [36] A. Jaggesar, H. Shahali, A. Mathew, P. Yarlagadda, Bio-mimicking nano and micro-structured surface fabrication for antibacterial properties in medical implants, *Journal of Nanobiotechnology*, 15(1), 64, 2017.
- [37] H. Su, X.R. Cheng, T. Endo, K. Kerman, Photonic crystals on copolymer film for label-free detection of DNA hybridization, *Biosensors and Bioelectronics*, 103, 158-162, 2018.
- [38] J. Ahn, S. Kwon, S. Jung, W.S. Lee, J. Jeong, H. Lim, Y.B. Shin, J. Lee, Fabrication of Pyrrole-Based Electrochemical Biosensor Platform Using Nanoimprint Lithography, *Advanced Materials Interfaces*, 5(8), 1701593, 2018.
- [39] M. Vaisman, N. Jain, Q. Li, K.M. Lau, E. Makoutz, T. Saenz, W.E. McMahon, A.C. Tamboli, E.L. Warren, GaAs Solar Cells on Nanopatterned Si substrates, *IEEE Journal of Photovoltaics*, 8(6), 1635-1640, 2018.
- [40] W.-C. Tsao, Q.-C. Zeng, Y.-H. Yeh, C.-H. Tsai, H.-F. Hong, C.-Y. Chen, T.-Y. Lin, Y.-Y. Huang, C.-W. Tsao, J.-W. Pan, Efficiency evaluation of a hybrid miniaturized concentrated photovoltaic for harvesting direct/diffused solar light, *Journal of Optics*, 21, 035901, 2019.
- [41] F. Viela, I. Navarro-Baena, J.J. Hernández, M.R. Osorio, I. Rodríguez, Moth-eye mimetic cyto-compatible bactericidal nanotopography: a convergent design, *Bioinspiration & Biomimetics*, 13(2), 026011, 2018.
- [42] F. Kantawong, K.E. Burgess, K. Jayawardena, A. Hart, R.J. Burchmore, N. Gadegaard, R.O. Oreffo, M.J. Dalby, Whole proteome analysis of osteoprogenitor differentiation induced by disordered nanotopography and mediated by ERK signalling, *Biomaterials*, 30(27), 4723-4731, 2009.

- [43] J.R. Wang, S.F. Ahmed, N. Gadegaard, R.D. Meek, M.J. Dalby, S.J. Yarwood, Nanotopology potentiates growth hormone signalling and osteogenesis of mesenchymal stem cells, *Growth Hormone & IGF Research*, 24(6), 245-250, 2014.
- [44] S. Li, D. Chu, A review of thin-film transistors/circuits fabrication with 3D self-aligned imprint lithography, *Flexible and Printed Electronics*, 2(1), 013002, 2017.
- [45] Z. Wang, P. Yi, L. Peng, X. Lai, J. Ni, Continuous fabrication of highly conductive and transparent Ag mesh electrodes for flexible electronics, *IEEE Transactions on Nanotechnology*, 16(4), 687-694, 2017.
- [46] X. Gao, Y. Huang, X. He, X. Fan, Y. Liu, H. Xu, D. Wu, C. Wan, Mechanically enhanced electrical conductivity of polydimethylsiloxane-based composites by a hot embossing process, *Polymers*, 11(1), 56, 2019.
- [47] S. Callens, D. Fan, I. van Hengel, M. Minneboo, L. Fratila-Apachitei, A.J.b. Zadpoor, Emergent collective organization of bone cells in complex curvature fields, bioRxiv preprint, 2020.
- [48] K. Modaresifar, M. Ganjian, L. Angeloni, M. Minneboo, M.K. Ghatkesar, P.L. Hagedoorn, L.E. Fratila-Apachitei, A.A. Zadpoor, On the Use of Black Ti as a Bone Substituting Biomaterial: Behind the Scenes of Dual-Functionality, *Small*, 2100706, 2021.
- [49] U. Horzum, B. Ozdil, D. Pesen-Okvur, Step-by-step quantitative analysis of focal adhesions, *MethodsX*, 1, 56-59, 2014.
- [50] V. Bhingardive, L. Menahem, M. Schwartzman, Soft thermal nanoimprint lithography using a nanocomposite mold, *Nano Research*, 11(5), 2705-2714, 2018.
- [51] K.L. Lai, M.H. Hon, I.C. Leu, Pattern formation on polymer resist by solvent-assisted nanoimprinting with PDMS mold as a solvent transport medium, *Journal of Micromechanics and Microengineering*, 21(7), 2011.
- [52] W.-X. Su, C.-Y. Wu, Y.-C. Lee, Anti-reflection nano-structures fabricated on curved surface of glass lens based on metal contact printing lithography, *Microelectronic Engineering*, 214, 15-20, 2019.
- [53] M.D. Cabezas, B. Meckes, C.A. Mirkin, M. Mrksich, Subcellular Control over Focal Adhesion Anisotropy, Independent of Cell Morphology, Dictates Stem Cell Fate, *ACS Nano*, 13(10), 11144-11152, 2019.
- [54] M. Bao, J. Xie, A. Piruska, W.T.J.N.c. Huck, 3D microniches reveal the importance of cell size and shape, *Nature Communications*, 8(1), 1-12, 2017.
- [55] F. Jiao, Y. Zhao, Q. Sun, B.J.J.o.B.M.R.P.A. Huo, Spreading area and shape regulate the apoptosis and osteogenesis of mesenchymal stem cells on circular and branched micropatterned islands, *Journal of Biomedical Materials Research Part A*, 108(10), 2080-2089, 2020.
- [56] A. Ron, E.U. Azeloglu, R.C. Calizo, M. Hu, S. Bhattacharya, Y. Chen, G. Jayaraman, S. Lee, S.R. Neves-Zaph, H. Li, Cell shape information is transduced through tension-independent mechanisms, *Nature Communications*, 8(1), 1-15, 2017.
- [57] H. Seong, S.G. Higgins, J. Penders, J.P. Armstrong, S.W. Crowder, A.C. Moore, J.E. Sero, M. Becce, M.M. Stevens, Size-Tunable Nanoneedle Arrays for Influencing Stem Cell Morphology, Gene Expression, and Nuclear Membrane Curvature, *ACS Nano*, 14(5), 5371-5381, 2020.

- [58] F. Viela, D. Granados, A. Ayuso-Sacido, I. Rodríguez, Biomechanical cell regulation by high aspect ratio nanoimprinted pillars, *Advanced Functional Materials*, 26(31), 5599-5609, 2016.
- [59] C.W. Kuo, D.-Y. Chueh, P. Chen, Investigation of size-dependent cell adhesion on nanostructured interfaces, *Journal of Nanobiotechnology*, 12(1), 1-10, 2014.
- [60] S.G. Higgins, M. Becce, A. Belessiotis-Richards, H. Seong, J.E. Sero, M.M. Stevens, High-Aspect-Ratio Nanostructured Surfaces as Biological Metamaterials, *Advanced Materials*, 1903862, 2020.
- [61] J. Hasan, S. Jain, K. Chatterjee, Nanoscale topography on black titanium imparts multi-biofunctional properties for orthopedic applications, *Scientific Reports*, 7, 41118, 2017.
- [62] A. Ray, O. Lee, Z. Win, R.M. Edwards, P.W. Alford, D.-H. Kim, P.P. Provenzano, Anisotropic forces from spatially constrained focal adhesions mediate contact guidance directed cell migration, *Nature Communications*, 8(1), 1-17, 2017.
- [63] M. Werner, S.B. Blanquer, S.P. Haimi, G. Korus, J.W. Dunlop, G.N. Duda, D.W. Grijpma, A. Petersen, Surface curvature differentially regulates stem cell migration and differentiation via altered attachment morphology and nuclear deformation, *Advanced Science*, 4(2), 1600347, 2017.
- [64] D.J.A.R.M.R. Quéré, Wetting and roughness, *Annual Review of Materials Research*, 38, 71-99, 2008.
- [65] N. Vrancken, S. Sergeant, G. Vereecke, G. Doumen, F. Holsteyns, H. Terryn, S. De Gendt, X.J.L. Xu, Superhydrophobic breakdown of nanostructured surfaces characterized in situ using ATR-FTIR, *Langmuir*, 33(15), 3601-3609, 2017.
- [66] E. Baquedano, R.V. Martinez, J.M. Llorens, P.A. Postigo, Fabrication of silicon nanobelts and nanopillars by soft lithography for hydrophobic and hydrophilic photonic surfaces, *Nanomaterials*, 7(5), 109, 2017.
- [67] T.W. Odom, J.C. Love, D.B. Wolfe, K.E. Paul, G.M. Whitesides, Improved pattern transfer in soft lithography using composite stamps, *Langmuir*, 18(13), 5314-5320, 2002.
- [68] C. Masciullo, A. Sonato, F. Romanato, M.J.N. Cecchini, Perfluoropolyether (PFPE) intermediate molds for high-resolution thermal nanoimprint lithography, *Nanomaterials*, 8(8), 609, 2018.
- [69] H. Schmid, B. Michel, Siloxane polymers for high-resolution, high-accuracy soft lithography, *Macromolecules*, 33(8), 3042-3049, 2000.
- [70] C. Zheng, *Nanofabrication: Principles, Capabilities, and Limits*. Springer. 442, 2016.
- [71] A. Shamsi, A. Amiri, P. Heydari, H. Hajghasem, M. Mohtashamifar, M. Esfandiari, Low cost method for hot embossing of microstructures on PMMA by SU-8 masters, *Microsystem Technologies*, 20(10-11), 1925-1931, 2013.
- [72] M. Kim, B.-U. Moon, C.H. Hidrovo, Enhancement of the thermo-mechanical properties of PDMS molds for the hot embossing of PMMA microfluidic devices, *Journal of Micromechanics and Microengineering*, 23(9), 095024, 2013.
- [73] J. Chen, J. Shi, A. Cattoni, D. Decanini, Z. Liu, Y. Chen, A.-M. Haghiri-Gosnet, A versatile pattern inversion process based on thermal and soft UV nanoimprint lithography techniques, *Microelectronic Engineering*, 87(5-8), 899-903, 2010.

On the use of black titanium

Despite the potential of small-scale pillars of black titanium (bTi) for killing the bacteria and directing the fate of stem cells, not much is known about the effects of the pillars' design parameters on their biological properties. Here, three distinct bTi surfaces are designed and fabricated through dry etching of the titanium, each featuring different pillar designs. The interactions of the surfaces with preosteoblast cells and *Staphylococcus aureus* bacteria are then investigated. Pillars with different heights and spatial organizations differently influenced the morphological characteristics of the cells, including their spreading area, aspect ratio, nucleus area, and cytoskeletal organization. The preferential formation of focal adhesions and their size variations also depend on the type of topography. When the pillars are neither fully separated nor extremely tall, the colocalization of actin fibers and FAs as well as enhanced matrix mineralization were observed. However, the killing efficiency of these pillars against the bacteria is not as high as that of fully separated and tall pillars. This chapter provides a new perspective on the dual-functionality of bTi surfaces and elucidates how the surface design and fabrication parameters can be used to achieve a surface topography with balanced bactericidal and osteogenic properties.

7.1 Introduction

The increased life expectancy of humankind has encouraged the medical device industry to develop functional devices that outlive the patients. In this regard, bone implants require a long list of properties and functionalities to serve their purpose most properly. In addition to primary stability^{1,2} and bone-matching mechanical properties³, bone implants need to be designed in such a way to promote host tissue regeneration and integration with the implant (*i.e.*, osteoinduction and osseointegration)⁴⁻⁶, as well as to combat implant-associated infections (IAIs)⁷⁻⁹, as one of the main causes of implant failure.

Developing designer biomaterials with better control over their biological properties and interactions with their host is proven crucial for enhancing the performance of implantable medical devices¹⁰. Yet achieving the optimal biological properties and controlling the interactions of bio-organisms with the biomaterial are highly dependent on the surface properties¹¹⁻¹⁴. For instance, enhancing cell adhesion, cell growth^{15,16}, and the desired differentiation of stem cells^{17,18} are among the steps required to optimize the osseointegration of implants. Similarly, preventing IAIs through the eradication of the adherent bacteria and the aversion of biofilm formation play important roles in this regard¹⁹. To this aim, exploiting the advances in surface modification techniques is a necessity to achieve those rare or unprecedented properties as the surface is the frontline where the success of a biomaterial is determined. Due to the complications associated with the use of antibacterial agents^{20,21} and growth factors²², including the high cost and resistance development by bacterial strains, the focus has largely shifted to the physical alterations of the surface.

Given the fact that the physical small-scale features of the surface play a vital role both in directing stem cells fate and resisting the bacterial colonization¹¹, the optimization of these features in terms of shape and geometry, dimensions, and spatial arrangement is of high importance^{23,24}. The adhesion of mammalian cells to the surface is facilitated via their transmembrane proteins, including integrins that act mechanically to bind the cell to its extracellular matrix (ECM)²⁵. The formation of focal adhesions (FAs) links the cell cytoskeleton to these integrin clusters and functions as a bridge for transferring physicochemical stimuli (*e.g.*, mechanical forces) from ECM to the nuclei. These complex and dynamic processes result in different interpretations of various surface topographies by the cells and may upregulate the expression of specific proteins in certain

cell lines^{26, 27}. Therefore, even subtle variations in the roughness²⁸, geometry²⁹, and dimensions of the physical features of the implant surface^{30, 31} may substantially impact the cell behavior. The recent advancements in nano-/microfabrication techniques have facilitated the fabrication of precisely controlled surface topographies, also known as surface patterns²⁹, which are capable of inducing osteogenic differentiation in stem cells³²⁻³⁴. The effects of different length scales on the osteogenic properties of the patterns is, however, not yet fully comprehended as contradictory effects have been reported for the different relevant length scales in the literature^{33, 35, 36}. Furthermore, one cannot easily correlate the short-term effects of patterns on cell morphology, spreading area, expression of FAs, and cytoskeleton organization with their long-term effects on the expression of osteogenic markers and matrix mineralization. Despite the vast efforts in recent years, the list of unknowns remains long because there are a plethora of design parameters (*e.g.*, geometry and arrangement), each imposing their influence on cells besides the complexity of cell structure and its intracellular pathways, which are not thoroughly understood till now^{23, 37}.

On the other hand, inspired by the unique naturally occurring structures³⁸⁻⁴⁰, synthetic bactericidal surface patterns have emerged with different geometries and dimensions⁴¹. Patterns that lie within a specific range of dimensions have been shown to mechanically kill different types of bacteria through a combination of different mechanisms^{24, 42, 43}.

Among numerous nano-/microfabrication techniques, reactive ion etching (RIE) is a simple and fast technique for creating an engineered surface topography⁴⁴. RIE works based on dry chemical etching and physical ion bombardment of the surface. Ivanova *et al.* used RIE to create high aspect ratio nanopillars on a silicon substrate and studied their bactericidal properties for the first time⁴⁵. The killing efficiency of the so-called black silicon (bSi, due to its black appearance) against both Gram-negative and Gram-positive bacteria was comparable to naturally occurring bactericidal surfaces. Ever since, many studies have investigated the effects of the height and density of nanopillars on the bactericidal properties of bSi, as well as the involved killing mechanisms^{46, 47}. Later on, Hasan *et al.* successfully fabricated similar nanopillars on a titanium substrate (a more relevant choice of material for orthopedic applications) using inductively coupled plasma RIE (ICP RIE)⁴⁸. They showed that bTi is as effective as bSi in killing the bacteria. Moreover, not only did bTi support the attachment and proliferation of human

mesenchymal stem cells (hMSCs) but also displayed a synergistic effect in stimulating the osteogenic differentiation of cells together with the osteogenic culture medium. So far, all the mentioned studies have produced bSi and bTi under identical conditions and have only changed the etching time as a variable to achieve different pillar height, whereas the geometry and organization of the pillars have been quite comparable in those studies. Recently, the effects of all the processing parameters of ICP RIE on the physicochemical characteristics of the resulting bTi nanostructures have been systematically studied ⁴⁴. Changing other processing parameters, such as the chamber pressure and temperature can also be used to fabricate distinct nanostructured surfaces.

Due to the remarkable structural and biological differences between mammalian and bacterial cells, designing a patterned surface that fulfills dual functionality is quite challenging. In this regard, bTi seems to be a very promising biomaterial for future clinical applications, given that it holds the potential for narrowing down the gap between osteogenic and bactericidal patterns as the essential step in developing cell-instructive biomaterials. However, there are still many unknowns about the behavior of cells interacting with bTi nanopillars and how their long-term osteogenic response is related to their short-term responses (*e.g.*, morphology, spreading area, the formation of FAs, *etc.*).

In the present study, we provide a new perspective on the dual-functionality of different bTi surfaces with the ultimate aim of devising a guideline for the application of bTi. We hypothesized that the viability and fate of bacteria and mammalian cells are significantly affected by the processing parameters of bTi surfaces and the geometrical characteristics of the pillars covering them. By adjusting the various ICP RIE processing parameters, we produced different types of bTi surfaces in our preliminary studies and selected three out of those that represent a gradual deviation from the flat Ti surface. These three types of bTi are distinct in terms of the height and spatial organization of their pillars. To answer the research question, cytocompatibility, morphological characteristics, the formation of FAs, and the osteogenic response of MC3T3-E1 preosteoblast cells cultured on these three different bTi surfaces, were quantitatively analyzed and the relationships between them were discussed. Furthermore, the bactericidal properties of the same bTi surfaces against *Staphylococcus aureus* bacteria (as the main relevant infectious pathogen involved in IAIs) were evaluated to enable the

possible identification of a bTi surface with the desired dual-functionality and to shed light on the possible killing mechanism of the studied surfaces.

7.2 Materials and Methods

7.2.1 Fabrication and characterization of bTi samples

Fabrication

Annealed titanium foils with a thickness of 125 μm (99.96% purity, Goodfellow, UK) were cut to the size of a 4-inch (diameter = 10.2 cm) silicon wafer and were polished by chemical-mechanical polishing (CMP Mecapol E460, France). The surface was then coated with a photoresist to protect it against damages. The titanium wafer was further cut into $8 \times 8 \text{ mm}^2$ pieces using a dicing saw (DAD3220, Disco Hi-Tec Europe GmbH, Germany). The photoresist layer was subsequently removed by acetone and the samples were cleaned in ethanol and isopropanol (IPA). The samples were spin-dried prior to surface modification by ICP RIE. An ICP RIE machine (PlasmaLab System 100, Oxford Instruments, UK) was used to create three types of structures on the titanium surface, which were distinct in terms of their morphological parameters and organization. Therefore, the polished samples were glued with diffusion oil on a 4-inch quartz wafer as the carrier. The etching process was performed with Cl_2 and Ar gases while the pressure of He (*i.e.*, the back-cooling gas) was kept at 1066 Pa. The following processing parameters were the same for all three types of modified surfaces: ICP source power = 600 W, RF power = 100 W, etching time = 10 minutes, Cl_2 flow rate = 30 sccm, and Ar flow rate = 2.5 sccm. However, the temperature and pressure of the chamber were changed for each type of surface as follows: 0 °C and 4.0 Pa for the first group, 40 °C and 2.0 Pa for the second condition, and 40 °C and 0.5 Pa for the third condition. Following the etching process, the samples were cleaned in acetone, ethanol, and IPA, respectively (each step lasted 30 minutes), and were then spin-dried for further characterization and experiments.

Morphological characterization

The etched surfaces were imaged by scanning electron microscopy (SEM) (Helios NanoLab 650, FEI, US). Top and tilted view (35°) images were acquired at different magnifications to assess the morphology and spatial organization of the resultant pillars. The mean roughness (R_a) and root mean squared roughness (R_q) were also estimated for each sample as the mean \pm SD of the values measured for three images of 100 μm^2 each

by atomic force microscopy (AFM) (JPK Nanowizard 4, Bruker, Germany) using a high aspect ratio probe (TESPA-HAR, Bruker, Germany) in the tapping mode.

Surface chemical composition

The elemental chemical composition of the surfaces was determined using energy-dispersive X-ray spectroscopy (EDS) performed inside the SEM (Helios Nanolab 650, FEI, US). The major chemical elements were identified from the EDS spectra.

Surface wettability

The wettability of the flat Ti surface (*i.e.*, polished, non-treated Ti surfaces) and bTi surfaces were evaluated by measuring the static water contact angle in duplicate using a drop shape analyzer (DSA 100, Krüss, Germany). A volume of 1.5 μl deionized water with a falling rate of 60 $\mu\text{l}/\text{min}$ was placed on the surface using a syringe. The images were recorded after 5 seconds.

7.2.2 Preosteoblast cell response to bTi surfaces

Pre-culture of cells and cell seeding

Preosteoblast MC3T3-E1 cells (Sigma-Aldrich, Germany) were cultured in alpha minimum essential medium (α -MEM) supplemented with 10% (v/v) fetal bovine serum and 1% (v/v) penicillin-streptomycin (all from Thermo Fisher Scientific, US). The medium was refreshed every 2 days. The samples were sterilized by immersion in 70% ethanol and exposure to UV light for 20 minutes. Upon reaching confluence, cells were detached from the cell culture flask using 1X trypsin-EDTA solution (Thermo Fisher Scientific, US) and were cultured on both flat Ti and bTi surfaces (2×10^4 cells per sample) in a 48 well-plate (Greiner, Bio-One, The Netherlands), and were incubated at 37 °C and 5% CO₂ (Life Technologies, US). This cell culture procedure was followed for all the cell experiments described in the following sections. In the case of experiments taking longer than 1 day, the medium was supplemented with 50 $\mu\text{g}/\text{ml}$ ascorbic acid and 4mM β -glycerophosphate (both from Sigma-Aldrich, Germany) from day 2 onward. All experiments, described in the following sections, were independently performed two times, each time in quadruplicates.

PrestoBlue assay

The metabolic activity of the cells seeded on flat Ti and bTi surfaces was measured by a PrestoBlue assay after 1, 4, 7, 11, and 14 days of culture. Therefore, all surfaces ($n =$

4 per group) were incubated in 250 μ l α -MEM supplemented with 25 μ l PrestoBlue reagent (Thermo Fisher Scientific, US) for 1 hour at 37 °C and 5% CO₂. Thereafter, 100 μ l of the supernatant from each well was transferred to a 96 well-plate (Greiner, Bio-One, The Netherlands) in duplicate. The fluorescence was measured at an excitation wavelength of 530 nm and an emission wavelength of 595 nm with a Victor X3 microplate reader (PerkinElmer, The Netherlands).

Immunocytochemical analysis of preosteoblast cells

In order to evaluate the short-term response of these cells to bTi surfaces and their morphological changes, the actin filaments, nucleus, and FAs of the cells were stained after 1 day of culture. The samples were first washed twice with 10X phosphate-buffered saline (PBS, Sigma-Aldrich, Germany) and the cells were fixed using a 4% (v/v) formaldehyde solution (Sigma-Aldrich, Germany). The cell membrane was permeabilized by adding 0.5% Triton X-100/PBS (Sigma-Aldrich, US) at 4 °C for 5 minutes, and then the samples were incubated in 1% BSA/PBS (Sigma-Aldrich, Germany) at 37 °C for 5 minutes. Subsequently, the samples were incubated in anti-vinculin mouse monoclonal primary antibody (1:100 in 1% BSA/PBS, Sigma-Aldrich, Germany) and rhodamine-conjugated phalloidin (1:1000 in 1% BSA/PBS, Thermo Fisher Scientific, US) for 1 hour at 37 °C. The cells were then washed three times (5 minutes each time) with 0.5% Tween-20/PBS (Sigma-Aldrich, US) before being incubated in Alexa Fluor 488, donkey anti-mouse polyclonal secondary antibody (1:200 in 1% BSA/PBS, Thermo Fisher Scientific, US) for 1 hour at room temperature. The samples were washed again three times with 0.5% Tween-20/PBS (5 minutes each time), followed by 5 minutes washing with 1X PBS. To simultaneously visualize the cell nuclei and properly mount the samples on microscopic glass slides, 10 μ l Prolong gold antifade reagent containing DAPI (4',6-diamidino-2-phenylindole) (Thermo Fisher Scientific, US) was laid on the surfaces and then five different locations of each sample were imaged using a fluorescence microscope (ZOE fluorescent cell imager, Bio-Rad, The Netherlands). For the SEM observations, the stained samples were washed twice with distilled water for 5 minutes and then dehydrated in 50%, 70%, and 96% ethanol solutions for 15, 20, and 20 minutes, respectively. Eventually, the samples were dried overnight at room temperature and were gold-sputtered before SEM imaging.

Investigation of the osteogenic properties of bTi surfaces

To investigate the long-term osteogenic response of preosteoblast cells, the expression of some of the early and late osteogenic markers (*i.e.*, Runx-related transcription factor 2 (Runx2) and calcium deposits) was studied.

For immunocytochemical staining of Runx2 (at day 9 of culture), a procedure similar to the previous section was followed. After fixation and permeabilization, the cells were incubated in recombinant anti-Runx2 rabbit monoclonal primary antibody (1:250 in 1% BSA/PBS, Abcam, UK). The cells were then incubated in Alexa Fluor 488, donkey anti-rabbit polyclonal secondary antibody (1:200 in 1% BSA/PBS, Thermo Fisher Scientific, US). Washing, mounting, imaging, and dehydration processes were followed similarly as described above.

Alizarin red S staining was performed on day 14 of culture to assess the deposition of calcium in the cells' matrix. Briefly, cells were washed and fixed as described above. The samples were then incubated in 2% (w/v) Alizarin red S solution (Sigma-Aldrich, Germany) for 30 minutes in the dark. The specimens were then rinsed five times with distilled water before being imaged by a ZOE fluorescent cell imager (Bio-Rad, The Netherlands) (five different locations of the surface).

Fluorescence image analysis

ImageJ 1.53c (NIH, US) and focal adhesion analysis server (FAAS)⁴⁹ were used to extract and quantify data from the fluorescence images. Each image overlay was split into separate channels for further evaluation of the nucleus, F-actin, and other proteins (*i.e.*, vinculin). By thresholding the grayscale images of F-actin and vinculin, the cell spreading area, cell nucleus area, and the number and area of FAs were quantified through the Analyze Particles command. By fitting ellipses to the cell area, the minor and major diameters were measured and used to determine the aspect ratio of the cells. A previously described method⁵⁰ was used to quantify the number and area of FA (for fully separated ones). Briefly, for 15 cells per study group, the background was subtracted from the grayscale images under the Sliding Paraboloid option with a rolling ball radius of 50 pixels. The local contrast of the image was then enhanced by running the CLAHE plugin with a block size of 19, histogram bins of 256, and a maximum slope of 6. To further minimize the background, the mathematical exponential function (EXP) was applied through the process menu. Thereafter, the brightness, contrast, and threshold were automatically adjusted before measurements using the Analyze Particles command.

Similar image processing was performed to quantify the expression of Runx2. The number of mineralized nodules and their total area on the surface was quantified by running the Analyze Particles command on the images of Alizarin red S assay.

7.2.3 Bacterial studies

Preparation of bacterial cultures

Gram-positive *S. aureus* bacteria (RN0450 strain) (BEI Resources, US) were grown on brain heart infusion (BHI) (Sigma-Aldrich, US) agar plates at 37 °C overnight. A pre-culture of bacteria was prepared by inoculating a single colony in 10 ml autoclaved BHI, shaken at 140 rpm at 37 °C. The bacterial cells were collected at their logarithmic stage of growth and the optical density of the inoculum at 600 nm wavelength (OD_{600}) in the medium solution was first measured by a WPA Biowave II spectrophotometer (Biochrom, UK) and was then adjusted to a value of 0.1 (equivalent to 4×10^8 colony-forming units (CFU) per milliliter) to be cultured on the flat Ti and bTi surfaces. All surfaces were sterilized by immersion in 70% ethanol and exposure to UV light for 20 minutes. 250 μ l of the bacterial inoculum was added to each surface in a 48 well-plate (Cell Star, Germany) (*i.e.*, 10^8 CFU per sample). All experiments, described in the following sections, were independently performed two times, each time in triplicate.

Bacterial metabolic activity (PrestoBlue assay)

To follow the metabolic activity of the adherent bacterial cells seeded on flat Ti and bTi surfaces, the PrestoBlue assay was performed at 1, 4, 8, and 18 hours of culture, using the same replicates for all the time points. At each time point, all surfaces were incubated in 250 μ l of BHI broth supplemented with 25 μ l PrestoBlue cell viability reagent (Thermo Fisher Scientific, US) for 1 hour at 37 °C. Thereafter, 100 μ l of the medium from each well was transferred to a 96 well-plate (Cell Star, Germany) in duplicate. The fluorescence was measured at an excitation wavelength of 530 nm and an emission wavelength of 595 nm using a Synergy 2 microplate reader (BioTek, US).

Furthermore, to visualize the morphological state of bacterial cells on the surfaces and investigate the interactions between bacteria and surfaces, the samples were imaged by SEM after 18 hours of culture. To this end, the adhered bacterial cells were fixed by immersion in a PBS solution containing 4% formaldehyde and 1% glutaraldehyde (both from Sigma-Aldrich, US) at 4 °C for 1 hour. Subsequently, the samples were dehydrated by washing with MilliQ water for 10 minutes, 50% ethanol for 15 minutes, 70% ethanol

for 20 minutes, and 96% ethanol for 20 minutes, respectively. Eventually, they were soaked in hexamethyldisilazane (Sigma-Aldrich, US) for 30 minutes. After being air-dried, a thin layer of gold was sputtered on the samples before imaging by SEM at different magnifications and the tilt angles of 0° and 45°.

Live/dead staining

To investigate the bactericidal properties of the surfaces, the live/dead staining of the adhered bacteria was performed using L7012 Live/Dead *BacLight* Bacterial Viability Kit (Invitrogen, US) after 18 hours of culture according to the manufacturer's instructions.⁴⁴ Briefly, the non-adherent bacteria were removed by removing the medium from the wells. The samples were then washed twice by 0.85% (w/v) NaCl solution. Subsequently, the adherent bacteria were stained by a 1:1 mixture of SYTO 9 green-fluorescent and propidium iodide red-fluorescent stains for 15 minutes at room temperature to distinguish between the live and dead bacteria based on their membrane integrity. Following the staining, the samples were rinsed again with 0.85% (w/v) NaCl solution and were then imaged (magnification: 20x) by a Luca R 604 widefield fluorescence microscope (Andor Technology, UK). Five different areas of each sample were imaged and the number of live and dead bacteria was quantified using the ImageJ Analyze Particles command. The percentage of dead cells per surface was reported as the killing efficiency of the surface.

CFU counting

CFU counting was performed as a complementary method to compare the bactericidal properties of flat Ti and bTi surfaces. After 18 hours of culture, the supernatant BHI broth was collected to quantify the number of non-adherent bacterial cells. 100 µl aliquots of ten-fold serial dilutions were plated on BHI agar plates and CFU were manually counted after overnight incubation at 37 °C. On the other hand, the bacterial cells adhered to each sample were collected by sterile cotton swabs and were ultrasonicated in 1 ml PBS for 15 minutes using an Elmasonic S 30 ultrasonic cleaning unit (Elma Schmidbauer GmbH, Germany). The detached bacterial cells were plated on Petrifilm aerobic count plates (3M, US) and were incubated at 37 °C overnight. The red dots appeared on the Petrifilms as indicators of viable cells were manually counted.

7.2.4 Statistical analysis

For all of the above-mentioned experiments, the raw data were first tested for normal distribution using the D'Agostino-Pearson omnibus normality test in Prism version 8.4.3 (GraphPad, US). In the cases where the sample size was too small for such a test, the Shapiro-Wilk normality test was performed. The Brown-Forsythe and Welch ANOVA test was then performed, followed by Dunnett's T3 multiple comparisons test to determine the statistical significance of the differences between the means of the different experimental groups. Since the results of the surface wettability and Runx2 staining experiments were found to be not normally distributed, the nonparametric Kruskal-Wallis test was performed, followed by Dunn's multiple comparisons test. In addition, the results of the PrestoBlue assay for both mammalian and bacterial cells were analyzed using the two-way ANOVA test, followed by Tukey's multiple comparisons *post hoc* analysis. A *p*-value below 0.05 was considered to indicate statistical significance.

7.3 Results

7.3.1 Physicochemical characterization of bTi surfaces

All Ti surfaces appeared black after the completion of the etching process as expected, due to the light absorption within the fabricated structures^{45, 48}. Scanning electron microscopy (SEM) observations showed that three types of surface topography had been created on Ti (Figure 7.1a). These were distinguishable based on their geometry and spatial organization, by changing two processing parameters, namely chamber pressure and temperature. The Ti surface topography changed from the polished flat surface (Figure S7.1a) due to the formation of pillar-shaped structures on the surface. A chamber temperature of 0 °C and a pressure of 4.0 Pa resulted in closely-packed and short pillars, mainly connected to each other at the tip, hence resembling a porous-like surface when viewed from the top. This type of bTi is, therefore, referred to as Porous. Here, the grain boundaries of the original polished surface were also visible (Figure 7.1a). By increasing the temperature to 40 °C and decreasing the pressure to 2.0 Pa, the pillars appeared to be taller and more separated from each other, meaning that the height of the pillars became distinguishable to some extent in the SEM images. The pillars were, however, still connected to some degree, forming partitions of pillars on the surface. Keeping the temperature at 40 °C while decreasing the pressure to 0.5 Pa resulted in the third type of morphology in which the pillars were taller and relatively widely separated

from each other, meaning that the height of the pillars could be measured. These pillars also showed clustering at the tip creating free interspaces between the clusters (Figure 7.1a). Henceforward, we call the former type of bTi Partition and the latter Sparse. Unlike controlled patterns consisting of surface pillars²⁴, it is not easy to attribute a precise interspacing value to these surface features. Precise, objective measurement of the diameter of the single pillars was also difficult as many pillars were closely connected to each other, especially in the Porous and Partition samples. However, the tip diameter of the pillars was always < 100 nm. From the SEM images, it could be estimated that the height of the pillars increased from the submicron scale, from ≈ 350 nm in the Porous, to a range of 700 nm to 1 μm in Partition, and then to the microscale in the Sparse samples (a range of 1.4 to 2.2 μm) (Figure 7.1a). Further atomic force microscopy (AFM) characterizations revealed that due to the formation of the pillars, the average roughness (R_a) of the surfaces increased from < 50 nm in the Porous group to > 150 nm in the Partition and Sparse groups (Table S7.1). Furthermore, the chemical characterization of the bTi surfaces indicated that the most abundant chemical elements of the surface are Ti and O (Figure 7.1b).

Additionally, while the flat Ti surface showed a static water contact angle of $\approx 75^\circ$, the bTi surfaces exhibited significantly lower contact angles, indicating their superhydrophilic properties. The approximate water contact angle measured for the Porous surface was 15° , which significantly decreased to $< 6.0^\circ$ for the Partition and Sparse groups (Figure 7.1c).

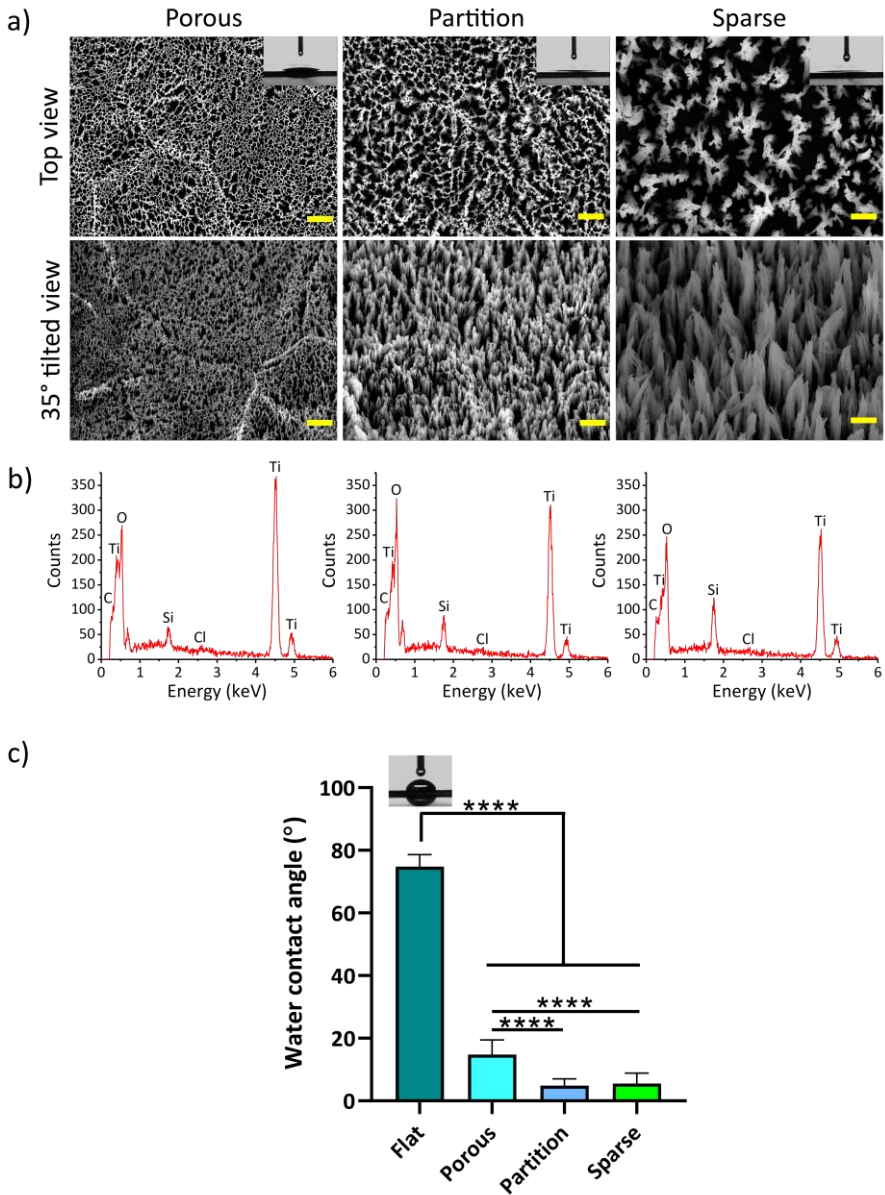


Figure 7.1. a) The top- and tilted-view SEM images of the Porous, Partition, and Sparse bTi specimens made through ICP RIE, showing distinct surface morphologies and spatial organization of the pillars. The insets depict the water droplets residing on each surface after 5 seconds. Scale bar = 1 μm. b) Representative EDS spectra of Porous, Partition, and Sparse bTi specimens, showing the most abundant chemical elements identified on each surface. c) The mean water contact angle of the bTi surfaces as compared to the flat Ti surface ($n = 3$ per group, Kruskal-Wallis test followed by Dunn’s test, **** $p < 0.0001$).

7.3.2 Short-term response of preosteoblast cells

MC3T3-E1 preosteoblast cells showed different morphologies on the different types of bTi after 1 day in culture (Figure 7.2a). While the cells possessed a well-spread and polygonal shape on flat Ti, their directionality highly increased on the etched samples, from the Porous to the Partition and to the Sparse specimens (Figure 7.2a). This change in shape was associated with a decrease in cell area and an increase in the aspect ratio (Figures 7.2a and 7.3a,b). On the Partition samples, the cells developed long filopodia around the cell periphery to attach on these surfaces whereas on the Sparse surfaces, the majority of the cells were highly elongated with a significant number of the cells also showing to be isotropic (*i.e.*, nearly fully rounded). None of the bTi surfaces were found to be cytotoxic, as the results of the PrestoBlue assay showed that the metabolic activity of the cells significantly increased over the course of the 14 days of culture without any significant differences compared to the flat Ti (Figure 7.2b). Moreover, the cells did not show any profound preferential adhesion toward any of the surfaces (flat Ti and bTi) as the average number of the adhered cells per mm² of the specimen surface was not significantly different between any of the experimental groups, including the control and bTi groups (Figure S7.2a).

In addition to differences in cell area and aspect ratio, the nucleus area of the cells was also significantly decreased on all types of bTi as compared to flat Ti (Figure 7.3c). However, the trend was not similar to the cell spreading area. For instance, although the cells had a larger area on the Porous specimens as compared to the Partition specimens, the opposite was observed for the cell nucleus area.

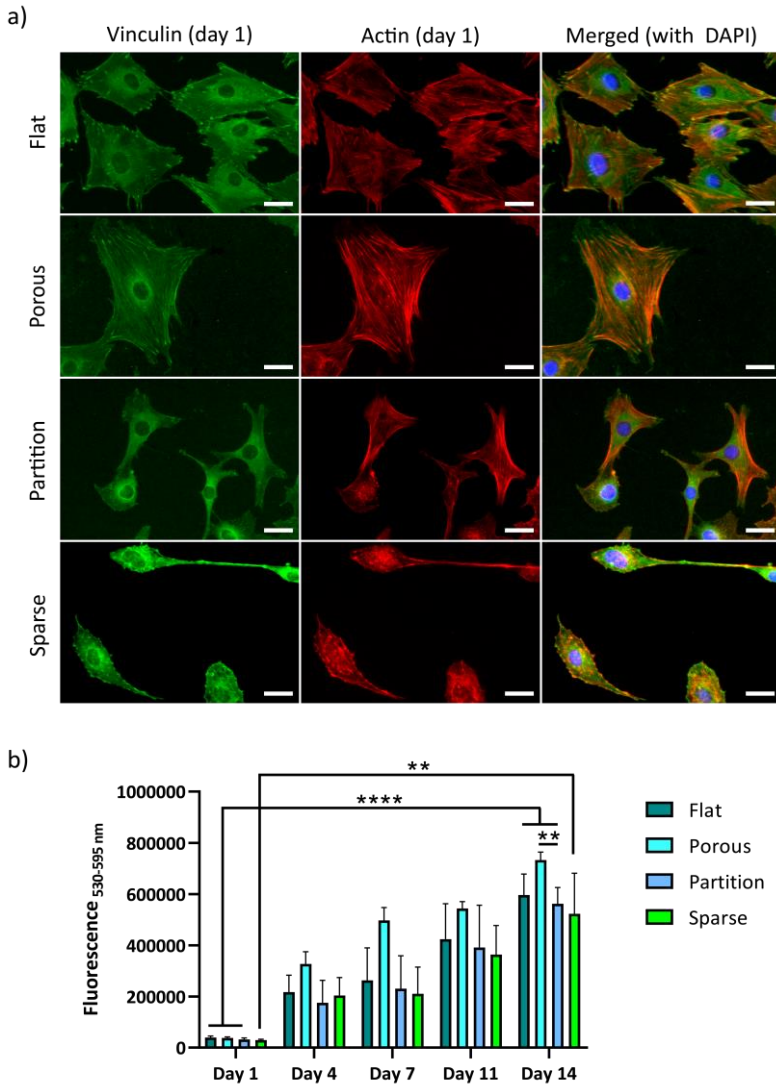


Figure 7.2. a) The immunocytochemical staining of vinculin (green), actin (red), and nucleus (blue, merged with the last two channels) for the MC3T3-E1 preosteoblast cells cultured on the flat Ti, Porous, Partition, and Sparse bTi specimens after 1 day. All surfaces except Sparse support the spreading of cells. Unlike the polygonal cell morphology on those samples, the majority of the cells are highly elongated on the Sparse specimens. Moreover, the colocalization of FAs and actin fibers can be detected in the Porous and Partition groups but not on the surface of the Sparse specimens. Scale bar = 30 μm. b) The metabolic activity of the preosteoblast cells cultured on the flat Ti and bTi surfaces measured by the PrestoBlue assay over 14 days. The increased metabolic activity of the cells with time indicates the cytocompatibility of all surfaces ($n = 4$ per group, Two-way ANOVA followed by Tukey’s test, ** $p < 0.01$ and **** $p < 0.0001$).

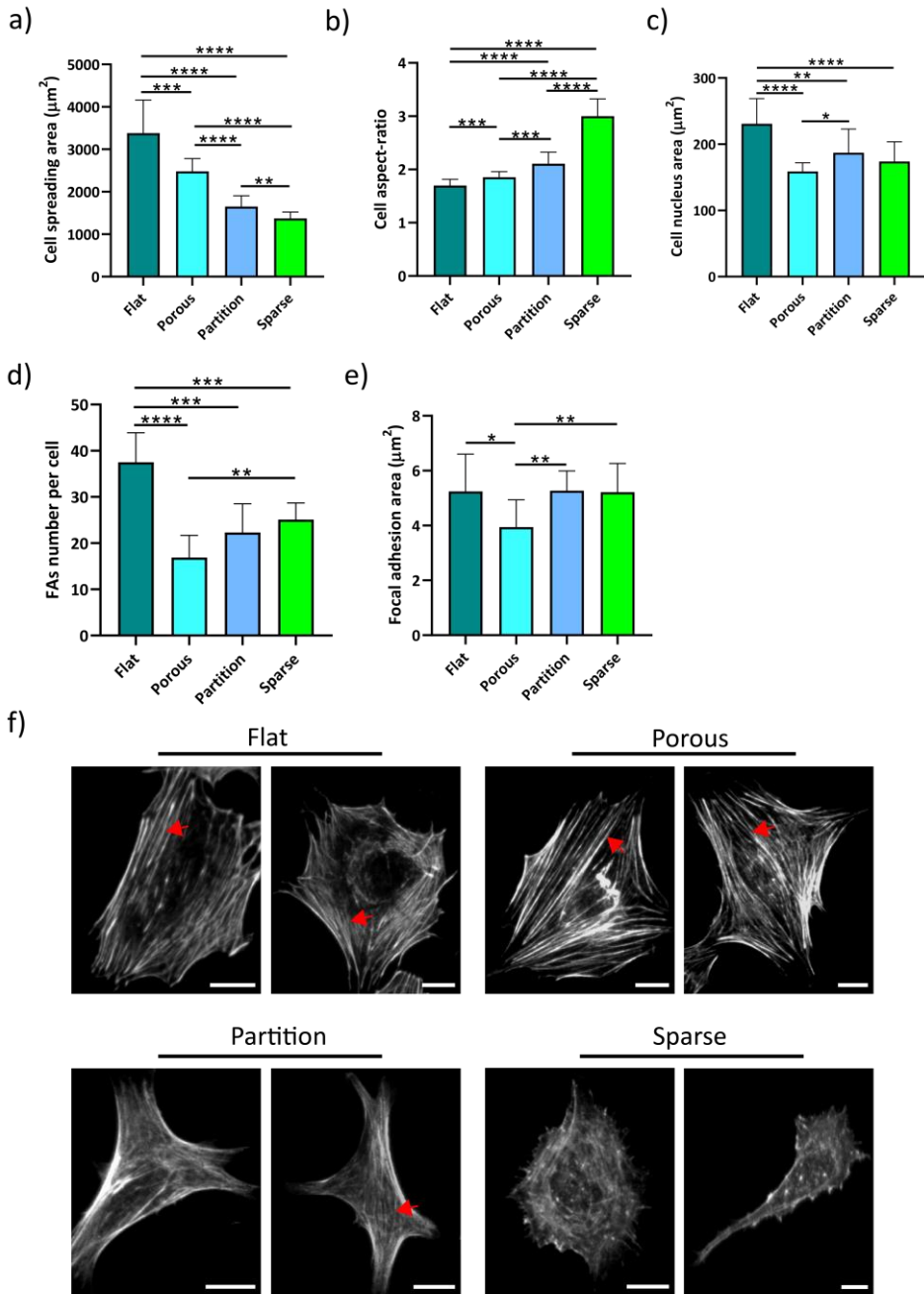


Figure 7.3. The morphological characteristics and early responses of the preosteoblast cells cultured on the flat Ti and bTi surfaces after 1 day of culture. a) Spreading area. The cells spreading area significantly decreased for taller and more separated pillars. b) Cell aspect ratio. The elongation of the cells (*i.e.*, their aspect ratio) gradually increased when going from the flat specimens to the Sparse specimens. c) Cell nucleus area. The cell nuclei were observed to be smaller on the bTi surfaces, especially in the case of the Porous group. Moreover, the fully rounded morphology of the nucleus on the surface of the Porous specimens slightly shifted to a more elongated morphology on the Partition and Sparse specimens (subfigure f). d) Number of FAs per cell. Cells residing on bTi specimens formed significantly lower number of FAs compared to the flat Ti (regardless of the type of topography). e) FA area. The cells residing on the Porous bTi were found to form smaller FAs as compared to those inhabiting the surface of flat Ti and other types of bTi ($n = 4$ per group, Brown-Forsythe and Welch ANOVA followed by Dunnett's T3 test, * $p < 0.05$, ** $p < 0.01$, *** $p < 0.001$, and **** $p < 0.0001$). f) The gray-scale images of the cytoskeleton. The organization of the cytoskeleton can be seen in the form of parallel actin fibers (shown by red arrows) on flat Ti and Porous bTi. Actin fibers appear to be partially organized in the case of the Partition specimens. No organization was observed in the case of the Sparse specimens. Scale bar = 20 μm .

The FAs formed at the periphery of the cells on the flat Ti, Partition, Porous, and Sparse specimens (Figure 7.2a). The average number of FAs per cell was significantly lower on all bTi specimens as compared to flat Ti (Figure 7.3d). The area of FA corresponding to flat Ti, Partition, and Sparse groups was on average 5.2 μm^2 , which significantly decreased to 3.9 μm^2 in the Porous samples (Figure 7.3e). The bending of the pillars of the Partition and Sparse specimens beneath the cell body, especially at the directional zones where FAs are present, was observed in SEM images (Figure 7.4a). In addition, even though the majority of the FAs formed on all surfaces had an area of 2-6 μm^2 , the cells residing on the Partition and Sparse samples formed some far larger FAs (Figure 7.4c). Furthermore, different cytoskeleton organization was observed. For the cells residing on the flat Ti and Porous specimens, clear actin stress fibers were formed, which were primarily oriented along the cell length (Figures 7.2a and 7.3f). This organization decreased on the Partition surfaces and almost disappeared on the Sparse surfaces.

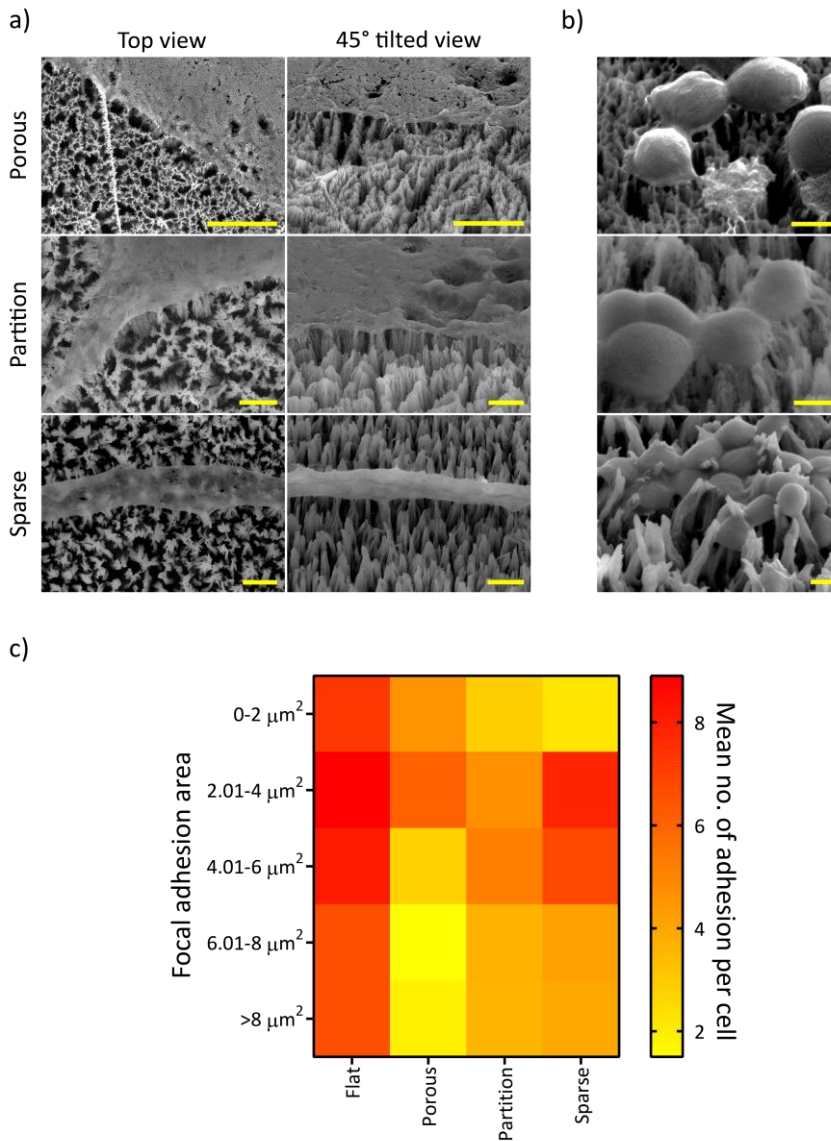


Figure 7.4. A closer look at the interactions of the preosteoblasts and bacterial cells with bTi surfaces. a) The top- and tilted-view SEM images of the directional regions of the preosteoblast cells. The cells can easily hold on to the abundant physical features present on the Porous surface as their anchorage points. On the Partition surfaces, it is not yet difficult to find enough anchorage points. The bending of the pillars can also be seen underneath the area in which FAs have been formed preferentially. The cells residing on the Sparse surfaces develop extremely long membrane extensions, probably in search of more contact points. Scale bar = 2 μm . b) The interactions of *S. aureus* with the bTi surfaces. Scale bar = 500 nm. c) The heat map of the size distribution of FAs on the flat Ti and bTi surfaces.

7.3.3 Expression of osteogenic markers in preosteoblast cells

After 9 days of culture, immunocytochemical staining revealed the presence of Runx2 in the nuclear area of the cells residing on the surfaces of the flat Ti, Porous, and Partition specimens (Figure 7.5a). The average stained area per cell was not significantly different between those three groups (Figure 7.5b). However, no Runx2 was detected in the vicinity of the nuclei of the cells cultured on the surface of the Sparse specimens. Furthermore, after 14 days, significantly higher numbers of calcium depositions were formed in the matrix of the cells populating the surfaces of the Porous and Partition specimens as compared to those associated with the flat Ti and Sparse specimens (Figures 7.5a and S7.2b). The largest area of mineralized nodules belonged to the Partition specimens, which was significantly higher than all other groups. Porous surface was in the second place, while flat Ti and Sparse samples showed a lower capacity for inducing calcium deposition (Figure 7.5c).

7.3.4 Early bactericidal effects of bTi surfaces

The live/dead staining of the adherent *S. aureus* bacteria after 18 hours (Figure 7.6a,b) showed that all bTi surfaces had bactericidal activity, which increased from the Porous to the Partition and to the Sparse surfaces. On average, only 8% of the bacterial cells were found dead on flat Ti samples. The mean percentage of dead bacteria increased to 25 (SD 5%), 35 (SD 5%), and 42 (SD 7%) for the Porous, Partition, and Sparse specimens, respectively. The morphological evaluation of bacteria by SEM showed that they had a normal coccoid shape on flat Ti while they were stretched on the Porous specimens with a flattened morphology (Figure 7.6a). On Partition surfaces, stretching of the bacteria between adjacent pillars was even more visible. The penetration of the pillars into the cell wall was also detected, especially in the cells residing on top of the pillars (Figure 7.6a). The bacteria also bent the pillars underneath them (Figure 7.4b), which might impose additional mechanical forces on the bacterial cell wall.⁵¹ The bacteria adhered to the Sparse samples were observed to be both stretched between the lateral sides of adjacent pillars and punctured by the sharp tips of the pillars (Figure 7.6a). The cells were even present in the interspaces between the clustered pillars as some of these spaces exceed the size of the bacteria (≈ 800 nm in diameter). Cells with normal morphology were hardly present on this type of surface. These findings were confirmed by the quantitative results of the CFU counting that showed that there is a significant difference

between the flat Ti and bTi (Partition and Sparse) in terms of the number of bacteria capable of forming a colony after being cultured on these samples (Figure 7.6c). As expected, none of the surfaces had an influence on the viability of non-adherent bacteria (Figure S7.2d). Moreover, performing the PrestoBlue assay at four different time points indicated that the bacterial metabolic activity is significantly lower on all bTi surfaces as compared to flat Ti at least after the first hour after culture (Figure 7.6d). This difference was also observed at 4, 8, and 18 hours of culture. Comparing the different types of bTi, the metabolic activity of the bacteria increased until 4 hours and then remained at the same level until 8 hours after which it declined.

7.4 Discussion

Developing cell-instructive biomaterials could shift the paradigm in the fabrication of orthopedic implants. The introduction of bactericidal bSi surfaces⁴⁵ drew attention to the use of (ICP) RIE for the fabrication of high aspect ratio pillars on the surface. Consequently, bactericidal bTi has been introduced as a promising biomaterial for preventing IAIs⁴⁸. To date, numerous studies^{46, 47, 52} have focused on the biological properties of bSi and bTi surfaces, trying to optimize the dimensions of the pillars by changing one single processing parameter (*i.e.*, etching time). It was reported that minute changes in the characteristics of such etched structures may influence their biological properties⁵³. Yet a wider range of surfaces can be produced by taking advantage of other (ICP) RIE processing parameters⁴⁴. Therefore, the optimum etched surfaces for a certain or multiple bio-functionality are yet to be established. Moreover, the literature offers limited data on the interactions of bTi surfaces with mammalian cells, especially those involved in the regeneration of bone tissue. Not much is known about the relationship between the early and long-term responses of the cells interacting with different bTi surfaces. Therefore, we tried to further explore the fabrication process (*i.e.*, the chlorine-based maskless ICP RIE of Ti) and generate a couple of distinct bTi surfaces in an attempt to find a surface that provides the best dual-functionality (from both osteogenic and bactericidal points of view).

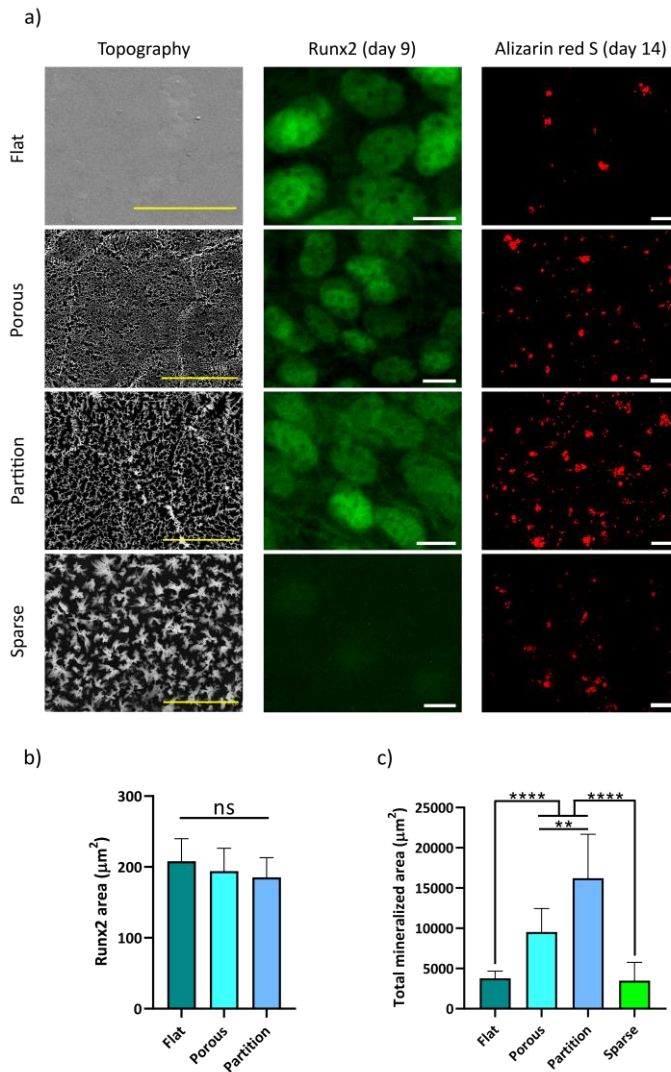


Figure 7.5. The long-term osteogenic response of the preosteoblasts cultured on the flat Ti and bTi surfaces. a) The immunocytochemical staining of Runx2 and visualization of calcium deposits in the matrix by Alizarin red S assay after 9 and 14 days of culture, respectively. Scale bar = 5, 15, and 100 µm, for representative images of surface topographies, Runx2 and Alizarin red S, respectively. While the Porous and Partition bTi groups supported the expression of Runx2 as an early marker of osteogenic differentiation, the Sparse group inhibited it. b) Runx2 expression ($n = 4$ per group, Kruskal-Wallis test followed by Dunn's test). Although the average stained area for Runx2 was not significantly different between flat Ti, Porous, and Partition, the last two significantly increased c) the total mineralized area on the surfaces ($n = 4$ per group, Brown-Forsythe and Welch ANOVA followed by Dunnett's T3 test, ** $p < 0.01$ and **** $p < 0.0001$). Overall, the Partition bTi specimens showed the highest osteogenic potential among the different surfaces considered here.

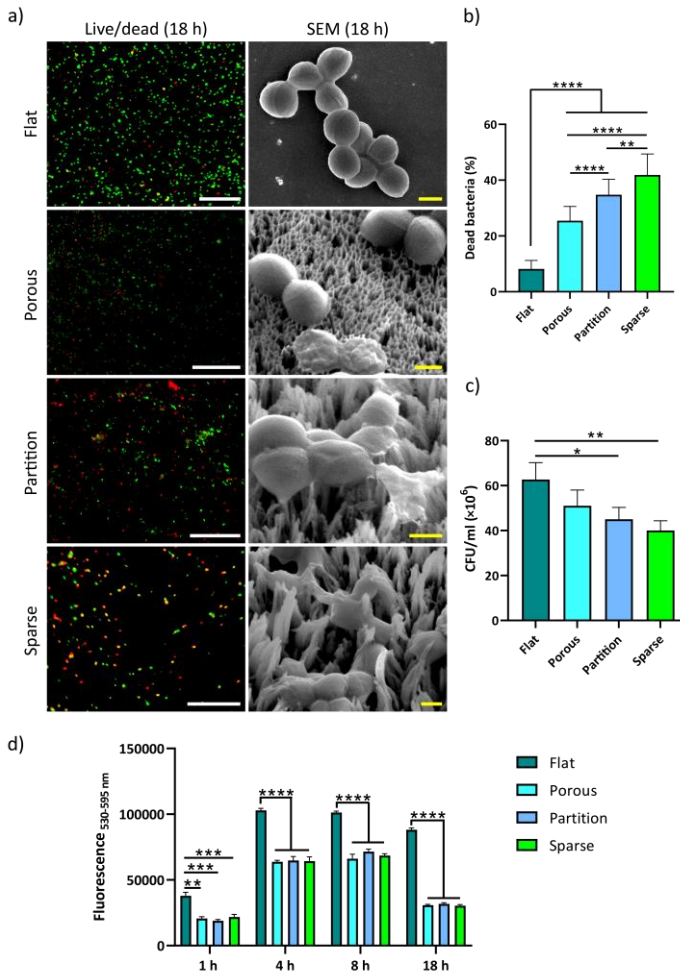


Figure 7.6. The bactericidal properties of flat Ti and bTi surfaces. a) The representative live/dead and SEM images of *S. aureus* cells cultured on surfaces for 18 hours. Green and red cells indicate viable and dead bacterial cells in the live/dead images, respectively. While *S. aureus* has a normal coccoid shape on flat Ti, unusual flattened and ruptured morphologies were observed on the bTi surfaces. Scale bar = 20 μm and 500 nm for the live/dead and SEM images, respectively. b) The quantification of non-viable bacterial cells based on live/dead images. All surfaces exhibited killing efficiencies significantly higher than that of the flat surface, with the Sparse group being the most efficient antibacterial surface. c) The results of CFU counting showed a similar trend regarding the bactericidal properties of the bTi surfaces. d) The metabolic activity of the bacterial cells cultured on the flat Ti and bTi surfaces, measured by the PrestoBlue assay over 18 hours. All the bTi surfaces significantly decreased the bacterial metabolic activity from the first hour of culture. At 4 hours, higher metabolic activity was measured but it did not continue increasing ($n = 3$ per group, Brown-Forsythe and Welch ANOVA followed by Dunnett's T3 test for b and c, Two-way ANOVA followed by Tukey's test for d, * $p < 0.05$, ** $p < 0.01$, *** $p < 0.001$, and **** $p < 0.0001$).

7.4.1 Looking at the Ti pillars from a physicochemical perspective

Among the ICP RIE processing parameters, the temperature and pressure of the chamber are two variables that significantly impact the etching rate and morphology of the resulting structures⁴⁴. At higher pressures, the energy of ions and radicals decreases as a result of the increased number of collisions between them, which eventually decreases the etching rate (*i.e.*, yields shorter pillars for a constant etching time). Increasing the temperature enhances the etching rate of the sidewalls of the initially formed pillars, resulting in further separation and lower compactness of the pillars. By changing these two conditions, we generated surfaces with increased pillar heights and interspaces between the clustered pillars. These changes are, however, not systematic as the height and interspace changed simultaneously in each bTi design. Yet, each surface was distinct from the rest by its unique combination of the height and organization of the pillars. Therefore, the biological properties of these surfaces should be associated with a combination of both of those parameters and not with the isolated effects of either. The height of the pillars increased from less than 400 nm to more than 1400 nm whereas the diameter was always less than 100 nm leading to an enhanced aspect ratio of the resultant structures. The interspace between the clustered/connected pillars also increased with the increase in height.

The chemical characterization of the bTi surfaces showed that the pillars mainly consist of Ti and O. The presence of an oxide layer on the surface has been confirmed by XPS analysis in other ICP RIE studies^{48, 53}. Furthermore, during the etching process, chlorine as the main etchant gas, the aluminum-made chamber wall, the quartz carrier wafer, and the organic solvents used for cleaning can respectively introduce negligible amounts of Cl, Al, Si, and C to the final etched Ti surface. Nevertheless, the bio-inertness of titanium is still preserved in form of TiO_x as the main component of the etched structures⁴⁴.

All bTi surfaces used in this study were found to be superhydrophilic. The trend of the measured water contact angle of the surfaces was in line with a previous study⁴⁴ that showed that decreasing the temperature and, thus, the formation of more compact nanostructures leads to larger water contact angles as compared to the specimens fabricated at higher temperatures (*e.g.*, 40 °C). Hasan *et al.*⁴⁸ have shown that the wettability of bTi enhances with increased surface roughness. Similarly, the rougher

samples in our study (Partition and Sparse) are the most hydrophilic surfaces. Yet the opposite trend in the relationship between wettability of bTi surfaces and the surface roughness in another study⁵³ suggests that the wettability model applicable to these types of surfaces is largely dependent on the dimensions of the pillars, as well as their interspacing⁵⁴.

7.4.2 Adaptation of preosteoblast cells to bTi surfaces

The results of this study together with other previous studies form a body of evidence to refute any possible cytotoxicity of bTi surfaces as long as the aspect ratio of the pillars remains below 20^{55, 56}. Based on the metabolic activity measurements and microscopic observations, preosteoblast cells could easily proliferate on all types of the bTi studied here. However, the cells varied in terms of their morphology and cytoskeleton organization, which influence the behavior of preosteoblasts as anchorage-dependent cells. Cells try to find as many suitable anchorage points as possible upon which the integrins can optimally bind to the protein ligands adsorbed on the surface^{29, 57}. On the Porous specimens, there are plenty of physical features that cells can reach onto without stretching their membrane extremely. This is starting to change on the Partition samples where cells need to develop membrane extensions in the form of filopodia to attach on the taller and partitioned pillars. The Sparse samples do not provide cells with close-enough features. Consequently, the cells tend to minimize their spreading area and keep connected via very long extensions leading to the elongated shapes observed⁵⁷. The gradual increase in the aspect ratio of the cells from flat Ti to Sparse surfaces should, therefore, be considered in this context.

The formation of FAs and the global cytoskeletal remodeling via the formation of actin bundles play a crucial role in determining the ultimate cell fate⁵⁸. Even the smallest surface features (2-4 nm in height) made of titanium have been shown to trigger a rapid reorganization of the cytoskeleton⁵⁹. The mechanical forces exerted on the cells are transferred to the cell nucleus via the complex chains of integrins, FAs, and actin fibers, and then processed via different pathways and feedback loops. The analysis of FAs showed that by developing more directional protrusions in the cells residing on the Partition and Sparse specimens, FAs are regularly formed in the proximity of these polarized regions. This phenomenon is corroborated by previous studies that showed that the anisotropy of FAs distribution increases as the cell aspect ratio increases^{60, 61}. On the flat Ti, however, the formation of FAs could be detected at the periphery of the cells and

also in the more internal regions of the cell body (closer to the cell nucleus). Moreover, on these surfaces, FAs were mainly oval-shaped and aligned with the actin fibers along their long axis (Figure 7.2a). The colocalization of FAs and actin fibers indicates the maturation of FAs and the establishment of a strong adhesion by coupling to the actin fibers (*i.e.*, stable FAs with a slow turnover rate)^{57,62}. On the contrary, the FAs of the cells residing on the Partition and Sparse specimens were relatively round and not yet mature. The colocalization of FAs and actin fibers is hardly recognizable on the Sparse samples. It can be assumed that short-lasting colocalization is another sign of a more migratory state in the cells residing on the Sparse specimens⁵⁷. The actin fibers are well-oriented only inside the well-spread cells on the flat Ti and Porous specimens. On the other surfaces, the cells may be either already in the polarization phase or the contractile spreading phase, according to their morphology and cytoskeletal organization (Figures 7.2a and 7.3f)⁶³. In the contractile spreading phase, the actin bundles are still being formed and the cells intend to form strong adhesion to the surface. The abundant presence of filopodia in these cells and their smaller areas indicate such effort by the cells. It can, therefore, be concluded that the cells undergo a more difficult or slower adaptation to the Partition and Sparse surfaces as compared to the other surfaces.

7.4.3 FA-mediated mechanical interactions with the surface

The difference in the size of FAs (denoted by their area) on different surfaces may also indicate different levels of mechanical tensions exerted on the cells. The average size of FAs is significantly larger on the Partition, Sparse, and flat Ti groups as compared to the Porous specimens. That is likely because the cells struggle to effectively adhere to very smooth surfaces (*e.g.*, flat Ti) or to highly separated pillars of the Sparse group, which is why they form larger FAs. The dynamic and force-dependent process of recruiting proteins, such as vinculin⁶⁴ to the FA sites is yet to be fully understood⁶⁵. Not only could this process be cell type-dependent¹¹ but may also vary when studying the different types of surface topography and different culturing times. For instance, similar to the results of this study, the MC3T3-E1 cells have been shown to form larger FAs on surfaces with increased pillar interspacing⁶⁶. In comparison, hMSCs form larger FAs as their spreading area increases⁶⁷ while neuronal stem cells exhibit an increased expression of FAs (increasing the adhesion) on grooves and pillars with smaller interspacing as compared to their more separated counterparts⁶⁸. Nevertheless, the variations in the size of FAs in this study indicate different local traction forces that the cells exert on the pillars. It has

been shown that although a correlation between the size of FAs and traction forces exists during the initial stages of adhesion, the same does not apply to mature adhesions⁶⁹. In other words, mature FAs can withstand extremely increased tensions (up to sixfold) without any changes in their size. As described above, the FAs of cells residing on the Porous samples are mature long-lasting ones while the FAs present on the surface of the Sparse specimens are rather nascent adhesions. Moreover, super-resolution imaging has shown that some of the studies that had concluded such correlations between the size of FAs and the generated force, had, in fact, considered multiple small adhesions as a large adhesion⁷⁰. The further evaluations of the adhesion forces using novel AFM-based methods and computational analysis are necessary to improve our understanding of FA-mediated mechanical interactions of cells with such pillars⁷¹.

The size and distribution of FAs also affect the nuclear morphology and remodeling as the nuclear dynamics are controlled by the tensions that are exerted at the adhesion points and propagate through the actin fibers to their nuclear cap^{72,73}. It has been argued that applying higher tensions to the cell nuclei via smaller FAs, which are unevenly distributed and, therefore, stretch the nuclei to some extent, enhances the osteogenic differentiation⁷³. In our study, the heterogeneous distribution of FAs in Partition and Sparse samples has changed the fully rounded morphology of cell nuclei in many cells toward a more elongated morphology (Figure 7.3f). The changes in the size and orientation of nuclei together with the forces exerted via FAs may explain the long-term osteogenic response of the cells on the different surfaces.

7.4.4 Osteogenic properties of bTi from a mechanotransduction perspective

The mechanotransduction pathways by which the environmental mechanical stimuli cause alterations in the expression of certain genes and the transcription of their correspondent proteins have been spotlighted but are not completely understood yet. A plethora of subcellular components are involved in these processes starting from the integrins bound to the membrane and continuing all the way to the inside of the nucleus. For instance, focal adhesion kinase (FAK) is known to play a vital role in the regulation of other components and can trigger a lot of such intracellular pathways^{65,74}. FAK is associated with the β -subunit of integrins, especially the $\beta 1$ subunit and is able to promote the expression of Runx2 via the FAK/extracellular signal-regulated kinase (ERK) pathway⁷⁵ and also by triggering the mitogen-activated protein kinase (MAPK) cascade^{16,76}. It has

been shown that in MSCs cultured on a variety of surfaces, Runx2 expression is correlated with the reinforcement of FAs⁷⁷. The results of Runx2 staining in our studies can be perceived accordingly. Unlike the flat Ti, Porous, and Partition groups, perinuclear Runx2 was not detected in the Sparse group where there was no cytoskeleton organization and FAs were less stable. FAK is also regarded as the upstream of RhoA activation, which affects cell contractility, spreading, and eventually the osteogenic differentiation of MSCs via the RhoA/ROCK pathway¹⁶. Our results suggest that the inhibition of FAK phosphorylation could be the reason for the downregulation of Runx2 in the Sparse samples. Nevertheless, further studies are required to examine this hypothesis. The analysis of calcium deposits in the matrix after 2 weeks of culture revealed that Porous and Partition surfaces highly enhance matrix mineralization as compared to flat Ti. Although an increased number of FAs is generally considered beneficial for osteogenesis⁷⁸, our findings highlight the importance of surface topography as Porous surface is significantly more osteogenic than flat Ti despite its fewer and smaller FAs. The higher potential of Partition as compared to Porous might also be associated with the different levels of cell spreading and contractility, which influences mechanotransduction pathways more in favor of osteogenesis on the Partition surfaces. A bTi surface consisting of high aspect ratio pillars with a second tier of shorter pillars has been recently shown to increase the calcium deposition in the matrix of human adipose-derived stem cells (hASCs)⁵⁶. Similar to our findings, hASCs had formed fewer FAs as compared to polished titanium samples⁵⁶. Another important intracellular signaling pathway to consider is Yes-associated protein (YAP)/transcriptional coactivator with PDZ-binding motif (TAZ). A higher percentage of YAP localized in the cell nucleus has been shown to be related to an increased formation of FAs and cell tension⁷⁸. Further dedicated experiments are needed to answer questions about the specific role of integrins, mechanotransduction pathways, and culture conditions⁷⁹ in the expression of late osteogenic markers induced by bTi surfaces.

In summary, not fully-separated Ti pillars with an approximate height between 700 and 1000 nm showed the highest potential for inducing matrix mineralization in preosteoblasts. This may be associated with the changes in cell morphology and strong attachment to the surface facilitated by stable FAs. It is noteworthy that the findings related to the adaptation and the osteogenic response of cells in this study cannot be necessarily generalized to other cell types, such as primary osteoblasts or hMSCs. Further

independent studies are required to elucidate the specific responses of those cells to bTi surfaces.

7.4.5 Early interactions of bacteria with bTi

Bactericidal properties are one of the core values of RIE-modified surfaces. The commonly accepted theories regarding the early stage interactions of the bacteria with such surfaces have been explained previously⁴². In the present study, no signs of pillar penetration were observed in the *S. aureus* bacteria interacting with the Porous specimens as all the pillars were connected to each other at their tips. Still, bacteria stretched their cell envelope to be able to find anchorage points on the surface (Figure 7.4b). While $25 \pm 5\%$ of the adhered bacteria were dead on the Porous specimens, the percentage of the dead bacteria reached its peak ($42 \pm 7\%$) for the Sparse group where a combination of the direct penetration of the pillars into the cell wall, the bending of the pillars, the stretching of the cell wall between adjacent pillars, and the sliding down between the pillars were observed (Figure 7.4b). The killing efficiency of these bTi surfaces is expected to be even higher against Gram-negative bacteria such as *Escherichia coli* and *Pseudomonas aeruginosa* due to their thinner cell wall and rod-shaped morphology that increase their susceptibility to the sharp tips of the pillars^{24, 45, 46}. Although the killing efficiency of the Sparse specimens against *S. aureus* is similar to Ti etched for 10 minutes in the study by Linklater *et al.*⁵³, higher killing efficiencies have been also reported for both bSi and bTi, in which the height and arrangement of the pillars are comparable to the Sparse group^{48, 55}. It is noteworthy that the killing efficiency of a surface could vary against different strains of a species due to the differences present in the strain-dependent characteristics of the cells including their motility⁸⁰.

It has been shown that the number of dead *S. aureus* cells on bTi surfaces significantly increases over time (from $\approx 20\%$ after 4 hours to more than 75% after 24 hours)⁴⁸. A similar conclusion can be made for our experiments. The metabolic activity of the bacterial cells attached to bTi surfaces is significantly lower than those attached to the flat Ti at any time point. However, comparing the metabolic activity of bacterial cells within the bTi groups, it increases up to 4 hours and then decreases therefrom. It might confirm that the first 4 hours is the window of opportunity within which bactericidal topographies can inhibit bacterial colonization on the surface. We cannot, however, attribute the decreased metabolic activity solely to the death of bacterial cells. Assuming that the different types of bTi surfaces in this study exert forces of different magnitudes

to the bacterial cells, it would be expected that different signaling pathways may come into play and regulate the cell adhesion, motility, metabolic activity, genomics, and proteomics of the bacteria⁸¹⁻⁸⁴. Further studies are required to scrutinize the killing mechanisms of such surfaces by using a mechanistic approach.

Overall, comparing the responses of the preosteoblast cells and bacteria to that of the bTi surfaces investigated in this study showed that the Partition surfaces with a pillar height of 700-1000 nm and a partially-separated organization exhibit both bactericidal and osteogenic properties. Such a surface was capable of killing a significant percentage of the adherent bacteria while promoting the osteogenic response of cells. These observations suggest that achieving a specific design with balanced bactericidal and osteogenic properties is possible within the capabilities of ICP RIE. In summary, etching the titanium surfaces for 10 minutes with a combination of Cl₂ and Ar gases (flow rates: 30 and 2.5 sccm, respectively), at a high temperature (*i.e.*, 40 °C), and under a moderate chamber pressure (*i.e.*, 2.0 Pa), produces pillars with differential effects on the bacteria and mammalian cells.

7.5 Conclusions

In summary, we investigated the dual-functionality of a series of bTi surfaces as well as the possible mechanisms behind those functionalities. Superhydrophilic etched Ti surfaces, containing pillars with distinct heights and spatial organization, were produced by changing the pressure and temperature of the chamber during the ICP RIE process. Although all groups of the modified Ti surfaces studied here were cytocompatible for the MC3T3-E1 preosteoblast cells, they induced significantly different cell shapes, area, aspect ratio, nucleus area, cytoskeletal organization, patterns of FA formation, and the extent of matrix mineralization. When the pillars were very tall and separated (*i.e.*, Sparse surfaces), the cells possessed the least area possible and exhibited extremely elongated shapes. Moreover, the actin fibers were no longer well-oriented and the colocalization of FAs and actin fibers was lost. On the other hand, on the Porous and Partition surfaces, the cells were well-spread with polygonal shapes. More stable FAs indicated that they may have more intensively transduced the forces exerted to the cells to the nuclei, improving the matrix mineralization most probably by triggering FA-mediated mechanotransduction pathways. Bacteria responded differently to these surfaces too. Sparse surfaces showed the highest killing efficiency against the bacteria. A combination of direct penetration of the pillars into the cell wall and cell wall stretching between

adjacent pillars was observed in this group. Overall, the results of this study show that various ICP RIE conditions can be used to create Ti surfaces that are capable of instructing mammalian cells while killing bacteria. Based on our findings, the Partition surfaces establish a balance between osteogenic and bactericidal properties, which makes it a good candidate for further studies in vivo as a prerequisite for its final use in clinical settings.

7.6 Supplementary information

Table S7.1. The roughness analysis of the bTi surfaces measured by AFM.

bTi surface	R_a (nm)	R_q (nm)
Porous	44 ± 11	55 ± 13
Partition	157 ± 6	203 ± 10
Sparse	151 ± 16	188 ± 14

Table S7.2. Statistical significance of differences within study groups in PrestoBlue assay (bacteria) at different time points (** $p < 0.01$ and **** $p < 0.0001$).

Flat	4 hours	8 hours	18 hours
1 hour	****	****	****
4 hours		ns	****
8 hours			****
Porous	4 hours	8 hours	18 hours
1 hour	****	****	****
4 hours		ns	****
8 hours			****
Partition	4 hours	8 hours	18 hours
1 hour	****	****	****
4 hours		**	****
8 hours			****
Sparse	4 hours	8 hours	18 hours
1 hour	****	****	**
4 hours		ns	****
8 hours			****

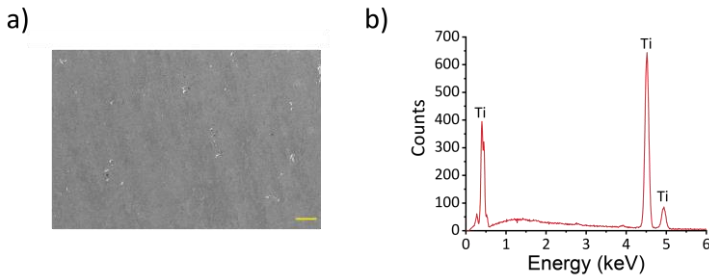


Figure S7.1. a) SEM image of polished non-etched Ti surface (flat Ti). Scale bar = 20 μm . b) Representative EDS spectrum of flat Ti.

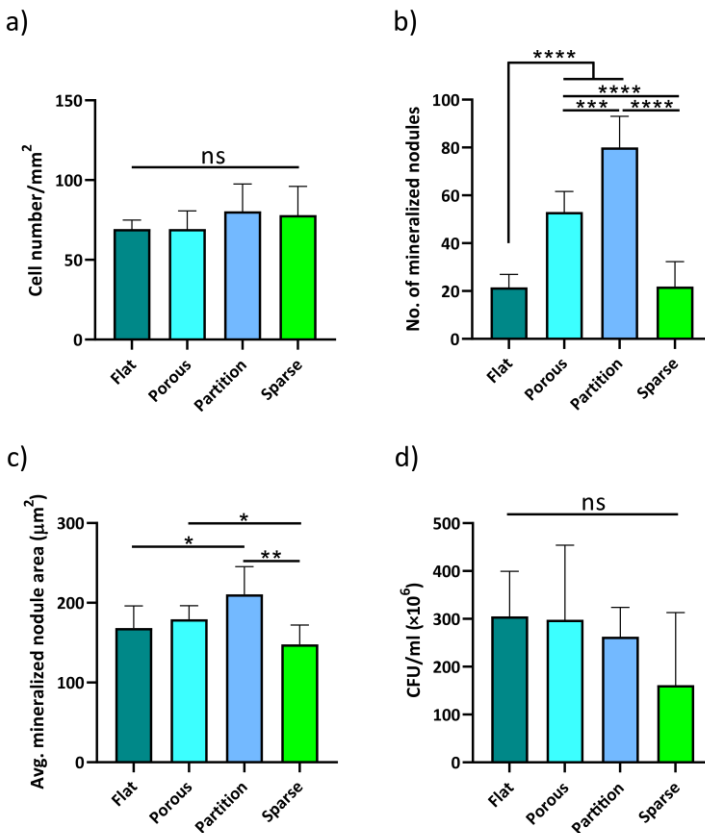


Figure S7.2. a) The average number of attached preosteoblast cells per mm² of flat Ti and bTi surfaces. b) The average number of mineralized nodules on different surfaces after 14 days of culture. c) The average area of single mineralized nodules deposited in matrix on flat Ti and bTi surfaces. d) The results of CFU counting of non-adherent bacterial cells ($n = 4$ per group for a, b, and c, $n = 3$ per group for d, Brown-Forsythe and Welch ANOVA followed by Dunnett's T3 test, * $p < 0.05$, ** $p < 0.01$, *** $p < 0.001$, and **** $p < 0.0001$).

Bibliography

- [1] A. Falco, M. Berardini, P. Trisi, Correlation Between Implant Geometry, Implant Surface, Insertion Torque, and Primary Stability: In Vitro Biomechanical Analysis, *International Journal of Oral & Maxillofacial Implants*, 33(4), 824-830, 2018.
- [2] I.C. Chou, S.Y. Lee, C.P. Jiang, Effects of implant neck design on primary stability and overload in a type IV mandibular bone, *International Journal for Numerical Methods in Biomedical Engineering*, 30(11), 1223-1237, 2014.
- [3] R. Hedayati, M. Sadighi, M. Mohammadi-Aghdam, A. Zadpoor, Mechanical behavior of additively manufactured porous biomaterials made from truncated cuboctahedron unit cells, *International Journal of Mechanical Sciences*, 106, 19-38, 2016.
- [4] E. García-Gareta, M.J. Coathup, G.W. Blunn, Osteoinduction of bone grafting materials for bone repair and regeneration, *Bone*, 81, 112-121, 2015.
- [5] A. Barradas, H. Yuan, C.A. van Blitterswijk, P. Habibovic, Osteoinductive biomaterials: current knowledge of properties, experimental models and biological mechanisms, *European Cells & Materials*, 21, 407-429, 2011.
- [6] A.L. Overmann, C. Aparicio, J.T. Richards, I. Mutreja, N.G. Fischer, S.M. Wade, B.K. Potter, T.A. Davis, J.E. Bechtold, J.A. Forsberg, Orthopaedic osseointegration: Implantology and future directions, *Journal of Orthopaedic Research*, 38(7), 1445-1454, 2020.
- [7] C.R. Arciola, D. Campoccia, L. Montanaro, Implant infections: adhesion, biofilm formation and immune evasion, *Nature Reviews Microbiology*, 397-409, 2018.
- [8] A. Trampuz, A.F. Widmer, Infections associated with orthopedic implants, *Current Opinion in Infectious Diseases*, 19(4), 349-356, 2006.
- [9] U. Filipović, R.G. Dahmane, S. Ghannouchi, A. Zore, K. Bohinc, Bacterial adhesion on orthopedic implants, *Advances in Colloid and Interface Science*, 283, 102228, 2020.
- [10] L. Li, J. Eyckmans, C.S. Chen, Designer biomaterials for mechanobiology, *Nature Materials*, 16(12), 1164-1168, 2017.
- [11] K. Anselme, P. Davidson, A. Popa, M. Giazzon, M. Liley, L. Ploux, The interaction of cells and bacteria with surfaces structured at the nanometre scale, *Acta Biomaterialia*, 6(10), 3824-3846, 2010.
- [12] M.M. Stevens, J.H. George, Exploring and engineering the cell surface interface, *Science*, 310(5751), 1135-1138, 2005.
- [13] H. Amani, H. Arzaghi, M. Bayandori, A.S. Dezfuli, H. Pazoki-Toroudi, A. Shafiee, L. Moradi, Controlling cell behavior through the design of biomaterial surfaces: a focus on surface modification techniques, *Advanced Materials Interfaces*, 6(13), 1900572, 2019.
- [14] D. Baptista, L. Teixeira, C. van Blitterswijk, S. Giselsbrecht, R. Truckenmüller, Overlooked? Underestimated? Effects of substrate curvature on cell behavior, *Trends in Biotechnology*, 37(8), 838-854, 2019.
- [15] X. Zhao, L. Jin, H. Shi, W. Tong, D. Gorin, Y. Kotelevtsev, Z. Mao, Recent advances of designing dynamic surfaces to regulate cell adhesion, *Colloid and Interface Science Communications*, 35, 100249, 2020.

- [16] K. Metavarayuth, P. Sitasuwan, X. Zhao, Y. Lin, Q. Wang, Influence of surface topographical cues on the differentiation of mesenchymal stem cells in vitro, *ACS Biomaterials Science & Engineering*, 2(2), 142-151, 2016.
- [17] N. Logan, P. Brett, The control of mesenchymal stromal cell osteogenic differentiation through modified surfaces, *Stem Cells International*, 2013, 2013.
- [18] G. Abagnale, M. Steger, V.H. Nguyen, N. Hersch, A. Sechi, S. Joussen, B. Denecke, R. Merkel, B. Hoffmann, A. Dreser, Surface topography enhances differentiation of mesenchymal stem cells towards osteogenic and adipogenic lineages, *Biomaterials*, 61, 316-326, 2015.
- [19] M. Croes, S. Bakhshandeh, I. van Hengel, K. Lietaert, K. van Kessel, B. Pouran, B. van der Wal, H. Vogely, W. Van Hecke, A. Fluit, Antibacterial and immunogenic behavior of silver coatings on additively manufactured porous titanium, *Acta Biomaterialia*, 81, 315-327, 2018.
- [20] A. Panáček, L. Kvítek, M. Smékalová, R. Večeřová, M. Kolář, M. Röderová, F. Dyčka, M. Šebela, R. Prucek, O. Tomanec, Bacterial resistance to silver nanoparticles and how to overcome it, *Nature Nanotechnology*, 13(1), 65-71, 2018.
- [21] S.B. Levy, B. Marshall, Antibacterial resistance worldwide: causes, challenges and responses, *Nature Medicine*, 10(12), S122-S129, 2004.
- [22] H.S. Azevedo, I. Pashkuleva, Biomimetic supramolecular designs for the controlled release of growth factors in bone regeneration, *Advanced Drug Delivery Reviews*, 94, 63-76, 2015.
- [23] S. Dobbenga, L.E. Fratila-Apachitei, A.A. Zadpoor, Nanopattern-induced osteogenic differentiation of stem cells—A systematic review, *Acta Biomaterialia*, 46, 3-14, 2016.
- [24] K. Modaresifar, S. Azizian, M. Ganjian, L.E. Fratila-Apachitei, A.A. Zadpoor, Bactericidal effects of nanopatterns: A systematic review, *Acta Biomaterialia*, 83, 29-36, 2019.
- [25] D.V. Iwamoto, D.A. Calderwood, Regulation of integrin-mediated adhesions, *Current Opinion in Cell Biology*, 36, 41-47, 2015.
- [26] N.C. Gauthier, P. Roca-Cusachs, Mechanosensing at integrin-mediated cell–matrix adhesions: from molecular to integrated mechanisms, *Current Opinion in Cell Biology*, 50, 20-26, 2018.
- [27] T.D. Ross, B.G. Coon, S. Yun, N. Baeyens, K. Tanaka, M. Ouyang, M.A. Schwartz, Integrins in mechanotransduction, *Current Opinion in Cell Biology*, 25(5), 613-618, 2013.
- [28] Y. Hou, W. Xie, L. Yu, L.C. Camacho, C. Nie, M. Zhang, R. Haag, Q. Wei, Surface Roughness Gradients Reveal Topography-Specific Mechanosensitive Responses in Human Mesenchymal Stem Cells, *Small*, 16(10), 1905422, 2020.
- [29] M. Ermis, E. Antmen, V. Hasirci, Micro and Nanofabrication methods to control cell–substrate interactions and cell behavior: A review from the tissue engineering perspective, *Bioactive Materials*, 3(3), 355-369, 2018.
- [30] S. Oh, K.S. Brammer, Y.J. Li, D. Teng, A.J. Engler, S. Chien, S. Jin, Stem cell fate dictated solely by altered nanotube dimension, *Proceedings of the National Academy of Sciences*, 106(7), 2130-2135, 2009.
- [31] M.J. Dalby, N. Gadegaard, R.O. Oreffo, Harnessing nanotopography and integrin–matrix interactions to influence stem cell fate, *Nature Materials*, 13(6), 558-569, 2014.

- [32] S. Watari, K. Hayashi, J.A. Wood, P. Russell, P.F. Nealey, C.J. Murphy, D.C. Genetos, Modulation of osteogenic differentiation in hMSCs cells by submicron topographically-patterned ridges and grooves, *Biomaterials*, 33(1), 128-136, 2012.
- [33] T. Sjöström, M.J. Dalby, A. Hart, R. Tare, R.O. Oreffo, B. Su, Fabrication of pillar-like titania nanostructures on titanium and their interactions with human skeletal stem cells, *Acta Biomaterialia*, 5(5), 1433-1441, 2009.
- [34] M.J. Dalby, N. Gadegaard, R. Tare, A. Andar, M.O. Riehle, P. Herzyk, C.D. Wilkinson, R.O. Oreffo, The control of human mesenchymal cell differentiation using nanoscale symmetry and disorder, *Nature Materials*, 6(12), 997-1003, 2007.
- [35] J. Lovmand, J. Justesen, M. Foss, R.H. Lauridsen, M. Lovmand, C. Modin, F. Besenbacher, F.S. Pedersen, M. Duch, The use of combinatorial topographical libraries for the screening of enhanced osteogenic expression and mineralization, *Biomaterials*, 30(11), 2015-2022, 2009.
- [36] L.E. McNamara, T. Sjöström, K.E. Burgess, J.J. Kim, E. Liu, S. Gordonov, P.V. Moghe, R.D. Meek, R.O. Oreffo, B. Su, Skeletal stem cell physiology on functionally distinct titania nanopopographies, *Biomaterials*, 32(30), 7403-7410, 2011.
- [37] Y. Sun, C.S. Chen, J. Fu, Forcing stem cells to behave: a biophysical perspective of the cellular microenvironment, *Annual Review of Biophysics*, 41, 519-542, 2012.
- [38] J. Hasan, H.K. Webb, V.K. Truong, S. Pogodin, V.A. Baulin, G.S. Watson, J.A. Watson, R.J. Crawford, E.P. Ivanova, Selective bactericidal activity of nanopatterned superhydrophobic cicada *Psaltoda claripennis* wing surfaces, *Applied Microbiology and Biotechnology*, 97(20), 9257-9262, 2013.
- [39] K. Nowlin, A. Boseman, A. Covell, D. LaJeunesse, Adhesion-dependent rupturing of *Saccharomyces cerevisiae* on biological antimicrobial nanostructured surfaces, *Journal of the Royal Society Interface*, 12(102), 20140999, 2015.
- [40] G.S. Watson, D.W. Green, L. Schwarzkopf, X. Li, B.W. Cribb, S. Myhra, J.A. Watson, A gecko skin micro/nano structure—A low adhesion, superhydrophobic, anti-wetting, self-cleaning, biocompatible, antibacterial surface, *Acta Biomaterialia*, 21, 109-122, 2015.
- [41] J. Hasan, R.J. Crawford, E.P. Ivanova, Antibacterial surfaces: the quest for a new generation of biomaterials, *Trends in Biotechnology*, 31(5), 295-304, 2013.
- [42] D.P. Linklater, V.A. Baulin, S. Juodkakis, R.J. Crawford, P. Stoodley, E.P. Ivanova, Mechano-bactericidal actions of nanostructured surfaces, *Nature Reviews Microbiology*, 19, 8-22, 2020.
- [43] M. Ganjian, L. Angeloni, M.J. Mirzaali, K. Modaresifar, C.W. Hagen, M.K. Ghatkesar, P.-L. Hagedoorn, L.E. Fratila-Apachitei, A.A. Zadpoor, Quantitative mechanics of 3D printed nanopillars interacting with bacterial cells, *Nanoscale*, 12(43), 21988-22001, 2020.
- [44] M. Ganjian, K. Modaresifar, H. Zhang, P.-L. Hagedoorn, L.E. Fratila-Apachitei, A.A. Zadpoor, Reactive ion etching for fabrication of biofunctional titanium nanostructures, *Scientific Reports*, 9(1), 1-20, 2019.
- [45] E.P. Ivanova, J. Hasan, H.K. Webb, G. Gervinskas, S. Juodkakis, V.K. Truong, A.H. Wu, R.N. Lamb, V.A. Baulin, G.S. Watson, Bactericidal activity of black silicon, *Nature Communications*, 4, 2013.

- [46] M. Michalska, F. Gambacorta, R. Divan, I.S. Aranson, A. Sokolov, P. Noirot, P.D. Laible, Tuning antimicrobial properties of biomimetic nanopatterned surfaces, *Nanoscale*, 10(14), 6639-6650, 2018.
- [47] G. Hazell, P.W. May, P. Taylor, A.H. Nobbs, C. Welch, B. Su, Studies of black silicon and black diamond as materials for antibacterial surfaces, *Biomaterials Science*, 6(6), 1424-1432, 2018.
- [48] J. Hasan, S. Jain, K. Chatterjee, Nanoscale topography on black titanium imparts multi-biofunctional properties for orthopedic applications, *Scientific Reports*, 7, 41118, 2017.
- [49] M.E. Berginski, S.M. Gomez, The Focal Adhesion Analysis Server: a web tool for analyzing focal adhesion dynamics, *F1000Research*, 2, 2013.
- [50] U. Horzum, B. Ozdil, D. Pesen-Okvur, Step-by-step quantitative analysis of focal adhesions, *MethodsX*, 1, 56-59, 2014.
- [51] E.P. Ivanova, D.P. Linklater, M. Werner, V.A. Baulin, X. Xu, N. Vrancken, S. Rubanov, E. Hanssen, J. Wandiyanto, V.K. Truong, The multi-faceted mechano-bactericidal mechanism of nanostructured surfaces, *Proceedings of the National Academy of Sciences*, 117(23), 12598-12605, 2020.
- [52] L.D. Ghosh, J. Hasan, A. Jain, N.R. Sundaresan, K. Chatterjee, A nanopillar array on black titanium prepared by reactive ion etching augments cardiomyogenic commitment of stem cells, *Nanoscale*, 11(43), 20766-20776, 2019.
- [53] D.P. Linklater, S. Juodkazis, R. Crawford, E. Ivanova, Mechanical inactivation of *Staphylococcus aureus* and *Pseudomonas aeruginosa* by titanium substrata with hierarchical surface structures, *Materialia*, 5, 100197, 2019.
- [54] M. Sun, G.S. Watson, Y. Zheng, J.A. Watson, A. Liang, Wetting properties on nanostructured surfaces of cicada wings, *Journal of Experimental Biology*, 212(19), 3148-3155, 2009.
- [55] J. Hasan, S. Raj, L. Yadav, K. Chatterjee, Engineering a nanostructured "super surface" with superhydrophobic and superkilling properties, *RSC Advances*, 5(56), 44953-44959, 2015.
- [56] T.L. Clainche, D. Linklater, S. Wong, P. Le, S. Juodkazis, X.L. Guével, J.-L. Coll, E.P. Ivanova, V. Martel-Frchet, Mechano-Bactericidal Titanium Surfaces for Bone Tissue Engineering, *ACS Applied Materials & Interfaces*, 12, 48272-48283, 2020.
- [57] Y. Zhukova, C. Hiepen, P. Knaus, M. Osterland, S. Prohaska, J.W. Dunlop, P. Fratzl, E.V. Skorb, The role of titanium surface nanostructuring on preosteoblast morphology, adhesion, and migration, *Advanced Healthcare Materials*, 6(15), 1601244, 2017.
- [58] P.S. Mathieu, E.G. Loba, Cytoskeletal and focal adhesion influences on mesenchymal stem cell shape, mechanical properties, and differentiation down osteogenic, adipogenic, and chondrogenic pathways, *Tissue Engineering Part B: Reviews*, 18(6), 436-444, 2012.
- [59] D. Khang, J. Choi, Y.-M. Im, Y.-J. Kim, J.-H. Jang, S.S. Kang, T.-H. Nam, J. Song, J.-W. Park, Role of subnano-, nano- and submicron-surface features on osteoblast differentiation of bone marrow mesenchymal stem cells, *Biomaterials*, 33(26), 5997-6007, 2012.
- [60] A. Ray, O. Lee, Z. Win, R.M. Edwards, P.W. Alford, D.-H. Kim, P.P. Provenzano, Anisotropic forces from spatially constrained focal adhesions mediate contact guidance directed cell migration, *Nature Communications*, 8(1), 1-17, 2017.

-
- [61] M.D. Cabezas, B. Meckes, C.A. Mirkin, M. Mrksich, Subcellular Control over Focal Adhesion Anisotropy, Independent of Cell Morphology, Dictates Stem Cell Fate, *ACS Nano*, 13(10), 11144-11152, 2019.
- [62] J. Xia, Y. Yuan, H. Wu, Y. Huang, D.A. Weitz, Decoupling the effects of nanopore size and surface roughness on the attachment, spreading and differentiation of bone marrow-derived stem cells, *Biomaterials*, 248, 120014, 2020.
- [63] N.C. Gauthier, T.A. Masters, M.P. Sheetz, Mechanical feedback between membrane tension and dynamics, *Trends in Cell Biology*, 22(10), 527-535, 2012.
- [64] D.W. Dumbauld, T.T. Lee, A. Singh, J. Scrimgeour, C.A. Gersbach, E.A. Zamir, J. Fu, C.S. Chen, J.E. Curtis, S.W. Craig, How vinculin regulates force transmission, *Proceedings of the National Academy of Sciences*, 110(24), 9788-9793, 2013.
- [65] F. Martino, A.R. Perestrelo, V. Vinarský, S. Pagliari, G. Forte, Cellular mechanotransduction: from tension to function, *Frontiers in Physiology*, 9, 824, 2018.
- [66] B. Ghezzi, P. Lagonegro, N. Fukata, L. Parisi, D. Calestani, C. Galli, G. Salviati, G.M. Macaluso, F. Rossi, Sub-Micropillar Spacing Modulates the Spatial Arrangement of Mouse MC3T3-E1 Osteoblastic Cells, *Nanomaterials*, 9(12), 1701, 2019.
- [67] X. Wang, X. Hu, I. Dulińska-Molak, N. Kawazoe, Y. Yang, G. Chen, Discriminating the independent influence of cell adhesion and spreading area on stem cell fate determination using micropatterned surfaces, *Scientific Reports*, 6(1), 1-13, 2016.
- [68] K. Yang, K. Jung, E. Ko, J. Kim, K.I. Park, J. Kim, S.-W. Cho, Nanotopographical manipulation of focal adhesion formation for enhanced differentiation of human neural stem cells, *ACS Applied Materials & Interfaces*, 5(21), 10529-10540, 2013.
- [69] J. Stricker, Y. Aratyn-Schaus, P.W. Oakes, M.L. Gardel, Spatiotemporal constraints on the force-dependent growth of focal adhesions, *Biophysical Journal*, 100(12), 2883-2893, 2011.
- [70] S. Di Cio, J.E. Gautrot, Cell sensing of physical properties at the nanoscale: Mechanisms and control of cell adhesion and phenotype, *Acta Biomaterialia*, 30, 26-48, 2016.
- [71] Y. Song, J. Soto, B. Chen, L. Yang, S. Li, Cell engineering: Biophysical regulation of the nucleus, *Biomaterials*, 234, 119743, 2020.
- [72] M. Versaevel, T. Grevesse, S. Gabriele, Spatial coordination between cell and nuclear shape within micropatterned endothelial cells, *Nature Communications*, 3(1), 1-11, 2012.
- [73] I. Casanellas, A. Lagunas, Y. Vida, E. Pérez-Inestrosa, J.A. Andrades, J. Becerra, J. Samitier, Matrix Nanopatterning Regulates Mesenchymal Differentiation through Focal Adhesion Size and Distribution According to Cell Fate, *Biomimetics*, 4(2), 43, 2019.
- [74] S. Stewart, A. Darwood, S. Masouros, C. Higgins, A. Ramasamy, Mechanotransduction in osteogenesis, *Bone & Joint Research*, 9(1), 1-14, 2020.
- [75] M.J.P. Biggs, M.J. Dalby, Focal adhesions in osteoneogenesis, *Proceedings of the Institution of Mechanical Engineers, Part H: Journal of Engineering in Medicine*, 224(12), 1441-1453, 2010.
- [76] C.B. Khatiwala, P.D. Kim, S.R. Peyton, A.J. Putnam, ECM compliance regulates osteogenesis by influencing MAPK signaling downstream of RhoA and ROCK, *Journal of Bone and Mineral Research*, 24(5), 886-898, 2009.

-
- [77] R.M. Salaszyk, R.F. Klees, W.A. Williams, A. Boskey, G.E. Plopper, Focal adhesion kinase signaling pathways regulate the osteogenic differentiation of human mesenchymal stem cells, *Experimental Cell Research*, 313(1), 22-37, 2007.
- [78] L. Yang, L. Ge, P. van Rijn, Synergistic effect of cell-derived extracellular matrix and topography on osteogenesis of mesenchymal stem cells, *ACS Applied Materials & Interfaces*, 12(23), 25591–25603, 2020.
- [79] M.J. Barron, C.-J. Tsai, S.W. Donahue, Mechanical stimulation mediates gene expression in MC3T3 osteoblastic cells differently in 2D and 3D environments, *Journal of Biomechanical Engineering*, 132(4), 2010.
- [80] K. Jindai, K. Nakade, K. Masuda, T. Sagawa, H. Kojima, T. Shimizu, S. Shingubara, T. Ito, Adhesion and bactericidal properties of nanostructured surfaces dependent on bacterial motility, *RSC Advances*, 10(10), 5673-5680, 2020.
- [81] L. Rizzello, B. Sorce, S. Sabella, G. Vecchio, A. Galeone, V. Brunetti, R. Cingolani, P.P. Pompa, Impact of nanoscale topography on genomics and proteomics of adherent bacteria, *ACS Nano*, 5(3), 1865-1876, 2011.
- [82] A. Persat, Bacterial mechanotransduction, *Current Opinion in Microbiology*, 36, 1-6, 2017.
- [83] C. Berne, C.K. Ellison, A. Ducret, Y.V. Brun, Bacterial adhesion at the single-cell level, *Nature Reviews Microbiology*, 16(10), 616-627, 2018.
- [84] Y.F. Dufrêne, A. Persat, Mechanomicrobiology: how bacteria sense and respond to forces, *Nature Reviews Microbiology*, 1-14, 2020.

Mechanotransduction in high aspect ratio nanopatterns

Black Ti (bTi) surfaces comprising high aspect ratio nanopillars exhibit a rare combination of bactericidal and osteogenic properties, framing them as cell-instructive meta-biomaterials. Despite the existing data indicating that bTi surfaces induce osteogenic differentiation in cells, the mechanisms by which this response is regulated are not fully understood. Here, we hypothesized that high aspect ratio bTi nanopillars regulate cell adhesion, contractility, and nuclear translocation of transcriptional factors, thereby inducing an osteogenic response in the cells. Upon the observation of significant changes in the morphological characteristics, nuclear localization of Yes-associated protein (YAP), and Runt-related transcription factor 2 (Runx2) expression in the human bone marrow-derived mesenchymal stem cells (hMSCs), we inhibited focal adhesion kinase (FAK), Rho-associated protein kinase (ROCK), and YAP in separate experiments to elucidate their effects on the subsequent expression of Runx2. Our findings indicate that the increased expression of Runx2 in the cells residing on the bTi nanopillars compared to the flat Ti is highly dependent on the activity of FAK and ROCK. A mechanotransduction pathway is then postulated in which the FAK-dependent adhesion of cells to the extreme topography of the surface is in close relation with ROCK to increase the endogenous forces within the cells, eventually determining the cell shape and area, the nuclear translocation of YAP, and the translation of mechanical stimuli to biochemical factors such as Runx2.

K. Modaresifar, M. Ganjian, P. J. Díaz-Payno, M. Klimopoulou, M. Koedam, B. C. J. van der Eerden, L. E. Fratila-Apachitei, A. A. Zadpoor, Mechanotransduction in high aspect ratio nanostructured meta-biomaterials: the role of cell adhesion, contractility, and transcriptional factors, *In revision*, 2022.

8.1 Introduction

Cell-instructive biomaterials, as a relatively new category of advanced functional materials, have expanded the horizon for tissue regeneration and cell therapy applications as they embody different functionalities that enhance their modulatory role with regard to the fate of the cells with which they interact^{1,2}. In this regard, the effects of biophysical interactions between the stem cells and the biomaterial's surface on their phenotype and lineage commitment has been extensively studied in recent years^{3,4}. Cells can sense the small-scale features of surfaces and transduce exogenous mechanical forces to their nuclei where these signals can be converted to different biochemical signals, eventually affecting the cell function⁵. Previous studies have revealed that the geometry (*i.e.*, shape, arrangement, and dimensions) of the surface features substantially contributes to the induction of a variety of responses in cells^{6,7}. High aspect ratio nanostructured surfaces, in particular, offer remarkable potential for manipulating and or controlling not only the biomechanical environment of the cells but also their biochemical and bioelectric environments⁸. For instance, they can be exploited as 1) carriers for intracellular delivery or extraction by harmlessly penetrating the cell membrane^{9, 10}, 2) a platform for investigating cell-material interactions including mechanotransduction pathways⁴, and 3) highly bactericidal surfaces to combat biomaterial-associated infections¹¹. The combination of the rare properties and functionalities displayed by these surfaces that result in unusual biological responses has framed them as meta-biomaterials^{8,12}.

High aspect ratio nanostructures come in different geometrical shapes (*e.g.*, pillars, cones, needles, *etc.*) and arrangements (*i.e.*, ordered or stochastic), and can be synthetically fabricated through a variety of subtractive or additive manufacturing techniques (*e.g.*, electron beam lithography (EBL), two-photon polymerization, dry etching, *etc.*)⁸. A recently reported fabrication process for generating high aspect ratio nanopillars on the Ti surface (as the most clinically-relevant material for orthopedic applications), also known as black Ti (bTi), is inductively coupled plasma reactive ion etching (ICP RIE)¹³. The effects of the processing parameters of ICP RIE on the geometry of the resultant nanopillars have been investigated before¹⁴. Rational changes in these parameters yield certain configurations of nanopillars that exhibit superior mechano-bactericidal properties^{7, 15}. The same surfaces also enhance matrix mineralization in murine preosteoblasts⁷ and human adipose-derived mesenchymal stem cells (hASCs)¹⁵. Although various theories have been presented regarding the mechano-bactericidal

actions of dry-etched surfaces, such as bTi¹⁶, less is known about the exact mechanisms leading to osteogenic differentiation in cells. For instance, changes in the cell morphology and distribution of focal adhesions (FAs) have been observed on bTi surfaces, yet the role of subcellular components in the eventual commitment toward osteogenic differentiation has not been fully understood^{7,13}.

Integrin signaling is known to play a crucial role in sensing the mechanical forces generated as a result of the interactions of a cell with the extracellular matrix (ECM)^{4,17}. To transduce the mechanical forces from the ECM to the nucleus, FAs play a mediatory role to connect membrane-bound integrins to the cytoskeleton. Focal adhesion kinase (FAK) is a major component of the FA complex that is mainly associated with the integrins' β 1 subunit and regulates the adhesion of cells to their underlying substrate. FAK is known to trigger and regulate multiple downstream pathways, which promote the expression of osteogenic markers^{4, 18}. Accordingly, silencing/inhibiting FAK downregulates the expression of osteogenic markers^{19, 20}. Moreover, the dynamic remodeling of the cytoskeleton is associated with externally exerted forces as well as the endogenous forces generated within the cells^{4,21}. Activation of RhoA from the Rho family of GTPases and its downstream Rho-associated protein kinase (ROCK) is essential for the phosphorylation of the myosin light chain (MLC) and promoting contractility via myosin II²¹. Therefore, the RhoA/ROCK pathway not only plays an important role in sustaining the integrity of the cytoskeleton and determining the cell shape but also affects the mechanical tensions sensed by the nucleus^{21,22}. The inhibition of this pathway has also been shown to hinder the osteogenic differentiation of human adipose-derived mesenchymal stem cells (hASCs)²⁰. In addition to cell adhesion and contractility, the role of transcriptional factors, such as Yes-associated protein (YAP) and co-activator with PDZ-binding motif (TAZ) in mechanotransduction has been a matter of interest^{23,24}. For instance, YAP has been shown to control the FA assembly and cell shape upon translocation to the nucleus but its nuclear translocation is dependent on the RhoA/ROCK pathway²⁵.

The potential intracellular mechanotransduction pathways triggered by high aspect ratio bTi nanopillars have not been studied before. Here, we investigate the possible intracellular pathways by which high aspect ratio bTi nanopillars promote the osteogenic differentiation of (stem) cells, focusing on the role of cell adhesion, contractility, and transcriptional factors. We use a unique configuration of bTi nanopillars, previously

shown to enhance the mineralization of murine preosteoblasts ⁷, to study the early adaptation of human mesenchymal stem cells (hMSCs) to such surfaces. We found that bTi surfaces enhance the expression of Runx2 in hMSCs compared to the flat Ti, which happens subsequent to changes in the cell morphology, the formation of FAs, and the nuclear localization of YAP in cells. Thereafter, we investigated three hypotheses, namely the osteogenic properties of bTi nanopillars are 1) FAK-dependent, 2) ROCK-dependent, and 3) YAP-dependent (Figure 8.1). We then discuss the relationship between these hypotheses to highlight their potential interdependencies.

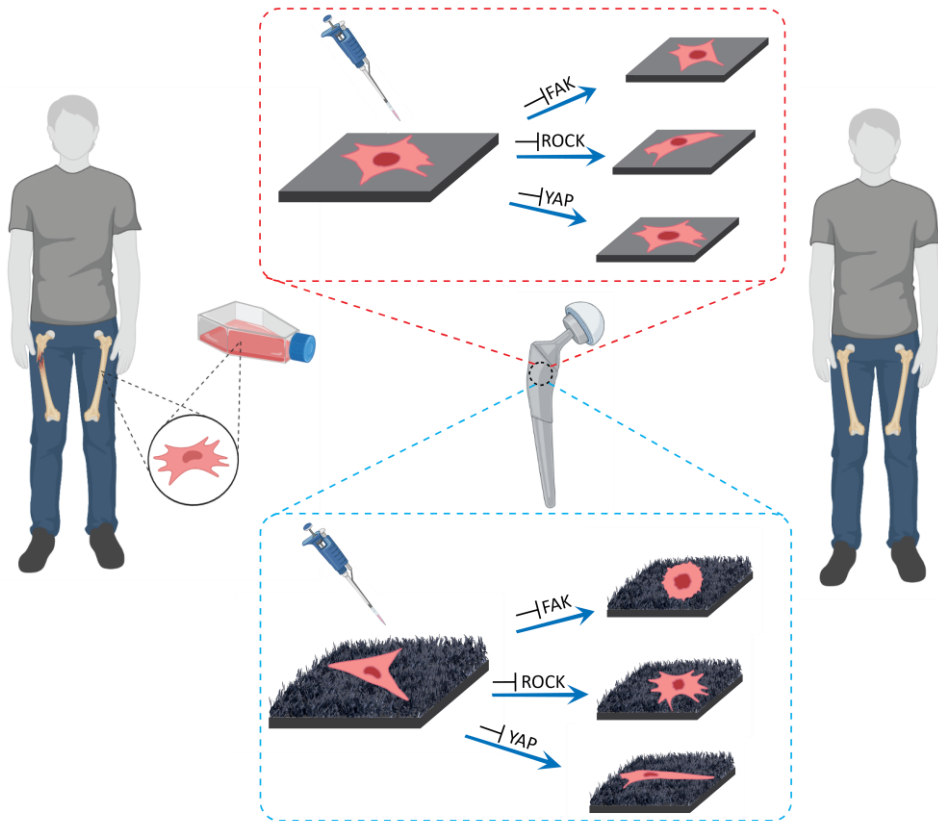


Figure 8.1. A schematic drawing of the experiments carried out in this study. The orthopedic implants with surfaces composed of conventional material (flat Ti) or meta-biomaterial (high aspect ratio bTi nanopillars) exhibit different osteoinductive potential. The cell responses to these surfaces and the intracellular mechanotransduction pathways that regulate them were investigated under normal or inhibitory conditions.

8.2 Materials and Methods

8.2.1 Fabrication and characterization of high aspect ratio bTi nanopillars

A previously described ICP RIE protocol^{7,14} was used to create high aspect ratio nanopillars on titanium surfaces. Briefly, annealed titanium foils with a thickness of 125 μm (99.96% purity, Goodfellow, UK) were cut to the size of a 4-inch (diameter = 10.2 cm) silicon wafer and were polished with chemical-mechanical polishing (CMP Mecapol E460, France). After being cut into $8 \times 8 \text{ mm}^2$ pieces, the surface of the titanium specimens (glued with a thermal paste atop a 4-inch quartz wafer as the carrier wafer) were etched with Cl_2 and Ar gases using an ICP RIE machine (PlasmaLab System 100, Oxford Instruments, UK) under the following conditions: ICP source power = 600 W, RF power = 100 W, etching time = 10 minutes, Cl_2 flow rate = 30 sccm, Ar flow rate = 2.5 sccm, chamber temperature = 40 $^\circ\text{C}$, and chamber pressure = 2 Pa. Once the etching process was concluded, the specimens were cleaned in acetone, ethanol, and isopropanol, respectively.

The etched surfaces were then imaged with a scanning electron microscope (SEM) (Helios NanoLab 650, FEI, US) from the top and 35° tilted positions. The height and the tip diameter of the nanopillars were then measured based on SEM images. Furthermore, the major chemical elements present on the surface of bTi specimens were identified by performing energy-dispersive X-ray spectroscopy (EDS) inside the SEM. Finally, the water contact angle of the specimens was measured by a drop shape analyzer (DSA 100, Krüss, Germany) as described before^{7,14}.

8.2.2 Investigating the response of hMSCs to high aspect ratio nanopillars

Pre-culture of cells and cell seeding

hMSCs isolated from the bone marrow of healthy donors and expanded to the second passage were purchased from Lonza (#19TL329433, PT-2501, Lonza Bioscience, The Netherlands). The cells were expanded until the fifth passage in the alpha minimum essential medium (α -MEM) supplemented with 10% (v/v) fetal bovine serum, 50 $\mu\text{g}/\text{ml}$ gentamicin, and 1.5 $\mu\text{g}/\text{ml}$ amphotericin B (all from Thermo Fisher Scientific, US). 1 ng/ml fibroblast growth factor-2 (Bio-Rad, The Netherlands) and 0.1 mM ascorbic acid (Sigma-Aldrich, Germany) were freshly added to the refreshing expansion medium²⁶.

Prior to the cell culture, the flat Ti and bTi samples were sterilized by immersion in 70% ethanol and then exposure to UV light for 20 minutes. Upon reaching confluence, the cells were detached from the cell culture flask using 1X trypsin-EDTA solution (Thermo Fisher Scientific, US), were cultured on both flat Ti and bTi surfaces (1×10^4 cells per sample) in a 48 well-plate (Greiner, Bio-One, The Netherlands), and were incubated at 37 °C with 5% CO₂ (Life Technologies, US). In the case of the experiments taking longer than 1 day, the α -MEM medium was supplemented with 0.1 mM ascorbic acid, 10 mM β -glycerophosphate, and 1 mM dexamethasone (all from Sigma-Aldrich, Germany) from day 2 onward. All the experiments, described in the following sections included three samples per study group.

Immunocytochemical analysis of hMSCs settled on high aspect ratio nanopillars

In order to evaluate the early-stage adaptation of hMSCs to bTi surfaces, the cells were stained for the actin filaments, nucleus, and FAs after 1 day of culture. Briefly, after washing the samples with 10X phosphate-buffered saline (PBS, Sigma-Aldrich, Germany), the cells were fixed using a 4% (v/v) formaldehyde solution (Sigma-Aldrich, Germany) and their membranes were permeabilized by adding 0.5% Triton X-100/PBS (Sigma-Aldrich, US) at 4 °C for 5 minutes. The samples were then incubated in 1% BSA/PBS (Sigma-Aldrich, Germany) at 37 °C for 5 minutes and were subsequently incubated in anti-vinculin mouse monoclonal primary antibody (1:100 in 1% BSA/PBS, Sigma-Aldrich, Germany) and rhodamine-conjugated phalloidin (1:1000 in 1% BSA/PBS, Thermo Fisher Scientific, US) for 1 hour at 37 °C. The immunofluorescence staining process was followed by washing the samples thrice with 0.5% Tween-20/PBS (Sigma-Aldrich, US) and incubating them in Alexa Fluor 488, donkey anti-mouse polyclonal secondary antibody (1:200 in 1% BSA/PBS, Thermo Fisher Scientific, US) for 1 hour at room temperature. The samples were washed again three times with 0.5% Tween-20/PBS, followed by 5 minutes washing with 1X PBS. The samples were mounted atop microscopic glass slides using 10 μ l Prolong gold antifade reagent containing DAPI (4',6-diamidino-2-phenylindole) (Thermo Fisher Scientific, US) and were imaged using a fluorescence microscope (ZOE fluorescent cell imager, Bio-Rad, The Netherlands). A similar immunocytochemical staining procedure was performed on separate samples to visualize and analyze YAP after 1 day of culture. To this end, a mouse monoclonal anti-YAP1 antibody (1:100 in 1% BSA/PBS, Santa Cruz Biotechnology, Germany) and Alexa

Fluor 488, donkey anti-mouse polyclonal secondary antibody (1:200 in 1% BSA/PBS, Thermo Fisher Scientific, US) were used.

Finally, in order to investigate the effects of surface topography on the expression of osteogenic markers in hMSCs, the cells were stained for Runx2 after 9 days of culture through incubation in recombinant anti-Runx2 rabbit monoclonal primary antibody (1:250 in 1% BSA/PBS, Abcam, UK). The cells were then incubated in Alexa Fluor 488, donkey anti-rabbit polyclonal secondary antibody (1:200 in 1% BSA/PBS, Thermo Fisher Scientific, US), before being washed and imaged as described above.

Investigation of cell-nanopillars interface

In order to further investigate the interactions between the cells and high aspect ratio nanopillars of bTi, focused ion beam scanning electron microscopy (FIB-SEM, Helios Nano Lab 650, FEI, US) was performed to acquire tilted and cross-sectional views of the interface between the cells and nanopillars. For the SEM observations, the samples stained for vinculin and actin on day 1 of culture were dehydrated using incremental volumes of ethanol (*i.e.*, washing samples with 50%, 70%, and 96% ethanol solutions for 15, 20, and 20 minutes, respectively), air-dried, and gold-sputtered before SEM imaging. To acquire cross-sectional views, the samples were tilted to 52°, at which angle the surface was milled using Gallium ions with a 7.7 pA ion beam ($Z = 1 \mu\text{m}$, operating voltage = 30 kV).

PrestoBlue assay

The metabolic activity of the hMSCs, seeded on the flat Ti and bTi surfaces, was measured by a PrestoBlue assay after 1, 4, and 7 days of culture. Briefly, all samples were incubated in 250 μl of culture medium supplemented with 25 μl PrestoBlue reagent (Thermo Fisher Scientific, US) for 1 hour at 37 °C and 5% CO₂. Thereafter, 100 μl of the supernatant from each well was transferred to a 96 well-plate (Greiner, Bio-One, The Netherlands) in duplicate. The fluorescence was measured at an excitation wavelength of 530 nm and an emission wavelength of 595 nm with a Victor X3 microplate reader (PerkinElmer, The Netherlands).

8.2.3 Inhibition studies

To study the role of FAK, ROCK, and YAP in the regulation of Runx2 as an osteogenic marker in hMSCs while exposed to high aspect ratio nanopillars, each of those factors was inhibited in separate dedicated experiments. The pre-culture, cell seeding, and

the composition of the culture medium were kept identical to the procedures described in the previous sections during these experiments while the following inhibitors were added to the culture medium upon cell seeding and medium refreshing: 10 μM PF-573228 (FAK inhibitor, Sigma-Aldrich, Germany), 10 μM Y-27632 (ROCK inhibitor, Abcam, The Netherlands), and 10 μM Verteporfin (YAP inhibitor, Sigma-Aldrich, Germany). The short-term adaptation of the cells to the surfaces under each new condition as well as the expression of a major osteogenic marker (*i.e.*, Runx2) were evaluated through immunocytochemical staining procedures that were identical to those applied in the previous sections.

8.2.4 Fluorescence image analysis

ImageJ 1.53c (NIH, US) was used to extract and quantify data from the fluorescence images. The quantification of the number and area of FAs (*i.e.*, vinculin) as well as morphological characteristics of the cell body and nucleus, such as their area and aspect ratio, under the normal or inhibition conditions, was carried out by thresholding the grayscale images of F-actin and vinculin and running the Analyze Particles command as described elsewhere^{7,27}. The shape index of the cell body and nucleus was calculated as follows²⁸:

$$\text{Shape index} = \frac{4\pi A}{P^2}$$

where A represents the cell or nucleus area and P is their perimeter.

The images of YAP (in the experiment with no inhibition) were also processed similarly to the FAs. Briefly, the background was subtracted using the Sliding Paraboloid option with a rolling ball radius of 50 pixels. The local contrast of the image was then enhanced by running the CLAHE plugin with a block size of 19, histogram bins of 256, and a maximum slope of 6. To further minimize the background, the mathematical exponential function (EXP) was applied. The brightness, contrast, and threshold were then automatically adjusted before measuring the stained area using the Analyze Particles command. The measured area was then normalized with respect to the area of the same cell. Moreover, for further comparisons based on the nuclear YAP intensity, the mean gray value of the expressed YAP was measured within the cell nucleus area. The signal intensity of Runx2 expressed by the cells was also measured similarly under all culture conditions.

8.2.5 Statistical analysis

For all the experiments, the raw data were first tested for normality using the D'Agostino-Pearson omnibus normality test in Prism (version 9.2.0, GraphPad, US). In the cases where the sample size was too small for such a test, the Shapiro-Wilk normality test was performed. For normally distributed datasets, the unpaired Student's *t*-test with the Welch's correction was performed to determine the statistical significance of the differences between the means of the different experimental groups. For the datasets that did not pass the normality test, the nonparametric Mann-Whitney test was employed. In addition, the results of the PrestoBlue assay were analyzed using two-way ANOVA, followed by Tukey's multiple comparisons *post hoc* analysis. All the data are presented as mean \pm standard deviation and a *p*-value below 0.05 was considered to indicate statistical significance.

8.3 Results

8.3.1 Characteristics of high aspect ratio bTi nanopillars

The ICP RIE processing conditions used in this study resulted in the generation of pillar-shaped structures on the Ti surface (Figure 8.2a,b) with a homogenous black appearance due to the light absorption within the fabricated structures, similar to the previous reports in the literature^{7, 13, 14}. SEM observations revealed that the tips of the pillars were separated from each other but the pillars were not sparsely distributed on the surface. In fact, the bTi surface seems to be comprised of partitions of pillars. Precise, objective measurement of the height of single pillars was not possible because the lowermost point of the pillars cannot be always detected (or even defined). However, the analysis of SEM images suggests a height of 700 nm to 1 μ m. The diameter of the single pillar tips was < 100 nm and the average value of aspect ratio for the pillars was approximately 12.1.

The chemical composition of the bTi surface was different from that of pure flat Ti as oxygen could be abundantly detected on its surface besides Ti (Figure 8.2c,d). The ICP RIE process had also introduced slight amounts of silicon and chlorine to the surface. Furthermore, the etching process resulted in a drastic change in the wettability of the Ti surfaces as their static water contact angle decreased from $75 \pm 3^\circ$ to $5 \pm 1^\circ$ after ICP RIE processing (insets of Figure 8.2a,b).

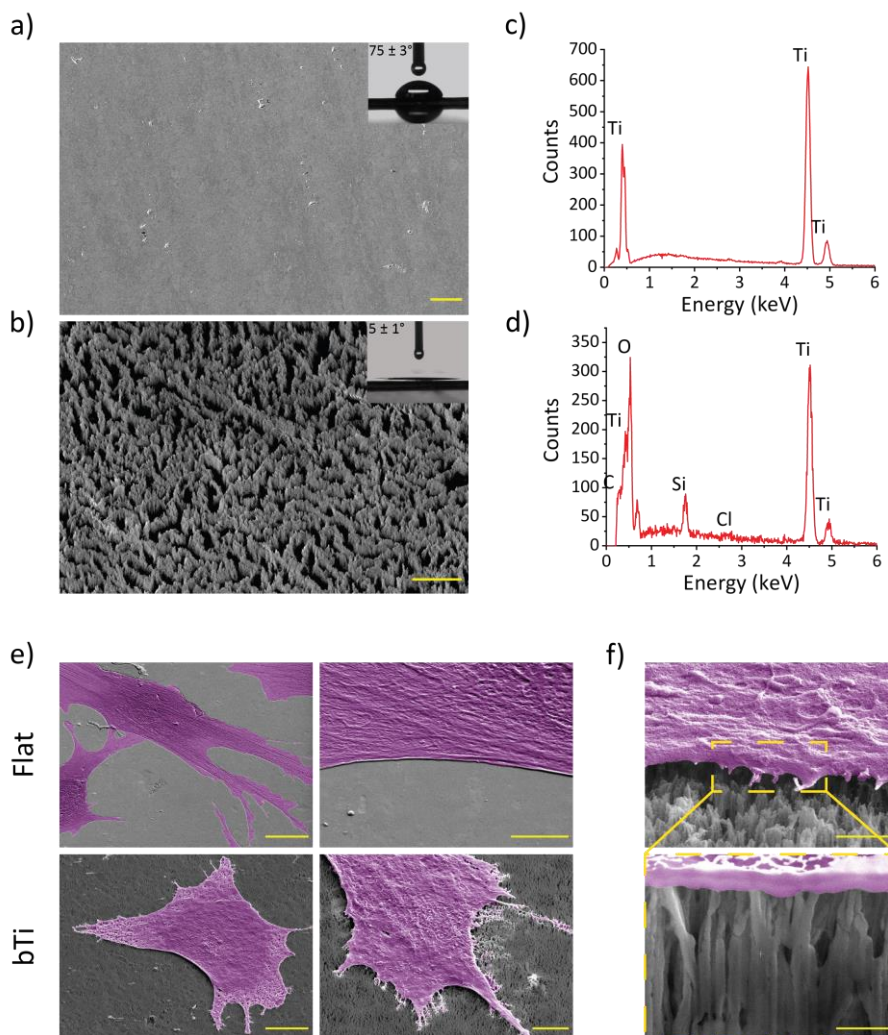


Figure 8.2. a) A top-view SEM image of the polished Ti surfaces before the application of the ICP RIE process. The inset depicts the water droplet residing on the surface after 5 s. Scale bar = 20 μm . b) A tilted-view SEM image of the bTi surfaces made through ICP RIE. The inset depicts the water droplet residing on the surface after 5 s. Scale bar = 5 μm . EDS spectra of c) flat Ti and d) bTi surfaces, showing the most abundant chemical elements identified on each surface. e) The representative SEM images of hMSCs settled on the flat Ti and bTi surfaces for 1 day. Left column: low magnification images showing the cell morphology. Scale bar = 20 μm . Right column: higher magnification images showing the presence (absence) of filopodia around the cell periphery on the bTi (flat Ti) surfaces. Scale bar = 5 μm . f) A high magnification tilted view of the cell periphery in contact with high aspect ratio nanopillars, scale bar = 1 μm , and a cross-sectional view of the interface (shown by yellow dashed lines), scale bar = 500 nm. The cells have been false colored for better visualization.

8.3.2 Effects of high aspect ratio nanopillars on the behavior of hMSCs

hMSCs maintained their fibroblast-like cell morphology when cultured on flat Ti and were observed to be well-spread on the surface already after 1 day of culture (Figure 8.3a). The cells attached to the high aspect ratio bTi nanopillars possessed a significantly smaller area as compared to the cells attached to the flat Ti surfaces (Figure 8.3b). Moreover, they had a lower (higher) aspect ratio (shape index) as compared to the cells cultured on flat Ti, indicating a less elongated (more rounded) morphology (Figure 8.3b). The evaluation of the morphology of the cell nuclei revealed an opposite trend. While the cell nucleus area was found to be smaller on the bTi samples, the aspect ratio (shape index) of the nucleus was higher (lower) on those surfaces (Figure 8.3b). On the flat Ti surfaces, the actin fibers of the cells were mostly oriented along the major axis of the cell body. In contrast, a uniform organization of actin fibers could not be identified in the cells cultured on the bTi surfaces where the actin fibers appeared to be thicker on the cell periphery, surrounding the more internal areas of the cell body (*e.g.*, cell nuclear area) (Figure 8.3a). Additionally, the cells formed FAs on both types of surfaces. On the bTi surfaces, they were mostly present on the cell periphery where filopodia had been also formed (Figure 8.3a). The average area of FAs and their number per cell were not significantly affected by the bTi nanopillars (Figure 8.3c).

The FIB-SEM images confirmed that the hMSCs form abundant filopodia around their periphery upon attachment to the bTi nanopillars. This was not observed in the cells residing on the flat Ti surfaces (Figure 8.2e). The cells had settled on the bTi nanopillars with a top state meaning that the whole cell body was spread on top of the nanopillars. Furthermore, we did not observe any signs of the deep penetration of the nanopillars into the cell body (*i.e.*, any ruptures or any signs of engulfment by the cell membrane) or local cell stretching in between the adjacent nanopillars (Figure 8.2f).

The results of the PrestoBlue assay showed that both types of surfaces can support the survival and proliferation of hMSCs and that there was no significant difference between the overall metabolic activity of the cells on the flat Ti and bTi surfaces within a time span of 1 week (Figure 8.3d).

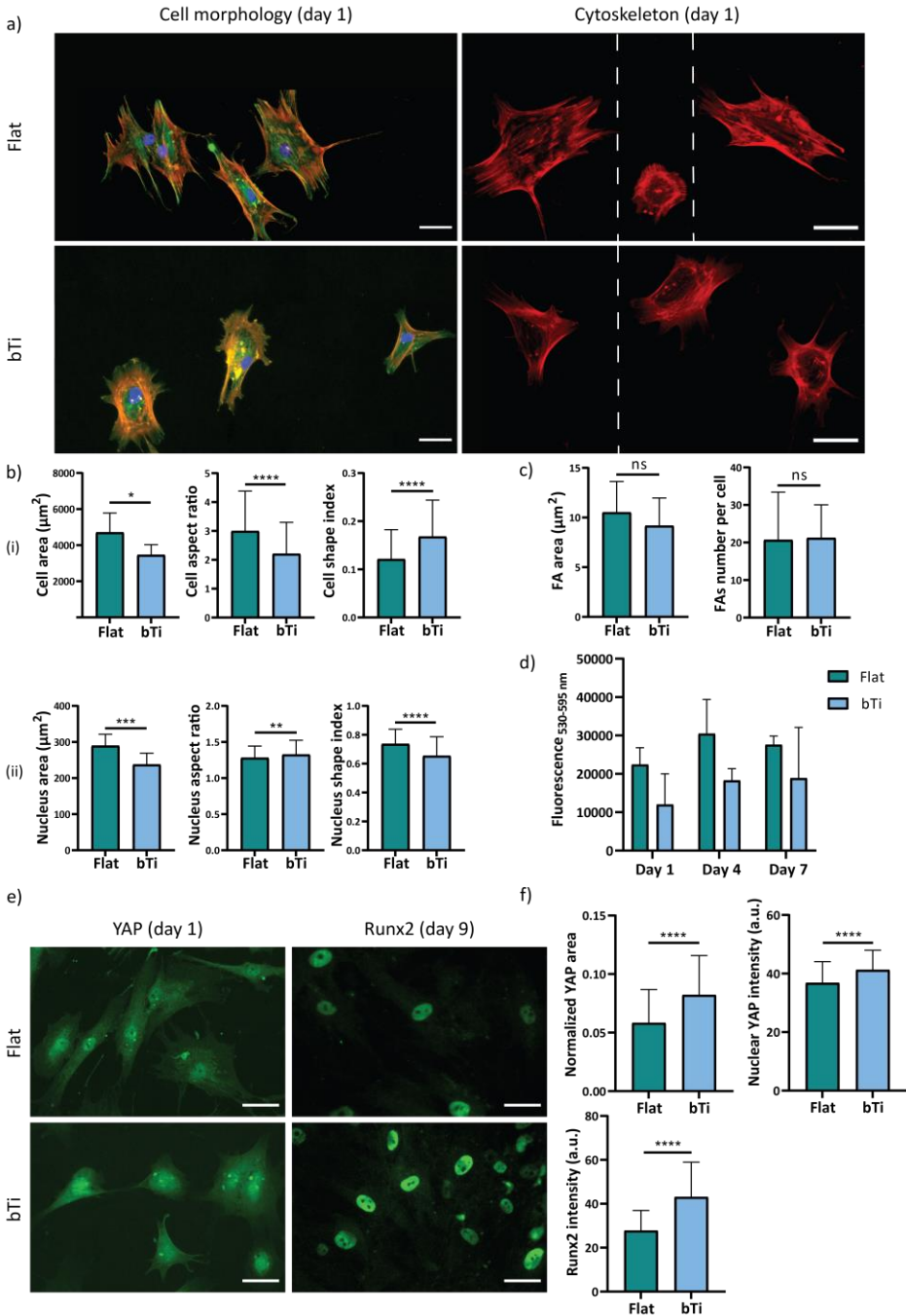


Figure 8.3. The adaptation and interactions of hMSCs with the flat Ti and bTi surfaces. a) The immunocytochemical staining of vinculin (green), actin (red), and nucleus (blue), visualizing the morphology, formation, and distribution of FAs as well as the cytoskeletal organization of the hMSCs cultured on the flat Ti and bTi surfaces for 1 day. The white dashed lines indicate a collage is made of images from different samples. Scale bar = 50 μm . b) The morphological characteristics of the cell body (i) and nucleus (ii), including the area (Welch's *t*-test), aspect ratio (Mann-Whitney test), and shape index (Mann-Whitney test). At least 200 cells were analyzed per study group. c) The average area (Welch's *t*-test) and number of FAs per cell (Mann-Whitney test) measured for 15 cells on the flat Ti and bTi surfaces. d) The metabolic activity of the hMSCs cultured on the flat Ti and bTi surfaces, measured by the PrestoBlue assay over 7 days (Two-way ANOVA followed by Tukey's test). e) The immunocytochemical staining of YAP and Runx2 for the hMSCs cultured on the flat Ti and bTi surfaces after 1 and 9 days, respectively. Scale bar = 50 μm . f) The average YAP area normalized with respect to the cell area (Mann-Whitney test), nuclear YAP signal intensity (Mann-Whitney test), and Runx2 signal intensity (Mann-Whitney test). 100 and 50 cells were analyzed per study group for YAP and Runx2, respectively (* $p < 0.05$, ** $p < 0.01$, *** $p < 0.001$, and **** $p < 0.0001$).

The hMSCs expressed YAP and Runx2 on days 1 and 9 of culture, respectively, regardless of the surface they were residing on (Figure 8.3e). However, significantly larger areas were stained for YAP in the cells residing on the bTi surfaces (when normalized to the actual cell area). In addition, the signal intensity of YAP within the cell nuclear area was significantly higher on the bTi surfaces (Figure 8.3f), indicating a higher presence of YAP in the nucleus. Similarly, the signal intensity of Runx2 expressed by the cells residing on the bTi surfaces was significantly higher than on flat Ti (Figure 8.3f).

8.3.3 Effects of FAK inhibition on hMSCs

The inhibition of FAK drastically affected the morphological characteristics of the hMSCs on both flat and bTi surfaces. After 1 day of culture, the cells still had a polygonal shape on flat Ti while their shape had changed to an extremely rounded state on the bTi samples (Figure 8.4a). On both types of surfaces, the cells had a significantly smaller area as compared to the no-inhibition conditions. In fact, the average area of cells on the flat and bTi samples under the normal condition dropped from around 4700 and 3500 μm^2 , respectively, to around 2000 and 650 μm^2 , respectively, upon FAK inhibition (Figures 8.3b and 8.4b). The values of the cell aspect ratio and shape index also confirmed the significant roundness of the cell morphology on bTi as compared to the flat Ti (Figure 8.4b). The changes were not only limited to the cell body but there was also a significant decrease in the cell nucleus area and elongation on the bTi samples as compared to the flat Ti (Figure 8.4b).

Furthermore, the immunocytochemical staining of Runx2 revealed that the inhibition of FAK downregulates the expression of Runx2 as the signal intensity significantly decreased in comparison with the normal conditions (Figures 8.3e,f and 8.4a,c).

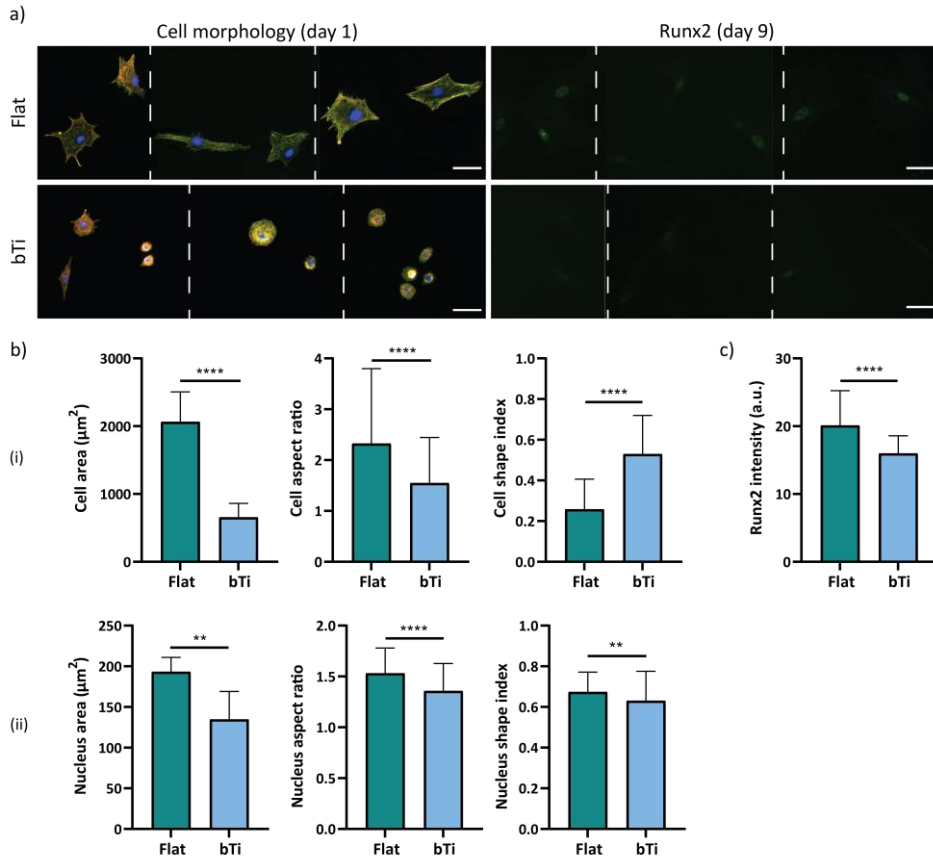


Figure 8.4. The adaptation and interactions of the hMSCs with the flat Ti and bTi surfaces after the inhibition of FAK. a) The morphology of hMSCs and expression of Runx2 after 1 and 9 days of culture, respectively, on the flat Ti and bTi surfaces. The white dashed lines indicate that a collagen is made of images from different samples. Scale bar = 50 μm . b) The morphological characteristics of the cell body (i) and nucleus (ii), including the area (Welch's *t*-test), aspect ratio (Mann-Whitney test), and shape index (Mann-Whitney test). At least 200 cells were analyzed per study group. c) The intensity of the Runx2 signal for the hMSCs residing on the flat Ti and bTi surfaces (Mann-Whitney test). At least 50 cells were analyzed per study group (** $p < 0.01$ and **** $p < 0.0001$).

8.3.4 Effects of ROCK inhibition on hMSCs

The inhibition of ROCK did not induce an apparent change in the polygonal morphology of the hMSCs on flat Ti but resulted in different morphologies displayed by the cells residing on the bTi surfaces, for instance stellate, polarized, and round shapes (Figure 8.5a). The average cell area was also significantly lower on the bTi samples as compared to the flat Ti (around $950 \mu\text{m}^2$ as compared to around $3000 \mu\text{m}^2$) (Figure 8.5b). Although the cells residing on the flat Ti had a higher aspect ratio than on the bTi samples, the differences in the cell shape index were insignificant, most likely due to the various cell shapes found on the bTi surfaces (Figure 8.5b). In addition, the presence of bTi nanopillars did not significantly affect the cell nucleus area. However, the nucleus was less elongated on these samples as compared to the flat Ti surfaces (Figure 8.5b). Similar to the normal conditions, the average FA area was not significantly different on the flat Ti and bTi surfaces (Figures 8.3c and 8.5c). But, the cells residing on the bTi samples had formed fewer FAs around their periphery (Figures 8.3c and 8.5c).

The expression of Runx2 was downregulated after ROCK inhibition on both the flat Ti and bTi samples (Figures 8.3e and 8.5a). Similar to the effects of FAK inhibition, the inhibition of ROCK was associated with a more remarkable decrease in the signal intensity of Runx2 in the cells residing on the bTi surfaces (Figures 8.3f and 8.5d).

8.3.5 Effects of YAP inhibition on hMSCs

The YAP-inhibited hMSCs cultured on the flat Ti samples did not show a very different morphology as compared to the cells not exposed to any inhibitory agent (Figures 8.3a and 8.6a). These cells maintained a polygonal shape and their area was not significantly affected (*i.e.*, an average area of around $4300 \mu\text{m}^2$ as compared to around $4700 \mu\text{m}^2$ under the normal conditions) (Figures 8.3b and 8.6b). However, the cells residing on the bTi surfaces displayed an altered morphology (*i.e.*, both stellate and highly elongated morphologies) (Figure 8.6a) and a significantly decreased spreading area (*i.e.*, $2100 \mu\text{m}^2$) (Figure 8.6b). Despite the differences in the cell area, the cell aspect ratio and shape index were not significantly different between the flat Ti and bTi surfaces (Figure 8.6b). Furthermore, similar to the normal conditions, the cells residing on the bTi surfaces had smaller but less rounded and more elongated nuclei as compared to the cells attached to the flat Ti surfaces (Figures 8.3b and 8.6b).

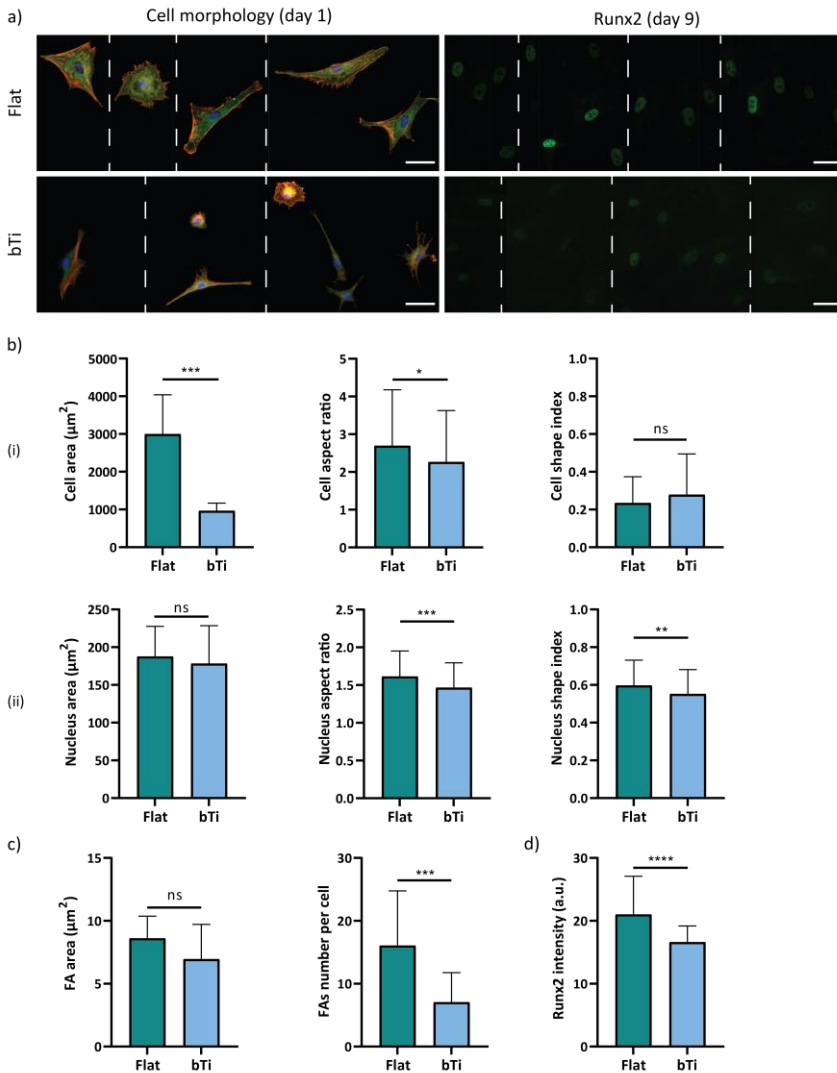


Figure 8.5. The adaptation and interactions of the hMSCs with the flat Ti and bTi surfaces after the inhibition of ROCK. a) The morphology of the hMSCs and expression of Runx2 after 1 and 9 days of culture, respectively, on the flat Ti and bTi surfaces. The white dashed lines indicate that a collage is made of images from different samples. Scale bar = 50 μm . b) The morphological characteristics of the cell body (i) and nucleus (ii), including the area (Welch's *t*-test), aspect ratio (Mann-Whitney test for i and Welch's *t*-test for ii), and shape index (Mann-Whitney test for i and Welch's *t*-test for ii). At least 100 cells were analyzed per study group. c) The average area (Welch's *t*-test) and number of FAs per cell (Mann-Whitney test) were measured for 15 cells on the flat Ti and bTi surfaces. d) The intensity of the Runx2 signal for the hMSCs residing on the flat Ti and bTi surfaces (Mann-Whitney test). At least 200 cells were analyzed per study group (* $p < 0.05$, ** $p < 0.01$, *** $p < 0.001$, and **** $p < 0.0001$).

Unlike the previous inhibition experiments, the YAP inhibition experiments increased the intensity of the Runx2 signal for the cells residing on the flat Ti surfaces (Figures 8.4c, 8.5d, and 8.6c). The bTi surfaces significantly reduced the intensity of the Runx2 signal but the intensity values were still much higher than in the FAK and ROCK inhibition experiments (Figures 8.4c, 8.5d, and 8.6c).

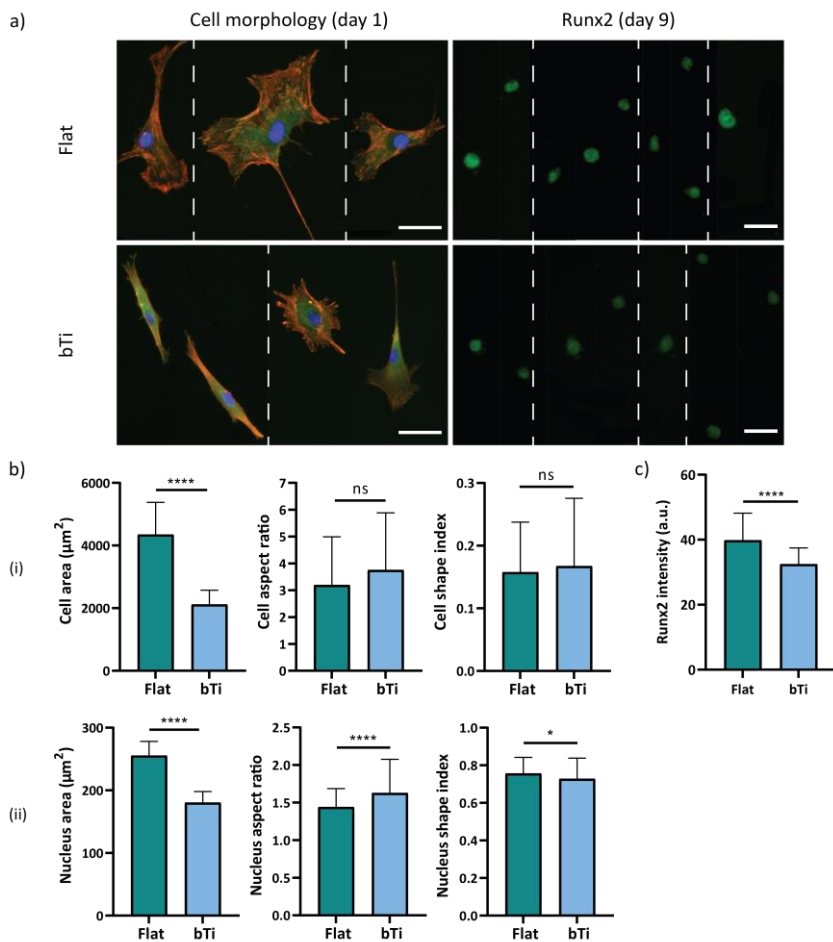


Figure 8.6. The adaptation and interactions of the hMSCs with the flat Ti and bTi surfaces after the inhibition of YAP. a) The morphology of the hMSCs and expression of Runx2 after 1 and 9 days of culture, respectively, on the flat Ti and bTi surfaces. The white dashed lines indicate that a collage is made of images from different samples. Scale bar = 100 μm . b) The morphological characteristics of the cell body (i) and nucleus (ii), including the area (Welch's *t*-test), aspect ratio (Mann-Whitney test), and shape index (Mann-Whitney test). At least 100 cells were analyzed per study group. c) The intensity of the Runx2 signal for the hMSCs residing on the flat Ti and bTi surfaces (Mann-Whitney test). At least 50 cells were analyzed per study group (* $p < 0.05$ and **** $p < 0.0001$).

8.4 Discussion

The emergence of high aspect ratio nanostructured surfaces has opened a new horizon in the design and manufacturing of cell-instructive biomaterials. These surfaces provide the cells with extreme topographical cues and alter their response to the extracellular microenvironment. The huge potential of these surfaces to influence the mechanosensing pathways of cells and the countless scenarios in which the cells undergo different differentiation processes have underscored the importance of in-depth studies on the function of such biological interfaces⁸. Previous studies have shown the effectiveness of (ICP) RIE in the production of bactericidal and osteogenic high aspect ratio nanopillars on Ti as the most clinically-relevant material for orthopedic applications^{7, 13-15}. The existing literature consistently shows that high aspect ratio bTi nanopillars affect the cell morphology, spreading area, and adhesion complexes in both primary cells^{13, 15} and cell lines⁷. However, the pathways involved in the transduction of mechanical forces, the interpretation of the cell shape, and, eventually, the transcription of osteogenic markers in the cell nucleus are not yet fully elucidated. In this study, we focused on the interactions of hMSCs with high aspect ratio bTi nanopillars and the role of FAK (as an important initiator-regulator of FA formation and maturation), ROCK (as a regulator of cell contractility), and YAP (as a nuclear transcriptional regulator) in the expression of osteogenic markers induced by the nanopillars.

While the high aspect ratio nanopillars did not impair the attachment, survival, and metabolic activity of the cells, they gave rise to a cell morphology that was different from the one observed on the polished flat surfaces. The extreme change in the surface topography provides the cells with a novel landscape of potential anchorage points. The initially (*i.e.*, day 1) confined cell area on the nanopillars as compared to the flat surface together with the development of abundant filopodia indicates that the cells are still probing the surface to establish more stable attachments by finding more suitable ligands for integrin binding, and an optimized membrane trafficking, resulting in a slower adaptation to the surface^{7, 29-31}. The altered cell morphology was also associated with differences in the organization of the cytoskeleton and the formation of FAs. Although the cells attached to the bTi nanopillars had, on average, a lower aspect ratio as compared to the cells residing on the flat Ti, they showed more cellular extensions. Developing these cell protrusions in different directions led to a higher cell shape index (*i.e.*, the perimeter closing in on the area). Interestingly, the poorly-organized F-actin can be mostly observed

to be oriented in the direction of these protrusions. The observed cytoskeleton organization in these cells could imply a contractile spreading phase³², which is in line with the previous points regarding the slower adaptation to the bTi surface. Moreover, an anisotropic distribution of FAs was observed on the bTi surface, as they were predominantly formed at those locally elongated cell edges. It is difficult to determine whether these FAs are merely nascent adhesions or long-lasting stable ones. On one hand, they are not completely co-localized with underdeveloped F-actin while, on the other hand, they are oval-shaped rather than round-shaped and have an average area that is comparable to the FAs formed on flat Ti. Further analysis of integrin clustering^{33,34} or the application of super-resolution microscopy and fluorescence resonance energy transfer (FRET) microscopy to detect the upward shifting of vinculin away from the cell membrane³⁵ could clarify these contradictory findings regarding the maturation of FAs on high aspect ratio nanopillars. Here, we may conclude that there are already sufficient forces generated via actomyosin contractility, resulting in the activation and recruitment of vinculin to the adhesion sites^{4,36}. Another point to consider is that the morphology and dynamics of the cell nuclei are influenced by forces transduced through FAs^{37,38}. For instance, unevenly distributed mature FAs could stretch the cell nucleus, thereby enhancing the osteogenic differentiation of the cells³⁸. Our findings showed that the cell nucleus is more elongated and less rounded on the bTi surfaces as compared to the flat Ti which might be linked to the different distribution of FAs.

Even though the hMSCs required more time to adapt to the bTi surfaces, they exhibited a higher intensity of the YAP signal in their nuclei and had a larger total cytoplasmic/nuclear YAP area. It is likely that the YAP nuclear translocation has been continuing to an even greater extent after this time point. Several studies have reported a connection between nuclear translocation of YAP and enhanced osteogenic differentiation³⁹⁻⁴². Particularly, an incremental nuclear translocation of YAP and Runx2 has been previously shown in hMSCs undergoing osteogenic differentiation induced by altered ECM ligand spacing⁴³ or cyclic stretch⁴⁴. In contrast, some studies on the osteogenic properties of TiO₂ nanotubes^{45,46} and electrospun nanofibers²² suggest that dissociation of nuclear YAP/Runx2 complexes and the expelling of YAP to the cytoplasm enable Runx2 to induce skeletal gene expression. Our results indicate that in the case of high aspect ratio bTi nanopillars, a correlation exists between the nuclear translocation of YAP and the expression of Runx2.

To further study the mechanisms underlying these observations, we investigated the effects of inhibiting FAK as a substantial component of the integrin signaling layer in FAs⁴⁷ which is crucial for the initiation of outside-in force transduction. The inhibition of FAK resulted in a decreased cell spreading area on both bTi and flat Ti surfaces, possibly due to the inability of the cells to secure strong adhesions on the surface. The inhibition was also correlated with a significantly decreased Runx2 signal intensity, which might be directly related to the disruption of FAs in the sense that force transduction from the integrins to the nucleus is hindered⁴⁸. The reduction in the Runx2 intensity was more severe in the cells residing on the bTi nanopillars. The extremely small and rounded morphology of these cells has most likely limited the cytoskeleton organization. In addition, the disappearance of the heterogeneous distribution of FAs on the bTi surface may have reduced the elongation of the nuclei as compared to the cells residing on the flat Ti surface, reinforcing the hypothesis that, unlike the normal condition, here the nuclei are undertensioned^{46, 49}. Measuring the adhesion forces⁵⁰ in future research would quantitatively confirm/reject this hypothesis.

Another intracellular pathway that plays a major role in perceiving the ECM mechanics is the RhoA/ROCK pathway. RhoA which is a member of the Rho family of GTPases regulates the activity of myosin II through its effector ROCK. Through the phosphorylation of the myosin light chain (MLC), ROCK increases the contractile force generated by myosin II on actin fibers. ROCK is, thus, considered as an important regulator of cell-generated forces⁵¹, which consequently affects the cell shape^{52, 53} and the activation of FAK in an inside-out signaling process⁵⁴. In this study, the effects of ROCK inhibition on the cell area and cell nucleus elongation and shape index were similar to those of FAK inhibition. The cell area was reduced on both flat Ti and bTi surfaces, but bTi induced a more drastic change. As explained earlier, less tensions seemed to have been exerted on the cell nucleus. Moreover, the ROCK-inhibited hMSCs showed very irregular morphologies on the bTi nanopillars, indicating the significant dependency of the cells on ROCK to display a fibroblast-like morphology when interacting with extreme topographies. The spindle-like stellar morphology has been previously observed in ROCK-inhibited hASCs²⁰. Our results are also in agreement with the results of the previous studies in which the cell area decreased upon ROCK inhibition^{22, 55}. In addition to the cell area, ROCK inhibition has been shown to decrease the formation of FAs and their size on micropatterned surfaces⁵⁵. Here, we did not observe a significant difference in the FA area between the flat Ti and bTi surfaces. However, the cells residing on the bTi

surfaces formed significantly lower numbers of FAs. We may conclude that the higher dependency of the bTi-dwelling cells on ROCK for regulating their shape, adhesion to the surface, and endogenous forces, results in the lower expression of Runx2 in comparison to the flat Ti-dwelling cells. Such a correlation between inhibiting ROCK and the suppression of osteogenic differentiation has been previously shown in the presence²² and absence²⁰ of nanostructured biomaterials.

An increased cytoskeletal tension regulated by the RhoA/ROCK pathway is believed to cause the nuclear localization of YAP^{23,56}. YAP shuttling between the cytoplasm and nucleus has been shown to be controlled by the cell area²⁵. Furthermore, it acts as a necessary downstream of RhoA/ROCK to regulate the formation of FAs by influencing the expression of FA-related genes²⁵. However, the role of YAP in mechanotransduction cannot be considered as being merely a downstream of other pathways as YAP can also regulate its upstream factors in a feedback loop^{24,57}. Based on these known facts about YAP, we expected no significant changes in the cell area after the YAP inhibition. Surprisingly, it was only true for the flat Ti surfaces and the cell area and morphology were significantly affected on the bTi nanopillars. On the flat Ti surface, the YAP inhibition was also correlated with increased Runx2 intensity as compared to the normal conditions while the Runx2 intensity significantly decreased on the bTi surfaces. Although it is not clear what exact connections exist between YAP and the regulation of the cell morphology and area on the bTi surfaces, our results suggest that the relationship between the YAP nuclear localization and the expression of Runx2 is mutually exclusive in the case of the flat Ti and bTi surfaces. Moreover, any forces exerted to the nucleus are likely regulated by the adhesion and contractility of the cells, as there was no altered trend in the morphological characteristics of the cell nuclei after YAP inhibition as compared to the normal conditions. It has been argued that the physical deformation of the nucleus through the LINC complex mediates the nuclear translocation of YAP⁵⁸. A more recent study suggests that the nuclear translocation of YAP requires the opening of the nuclear pore complex as a result of the physical stretching of the nucleus membrane⁵⁹. Furthermore, Lamin A/C plays a crucial role in resisting any nuclear deformations and contributing to nuclear stability and mechanics⁶⁰. We did not observe a severe penetration of the cell body by high aspect ratio bTi nanopillars, nor did the cells engulf the nanopillars in this study. These different methods of interfacing, commonly observed in the high aspect ratio nanostructured materials, have been suggested to initiate other

events such as direct nuclear mechanotransduction and endocytosis⁸. Further analysis of the nuclear mechanics and its connection to cell adhesion and contractility in future studies may clarify how YAP nuclear translocation upregulates the expression of osteogenic markers.

In summary, our findings indicate that high aspect ratio bTi nanopillars have a remarkable potential to direct hMSCs toward osteogenic lineage commitment by manipulating cell adhesion as regulated by FAK, cell contractility as regulated by ROCK, and the nuclear translocation of transcriptional factors (*e.g.*, YAP). Furthermore, these factors are interrelated and can modulate each other's roles. In other words, an osteogenic mechanotransduction pathway can be postulated in which the adhesion and adaptation of the cells to the extreme topography of the surface is highly dependent on FAK which works in close liaison with ROCK to increase the endogenous forces within the cells and determines the cell shape and area. Whether directly transducing the forces to the nucleus or indirectly enhancing the nuclear translocation of YAP, mechanical stimuli can be translated to biochemical factors, such as Runx2 in the nucleus.

8.5 Conclusions

High aspect ratio nanopillars created through reactive ion etching of the Ti surface hold tremendous potential for selective behavior against mammalian and bacterial cells. The rare combination of osteogenic and bactericidal properties of bTi places it in the category of cell-instructive meta-biomaterials. Here, we showed that a specific configuration of bTi nanopillars induces an increased level of Runx2 expression in hMSCs. The adaptation of the hMSCs to this surface was also associated with significant changes in the cell morphology, cytoskeleton organization, and nuclear translocation of YAP. Further investigations revealed that these phenomena are highly dependent on FAK and ROCK as the master regulators of cell adhesion and contractility, which eventually determine the cell shape and area. The mechanotransduction pathway involving FAK and ROCK either directly or indirectly (by enhancing nuclear translocation of YAP) affects the transduction of mechanical stimuli by the cell nucleus and results in the upregulation of Runx2 as a major osteogenic marker. Understanding the action mechanism of bTi nanopillars would contribute to the rational design of cell-instructive biomaterials with the aim of directing stem cells fate toward specific lineages.

Bibliography

- [1] M. Ventre, P.A. Netti, Engineering cell instructive materials to control cell fate and functions through material cues and surface patterning, *ACS Applied Materials & Interfaces*, 8(24), 14896-14908, 2016.
- [2] A.L. Facklam, L.R. Volpatti, D.G. Anderson, Biomaterials for personalized cell therapy, *Advanced Materials*, 32(13), 1902005, 2020.
- [3] L. Li, J. Eyckmans, C.S. Chen, Designer biomaterials for mechanobiology, *Nature Materials*, 16(12), 1164-1168, 2017.
- [4] S. Di Cio, J.E. Gautrot, Cell sensing of physical properties at the nanoscale: Mechanisms and control of cell adhesion and phenotype, *Acta Biomaterialia*, 30, 26-48, 2016.
- [5] Y. Sun, C.S. Chen, J. Fu, Forcing stem cells to behave: a biophysical perspective of the cellular microenvironment, *Annual Review of Biophysics*, 41, 519-542, 2012.
- [6] G. Abagnale, M. Steger, V.H. Nguyen, N. Hersch, A. Sechi, S. Joussem, B. Denecke, R. Merkel, B. Hoffmann, A. Dreser, Surface topography enhances differentiation of mesenchymal stem cells towards osteogenic and adipogenic lineages, *Biomaterials*, 61, 316-326, 2015.
- [7] K. Modaresifar, M. Ganjian, L. Angeloni, M. Minneboo, M.K. Ghatkesar, P.L. Hagedoorn, L.E. Fratila-Apachitei, A.A. Zadpoor, On the Use of Black Ti as a Bone Substituting Biomaterial: Behind the Scenes of Dual-Functionality, *Small*, 2100706, 2021.
- [8] S.G. Higgins, M. Becce, A. Belessiotis-Richards, H. Seong, J.E. Sero, M.M. Stevens, High-Aspect-Ratio Nanostructured Surfaces as Biological Metamaterials, *Advanced Materials*, 1903862, 2020.
- [9] Y. Wang, Y. Yang, L. Yan, S.Y. Kwok, W. Li, Z. Wang, X. Zhu, G. Zhu, W. Zhang, X. Chen, Poking cells for efficient vector-free intracellular delivery, *Nature Communications*, 5(1), 1-9, 2014.
- [10] Y. Cao, M. Hjort, H. Chen, F. Birey, S.A. Leal-Ortiz, C.M. Han, J.G. Santiago, S.P. Paşca, J.C. Wu, N.A. Melosh, Nondestructive nanostraw intracellular sampling for longitudinal cell monitoring, *Proceedings of the National Academy of Sciences*, 114(10), E1866-E1874, 2017.
- [11] K. Modaresifar, S. Azizian, M. Ganjian, L.E. Fratila-Apachitei, A.A. Zadpoor, Bactericidal effects of nanopatterns: A systematic review, *Acta Biomaterialia*, 83, 29-36, 2019.
- [12] A.A. Zadpoor, Meta-biomaterials, *Biomaterials Science*, 8(1), 18-38, 2020.
- [13] J. Hasan, S. Jain, K. Chatterjee, Nanoscale topography on black titanium imparts multi-biofunctional properties for orthopedic applications, *Scientific Reports*, 7, 41118, 2017.
- [14] M. Ganjian, K. Modaresifar, H. Zhang, P.-L. Hagedoorn, L.E. Fratila-Apachitei, A.A. Zadpoor, Reactive ion etching for fabrication of biofunctional titanium nanostructures, *Scientific Reports*, 9(1), 1-20, 2019.
- [15] T.L. Clainche, D. Linklater, S. Wong, P. Le, S. Juodkakis, X.L. Guével, J.-L. Coll, E.P. Ivanova, V. Martel-Frchet, Mechano-Bactericidal Titanium Surfaces for Bone Tissue Engineering, *ACS Applied Materials & Interfaces*, 12, 48272-48283, 2020.
- [16] D.P. Linklater, V.A. Baulin, S. Juodkakis, R.J. Crawford, P. Stoodley, E.P. Ivanova, Mechano-bactericidal actions of nanostructured surfaces, *Nature Reviews Microbiology*, 19, 8-22, 2020.

-
- [17] T.D. Ross, B.G. Coon, S. Yun, N. Baeyens, K. Tanaka, M. Ouyang, M.A. Schwartz, Integrins in mechanotransduction, *Current Opinion in Cell Biology*, 25(5), 613-618, 2013.
- [18] M.J.P. Biggs, M.J. Dalby, Focal adhesions in osteoneogenesis, *Proceedings of the Institution of Mechanical Engineers, Part H: Journal of Engineering in Medicine*, 224(12), 1441-1453, 2010.
- [19] P. Hu, X. Zhu, C. Zhao, J. Hu, E. Luo, B. Ye, Fak silencing impairs osteogenic differentiation of bone mesenchymal stem cells induced by uniaxial mechanical stretch, *Journal of Dental Sciences*, 14(3), 225-233, 2019.
- [20] L. Hyväri, M. Ojansivu, M. Juntunen, K. Kartasalo, S. Miettinen, S. Vanhatupa, Focal adhesion kinase and ROCK signaling are switch-like regulators of human adipose stem cell differentiation towards osteogenic and adipogenic lineages, *Stem Cells International*, 2018, 2018.
- [21] E.C. Lessey, C. Guilly, K. Burrige, From mechanical force to RhoA activation, *Biochemistry*, 51(38), 7420-7432, 2012.
- [22] B. Chang, C. Ma, X. Liu, Nanofibers regulate single bone marrow stem cell osteogenesis via FAK/RhoA/YAP1 pathway, *ACS Applied Materials & Interfaces*, 10(39), 33022-33031, 2018.
- [23] S. Dupont, L. Morsut, M. Aragona, E. Enzo, S. Giullitti, M. Cordenonsi, F. Zanconato, J. Le Digabel, M. Forcato, S. Bicciato, Role of YAP/TAZ in mechanotransduction, *Nature*, 474(7350), 179-183, 2011.
- [24] C.D. Kegelman, J.M. Collins, M.P. Nijssure, E.A. Eastburn, J.D. Boerckel, Gone caving: roles of the transcriptional regulators YAP and TAZ in skeletal development, *Current Osteoporosis Reports*, 1-15, 2020.
- [25] G. Nardone, J. Oliver-De La Cruz, J. Vrbsky, C. Martini, J. Pribyl, P. Skládal, M. Pešl, G. Caluori, S. Pagliari, F. Martino, YAP regulates cell mechanics by controlling focal adhesion assembly, *Nature Communications*, 8(1), 1-13, 2017.
- [26] R. Narcisi, W.J. Koevoet, G.J. van Osch, *Expansion and Chondrogenic Differentiation of Human Bone Marrow-Derived Mesenchymal Stromal Cells*, in *Osteoporosis and Osteoarthritis*. 2021, Springer. p. 15-28.
- [27] U. Horzum, B. Ozdil, D. Pesen-Okvur, Step-by-step quantitative analysis of focal adhesions, *MethodsX*, 1, 56-59, 2014.
- [28] S. Park, H.-H. Park, K. Sun, Y. Gwon, M. Seong, S. Kim, T.-E. Park, H. Hyun, Y.-H. Choung, J. Kim, Hydrogel nanospine patch as a flexible anti-pathogenic scaffold for regulating stem cell behavior, *ACS Nano*, 13(10), 11181-11193, 2019.
- [29] F. Viela, D. Granados, A. Ayuso-Sacido, I. Rodríguez, Biomechanical cell regulation by high aspect ratio nanoimprinted pillars, *Advanced Functional Materials*, 26(31), 5599-5609, 2016.
- [30] Y. Zhukova, C. Hiepen, P. Knaus, M. Osterland, S. Prohaska, J.W. Dunlop, P. Fratzl, E.V. Skorb, The role of titanium surface nanostructuring on preosteoblast morphology, adhesion, and migration, *Advanced Healthcare Materials*, 6(15), 1601244, 2017.
- [31] M. Ermis, E. Antmen, V. Hasirci, Micro and Nanofabrication methods to control cell-substrate interactions and cell behavior: A review from the tissue engineering perspective, *Bioactive Materials*, 3(3), 355-369, 2018.
- [32] N.C. Gauthier, T.A. Masters, M.P. Sheetz, Mechanical feedback between membrane tension and dynamics, *Trends in Cell Biology*, 22(10), 527-535, 2012.

- [33] O. Rossier, V. Oceau, J.-B. Sibarita, C. Leduc, B. Tessier, D. Nair, V. Gatterdam, O. Destaing, C. Albiges-Rizo, R. Tampé, Integrins β 1 and β 3 exhibit distinct dynamic nanoscale organizations inside focal adhesions, *Nature Cell Biology*, 14(10), 1057-1067, 2012.
- [34] P. Roca-Cusachs, A. Del Rio, E. Puklin-Faucher, N.C. Gauthier, N. Biais, M.P. Sheetz, Integrin-dependent force transmission to the extracellular matrix by α -actinin triggers adhesion maturation, *Proceedings of the National Academy of Sciences*, 110(15), E1361-E1370, 2013.
- [35] L.B. Case, M.A. Baird, G. Shtengel, S.L. Campbell, H.F. Hess, M.W. Davidson, C.M. Waterman, Molecular mechanism of vinculin activation and nanoscale spatial organization in focal adhesions, *Nature Cell Biology*, 17(7), 880-892, 2015.
- [36] D.W. Dumbauld, T.T. Lee, A. Singh, J. Scrimgeour, C.A. Gersbach, E.A. Zamir, J. Fu, C.S. Chen, J.E. Curtis, S.W. Craig, How vinculin regulates force transmission, *Proceedings of the National Academy of Sciences*, 110(24), 9788-9793, 2013.
- [37] M. Versaevael, T. Grevesse, S. Gabriele, Spatial coordination between cell and nuclear shape within micropatterned endothelial cells, *Nature Communications*, 3(1), 1-11, 2012.
- [38] I. Casanellas, A. Lagunas, Y. Vida, E. Pérez-Inestrosa, J.A. Andrades, J. Becerra, J. Samitier, Matrix Nanopatterning Regulates Mesenchymal Differentiation through Focal Adhesion Size and Distribution According to Cell Fate, *Biomimetics*, 4(2), 43, 2019.
- [39] L. Yang, L. Ge, Q. Zhou, T. Mokabber, Y. Pei, R. Bron, P. van Rijn, Biomimetic Multiscale Hierarchical Topography Enhances Osteogenic Differentiation of Human Mesenchymal Stem Cells, *Advanced Materials Interfaces*, 2000385, 2020.
- [40] L. Yang, L. Ge, P. van Rijn, Synergistic effect of cell-derived extracellular matrix and topography on osteogenesis of mesenchymal stem cells, *ACS Applied Materials & Interfaces*, 12(23), 25591-25603, 2020.
- [41] X. Xue, X. Hong, Z. Li, C.X. Deng, J. Fu, Acoustic tweezing cytometry enhances osteogenesis of human mesenchymal stem cells through cytoskeletal contractility and YAP activation, *Biomaterials*, 134, 22-30, 2017.
- [42] L. Li, S. Yang, L. Xu, Y. Li, Y. Fu, H. Zhang, J. Song, Nanotopography on titanium promotes osteogenesis via autophagy-mediated signaling between YAP and β -catenin, *Acta Biomaterialia*, 96, 674-685, 2019.
- [43] P. Han, J.E. Frith, G.A. Gomez, A.S. Yap, G.M. O'Neill, J.J. Cooper-White, Five piconewtons: the difference between osteogenic and adipogenic fate choice in human mesenchymal stem cells, *ACS Nano*, 13(10), 11129-11143, 2019.
- [44] Y. Wei, X. Mo, P. Zhang, Y. Li, J. Liao, Y. Li, J. Zhang, C. Ning, S. Wang, X. Deng, Directing stem cell differentiation via electrochemical reversible switching between nanotubes and nanotips of polypyrrole array, *ACS Nano*, 11(6), 5915-5924, 2017.
- [45] H. Zhang, L.F. Cooper, X. Zhang, Y. Zhang, F. Deng, J. Song, S. Yang, Titanium nanotubes induce osteogenic differentiation through the FAK/RhoA/YAP cascade, *RSC Advances*, 6(50), 44062-44069, 2016.
- [46] M.G. Necula, A. Mazare, R.N. Ion, S. Ozkan, J. Park, P. Schmuki, A. Cimpean, Lateral spacing of TiO₂ nanotubes modulates osteoblast behavior, *Materials*, 12(18), 2956, 2019.
- [47] P. Tapial Martínez, P. López Navajas, D. Lietha, FAK structure and regulation by membrane interactions and force in focal adhesions, *Biomolecules*, 10(2), 179, 2020.

- [48] R.M. Salasznyk, R.F. Klees, W.A. Williams, A. Boskey, G.E. Plopper, Focal adhesion kinase signaling pathways regulate the osteogenic differentiation of human mesenchymal stem cells, *Experimental Cell Research*, 313(1), 22-37, 2007.
- [49] R. Domura, R. Sasaki, M. Okamoto, M. Hirano, K. Kohda, B. Napiwocki, L.-S. Turng, Comprehensive study on cellular morphologies, proliferation, motility, and epithelial-mesenchymal transition of breast cancer cells incubated on electrospun polymeric fiber substrates, *Journal of Materials Chemistry B*, 5(14), 2588-2600, 2017.
- [50] M. Nouri-Goushki, L. Angeloni, K. Modaresifar, M. Minneboo, P.E. Boukany, M.J. Mirzaali, M.K. Ghatkesar, L.E. Fratila-Apachitei, A.A. Zadpoor, 3D-Printed Submicron Patterns Reveal the Interrelation between Cell Adhesion, Cell Mechanics, and Osteogenesis, *ACS Applied Materials & Interfaces*, 13(29), 33767-33781, 2021.
- [51] K. Burrridge, C. Guilluy, Focal adhesions, stress fibers and mechanical tension, *Experimental Cell Research*, 343(1), 14-20, 2016.
- [52] M. Bao, J. Xie, A. Piruska, W.T. Huck, 3D microniches reveal the importance of cell size and shape, *Nature Communications*, 8(1), 1-12, 2017.
- [53] R. McBeath, D.M. Pirone, C.M. Nelson, K. Bhadriraju, C.S. Chen, Cell shape, cytoskeletal tension, and RhoA regulate stem cell lineage commitment, *Developmental Cell*, 6(4), 483-495, 2004.
- [54] D.D. Schlaepfer, C.R. Hauck, D.J. Sieg, Signaling through focal adhesion kinase, *Progress in Biophysics & Molecular Biology*, 71(3-4), 435-478, 1999.
- [55] C.H. Seo, K. Furukawa, K. Montagne, H. Jeong, T. Ushida, The effect of substrate microtopography on focal adhesion maturation and actin organization via the RhoA/ROCK pathway, *Biomaterials*, 32(36), 9568-9575, 2011.
- [56] M. Aragona, T. Panciera, A. Manfrin, S. Giullitti, F. Michielin, N. Elvassore, S. Dupont, S. Piccolo, A mechanical checkpoint controls multicellular growth through YAP/TAZ regulation by actin-processing factors, *Cell*, 154(5), 1047-1059, 2013.
- [57] D.E. Mason, J.M. Collins, J.H. Dawahare, T.D. Nguyen, Y. Lin, S.L. Voytik-Harbin, P. Zorlutuna, M.C. Yoder, J.D. Boerckel, YAP and TAZ limit cytoskeletal and focal adhesion maturation to enable persistent cell motility, *Journal of Cell Biology*, 218(4), 1369-1389, 2019.
- [58] T.P. Driscoll, B.D. Cosgrove, S.-J. Heo, Z.E. Shurden, R.L. Mauck, Cytoskeletal to nuclear strain transfer regulates YAP signaling in mesenchymal stem cells, *Biophysical Journal*, 108(12), 2783-2793, 2015.
- [59] A. Elosegui-Artola, I. Andreu, A.E. Beedle, A. Lezamiz, M. Uroz, A.J. Kosmalska, R. Oria, J.Z. Kechagia, P. Rico-Lastres, A.-L. Le Roux, Force triggers YAP nuclear entry by regulating transport across nuclear pores, *Cell*, 171(6), 1397-1410. e1314, 2017.
- [60] J. Lammerding, L.G. Fong, J.Y. Ji, K. Reue, C.L. Stewart, S.G. Young, R.T. Lee, Lamins A and C but not lamin B1 regulate nuclear mechanics, *Journal of Biological Chemistry*, 281(35), 25768-25780, 2006.

9

Concluding remarks

“The most common reaction of the human mind to achievement is not satisfaction, but craving for more.”

- Yuval Noah Harari

9.1 Main findings of this thesis

In this thesis, we adopted an experimental approach to advance the fundamental knowledge regarding the differential interactions of bacteria and mammalian cells with surface nanopatterns, and to devise a set of general guidelines for the rational design of nanopatterned surfaces with distinct or dual functionalities, suitable for future orthopedic applications. Here, we summarize the main findings pertaining to the research objectives of this thesis, as outlined in the Introduction chapter.

What are the geometrical characteristics of bactericidal nanopatterns?

According to the findings of this thesis and as supported by many studies available in the literature, a specific range of dimensions can be considered beyond which the bactericidal properties are very unlikely to be observed. Our findings suggest that a combination of heights between 100 nm and 1 μm and diameters between 10 nm and 300 nm would effectively lead to mechano-bactericidal activity against both Gram-negative and Gram-positive bacteria, provided that the aspect ratio of the nanopattern is at least 2. In addition, considering the potential mechano-killing mechanisms of nanopatterned surfaces, we conclude that the interspacing of the nanopatterns is one of the most decisive geometrical features. Interspacing values between 300 nm and 500 nm were found to induce limited bactericidal effects while reducing the interspacing from 300 nm to a minimum of 100 nm would maximize the killing efficiency of the surface. Moreover, we showed that in the case of nanopillars with precisely controlled dimensions, the spatial arrangement of the pillars (*i.e.*, ordered *vs.* controlled disordered configurations) has no impact on the bactericidal properties. This was an important finding since the controlled disordered nanopatterns of different shapes (*i.e.*, nanopits) have been previously shown to enhance the osteogenic differentiation of stem cells¹.

How do the bactericidal nanopatterns kill the bacteria?

The exact mechano-bactericidal mechanisms of nanopatterned surfaces are still a matter of debate². In recent years, however, extensive experimental and simulation studies have provided a clearer insight into the potential underlying mechanisms³⁻⁶. Hypothesizing that the killing mechanisms of nanopatterned surfaces are purely mechanical, we focused on the interface between the nanopatterns and bacteria to identify the cause of severe structural deformations in the bacteria. We found that Gram-positive *S. aureus* gets penetrated by the sharp tip of the nanopillars. The intruding length of the

nanopillars exceeds the thickness of the bacterial cell wall. We can, therefore, conclude that the disruption of the cell wall integrity (and maybe even that of the membrane) results in the death of bacteria. In the case of the rod-shaped Gram-negative *E. coli*, the structural deformations were so drastic that the bacterial cell morphology was barely recognizable. The intrusion of the tips of the nanopillars into the cell wall of *E. coli* was observed to occur at a higher number of sites as *E. coli* has a larger area for making contact with the nanopillars.

It is noteworthy that “penetration” described above, has been argued to happen via the local stretching of the cell wall/membrane that disrupts their integrity². Indeed, we observed the stretching of the cell wall on the porous configuration of bTi surfaces where the nanopillars were not separated enough at their apexes to intrude the cell wall individually. We may conclude that the killing mechanisms of nanopatterned surfaces highly depend on the geometry and spatial arrangement of the nanopatterns. Nonetheless, experimental limitations, inconsistencies over the assessment methods, and several other methodological factors need to be considered when discussing the mechano-bactericidal mechanisms of the nanopatterned surfaces. These points are briefly discussed in the next section of this chapter.

How should an osteogenic nanopattern be designed?

The existing literature suggests that the physical features of the surfaces that induce an osteogenic response in cells fall within a broad range of shapes and dimensions from the nanoscale (*i.e.*, feature sizes < 100 nm) to the microscale (*i.e.*, feature sizes up to 100 μm), as the cell behavior can be directed both at the subcellular and cellular levels⁷. Considering the limitations of highly precise nanofabrication techniques in patterning a large area required for cell studies, we used alternative techniques and systematically studied a wider range of dimensions within the submicron scale. We found that there is a direct relationship between the aspect ratio of the nanopatterns and their osteogenic properties. In other words, increasing the height of the nanopatterns when their diameter is kept constant enhances the osteogenic activity of the surface. Interestingly, the effects of interspacing vary based on the type and, thus, properties of the material from which the nanopattern are made. When the cells can bend the nanopatterns, a lower interspacing is more pro-osteogenic. In contrast, when the nanopatterns are too rigid to be bent, an increased interspacing enhances the osteogenic properties. Nevertheless, the interactions of the cells with the nanopatterned surfaces are way more complicated than bacteria. The

larger size and structural complexity of the cells dwarf the isolated effects of single dimensions of the nanopatterns. What matters most in the design of an osteogenic nanopattern is the impact it has on the cells during the early stages of cell adaptation to the surfaces. We found that there is a connection between the short-term adaptation of the cells to the nanopatterned surfaces and their long-term osteogenic response. Based on the findings of this thesis, we conclude that high aspect ratio nanopillars that cause mild changes in the morphological characteristics of the cell body and nucleus, cause the heterogeneous formation of focal adhesions and increase the adhesion forces and contractility in the cells, thereby directing the cells toward the osteogenic lineage. We discuss this point further below.

How is a cell directed toward the osteogenic lineage?

As already mentioned, a connection exists between the early-stage adaptation of the cells to the nanopatterned surfaces (*e.g.*, adhesion, morphology, contractility, *etc.*) and the subsequent osteogenic response. We found that the osteogenic nanopatterns studied in this thesis significantly reduce the spreading area of the cells as compared to the non-patterned flat surfaces. This reduction in cell area is usually associated with a perturbed cytoskeletal organization. Although the altered morphological characteristics and cytoskeletal organization may indicate a slower adaptation of the cells to the nanopatterned surfaces in comparison with non-patterned flat surfaces, they can eventually result in the upregulation of the osteogenic markers. The increased adhesion forces on nanopatterned surfaces and traction forces that can bend the nanopillars suggest that the focal adhesions formed on nanopatterned surfaces could withstand higher forces even though their area is not necessarily larger than those formed on flat surfaces. We showed that FAK plays a substantial role in regulating cell adhesion to the nanopatterned surfaces and its inhibition significantly downregulates the expression of osteogenic markers such as Runx2. Additionally, the contractility of the cells is another important factor affecting cell fate. We found that the cells undergoing osteogenic differentiation on nanopatterned surfaces have a higher stiffness (*i.e.*, elastic modulus) as compared to the cells residing on flat surfaces. We showed that RhoA/ROCK pathway regulates the contractility and endogenous forces generated within the cell body on nanopatterned surfaces. These forces may alter the transcriptional activity of the nucleus upon being transduced to the nucleus. We may conclude that an interrelated process involving the initial adhesion forces, cytoskeletal organization and contractility, cell shape and area, and

the nuclear translocation of transcriptional factors are triggered by high aspect ratio nanopatterns and eventually results in the osteogenic differentiation of the cells.

In summary, we showed that it is possible to close the gap between bactericidal and osteogenic nanopatterns through the rational design of nanopatterns with specific dimensions and arrangements (to mechanically kill the bacteria) that direct the cells to generate and transduce forces to their nucleus (to induce osteogenic differentiation).

9.2 Additional remarks and recommendations

On the bactericidal nanopatterns

The number of studies on the bactericidal properties of nanopatterned surfaces has drastically increased since 2017. Despite promising reports over the fabrication of nanopatterns that are highly effective in killing the bacteria, some inconsistencies between these reports make it difficult to compare their results.

The first inconsistency concerns the terminology exploited by researchers in this field. For better scientific communication, it is necessary for the involved researchers to agree upon certain terms they use to describe the shape of nanopatterns they create as well as the function of the nanopatterned surface. For instance, terms such as “nanopillar” and “nanowire” or “mechano-bactericidal” and “anti-bacterial” happen to be used interchangeably to describe quite similar nanopatterns or surfaces with similar functionality in different studies. Furthermore, all the methodological details required for reproducing the results should be reported in the published literature. The way the bacteria are cultured and exposed to the nanopatterned surfaces and the experimental details of their viability assessment methods can affect the obtained results. For instance, it has been recently reported that external forces caused by the movement of the air-liquid interface in the incubation setup highly increase the bacterial death rate⁸. One can, therefore, argue that the different methods of exposing bacteria to the nanopatterned surfaces (*e.g.*, dropping the bacterial inoculum on top of the surface or submerging the surface into the bacterial suspension) result in the generation of different levels of such forces and consequently affect the final measured bactericidal efficiency. The same bias could be introduced during the evaluation phase when the surfaces are usually first washed and then stained by live/dead assay kits.

Similar remarks should be taken into consideration when assessing the killing efficiency of nanopatterned surfaces. Early studies relied on SEM observations to

determine the viability of bacterial cells based on their intact/deformed morphologies. This method is inadequate in the sense that it makes the evaluation quite subjective. On the other hand, it may underrate the killing efficiency as some bacterial cells may display a relatively normal morphology while they are inactivated due to perturbation of their cell wall/membrane. Nevertheless, in the case of nanopatterns fabricated by low-throughput techniques (*e.g.*, EBID), SEM-based evaluation is still the only practical evaluation method as patterning a large area that allows for live/dead staining and CFU counting is extremely time-consuming. However, the new nanofabrication process presented in this thesis would overcome this challenge for future studies. The other commonly used assessment methods also suffer from some disadvantages^{9,10}. For example, CFU counting may yield misleading results as the full removal of the bacteria from the nanopatterned surface may not always be achieved. In addition, this method may overestimate or underestimate the killing efficiency of the surface. For instance, removing bacteria from the surface using sonication might kill the live cells that survived from the nanopatterns. In another scenario, the dead cells, removed from the surface into the suspension upon their death, cannot be counted by this method. Optimizing the experimental design concerning these details, therefore, appears to be crucial for any future studies^{11,12}.

A proper experimental design that illustrates the mechano-bactericidal mechanisms more clearly also requires a deeper understanding of the relevant mechano-microbiological pathways including those pertaining to the way bacteria sense and respond to forces. Gravity and Brownian motions facilitate the passive transport of bacteria to the surface¹³. While gravity has been widely considered as the major driving force, the role of active movement of the bacteria (for instance, facilitated by flagella in certain strains) toward the surface, the forces stored and released upon bending of the nanopatterns, the forces associated with the bacterial cell division, and the bacterial strain motility have only occasionally been discussed^{3, 14-16}. Advanced live imaging techniques enable following the bacteria trajectory toward the surface and tracking any structural deformation in a real-time manner. Moreover, similar to the studies on the adhesion of mammalian cells to the nanopatterns, AFM can be used to quantitatively measure the bacterial adhesion forces and investigate its correlation with the killing efficiency of the surface¹⁷.

Considering the bactericidal nanopatterned surfaces for end applications, such as orthopedic implants, raises questions about whether the performance of these surfaces

changes from *in vitro* to *in vivo* environments. In the human body, blood proteins may immediately form a film on the surface before bacteria have the opportunity to reach it. The effect of protein preconditioning of the nanopatterned surfaces on their bactericidal properties requires further research. Additionally, introducing fluid shear stresses to the currently static culture conditions partly mimics the real implantation site.

Finally, it should be noted that the bactericidal mechanisms of nanopatterned surfaces may not be purely mechanical as it is currently assumed. It has been recently shown that when bacteria are exposed to extreme topographies, they start producing reactive oxygen species (ROS) to an intolerable level that finally results in the death of bacteria⁴. This indicates that the killing mechanisms of nanopatterned surfaces can be multi-faceted, affecting the bacteria both biomechanically and biochemically¹⁸.

On the osteogenic nanopatterns

In this thesis, we screened the osteogenic properties of nanopatterns with a wide range of dimensions and configurations to shed light on the essential changes they impose on cells to direct them toward the osteogenic lineage. While we used the state-of-the-art techniques to investigate the osteogenic properties of the nanopatterned surfaces, there is still room for improvements in the applied methodology.

We encourage the further use of traction force microscopy to provide an extended quantitative mechanistic insight into the interactions of the cells with the nanopatterns. The live imaging of cells, especially during the initial phases of adhesion to the surface, would also give valuable information regarding the cell adaptation to the surface. Exploiting these techniques, however, requires sophisticated equipment and multidisciplinary training. Moreover, after confirming the general osteogenic potential of a surface, further molecular biology evaluation (investigating the osteogenic markers' gene expression) would be a preferred and complementary approach as it provides more extensive data regarding the ongoing cellular events.

As discussed in the previous chapters, a plethora of subcellular components orchestrate the cell response to the surface. Due to the limited potential of experimental approaches to control/manipulate a high number of factors simultaneously, simulation studies should be performed to supplement the available empirical data. For instance, the changes in the cell area, formation of focal adhesions, the orientation of actin fibers, and mechanical properties of cells can be used as input to predict the cell fate upon

interactions with various types of nanopatterned surfaces. Going further, we would like to highlight the importance of establishing an open access database to document the findings of relevant studies. Such a database could make it possible to use artificial intelligence to predict the fate of different cell types exposed to a previously unexplored nanopattern¹⁹.

Last but not least, *in vivo* studies are needed to take the osteogenic nanopatterns to the next level²⁰. As discussed earlier, *in vivo* models provide a more realistic environment to assess the potential of nanopatterned surfaces in regenerating new bone tissue. Future research should concern the development of large-scale nanopatterned structures suitable for implantation in animal models.

On the fabrication of nanopatterns

We used and discussed the advantages and disadvantages of different nanofabrication methods in this thesis. In addition to the fact that the precision and throughput of these techniques usually do not go hand in hand, an appropriate nanofabrication technique needs to be applicable to titanium as the most relevant choice of material for orthopedic applications. Nanopatterns fabricated on other substrates (*e.g.*, glass slides in two-photon polymerization) may be unsuitable for further *in vivo* and translational studies. We showed that ICP RIE is a facile technique for directly patterning the pure titanium surface. However, we did not optimize its processing parameters to generate comparable configurations of nanopillars on the surface of Ti-6Al-4V as the golden standard titanium alloy used for the fabrication of metallic bone implants. This can be addressed by performing parametric studies similar to what we did before for pure titanium²¹. The other fabrication process that we developed by combining EBL and NIL would also resolve the known challenges in the fabrication of nanopatterns. Our method also allows for the replication of precisely controlled nanopatterns over a large area, on different substrates, and more interestingly, over curved substrates. As curvature also acts as an important geometrical cue in influencing the cell behavior²², the new fabrication process presented in this thesis would allow for new studies on the combined effects of nanopatterns and curvature.

Finally, given that the current nanofabrication techniques can only pattern a flat 2D surface and not a complex 3D structure, developing 2D to 3D transition mechanisms are required to transform a 2D nanopatterned sheet into a 3D nanopatterned stiff structure. This is a prerequisite for designing appropriate *in vivo* studies to assess the performance

of this new class of biomaterials in a more realistic setting. Some recent studies have proposed such mechanisms as folding²³ and crumpling for transforming a 2D nanopatterned sheet to a 3D complex nanopatterned structure without affecting the functionalities associated with the nanopatterns.

9.3 Future research outlook

In addition to mentioning the limitations of the current studies and recommendations for improving the future studies in the previous section, here, we point out a number of potential research directions from a broader perspective regarding the rare properties of nanopatterned surfaces.

Firstly, as the immune response largely determines the success of a biomaterial, it is important to further study the immunomodulatory properties of nanopatterned surfaces. Designing dual-functional nanopatterns (*i.e.*, bactericidal and osteogenic) that can temporally control the transition between M1 and M2 phenotypes in macrophages would accelerate the pro-healing process and prevent foreign body response in orthopedic applications^{24,25}. Another research question concerning the interactions of immune cells with the nanopatterned surfaces is how they can clean up the surface from the dead bacteria. It is currently unclear what happens to the dead bacteria upon interactions with the nanopatterns. Do they spontaneously get released to the surrounding environment due to the fluid shear stresses or do the immune cells need to intervene? If the latter happens, how strong would be the immune response triggered? Does it impair the expected osteogenic properties of the nanopatterns? Can the host cells populate a surface previously colonized by bacteria? As suggested earlier, *in vivo* studies would be the best option for mimicking such a complex biological environment and revealing the possible outcomes.

Secondly, incorporating precisely controlled nanopatterns into microfluidic chips²⁶ may enable high-throughput cell screening for diagnostic applications. Differential adhesion forces associated with the geometrical characteristics of nanopatterns can serve as a basis for distinguishing the healthy and malignant cells in a clinical sample.

The application of nanopatterned surfaces can be extended further to the field of oncology²⁷. Understanding the mechanics of the tumor microenvironment as well as the differences between cancer and healthy cells in generating endogenous forces are crucial for more effective prevention/treatment of cancer. Therefore, nanopatterned surfaces can

be used as a useful platform to study cancer cell adhesion, proliferation, and migration. Such studies may reveal the most influential factors that affect the cell/tissue mechanics in cancer²⁸ and give rise to interventions that particularly target those factors.

The final research direction that we envision here is combining the use of high aspect ratio nanopatterns and the commonly used antibiotic/growth factor delivery systems. Nanoneedle patches have been extensively studied for years as an effective transdermal drug delivery system²⁹. A similar concept^{30,31} can be adopted for developing hollow or coated high aspect ratio nanopatterns that can release a cargo of antibacterial and osteogenic factors in a temporally-controlled manner, for instance, according to the timeline of the interactions with different bio-organisms or based on the biodegradation rate of the coating.

In conclusion, we bridged between different disciplines, from nanotechnology to engineering design and to (micro)biology to light a beacon in the realm of mechanobiology, hoping that it will shed some light on some important unknowns in the human's path toward a better and healthier life. Going back to the opening paragraph of this thesis, we may say that perhaps it is too soon and ambitious to think of immortality but any genuine endeavor to approach that may forever expand our understanding of life.

Bibliography

- [1] M.J. Dalby, N. Gadegaard, R. Tare, A. Andar, M.O. Riehle, P. Herzyk, C.D. Wilkinson, R.O. Oreffo, The control of human mesenchymal cell differentiation using nanoscale symmetry and disorder, *Nature Materials*, 6(12), 997-1003, 2007.
- [2] D.P. Linklater, V.A. Baulin, S. Juodkazis, R.J. Crawford, P. Stoodley, E.P. Ivanova, Mechano-bactericidal actions of nanostructured surfaces, *Nature Reviews Microbiology*, 19, 8-22, 2020.
- [3] D.P. Linklater, M. De Volder, V.A. Baulin, M. Werner, S. Jessl, M. Golozar, L. Maggini, S. Rubanov, E. Hanssen, S. Juodkazis, High aspect ratio nanostructures kill bacteria via storage and release of mechanical energy, *ACS Nano*, 12(7), 6657-6667, 2018.
- [4] J. Jenkins, J. Mantell, C. Neal, A. Gholinia, P. Verkade, A.H. Nobbs, B. Su, Antibacterial effects of nanopillar surfaces are mediated by cell impedance, penetration and induction of oxidative stress, *Nature Communications*, 11(1), 1-14, 2020.
- [5] S. Pogodin, J. Hasan, V.A. Baulin, H.K. Webb, V.K. Truong, V. Boshkovikj, C.J. Fluke, G.S. Watson, J.A. Watson, R.J. Crawford, Biophysical model of bacterial cell interactions with nanopatterned cicada wing surfaces, *Biophysical Journal*, 104(4), 835-840, 2013.
- [6] E.P. Ivanova, J. Hasan, H.K. Webb, V.K. Truong, G.S. Watson, J.A. Watson, V.A. Baulin, S. Pogodin, J.Y. Wang, M.J. Tobin, Natural bactericidal surfaces: mechanical rupture of *Pseudomonas aeruginosa* cells by cicada wings, *Small*, 8(16), 2489-2494, 2012.
- [7] M.J. Dalby, N. Gadegaard, R.O. Oreffo, Harnessing nanotopography and integrin-matrix interactions to influence stem cell fate, *Nature Materials*, 13(6), 558-569, 2014.
- [8] A. Valiei, N. Lin, J.-F. Bryche, G. McKay, M. Canva, P.G. Charette, D. Nguyen, C. Moraes, N. Tufenkji, Hydrophilic Mechano-Bactericidal Nanopillars Require External Forces to Rapidly Kill Bacteria, *Nano Letters*, 20(8), 5720-5727, 2020.
- [9] M. Rosenberg, N.F. Azevedo, A. Ivask, Propidium iodide staining underestimates viability of adherent bacterial cells, *Scientific Reports*, 9(1), 1-12, 2019.
- [10] M. Ribeiro, F.J. Monteiro, M.P. Ferraz, Infection of orthopedic implants with emphasis on bacterial adhesion process and techniques used in studying bacterial-material interactions, *Biomatter*, 2(4), 176-194, 2012.
- [11] J. Sjollem, S.A. Zaat, V. Fontaine, M. Ramstedt, R. Luginbuehl, K. Thevissen, J. Li, H.C. van der Mei, H.J. Busscher, In vitro methods for the evaluation of antimicrobial surface designs, *Acta Biomaterialia*, 2018.
- [12] M. van de Lagemaat, A. Grotenhuis, B. van de Belt-Gritter, S. Roest, T.J. Loontjens, H.J. Busscher, H.C. van der Mei, Y. Ren, Comparison of methods to evaluate bacterial contact-killing materials, *Acta Biomaterialia*, 59, 139-147, 2017.
- [13] C. Berne, C.K. Ellison, A. Ducret, Y.V. Brun, Bacterial adhesion at the single-cell level, *Nature Reviews Microbiology*, 16(10), 616-627, 2018.
- [14] Y.F. Dufrêne, A. Persat, Mechanomicrobiology: how bacteria sense and respond to forces, *Nature Reviews Microbiology*, 1-14, 2020.
- [15] M. Köller, N. Ziegler, C. Sengstock, T.A. Schildhauer, A. Ludwig, Bacterial cell division is involved in the damage of gram-negative bacteria on a nano-pillar titanium surface, *Biomedical Physics & Engineering Express*, 4(5), 055002, 2018.
- [16] T. Diu, N. Faruqui, T. Sjöström, B. Lamarre, H.F. Jenkinson, B. Su, M.G. Ryadnov, Cicada-inspired cell-instructive nanopatterned arrays, *Scientific Reports*, 4, 7122, 2014.

- [17] F. Hizal, C.-H. Choi, H.J. Busscher, H.C. van der Mei, Staphylococcal adhesion, detachment and transmission on nanopillared si surfaces, *ACS Applied Materials & Interfaces*, 8(44), 30430-30439, 2016.
- [18] L. Rizzello, B. Sorce, S. Sabella, G. Vecchio, A. Galeone, V. Brunetti, R. Cingolani, P.P. Pompa, Impact of nanoscale topography on genomics and proteomics of adherent bacteria, *ACS Nano*, 5(3), 1865-1876, 2011.
- [19] L. Yang, S. Pijuan-Galito, H.S. Rho, A.S. Vasilevich, A.D. Eren, L. Ge, P. Habibović, M.R. Alexander, J. de Boer, A. Carlier, High-throughput methods in the discovery and study of biomaterials and materiobiology, *Chemical Reviews*, 121(8), 4561-4677, 2021.
- [20] A.I. Greer, V. Goriainov, J. Kanczler, C.R. Black, L.-A. Turner, R.M. Meek, K. Burgess, I. MacLaren, M.J. Dalby, R.O. Oreffo, Nanopatterned titanium implants accelerate bone formation in vivo, *ACS Applied Materials & Interfaces*, 12(30), 33541-33549, 2020.
- [21] M. Ganjian, K. Modaresifar, H. Zhang, P.-L. Hagedoorn, L.E. Fratila-Apachitei, A.A. Zadpoor, Reactive ion etching for fabrication of biofunctional titanium nanostructures, *Scientific Reports*, 9(1), 1-20, 2019.
- [22] S.J. Callens, R.J. Uyttendaele, L.E. Fratila-Apachitei, A.A. Zadpoor, Substrate curvature as a cue to guide spatiotemporal cell and tissue organization, *Biomaterials*, 232, 119739, 2020.
- [23] T. van Manen, M. Ganjian, K. Modaresifar, L.E. Fratila-Apachitei, A.A. Zadpoor, Automated folding of origami lattices: from nanopatterned sheets to stiff meta-biomaterial, *arXiv preprint arXiv:2111.03878*, 2021.
- [24] Z. Chen, A. Bachhuka, F. Wei, X. Wang, G. Liu, K. Vasilev, Y. Xiao, Nanotopography-based strategy for the precise manipulation of osteoimmunomodulation in bone regeneration, *Nanoscale*, 9(46), 18129-18152, 2017.
- [25] M. Nouri-Goushki, A. Isaakidou, B. Eijkel, M. Minneboo, Q. Liu, P. Boukany, M. Mirzaali, L. Fratila-Apachitei, A. Zadpoor, 3D printed submicron patterns orchestrate the response of macrophages, *Nanoscale*, 13(34), 14304-14315, 2021.
- [26] M. Nouri-Goushki, A. Sharma, L. Sasso, S. Zhang, B.C. Van der Eerden, U. Staufer, L.E. Fratila-Apachitei, A.A. Zadpoor, Submicron Patterns-on-a-Chip: Fabrication of a Microfluidic Device Incorporating 3D Printed Surface Ornaments, *ACS Biomaterials Science & Engineering*, 5(11), 6127-6136, 2019.
- [27] U. Horzum, B. Ozdil, D. Pesen-Okvur, Differentiation of normal and cancer cell adhesion on custom designed protein nanopatterns, *Nano Letters*, 15(8), 5393-5403, 2015.
- [28] L. Xie, H. Huang, Z. Zheng, Q. Yang, S. Wang, Y. Chen, J. Yu, C. Cui, MYO1B enhances colorectal cancer metastasis by promoting the F-actin rearrangement and focal adhesion assembly via RhoA/ROCK/FAK signaling, *Annals of Translational Medicine*, 9(20), 2021.
- [29] L. Yan, Y. Yang, W. Zhang, X. Chen, Advanced materials and nanotechnology for drug delivery, *Advanced Materials*, 26(31), 5533-5540, 2014.
- [30] J. Smith, N. Tran, T. Song, D. Liang, M. Qian, Robust bulk micro-nano hierarchical copper structures possessing exceptional bactericidal efficacy, *Biomaterials*, 121271, 2021.
- [31] S. Maher, D. Linklater, H. Rastin, S.T.-Y. Liao, K. Martins de Sousa, L. Lima-Marques, P. Kingshott, H. Thissen, E.P. Ivanova, D. Losic, Advancing of 3D-Printed Titanium Implants with Combined Antibacterial Protection Using Ultrasharp Nanostructured Surface and Gallium-Releasing Agents, *ACS Biomaterials Science & Engineering*, 2021.

Acknowledgements

To my surprise as a diehard fan of Arsenal Football Club, the club's motto describes pretty well what one needs to succeed in his/her academic endeavors: "*Victoria Concordia Crescit*"; victory through harmony. After about four years of working on my PhD project, I realize that being in harmony with people around you, in both your professional and personal life is desired. Because without harmony, it would be impossible to survive the ups and downs of a PhD tenure, no matter how intellectual, skillful, and motivated you are. I was, luckily, privileged by having many amazing individuals around me to whom I am grateful for helping me have a pleasant and productive time as a PhD researcher at TU Delft.

First and foremost, I am grateful to **Amir** for his trust in me to join his research group. **Amir**, you gave me the opportunity to grow scientifically by letting me work on this literally multi-disciplinary and very exciting project. You also always encouraged me to set the standards very high and to be ambitious for the outcome of my research while being fearless of failure as there is always something to learn from the failures. Your amazing ability in reviewing my manuscripts and making important decisions in the shortest time possible saved me so much time and effort on many occasions. I genuinely appreciate your support and guidance during my PhD, especially when things were not working out for me and I was under pressure from every direction. Your understanding and empathy immediately turned the page for me and enabled me to enjoy the rest of my path. Although you were usually extremely busy, I could always knock on your office door and start a conversation about any possible topic. I truly enjoyed and learned a lot from our chats about science, academic life, and living in the Netherlands. The thing I appreciate the most about you is your modesty in sharing your knowledge and experience with others.

I would like to extend my gratitude to **Lidy** whom I was working with in close liaison in the past four years. **Lidy**, without your guidance, I would have struggled to manage a broad project like the one I worked on. While **Amir** gave me the plot of a building, you helped me build it brick by brick. You invested a lot of time in me and my project so that I could swiftly adapt to my new working environment and overcome the initial challenges in my work. I will never forget that despite your extremely busy schedule, you would

always have time for me when I needed to talk about my research. I am grateful for your unconditional support in the past years and truly appreciate your commitment to providing a healthy environment in our bio-lab where we could independently carry out the major studies of our projects. Furthermore, your help enabled me to expand my network and collaborate with many other researchers from different labs when it was required.

When it comes to lab work, it is impossible to successfully perform even the most trivial experiments without proper lab management. I would like to thank our dear (bio)technicians who always strive to maintain the workflow system in our labs. **Michelle**, you officially brought the bio-lab to life shortly after you joined our group. Thank you for the preparation and arrangement of countless protocols, training sessions, and brainstorming meetings. It was a great pleasure to work with you in the lab as you are a highly motivated, committed, and professional individual. Our chats about the Dutch culture, Aruba, and our holiday plans made my time in the lab even more pleasant. I learned a lot from you and managed to find the answer to many important research questions with your support. I wish you all the best in your new job. After **Michelle** left our group, things were about to become chaotic in the lab. Luckily, **Maria** joined us as the new bio-technician and saved us all! Thank you, **Maria**, for bringing the lab back to life. Although you have joined us less than a year ago, you already have increased the amount of established protocols and equipment for the lab. I have enjoyed our chats about movies, books, and social issues and am looking forward to continue working with you in the lab. I am also thankful to **Sander** whose skills, experience, and creativity are unrivaled in giving a solution to any engineering and design problem. Thank you, **Sander**, for providing many things that I needed for my work and for taking care of our safety in the labs area.

Iulian, Jie, and Paul thank you for the chats we had every time we met in the hallway. These conversations usually distracted me from the unnecessary concerns I was holding at the time. I am also thankful to other staff of our department. **Sabrina, Angelique, Nadine, Marjolijn, Mirjam, Marit, and Mascha** thank you for managing all the administrative tasks.

The multidisciplinary nature of my PhD project required me to work in different labs across the TU Delft campus where I had the pleasure of meeting and working with many amazing people. I am thankful to **Peter-Leon** and **Linda** for giving me access to the

microbiological labs of the Biocatalysis group to run the experiments involving bacteria. Thank you, **Peter-Leon** for guiding me in the initial phase of my work. Your insights helped me design my experiments authentically. **Linda**, thank you for teaching me everything I needed to know to perform any assay independently after a short while. Since I started learning Dutch, you and **Laura** always encouraged me to speak with you in Dutch. This definitely enhanced my self-confidence in speaking Dutch. Thanks for all the “roddelen”! I am also grateful to other staff, PhDs, and technicians who helped me on different occasions and did not let me feel like a stranger in the group. Thank you, **Laura, Duncan, Jeremie, Stefan, Sam, Jannie, Rhody**, and **Apilena**.

Nanofabrication was another realm that I had to walk into. I would like to thank the Kavli nanolab staff for facilitating the use of state-of-the-art equipment and processes relevant to my research. Thank you, **Marc, Charles, Eugene, Pauline, Anja, Ewan**, and **Carel**. I am also grateful to **Kees, Dustin**, and **Aya** of the Applied Physics department for their help and support in the imaging and characterization of my samples.

I had the chance to improve the quality and impact of my research through collaboration with many of my colleagues. Thank you, **Mahya, Pedro, Mahdiyeh, Livia, Mohammad, Nazli, Murali**, and **Bram** for our fruitful collaborations. **Nazli**, it was always great to diverge from a discussion on biostatistics to a chat about cats, chocolate, and gummy bears! Thank you for always sharing your delicious snacks with me. Moreover, during my PhD years, I was fortunate to supervise a number of highly talented students which really helped me thrive in another aspect of my academic career. **Manon** and **Lorenzo** (the doctors-to-be!), it was a great pleasure to help you with your MSc thesis projects. Thank you for the pleasant chats about the Netherlands, cats, and bacteria! **Jooske**, your project has just started but I am certain that I will be proud of you when it is finished.

Writing of friends, I am afraid that words would fail me to properly acknowledge their value to me. I was embraced by a super friendly atmosphere in Delft and surrounded by many lovely people who helped me settle down in a blink of an eye. **Mahya**, you were the first person I met in our group and since then, we have shared our office (except for a short time in between). I appreciate your professionalism, commitment, and honesty that let me enjoy not only our friendship but also our collaborations on so many papers, conference abstracts, and presentations. I am not sure if any other two PhD candidates

have ever done that more than we did! Thank you for all the nice memories we made in the office, lab, and football stadiums!

Françoise, I am speechless to thank you for all your help since I moved to the Netherlands. I am thankful for all the times that you selflessly helped me with any issue or question I confronted you with/ I was confronted with about living in the Netherlands. And I appreciate that you encouraged me to speak Dutch and teaching me a lot about it. Your enthusiasm for arranging several events and outings was a profound antidote to the work pressure and brought everyone closer to each other. It was the sweetest of times to be spent with the calm, kind, and enjoyable characters that you, **Thomas**, and **Alex** are. I am sure we will enjoy many more moments together in the future.

Ingmar, I am so glad that I got to know you during my PhD. Our conversations about research, the Dutch language and culture, football, and your funny videos and gifs always made my day. Thank you for helping me with different issues about and beyond my research. I will never forget those cold days in November when we were working on the animal studies in Utrecht. What an experience it was!

Sebastien, it was a pleasure to have you as a colleague. You set very high standards for your work and I, for one, looked up to you and tried to improve my work too. I have enjoyed our philosophical conversations every time we met in the hallway or at the coffee corner. I will never forget the homemade waffles you treated us with every now and then! I wish you and **Delphine** all the best in your future academic career.

Eline, we shared the office for more than a year and during that time you helped me, directly and sometimes indirectly, understand the Dutch culture to a deeper extent. It indeed accelerated the process of integration into the Dutch society for me. I truly enjoyed all our conversations about cats, football, holiday destinations, and nice restaurants in Rotterdam. Best of luck with your new job and hope we meet again in the future.

Niko, **Katerina**, **Pedro**, and **Jiahui** thank you for making the work more pleasant by your presence inside and outside of the lab which usually led to funny and energetic conversations. **Yageng**, I am thankful for the great moments we had playing table tennis and drinking beer. **Costanza**, thanks for bringing immense energy to every conversation and event. The international dinner at your place is a memory I will never forget. I am also happy to have shared very nice moments during lunch or other events with many other friends and colleagues. Thank you, **Teunis**, **Shahram**, **Pedro**, **Juan**, **Gerwin**, **Dirk**,

Monika, Mauricio, Helda, Ebrahim, Vahid, Kirsten, Merle, Fabian, Jelle, Pier, Jette, Jinlai, Yujiang, Bob, Esther, Günnur, Mostafa, Marike, and Shima.

Moving to a new country changes one's personal life dramatically as his/her close friends and family are not around anymore. I was blessed by having true friends who let me go on with my normal social life outside office hours. I would like to particularly thank my dear friends **Hamid** and **Hengameh** for being more than friends to me over the past few years. Thank you for accompanying me through thick and thin, through happiness and sorrow, and for all the unforgettable memories.

I am afraid that any attempt to express my gratitude toward my family would be futile. **Mom, Dad,** and **Arash**, thank you for your love and support, and everything that you did to help me achieve my goals. I am also thankful to my **family-in-law** for their tremendous support and kindness toward me all these years.

Finally, my greatest word of appreciation goes to the love of my life. My lovely, beautiful **Sara**, my whole life changed since the moment I met you. Not a day goes by for me without thinking about how much you have always helped me to be a better version of myself. I am grateful for your unconditional love and support, especially in the last four years that brought me some extremely difficult periods. I could not have finished my PhD without your help. Thank you for your patience with me when I was drowned in work, for cheering me up when I was down, and for helping me by sharing your opinions. I would never worry about what the future brings as I know that you will be there standing by my side.

Doing a PhD was my dream from a very young age. Thank you all for accompanying me in my journey toward it.

List of publications

A. Peer-reviewed journal publications

- **K. Modaresifar**, M. Ganjian, P. J. Díaz-Payno, M. Klimopoulou, M. Koedam, B. C. J. van der Eerden, L. E. Fratila-Apachitei, A. A. Zadpoor, Mechanotransduction in high aspect ratio nanostructured meta-biomaterials: the role of cell adhesion, contractility, and transcriptional factors, In revision, 2022.
- M. Ganjian, S. Janbaz, T. van Mannen, N. Tümer, **K. Modaresifar**, M. Minneboo, L. E. Fratila-Apachitei, A. A. Zadpoor, Controlled metal crumpling as an alternative to folding for the fabrication of nanopatterned meta-biomaterials, In revision, 2022.
- **K. Modaresifar**, M. Ganjian, L. Angeloni, M. Minneboo, M. K. Ghatkesar, P-L. Hagedoorn, L. E. Fratila-Apachitei, A. A. Zadpoor, On the use of black Ti as a bone substituting biomaterial: behind the scenes of dual-functionality, *Small*, 17(24), 2100706, 2021.
- M. Ganjian, **K. Modaresifar**, D. Rompolas, L. E. Fratila-Apachitei, A. A. Zadpoor, Nanoimprinting for high-throughput replication of geometrically precise pillars in fused silica to regulate cell behavior, *Acta Biomaterialia*, 140, 717-729, 2021.
- T. van Mannen, M. Ganjian, **K. Modaresifar**, L. E. Fratila-Apachitei, A. A. Zadpoor, Automated folding of origami lattices: from nanopatterned sheets to stiff meta-biomaterial, arXiv preprint, 2111.03878, 2021.
- M. Nouri-Goushki, L. Angeloni, **K. Modaresifar**, M. Minneboo, P. E. Boukany, M. J. Mirzaali, M. K. Ghatkesar, L. E. Fratila-Apachitei, A. A. Zadpoor, 3D-printed submicron patterns reveal the interrelation between cell adhesion, cell mechanics, and osteogenesis, *ACS Applied Materials & Interfaces*, 13(29), 33767-33781, 2021.
- M. Fazel, H. R. Salimijazi, M. Shamanian, M. Minneboo, **K. Modaresifar**, I. A. J. van Hengel, L. E. Fratila-Apachitei, I. Apachitei, A. A. Zadpoor, Osteogenic and antibacterial surfaces on additively manufactured porous Ti-6Al-4V implants: combining silver nanoparticles with hydrothermally synthesized HA nanocrystals, *Materials Science and Engineering: C*, 120, 111745, 2021.

-
- **K. Modaresifar**, L. B. Kunkels, M. Ganjian, N. Tümer, C. W. Hagen, L. G. Otten, P-L. Hagedoorn, L. Angeloni, M. K. Ghatkesar, L. E. Fratila-Apachitei, A. A. Zadpoor, Deciphering the roles of interspace and controlled disorder in the bactericidal properties of nanopatterns against *Staphylococcus aureus*, *Nanomaterials*, 10(2), 347, 2020.
 - M. Ganjian, L. Angeloni, M. J. Mirzaali, **K. Modaresifar**, C. W. Hagen, M. K. Ghatkesar, P-L. Hagedoorn, L. E. Fratila-Apachitei, A. A. Zadpoor, Quantitative mechanics of 3D printed nanopillars interacting with bacterial cells, *Nanoscale*, 12(43), 21988-22001, 2020.
 - M. Ganjian, **K. Modaresifar**, M. R. O. Ligeon, L. B. Kunkels, N. Tümer, L. Angeloni, C. W. Hagen, L. G. Otten, P-L. Hagedoorn, I. Apachitei, L. E. Fratila-Apachitei, A. A. Zadpoor, Nature helps: toward bioinspired bactericidal nanopatterns, *Advanced Materials Interfaces*, 6(16), 1900640, 2019.
 - M. Ganjian, **K. Modaresifar**, H. Zhang, P-L. Hagedoorn, L. E. Fratila-Apachitei, and A. A. Zadpoor, Reactive ion etching for fabrication of biofunctional titanium nanostructures, *Scientific Reports*, 9(1), 18815, 2019.
 - **K. Modaresifar**, S. Azizian, M. Ganjian, L. E. Fratila-Apachitei, A. A. Zadpoor, Bactericidal effects of nanopatterns: a systematic review, *Acta Biomaterialia*, 83, 29-36, 2019.
 - **K. Modaresifar**, A. Hadjizadeh, H. Niknejad, Design and fabrication of GelMA/chitosan nanoparticles composite hydrogel for angiogenic growth factor delivery, *Artificial Cells, Nanomedicine, and Biotechnology*, 46(8), 1799-1808, 2018.
 - B. Farhadihosseinabadi, M. Farahani, T. Tayebi, A. Jafari, F. Biniazan, **K. Modaresifar**, H. Moravvej, S. Bahrami, H. Redl, L. Tayebi, H. Niknejad, Amniotic membrane and its epithelial and mesenchymal stem cells as an appropriate source for skin tissue engineering and regenerative medicine. *Artificial Cells, Nanomedicine, and Biotechnology*, 46(sup2), 431-440, 2018.
 - S. Azizian, F. Khatami, **K. Modaresifar**, N. Mosaffa, H. Peirovi, L. Tayebi, S. Bahrami, H. Redl, H. Niknejad, Immunological compatibility status of placenta-derived stem cells is mediated by scaffold 3D structure, *Artificial Cells, Nanomedicine, and Biotechnology*, 46(sup1), 876-884, 2018.

-
- F. A. Tehrani, S. Azizian, **K. Modaresifar**, H. Peirovi, H. Niknejad, The antibacterial effect of low temperature stored amnion on growth of *Escherichia coli*, *Staphylococcus aureus*, and *Pseudomonas aeruginosa*, *Journal of Babol University of Medical Sciences*, 20(1), 13-19, 2018.
 - F. A. Tehrani, **K. Modaresifar**, S. Azizian, H. Niknejad, Induction of antimicrobial peptides secretion by IL-1 β enhances human amniotic membrane for regenerative medicine, *Scientific Reports*, 7, 17022, 2017.
 - M. Mirmasoumi, S. Azizian, **K. Modaresifar**, H. Moravvej, H. Niknejad, Evaluation of the effect of amniotic membrane conditioned medium on the activity of Heat Shock protein 90 in cervical and breast cancer cells, *Journal of Advanced Medical and Biomedical Research*, 25(112), 10-20, 2017.
 - **K. Modaresifar**, S. Azizian, M. Zolghadr, H. Moravvej, A. Ahmadiani, H. Niknejad, The effect of cryopreservation on anti-cancer activity of human amniotic membrane, *Cryobiology*, 74, 61-67, 2017.
 - M. Zolghadr, **K. Modaresifar**, S. Azizian, H. Niknejad, Evaluating the effects of fresh and cryopreserved amniotic membrane on viability of HeLa and MDA-MB-231 cancer cells and angiogenesis of rat aorta ring, *Journal of Isfahan Medical School*, 35(424), 340-344, 2017.
 - **K. Modaresifar**, S. Azizian, A. Hadjizadeh, Nano/biomimetic tissue adhesives development: from research to clinical application, *Polymer Reviews*, 56(2), 329-361, 2016.

B. Selected conference presentations

- **K. Modaresifar**, M. Ganjian, M. Minneboo, L. G. Otten, P-L. Hagedoorn, L. E. Fratila-Apachitei, A. A. Zadpoor, Dual-functional small-scale pillars produced by RIE on Ti surface, 11th World Biomaterials Congress (WBC2020: virtual), Glasgow, United Kingdom (2020, oral presentation).
- **K. Modaresifar**, M. Ganjian, M. R. O Ligeon, D. S. Widyaratih, C. W. Hagen, P-L. Hagedoorn, L. G. Otten, L. E. Fratila-Apachitei, A.A. Zadpoor, Physical surface nanofeatures with bactericidal activity, 7th Dutch Bio-Medical Engineering Conference, Egmond aan Zee, The Netherlands (2019, oral presentation).

Curriculum Vitae

Khashayar Modaresifar was born on 22 March 1992 in Tehran, Iran. He graduated from Khatam High School in 2010 and subsequently entered Amirkabir University of Technology to pursue a BSc in Biomedical Engineering with a specialization in Biomaterials. He continued his education with an MSc in Biomedical Engineering (Biomaterials) and graduated in 2017 with a thesis on nano/microstructured hydrogel scaffolds for promoting angiogenesis.

In September 2017, Khashayar moved to The Netherlands to pursue a PhD under the supervision of Prof. Amir A. Zadpoor and Dr. Lidy E. Fratila-Apachitei in the Biomechanical Engineering department at the faculty of Mechanical, Maritime, and Materials Engineering of Delft University of Technology where he conducted research on the development of cell-instructive and bactericidal nanopatterned meta-biomaterials for bone tissue regeneration. He is currently working as a postdoctoral researcher on the role of 3D scaffold architecture and surface curvature on in vitro mineralization in the same research group.

Apart from research, Khashayar has a huge passion for history, politics, philosophy of science, and football. He lives with his spouse, Sara, and their two cats, Lapoe and Halloumi, in Ypenburg, The Hague.

